LUND UNIVERSITY

60 GHz Wireless Propagation Channels: Characterization, Modeling and Evaluation

Gustafson, Carl

2014

Link to publication

Citation for published version (APA):
Gustafson, C. (2014). *60 GHz Wireless Propagation Channels: Characterization, Modeling and Evaluation*. [Doctoral Thesis (compilation), Department of Electrical and Information Technology].

Total number of authors:
1

General rights
Unless other specific re-use rights are stated the following general rights apply:
Copyright and moral rights for the publications made accessible in the public portal are retained by the authors and/or other copyright owners and it is a condition of accessing publications that users recognise and abide by the legal requirements associated with these rights.
• Users may download and print one copy of any publication from the public portal for the purpose of private study or research.
• You may not further distribute the material or use it for any profit-making activity or commercial gain
• You may freely distribute the URL identifying the publication in the public portal

Read more about Creative commons licenses: https://creativecommons.org/licenses/

Take down policy
If you believe that this document breaches copyright please contact us providing details, and we will remove access to the work immediately and investigate your claim.

LUND UNIVERSITY

PO Box 117
221 00 Lund
+46 46-222 00 00

Download date: 20. Dec. 2025

60 GHz Wireless Propagation Channels: Characterization, Modeling and Evaluation

–

Carl Gustafson

Lund 2014

Department of Electrical and Information Technology
Lund University
Box 118, SE-221 00 LUND
SWEDEN

This thesis is set in Computer Modern 10pt
with the LaTeX Documentation System

Series of licentiate and doctoral theses
No. 69
ISSN 1654-790X
ISBN 978-91-7623-183-8

© Carl Gustafson 2014
Printed in Sweden by *Tryckeriet i E-huset*, Lund.
November 2014.

To my friends and family

"The following signal is recorded equally on both channels,
but is out of phase."

from the song
"Jenny Ondioline (Alternate Version)"

on the album
"Transient Random-Noise Bursts With Announcements"

by Stereolab

Sammanfattning

Att trådlöst kunna koppla upp sig mot internet är numera en del av vardagen och antalet enheter som använder sig av trådlös kommunikation har ökat explosionsartat under de senaste årtiondena. År 2018 väntas antalet mobila enheter och anslutningar ha ökat till 10.2 miljarder[1] och väntas därmed överstiga den samlade befolkningen i världen. Dessutom väntas den månatliga mobila datatrafiken i världen år 2018 överstiga 15 exabytes ($15 \cdot 10^{18}$ bytes), vilket är mer än tio gånger som mycket som motsvarande siffra för 2013. Utöver detta så har användandet av strömmande media, s.k. *streamed media*, ökat stadigt genom företag såsom Netflix och Spotify. Under kvällstid i Nordamerika står Netflix för så mycket som 34 % av all trådbunden datatrafik och tillsammans med Youtube utgör de uppemot 50 % av all trådbunden datatrafik.[2] Denna utveckling förväntas fortsätta och kommer i allt större grad omfattas av trådlösa enheter som smartphones, tablets och trådlösa routers. Framtidens trådlösa enheter förväntas därför kunna stödja mycket högre bithastigheter, fler användare och långt fler olika typer av applikationer än vad som är fallet idag. Vi har redan börjat se en utveckling som går mot *prylarnas internet*, eller *the Internet of Things* (IoT), där saker som klockor, hushållsapparater, bilar och olika typer av sensorer kommunicerar med varandra och med internet.

Mobilindustrin och forskare inom en rad olika områden arbetar därför med olika typer av nya teknologier och lösningar på hur framtidens trådlösa kommunkationssystem ska kunna bidra med högre bithastigheter, bättre Quality-of-Service (QoS), samt hur de ska kunna stödja fler användare. Ett stort problem relaterat till detta är att det tillgängliga frekvensutrymmet är begränsat. En lovande dellösning på dessa problem är att utnyttja frekvensbanden inom mm-vågsområdet på 30-300 GHz, som än så länge varit i stort sett outnyttjat av allmänheten. För höghastighetskommunikation över korta avstånd (upp till 10 m) har särskilt stort intresse har riktats mot det frekvensband som ligger kring 60 GHz, där det runtom i världen finns en bandbredd på omkring 7 GHz avsatt,

[1] Detta enligt en prognos framtagen år 2014 av företaget Cisco.
[2] Detta enligt en rapport från Sanvine 2013.

att tillgåför kommunikation. Denna stora bandbredd väntas möjliggöra trådlös kommunikation med bithastigheter upp till 7 Gbit/s. Detta kan jämföras med dagens trådlösa WLAN-system som typiskt uppnår hastigheter upp till 0.6 Gbit/s.

Presentandan som kan uppnås av ett trådlöst kommunikationssytem är emellertid starkt beroende av egenskaperna hos den trådlösa utbredningskanalen, vilket är kanalen som binder samman en radiosändare med en mottagare. Den beskriver hur den mottagna radiosignalen har påverkats i förhållande till den utsända signalen och beror starkt på bl. a. vilken omgivning sändaren och mottagaren befinner sig i och vilken frekvens som används. Mycket forskning har bedrivits kring utbredningskanalens egenskaper för de frekvensband som används idag för mobil kommunikation. Däremot så har det inte forskats alls lika mycket kring utbredningskanalens egenskaper i mm-vågsbandet eller 60 GHz-bandet. På grund av den stora våglängdsskillanden mellan millimetervågor, med våglängder på 1-10 mm, och våglängderna hos de frekvensband som används idag, där våglängden är ca 10 cm, så är utbredningskanalens egenskaper för mm-vågor vitt skilda från egenskaperna hos utbredningskanaler för lägre frekvener. Av denna anledning behöver forskning bedrivas runt egenskaperna hos typiska utbredningskanaler i mm-vågsbandet. Den här avhandlingen fokuserar på typiska inomhus-kanaler i 60 GHz-bandet och innehåller en samling artiklar som karakteriserar, modellerar och utvärderar utbredningskanalens egenskaper för framtida 60 GHz-system.

Artikel I undersöker riktningsegenskaperna hos den trådlösa radiokanalen vid 60 GHz, baserat på mätningar i ett konferensrum. I artikeln identifieras radivågornas typiska utbredningsvägar inom rummet, vilket gör det möjligt att karakterisera hur den mottagna effekten beror på olika riktningar sett från sändarsidan och mottagarsidan, samt hur effekten beror på den fördröjning som sker på grund av att de olika utbredningsvägarna är olika långa. Resultaten visar att huvuddelen av den mottagna effekten kommer från utbredningsvägar med en eller två interaktioner med omgivande föremål. Dessutom visar resultaten att föremål som taklampor och andra mindre föremål ofta är inblandade i betydelsefulla utbredningsvägar.

Artikel II presenterar en kanalmodell för flerantennsystem vid 60 GHz genom att bygga vidare på resultaten från artikel I. Modellen är giltig för godtyckliga antennelement och kan återskapa hur den mottagna signalen typiskt beror på olika riktningar och fördröjningar. Kanalmodellen jämförs även med de kanalmodeller för 60 GHz-system som utvecklats för industristandarderna IEEE802.15.3c och IEEE802.11ad. I artikeln visas också att den presenterade kanamodellen stämmer väl överens med de statistiska egenskaperna hos de uppmätta kanalerna.

Artikel III studerar effekten av människor och andra objekt som block-

erar (d.v.s. skuggar) direktvågen mellan sändaren och mottagaren. Vid lägre frekvenser är påverkan av objekt som skuggar mottagaren oftast inget probelm, eftersom signalen ändå kan ta sig fram genom diffraktion kring det skuggande objektet och genom andra utbredningsvägar runt det skuggande objektet. Vid 60 GHz är dämpningseffekterna från denna typ av skuggning mycket svårare och den mottagna effekten kan vara mycket låg. Av denna anledning väntas 60 GHz-system behöva utnyttja sig av riktade antennstrålar för att kunna ta sig runt skuggande objekt. Detta gör det nödvändigt att kunna karakterisera och modeller effekterna av denna typ av skuggning. I artikeln presenteras mätningar som kvantifierar effekten av skuggdämpningen från objekt som metallcylindrar, plastcylindrar och ett antal olika personers ben. Artikeln visar att dämpningen från dessa olika objekt är likartade och att dämpningen från metallcylindern kan bestämmas med hjälp av en teoretisk modell baserad på geometrisk optik. I artikeln jämförs också dämpningen orsakad av människor med dämpningen från en människofantom (en ihålig modell av en människa utan armar och ben) som fyllts med vatten. Resultaten visar att den vattenfyllda människofantomen har liknande dämpningsegenskaper och kan därför används i mätningar för att simulera skuggdämpningen orsakad av människor.

Artikel IV presenterar ett nytt sätt att modellera och estimera hur den mottagna effekten avtar som funktion av fördröjningen. Tidigare estimerades detta oftast genom att anpassa en rät linje till mätdatan utan att ta hänsyn till att det finns ett brusgolv i mätdatan som gör att det inte går att observera data som råkar befinna sig under nivån som sätts av brusgolvet. Utöver detta så är den uppmätta datan påverkad av slumpmässiga signalvariationer, s.k. *fädning*, vilket också påverkar estimeringen. I den här artikeln presenterar vi en estimeringsmetod som tar hänsyn till alla dessa effekter och estimerar simultant både fädningen och effektavtagandet. I artikeln visas att detta sätt att estimera kan förbättra de estimerade parametrarna avsevärt. Resultaten användes i artikel II och gör att kanalmodellen stämmer bättre överens med de statistiska egenskaperna från mätningarna. Estimeringsmetoden som presenterats i den här artikeln har även applicerats på ett annat estimeringsprobelm gällande utbredningsförluster (s.k. *path loss*).

Artikel V utvärderar kapacitetsförbättringen, i termer av bithastighet, som kan uppnås med hjälp av riktade antennstrålar och genom s.k. spatiell multiplexering där flera dataströmmar skickas parallellt genom att utnyttja separata utbredningsvägar för de olika dataströmmarna. Artikeln jämför dessutom dessa två tekniker och visar under vilka förutsättningar som det är lönsamt att använda sig av spatiell multiplexering istället för riktade antennstrålar. Vidare presenteras ett mått på hur många antenner som krävs för att kunna åstadkomma effektiv spatiell multiplexering.

Artikel VI beskriver ett antal olika metoder för att gruppera olika radiovågor

i kluster baserat på deras riktningar och fördröjningar. Klustringen av data är ett viktigt steg i estimeringen av en riktningsbaserad kanalmodell, eftersom dessa bygger på att man observerat att radiovågskomponenterna dyker upp i specifika kluster i tid och rum. I kanalmodelleringssammanhang har klustringsalgoritmen *K-means* varit den dominerande metoden och användes i artikel II. I den här artikeln påpekar vi att K-means är ett specialfall av en s.k. *mixture* av normalfördelningar. Med anledning av detta presenteras en klustringsmetod baserat på en sådan mixture av normalfördelningar, vilket alltsåär en mer generell klustringsmetod. Denna metod kan hantera kluster med olika stora spridningar i de olika dimensionerna, vilket är något som K-means-algoritmen har svårt att hantera. Efter detta presenteras också en klustringsmetod som bygger på en mixture av asymmetriska Laplace-fördelningar. Denna metod gör det möjligt att identifiera kluster med en assymetrisk form, vilket inte fungerar bra om en mixture av normalfördelningar antas. Dessutom presenteras en hierarkisk klustringsmetod som kan användas för att initiera de övriga klustringsmetoderna.

Artikel VII omfattar kanalmätningar vid 60 GHz i ett stort och ett litet rum, där sändar- och mottagarantennerna är dubbelpolariserade, d.v.s., varje antennelement omfattas av både horisontell och vertikal polarisationsorientering. Med hjälp av dessa mätningar karakteriseras hur polarisationskomponenten hos de olika radiovågorna påverkas av utbredningskanalen. I artikeln undersöks dessutom hur kapaciteten kan förbättras om dubbelpolariserade antennelement används. Utöver detta inkluderar dessa mätningar den vattenfyllda fantomen som presenterats i artikel III för att emulera effekterna av skuggdämpningen från en människa. Resultaten visar att kapaciteten kan förbättras avsevärt genom att använda sig av dubbelpolariserade element och att korspolarisationskopplingen är lägre jämfört med typiska värden för lägre frekvenser.

Sammanfattningsvis har den här avhandlingen förhoppningsvis kunnat bidra med en ökad förståelse för hur den trådlösa utbredningskanalen beter sig för mm-vågssystem i allmänhet och för 60 GHz-system i synnerhet.

Abstract

To be able to connect wirelessly to the internet is nowadays a part of everyday life and the number of wireless devices accessing wireless networks worldwide are increasing rapidly. However, with the increasing number of wireless devices and applications and the amount available bandwidth, spectrum shortage is an issue. A promising way to increase the amount of available spectrum is to utilize frequency bands in the mm-wave range of 30-300 GHz that previously have not been used for typical consumer applications. The 60 GHz band has been pointed out as a good candidate for short range, high data rate communications, as the amount of available bandwidth is at least 5 GHz worldwide, with most countries having 7 GHz of bandwidth available in this band. This large bandwidth is expected to allow for wireless communication with bit rates up to 7 Gbit/s, which can be compared to the typical WLAN systems of today that typically provide bit rates up to 0.6 Gbit/s. However, the performance of any wireless system is highly dependent on the properties and characteristics of the wireless propagation channel. A lot of research has been dedicated to the characterization and modeling of propagation channel properties for frequencies up to 10 GHz. However, due to the much shorter wavelengths, the propagation channel properties for mm-wave bands are quite different from those of lower frequency bands. For this reason, a lot of new research has to be conducted to characterize, model and evaluate the propagation channel properties for mm-Wave bands.

This thesis focuses on indoor short range wireless propagation channels in the 60 GHz band and contains a collection of papers that characterizes, models and evaluates different aspects that are directly related to the propagation channel properties.

Paper I investigates the directional properties of the indoor 60 GHz wireless radio channel based on a set of indoor measurements in a conference room. In the paper, the signal pathways and propagation mechanisms for the strongest paths are identified. The results show that first and second order interactions account for the major contribution of the received power. The results also

show that finer structures, such as ceiling lamps, can be significant interacting objects. Lastly, the multi-path components appear to be clustered in the angular-delay domain, indicating that the 60 GHz channel could be efficiently modeled by a cluster-based double directional model.

Paper II presents a cluster-based double-directional channel model for 60 GHz indoor multiple-input multiple-output (MIMO) systems. This paper is a direct continuation of the results in paper I. The model supports arbitrary antenna elements and array configurations and is validated against measurement data. The validation shows that the channel model is able to efficiently reproduce the statistical properties of the measured channels. The presented channel model is also compared with the 60 GHz channel models developed for the industry standards IEEE802.15.3c and IEEE802.11ad.

Paper III characterizes the effect of shadowing due to humans and other objects. Measurements of the shadowing gain for human legs, metallic sheets, as well as metallic and plastic cylinders are presented. It is shown that the shadowing gain of these objects are fairly similar and that the shadowing due to the metal cylinder can be determined based on the geometrical theory of diffraction. Basic measurements of the impact of polarization are also presented. Next, the shadowing due to a water-filled human body phantom is compared with the shadowing due to real humans. The results show that the water-filled phantom has shadowing properties similar to those of humans and is therefore suitable for use in 60 GHz human body shadowing measurements.

Paper IV presents a novel way of estimating the cluster decay and cluster fading. Previously, the cluster decay has usually been determined by performing a simple linear regression, without considering the effects of the noise floor and cluster fading. The noise floor makes it impossible to observe any possible clusters that are located below the noise floor. Furthermore, the distribution of the cluster fading distribution is being truncated by the noise floor at a certain point depending on the exact delay. The paper presents an estimation method which takes these effects into account and jointly estimates both the cluster decay and cluster fading. It is shown that this estimation method can greatly improve the estimated parameters. It is also shown that if the effects of the noise floor are not taken into account when estimating the cluster decay, the estimated parameters might adversely affect the modeled delay spread. This estimation method was applied in paper II and was also applied to different problem in a paper on path loss estimation techniques.

Paper V evaluates the capacity improvement capability of spatial multiplexing and beamforming techniques for 60 GHz systems in an indoor environment. In this paper, beamforming refers to conventional gain focusing in the direction of the strongest propagation path. The paper uses a capacity metric that only depends on the multi-path richness of the propagation channel and the antenna

aperture size. In the paper, it is shown that, when the link budget is limited due to electrically small antennas and long Tx-Rx separation distances, beamforming approximates the capacity of spatial multiplexing. However, spatial multiplexing is a worthwhile option when Rx SNR is favorable and a higher peak data rate is required. For a transmit power of -10 dBm, a high receive SNR is guaranteed when the antenna aperture is larger than $1\lambda^2$ and $9\lambda^2$ in the LOS and NLOS scenarios, respectively.

Paper VI describes different methods for the clustering of wireless multipath components. In the literature, the clustering method that is predominantly used is the K-means algorithm, or a power-weighted version of K-means, called K-power means. In this paper, we point out that K-means is a special case of a Gaussian mixture model (GMM). The paper presents a clustering method based on a GMM. This method is able to handle arbitrary cluster spreads in the different dimensions better than the K-means algorithm. A power-weighted version of the GMM is also presented. In addition to this, a mixture model based on asymmetric Laplace distributions is also presented, with and without power-weighting. Lastly, a hierarchical method is also presented, which is suggested to be used to initialize the other clustering methods.

Paper VII is based on channel measurements in a small and a large room, where the Tx and Rx arrays have dual polarized elements. Using these measurements, the cross-polarization ratio (XPR) of the multi-path components are characterized. This gives valuable information on how the MPCs are affected by the propagation channel. A statistical description of the XPR is also needed for the development of a propagation channel model that supports polarization. The paper also investigates the eigenvalue spreads for single and dual polarized elements. Furthermore, the measurements include LOS and NLOS measurement, where the NLOS scenarios include water-filled human presented in paper III. The results show that the capacity can be greatly improved if dual-polarized elements are used, and that the XPR values are in general higher compared to lower frequencies.

In summary, this thesis contributes to an increased understanding and knowledge of the behavior and characteristics of propagation channels for mm-wave systems in general and for 60 GHz systems in particular. The results in the thesis are thus useful for the design and development of future wireless systems in the mm-wave range.

Preface

After finishing my Master's Thesis on the interesting topic of antenna design for breast cancer scanning systems, I was encouraged to apply for an open Ph.D. position in the field of 60 GHz wireless propagation. Even though this field was entirely new to me, I was really intrigued by both the topic and the possible opportunity to pursue a career in this new field. After some time, I got the fantastic news that I had gotten the position and I could look forward to delving into a lot of different areas related to the 60 GHz wireless channel.

At the time when I started my Ph.D. studies, the field of 60 GHz wireless communications was buzzing, but had still not quite taken off. Different industrial standards were being worked on and only a small part of the research community were working directly with measured 60 GHz wireless radio channels. We managed to report several relevant findings that are related to the 60 GHz propagation channel. We reported on the directional properties of the indoor 60 GHz channel and derived a MIMO model that was compared with the industry standards. We also looked at shadowing introduced by humans and various objects and how to model this behavior. Also, we investigated how to most effectively transmit data, by comparing spatial multiplexing with beamforming. Lastly, we also report on some estimation problems that are related to the modeling part of my work. Looking back at my work, I realize that my main findings are all, in one way or another, related to the characterization, modeling and/or evaluation of 60 GHz (and millimeter-wave) propagation channels; hence the title of my thesis. Now, almost five years later, it is inspiring to see that the research on 60 GHz and other various mm-wave bands have really taken off. It is also worth mentioning that, even though most of the work in this thesis focuses on the 60 GHz band, a lot of the concepts, ideas and findings in this thesis are applicable to other frequency bands and problems.

This doctoral thesis concludes my work as a Ph.D. student, and is comprised of two parts. The first part gives an overview of the research field in which I have been working during my Ph.D. studies and a brief summary of my contribution in it. The second part is composed of seven included papers that

constitute my main scientific work:

[1] C. Gustafson, F. Tufvesson, S. Wyne, K. Haneda, A. F. Molisch, "Directional analysis of measured 60 GHz indoor radio channels using SAGE", in *IEEE 73rd Vehicular Technology Conference* (VTC Spring), Budapest, Hungary, 2011

[2] C. Gustafson, K. Haneda, S. Wyne, F. Tufvesson, "On mm-Wave Multipath Clustering and Channel Modeling", in *IEEE Transactions on Antennas and Propagation*, Vol. 62, No. 3, pp. 1445-1455, 2014.

[3] C. Gustafson, F. Tufvesson, "Characterization of 60 GHz Shadowing by Human Bodies and Simple Phantoms", in *Radioengineering*, Vol. 21, No. 4, pp. 979-984, 2012.

[4] C. Gustafson, D. Bolin, F. Tufvesson, "Modeling the Cluster Decay in mm-Wave Channels", in *8th European Conference on Antennas and Propagation (EuCAP)*, pp.804-808, 6-11 April 2014.

[5] K. Haneda, C. Gustafson, S. Wyne, "60 GHz Spatial Radio Transmission: Multiplexing or Beamforming?", in *IEEE Transactions on Antennas and Propagation*, Vol. 61, No. 11, pp. 5735-5743, 2013.

[6] C. Gustafson, D. Bolin, J. Wallin, F. Tufvesson, "A Note on Clustering Methods for Wireless Channel Models", (submitted to *IEEE Transactions on Wireless Communications*, Nov. 2014.)

[7] C. Gustafson, F. Tufvesson, "Polarimetric Propagation Channel Characterization at 60 GHz with Realistic Shadowing", (submitted to *IEEE Antennas and Wireless Propagation Letters* Nov. 2014).

During my Ph.D. studies, I have also contributed to the following publications. However, these publications are not included in the thesis:

[7] L. Ohlsson, T. Bryllert, C. Gustafson, D. Sjöberg, M. Egard, M. Ärlelid, L. E. Wernersson, "Slot-Coupled Millimeter-Wave Dielectric Resonator Antenna for High-Efficiency Monolithic Integration", in *IEEE Transactions on Antenas and Propagation*, Vol. 61, No. 4, pp. 1599-1607, 2013.

[8] A. Bernland, M. Gustafsson, C. Gustafson, F. Tufvesson, "Estimation of Spherical Wave Coefficients from 3D Positioner Channel Measurements", in *IEEE Antennas and Wireless Propagation Letters*, Vol. 11, pp. 608-611, 2012.

[9] K. Haneda, K. Afroza, C. Gustafson, S. Wyne, "Spatial Degrees-of-Freedom of 60 GHz Multiple-Antenna Channels", in *IEEE 77th Vehicular Technology Conference* (VTC Spring), 2013, Dresden, Germany, June 2013.

[10] C. Gustafson, F. Tufvesson, "Characterization of 60 GHz Shadowing by Human Bodies and Simple Phantoms", in *6th European Conference on Antennas and Propagation* (EuCAP), Prague, Czech Republic, pp. 473-477, March 2012.

[11] C. Gustafson, A. Johansson, "Archimedean spiral antenna for underground soil measurements in Greenland", in *4th European Conference on Antennas and Propagation* (EuCAP), Barcelona, Spain, April 2010.

[12] T. Abbas, C. Gustafson, F. Tufvesson, "Pathloss Estimation Techniques for Incomplete Channel Measurement Data", in *IC1004 10th Management Committee and Scientific Meeting* (COST), Aalborg, Denmark, May 2014.

[13] C. Gustafson, D. Bolin, J. Wallin, F. Tufvesson, "A Note on Clustering Methods for Wireless Channel Models", in *IC1004 10th Management Committee and Scientific Meeting* (COST), Aalborg, Denmark, May 2014.

[14] A. Bernland, M. Gustafsson, C. Gustafson, F. Tufvesson, "Estimation of Spherical Wave Coefficients from 3D Positioner Channel Measurements", in *Technical Report LUTEDX/(TEAT-7215)/1-11*, 2012.

Acknowledgements

First and foremost, I would like to express my sincere thanks to my supervisor, Professor Fredrik Tufvesson, for his support, encouragement, valuable feedback, and for his professional and positive attitude towards research. His deep knowledge in the field of wireless research and original ideas have been a constant source of inspiration. Working with Fredrik has been a wonderful experience. I am also grateful to my two co-supervisors, Professor Daniel Sjöberg and Dr. Anders J Johansson for their support in various scientific (and un-scientific) matter and fruitful discussions. I also want to thank Professor Andreas F. Molisch for invaluable discussions and feedback on various research ideas. I always felt that his presence at the department during his short visits were always highly appreciated by everyone involved. Another person that has been a constant source of inspiration is Dr. Katsuyuki Haneda. I am deeply grateful for having had the pleasure of collaborating with him on several different research projects. His ideas, comments and suggestions has inspired me on many different levels.

I especially want to thank my friend Dr. David Bolin for being a really good friend and for sharing his great personal taste in music. During the later years of my Ph.D. studies, I also had the pleasure of collaborating with David on a professional level. His great expertise in the field of mathematical statistics and his ability to come up with great ideas on the spot has been a true source of inspiration. My sincere thanks also goes out to Dr. Taimoor Abbas, for being a great colleague and for his great attitude and positivity. Taimoor was always happy to share his ideas and thoughts on things, large and small.

I am also very happy to have been a part of the mm-wave research group, that was a part of the SSF Cneter for High Speed Wireless Communication, and want to thank everyone involved in this project for their ideas and for all the fruitful collaborations within this group. I want to thank Professor Lars-Erik Wernersson, Professor Mats Gustafsson, Professor Daniel Sjöberg, Professor John B. Anderson, Professor Henrik Sjöland, Dr. Erik Lind, Dr. Mats Ärlelid, Dr. Mikael Egard, Alexander Bondarik, Lars Ohlson and Iman Vakili for all

their support and encouragement.

I grateful to all my research partners, co-authors and collegues, including, but not limited to: Professor Ove Edfors, Dr. Tommy Hult, Dr. Ghassan Dahman, Dr. Johan Kåredal, Dr. Buon Kion Lau, Dr. Fredrik Rusek, Dr. Kristin Persson, Dr. Anders Bernland, Dr. Rohit Chandra, Dr. Meifang Zhu, Xiang Gao, M. Atif Yaqoob, Nafiseh Seyed Mazloum, Jose Flordelis, Mikael Nilsson, Joao Vieira and Muris Sarajlic.

I also want to thank the technical and administrative staff at the department, for their dedicated work and prompt responses. I want to thank Lars Hedenstjärna for his ingenious technical solutions for my measurement-related equipment.

I want to give special thanks to the Swedish Foundation for Strategic Research for funding my research. I also want to give special thanks to Professor Lars-Erik Wernersson and Vetenskapsråget, for the funding for the last years of my research.

Finally, I would like to thank my family, without whom I could not have achieved this much. I am deeply grateful for the endless support and encouragement from my parents, Anna and Lasse, and from my brother, Erik. I also want to express my gratitude to all my friends. You know who You are.

Carl Gustafson

List of Acronyms and Abbreviations

ACF auto-correlation function

AL Asymmetric Laplace

AOA Angle of arrival

AOD Angle of departure

CDF Cumulative distribution function

CIR Channel impulse response

CSI Channel state information

DOA Direction of arrival

DOD Direction of departure

DS Delay spread

EM Electromagnetic

ETSI European telecommunication standards institute

FDTD Finite-difference time-domain

FEM Finite element method

GMM Gaussian mixture model

GSCM Geometry based stochastic channel model

GSM Global system for mobile communications

IEEE Institute of Electrical and Electronics Engineers

IoT Internet of things

ISI Inter-symbol-interference

LOS Line-of-sight

LTE Long-term evolution

LTI Linear time invariant

LTV Linear time variant

MBCM Measurement based channel modeling

ML Maximum-likelihood

MIMO Multiple-input multiple-output

MSE Mean square error

MSRRE Mean square relative reconstruction error

MPC Multi-path component

NLOS Non line-of-sight

OFDM Orthogonal frequency division multiplexing

OLS Ordinary least squares

OLOS Obstructed line-of-sight

PDP Power delay profile

PDF Probability density function

RMS Root mean square

RT Ray-tracing

RX Receiver

SAGE Space-alternating generalized expectation maximization

SF Shadow fading

SISO Single-input single-output

SVD Singular value decomposition

TDL Tap-delay-line

TX Transmitter

US Uncorrelated scattering

WLAN Wireless local area network

WPAN Wireless personal area network

WSSUS wide-sense-stationary uncorrelated-scattering

Contents

Part I

Overview of Research Field

Chapter 1

Introduction

Sir Jagadish Chandra Bose held a public demonstration in the late 1800s, where he ignited gunpowder and rang a bell at a distance using millimetre range wavelength microwaves, signaling the start of mm-wave wireless research. Furthermore, it has been claimed that the wireless detection device used by Marconi to receive the first transatlantic wireless signal on December 12, 1901, was in fact invented by Sir J.C. Bose [1]. Since then, the wireless techniques have gradually become more and more sophisticated, and have now been integrated with our everyday lives and are being used in numerous different applications.

However, the number of users and applications are still growing, and there is still a need for higher data rates. This is an issue, sine the available bandwidth is a limited resource. A promising way to increase the amount of available bandwidth is to use higher frequency bands such as the mm-wave frequency bands. Much like in the demonstration by Sir Bose, the 60 GHz band is intended for short range wireless transmission. However, the mm-wave systems of tomorrow are expected to provide wireless data rates that are significantly higher compared to what is typically achieved in the lower frequency bands that are commonly used today.

The use of mm-wave frequencies also requires a lot of dedicated research. The propagation properties for typical mm-wave wireless channels are widely different from those of lower frequency bands. So, in order to facilitate the development of mm-wave systems, the propagation characteristics of mm-wave wireless channels need to be characterized, modeled and evaluated.

Wireless systems in the mm-wave range are expected to be used for various applications, ranging from short range communication and on-body wireless devices, to cellular communication and inter-chip communication. Another benefit of mm-wave systems is that the form factor of the antennas are much smaller,

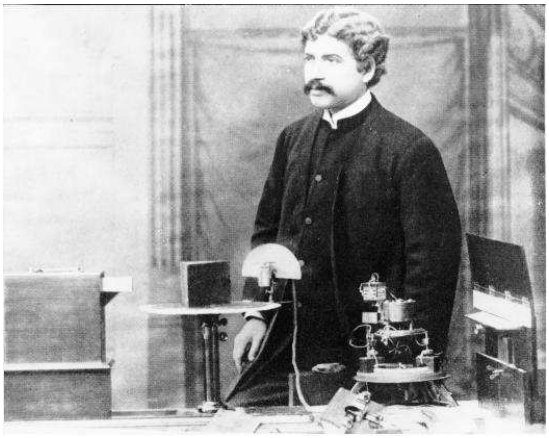

Figure 1.1: Sir Jagadish Chandra Bose.

making it possible to put a large number of antennas on a small area. This is truly beneficial, as the mm-wave systems are expected to use beam-forming to ensure reliable communication. Also, multiple-input multiple-output techniques such as spatial multiplexing, where the data is transmitted in several parallel spatial streams, could be of use in some mm-wave systems.

This thesis focuses on the propagation channel for 60 GHz systems. Chapter 2 gives an introduction to 60 GHz and millimeter-wave wireless communication. Chapter 3 discusses propagation channel aspects such as channel modeling approaches and channel models for 60 GHz and mm-wave systems. Chapter 4 treats different estimation methods that are necessary for the development of wireless channel models. Chapter 5 presents different measurements techniques for wireless channel measurements as well as antenna measurements. Finally, chapter 6 summarizes the contributions of the thesis and lists topics for future work in this field.

Chapter 2

60 GHz and millimeter-wave wireless systems

The number of wireless devices accessing wireless networks worldwide are increasing rapidly. According to a forecast by Cisco in 2014 [2], the number of mobile devices and connections will grow to 10.2 billion by 2018, exceeding the world's population. Furthermore, the monthly global mobile data traffic is expected to surpass 15 exabytes by 2018, which is more than ten times that of 2013. Also, over the last few years, there has been a tremendous increase of streamed media through networking services such as YouTube, Netflix and others. This puts a huge pressure on the mobile industry and research community to come up with new technologies and solutions to provide wireless systems that offers a good quality of service (QoS) and high data rates at a reasonable price. Bandwidth is a key resource that is essential for any wireless system. With the increasing number of wireless devices and applications and the amount available bandwidth, spectrum shortage is an issue. A promising way to increase to amount of available spectrum is to utilize frequency bands in the mm-wave range of 30-300 GHz that previously have not been used for typical consumer applications.

2.1 Why mm-Waves?

The mm-wave band refers to the frequency band of 30-300 GHz, where the wavelength are in the range of 1-10 mm, hence the name mm-waves. An important question to be asked is: Should we use mm-wave frequencies for everyday consumer applications? The answer to this question is yes. With the increasing number of users and applications, spectrum shortage is an issue, and a promising way to increase the amount of available spectrum is to utilize frequency bands in the mm-wave range that previously have not been used for typical consumer applications. With the advance of radio and CMOS technology, typical consumer applications at mm-wave frequencies are nowadays feasible both in terms of performance and cost.

However, mm-wave systems are inherently different from lower frequency band systems, and a lot of this is related to differences in the physical propagation mechanisms at different frequencies. An important difference for mm-wave systems, compared to systems at lower frequencies, is that the radio waves in general experience greater attenuation. Systems at mm-wave frequencies suffers from a larger free space pathloss (assuming constant-gain antennas), a higher penetration loss and more significant shadowing due to obstructing objects. As a result, the achievable communication range is in general shorter for mm-wave systems, although long-range point-to-point mm-wave links do exist. As an example, the 60 GHz band is targeted for short-range, high data rate communications for device-to-device and and WLAN communications. However, due to the nature of 60 GHz radio propagation, the communication range is typically confined within a single room. This is due to the large pathloss and penetration loss at 60 GHz. However, this may also be a benefit for the system, since it will experience less interference from other nearby users operating at the same frequency, allowing for a larger potential of frequency reuse. Also, the large bandwidths available at mm-wave frequency bands will allow for wireless data rates that are significantly higher compared to today. This could for instance allow uncompressed wireless streaming of high-definition (HD) video.

Another interesting aspect of mm-wave systems is the small form factor of the antennas. The antenna size is related to the wavelength, which means that multiple antenna elements can be packaged onto a small area and can even be integrated on a chip. See for instance [3, 4] and the references therein.

2.2 Applications and Industry Standards

A large number of different mm-wave applications are envisioned. Some that are already in use include high data rate WPAN systems, car radars and satel-

lite systems. Other future applications include the following:

- Millimeter wave communication for fifth generation (5G) broadband cellular communication [5].
- Millimeter-wave for wireless backhaul connections [6].
- High data rate device-to-deivce, in-plane [7, 8] and in-car [9] communications.
- High data rate inter-chip communications [10, 11].
- Wireless short-range, high-precision localization systems [12].

This thesis focuses mostly on the 60 GHz indoor propagation channel. Table 2.1 shows the frequency allocation in the major regions worldwide, for systems operating in the 60 GHz band. In most of these regions, at least 5 GHz is available. In Europe, as much as 9 GHz of continuous spectrum is available.

Table 2.1: Worldwide frequency allocation for 60 GHz wireless systems.

Region	Frequency band (GHz)	Bandwidth (GHz)
Australia	59.4-62.9	3.5
Canada & USA	57-64	7
China	59-64	5
Europe	57-66	9
Japan	59-66	7

Some of the industry standards that drive the development of mm-wave wireless multi-gigabit wireless communications technology include the IEEE.802.15.3c [13] and IEEE.802.11ad [14] standards. Previously, the Wireless Gigabit Aliance (WiGig), was a trade association that promoted the use of the unlicensed 60 GHz band for muti-gigbit wireless communications. The Wi-Fi Alliance and WiGig Alliance finalized a unification in March, 2013, and now operates under the Wi-Fi alliance name.

2.3 mm-Wave Systems, MIMO and Capacity

A MIMO radio or propagation channel matrix, $\mathbf{H}$, for a system with N_r receive antennas and N_t transmit antennas, can be described as

$$\mathbf{H}(t,\tau) = \begin{pmatrix} h_{1,1}(t,\tau) & h_{1,2}(t,\tau) & \cdots & h_{1,N_t}(t,\tau) \\ h_{2,1}(t,\tau) & h_{2,2}(t,\tau) & \cdots & h_{2,N_t}(t,\tau) \\ \vdots & \vdots & \ddots & \vdots \\ h_{N_r,1} & h_{N_r,2} & \cdots & h_{N_r,N_t}(t,\tau) \end{pmatrix} \in \mathbb{C}^{N_r \times N_t}, \tag{2.1}$$

where $h_{m,n}(t,\tau)$ is the impulse response at time t and delay τ, between the nth and mth transmit and receive antenna, respectively. The input-output relation of the MIMO channel can then be described in matrix notation as

$$\mathbf{y}(t,\tau) = \mathbf{H}(t,\tau) \star \mathbf{s}(t,\tau) + \mathbf{n}(t,\tau), \tag{2.2}$$

where $\star$ denotes the convolution operator, $\mathbf{y} \in \mathbb{C}^{N_r \times 1}$ is the received signal vector, $\mathbf{s} \in \mathbb{C}^{N_t \times 1}$ is the transmitted signal vector and $\mathbf{n} \in \mathbb{C}^{N_t \times 1}$ is the noise vector. For a narrowband (*i.e.*, frequency flat) MIMO link, this relation can be written as

$$\mathbf{y}(t) = \mathbf{H}(t)\mathbf{s}(t) + \mathbf{n}(t) = \sqrt{\frac{\rho}{N_t}}\hat{\mathbf{H}}(t)\mathbf{s}(t) + \mathbf{n}(t), \tag{2.3}$$

where ρ is the SNR per receiver branch. For such a narrowband MIMO channel, the capacity, in units of bits/s/Hz, can be shown to be given by

$$C = \max_{\mathrm{Tr}(\mathbf{R_{ss}})=\mathrm{N_t}} \left\{ \log_2 \det \left(\mathbf{I}_{N_r} + \frac{\rho}{N_t} \hat{\mathbf{H}} \mathbf{R_{ss}} \hat{\mathbf{H}}^H \right) \right\}, \tag{2.4}$$

where $\mathbf{R_{ss}} = \mathrm{E}\{\mathbf{s}\mathbf{s}^H\}$ is the covariance matrix of $\mathbf{s}$.[1] Eq. 2.4 is suitable for use when comparing measurements from different locations as a function of the SNR, ρ.

If the channel is completely unknown to the transmitter, so that is has no channel state information (CSI), then $\mathbf{s}$ may be chosen with equal power allocation to all the transmit antennas such that $\mathbf{R_{ss}} = \mathbf{I}_{N_t}$. For this case, it can be shown that the capacity is given by

$$C = \sum_{i=1}^{r} \log_2 \left(1 + \frac{\rho}{N_t} \lambda_i \right), \tag{2.5}$$

[1] Furthermore, $\mathrm{Tr}(\cdot)$ denotes the trace of a matrix, $(\cdot)^H$ denotes Hermitian transpose, $\det(\cdot)$ denotes a matrix determinant and $\mathbf{I}$ is an identity matrix.

where r is the rank of the channel and λ_i is the ith positive eigenvalue of $\hat{\mathbf{H}}\hat{\mathbf{H}}^H$. If the transmitter instead has perfect CSI, *i.e.*, the capacity can be optimized by solving the maximization problem

$$C = \max_{\sum \gamma_i = N_t} \left\{ \sum_{i=1}^{r} \log_2 \left(1 + \frac{\rho \gamma_i}{N_t} \lambda_i \right) \right\}, \tag{2.6}$$

where γ_i is the transmit energy in the ith sub-channel, subject to $\sum_i \gamma_i = N_t$. This optimization problem can be solved by the solved by the so-called water-pouring algorithm.

Chapter 3

60 GHz and millimeter-wave Propagation Channels

In this chapter, various aspects related to the millimeter-wave propagation channel are treated. Different channel modeling approaches are discussed and related to mm-wave systems. Then, large-scale channel parameters such as pathloss, large-scale fading and human body shadowing are treated. Finally, double-directional MIMO channel models for 60 GHz and mm-wave systems, which include both large-scale and small-scale effects, are presented.

3.1 Wireless Channel Modeling Approaches

A realistic wireless channel model is vital for the development of a reliable wireless system design. Before any detailed system design can be performed, accurate characterization and modeling of the propagation channel is required, since all the different layers of a wireless system need to relate to the characteristics of the propagation channel at hand. A good wireless channel model can efficiently reproduce the typical behavior of the wireless channel and give insights into the most relevant radio propagation mechanisms. These channel models are often implemented as channel emulators and simulators, so that the performance aspects of many different parts of the wireless system of interest can be evaluated and optimized.

However, modeling the wireless channel is challenging due to the many dif-

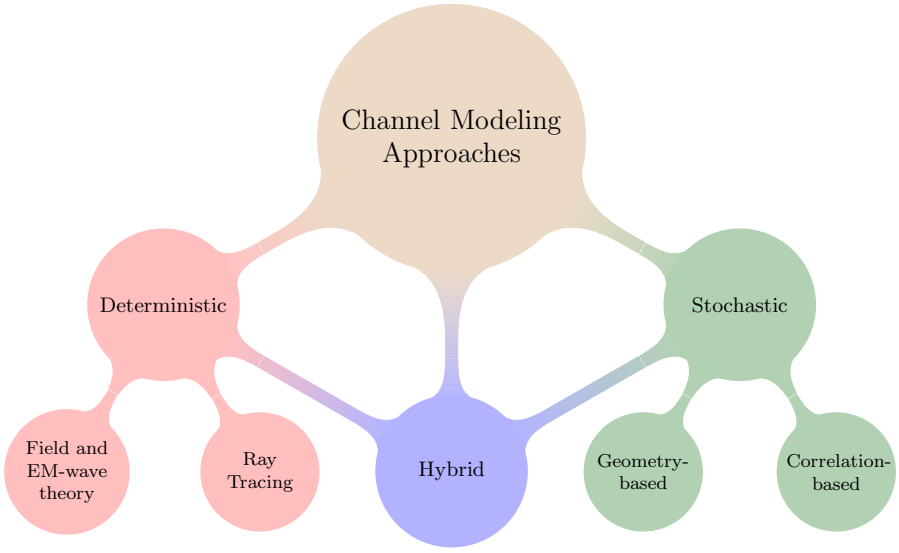

Figure 3.1: Modeling approaches for wireless channels.

ferent complex mechanisms that govern wireless propagation. Therefore, most channel models rely on a tradeoff between accuracy and simplicity. Hence, the goal of a channel model is often to capture the aspects that are of importance to the wireless system, without being too complex so that it is easy to implement and use. Different channel modeling approaches are used depending on the system in question and its intended use. Factors like carrier frequency, bandwidth and propagation environment play an important role when it comes to choosing an appropriate modeling approach.

Figure 3.1 shows a classification of the most common types of channel modeling approaches. The two main categories are *stochastic* and *deterministic* modeling approaches, which can be sub-categorized further. Deterministic modeling approaches can be based on, for instance, ray tracing, field theory or electromagnetic wave theory using Maxwell's equations. Another example of a deterministic channel modeling approach is to directly use measured data. However, such a model relies on the use of a large amount of measurement data, making it impractical to use and distribute. Furthermore, when using measurement data directly, it is difficult to get a grasp of the physical processes that are causing the measurement data to behave in a certain way.

Many deterministic approaches, such as ray tracing or electromagnetic sim-

ulations, are inherently site-specific, which makes them better suited for cases when this is desired, such as for base station placement or coverage analysis for a specific environment. For these cases, deterministic approaches can be of great value. On the other hand, site-specific approaches require an environment model, which can be very complex depending on the environment and the desired modeling accuracy. Hence, these methods can often be computationally expensive.

Stochastic approaches aim at reproducing the statistical behavior of the channel. Correlation-based methods do this modeling the correlation properties of the channel. This can be done using the full correlation matrix between all Tx and Rx elements for a given MIMO channel. However, using the full correlation matrix requires a large number of model parameters, which often makes it too complex. Instead, simplified models, such as the Kronecker model [15], are often used. The more sophisticated Weichselberger model [16] is a another popular correlation-based model.

In geometry-based stochastic channel models (GSCMs), an ensemble of point scatterers are typically placed in different geometrical positions based on statistical distributions. Different scatterers can be assigned different properties and the channel is determined by summing the contribution from the different scatterers at the receiver [17]. Cluster-based double-directional channel models can also be seen as GSCMs. In these models, multi-path component (MPC) cluster centroids, as well as the MPCs within each cluster, are determined based on statistical distributions for the delays and angles. A benefit of GSCMs are that the directional aspect of the channel is included in the modeling, making it possible to use these models for theoretical analysis that involves the directional properties of the channel. Also, it is easier to relate the model parameters to the physical propagation mechanisms that are involved. More importantly, as the modeling involves directions, the influence of the antenna gain can be de-embedded, making it possible to derive a model that is truly describing the *propagation channel*.

Fig. 3.2 highlights the difference between a *radio channel* and a *propagation channel*. In the radio channel, the effects of the Tx and Rx antenna (antenna gain, polarization mismatch, etc.) are included in the channel, whereas the propagation channel only describes the effect of the channel without any influence of the antennas. Ideally, the propagation channel is the channel that the radio system would experience when using isotropic Tx and Rx antenna elements. A GSCM that describes the propagation channel is valid for arbitrary antenna elements and array configurations, and the radio channel for a given antenna array can be derived from the propagation channel model simply by adding the antenna patterns and array configuration for the antenna array of interest.

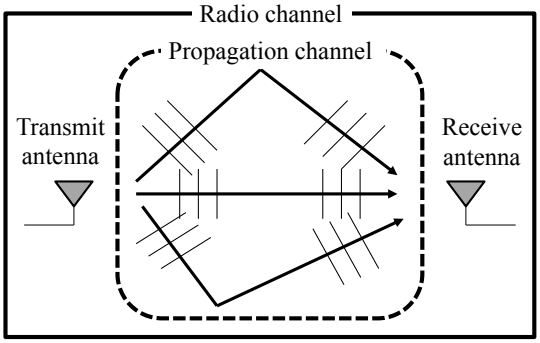

Figure 3.2: The propagation channel can be extracted from radio channel measurements if the double-directional channel is estimated using the radiation patterns of the Tx and Rx antennas.

Hybrid models are based on a combination of stochastic and deterministic parts. For instance, a GSCM might be used together with ray-tracing, so that the cluster positions are determined using ray-tracing, but the MPCs within a cluster are stochastic.

3.1.1 Modeling Approaches for mm-wave Systems

For any type of wireless system, the modeling approach usually depends on the intended use of the system and the intended use of the model. For mm-wave backhaul links, simpler modeling approaches that include pathloss and additional losses due to oxygen absorption and precipitation might suffice. However, for indoor, in-car or in-plane mm-wave scenarios, a more general model approach is usually required. A popular approach for wideband multi-antenna systems has so far has been to use a GSCM, with or without parts that are deterministic.

In the literature, many 60 GHz indoor models are rooted in the Saleh-Valenzuela (SV) model [18], in which the multi-path components (MPCs) arrive in clusters in the delay domain. The mean cluster power is exponentially decaying with delay according to a certain time decay constant. The mean power of the MPCs in each cluster is also decaying exponentially with delay, but with a different decay constant. The SV model has also been extended to include the angular domain [19]. In [20], the double-directional model was proposed, in which the channel is described as a sum of a number of plane waves (MPCs) each having a certain complex amplitude, delay and directions of departure and arrival. Most of the recent work on 60 GHz indoor channel

modeling is based on a double-directional modeling approach with a modified SV model that is extended to the angular domain. In Table 3.1, a number of 60 GHz indoor models in the literature are summarized, and the included domains in each reference are listed. Here, τ is the delay, ϕ_{Tx} and θ_{Tx} are the azimuth and elevation direction of departure (DOD) and ϕ_{Rx} and θ_{Rx} are the azimuth and elevation direction of arrival (DOA), respectively. Although not exhaustive, Table 3.1 shows that modeling approaches are moving towards approaches where all the different domains are included.

Table 3.1: Various 60 GHz indoor channel models in the literature.

Environment	τ	ϕ_{Tx}	θ_{Tx}	ϕ_{Rx}	θ_{Rx}	Ref.	Year	Note
Various	✓	-	-	-	-	[21]	2005	
Laboratory	✓	-	-	-	-	[22]	2010	
Hospital	✓	-	-	-	-	[23]	2012	
Corridor	✓	-	-	✓	-	[24]	2005	
Various	✓	-	-	✓	-	[13]	2009	802.15.3c
Room	✓	-	-	✓	✓	[25]	2009	
Various	✓	✓	✓	✓	✓	[14]	2010	802.11ad
Conf. Room	✓	✓	✓	✓	✓	[26]	2014	This work

The IEEE802.11ad channel model [14] constitutes a mix of measurement-based stochastic parameters, ray tracing, empirical distributions and theoretical models. Ray tracing is used to determine the cluster delays and angles, empirical distributions are used for the amplitude and intra-cluster angular distribution of reflected rays and theoretical models for the polarization properties. Blockage models for human body shadowing are included on top of the modeling framework. The IEEE802.15.3c channel model [13] is a SIMO channel model that only includes the azimuth DOD. The details of these two industrial channel models will be discussed in more detail in the next chapter.

For general mm-wave channel modeling, a stochastic or hybrid GSCM is an attractive approach. The main reasons as to why this is the case can be summarized as they:

- Support wideband channel modeling.
- Include both large-scale and small-scale fading effects and the antenna correlation.
- Can be used to derive a propagation channel model that is valid for arbitrary antenna elements and array configurations.

- Model the directional properties of the channel, which is vital for beamforming and human body shadowing analysis.
- Support geometrical human body shadowing models that can easily be added to the model framework [27].

3.2 SISO Channel Characterization & Modeling

SISO channel models constitute more of a characterization of some important measures, such as path loss, large scale fading (shadow fading), power delay profile, delay spread, etc.

3.2.1 Pathloss and Large-scale Fading

The pathloss can be defined as the ratio of the transmit power to the received signal power power as a function of the Tx-Rx separation distance. A good pathloss model is essential for link budget analysis and network planning. Before we consider the general pathloss models, we will briefly look at the free space pathloss (FSPL), which is the pathloss for two isotropic antennas in free space separated by a distance d, and is given by

$$\mathrm{FSPL}(d) = \left(\frac{4\pi d}{\lambda}\right)^2 = \left(\frac{4\pi df}{c_0}\right)^2. \tag{3.1}$$

Here, it is seen that the FSPL is proportional to the square of the carrier frequency, *i.e.*, FSPL $\propto f^2$, resulting in a much more severe FSPL for mm-wave systems. Fig. 3.3 shows the FSPL at 2.4, 60 and 300 GHz, as a function of distance. Compared to the FSPL for a given distance at 2.4 GHz, the FSPL is about 28 dB larger for 60 GHz and about 42 dB larger for 300 GHz.[1] It is possible to combat the increased FSPL at mm-wave frequencies by using antennas with higher gain or using multiple antenna array elements to achieve beamforming gain.

However, in a realistic multi-path environment, the antennas are no longer in free space and the signal will reach the Rx through several different paths. For these cases, the path loss is often modeled by a log-distance power law [28], which in units of dB can be written as

[1] Note that this is due the assumption that the antenna gain is constant over frequency, resulting in a smaller antenna aperture at higher frequencies. The so called "loss" is due to the expansion of the radio wave front in free space.

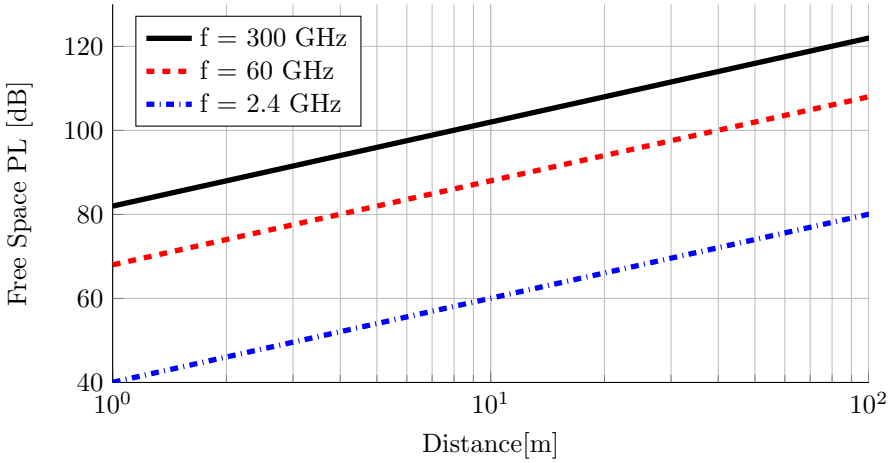

Figure 3.3: Free space pathloss at 2.4, 60 and 300 GHz as a function of distance.

$$PL(d) = PL(d_0) + 10n\log_{10}\left(\frac{d}{d_0}\right) + \Psi_\sigma, d \geq d_0, \tag{3.2}$$

where d is the distance, n is the pathloss exponent, $PL(d_0)$ is the pathloss at a reference distance of d_0 and Ψ_σ is a random variable that describes the large-scale fading about the distance-dependent mean path loss. If the effect of the small scale fading is removed from the data set by averaging the data over the time samples corresponding to a wide-sense-stationary region, the large-scale fading can be modeled as a log-normal distribution which in the dB-domain corresponds to a zero-mean Gaussian distribution with standard deviation σ, i.e., $\Psi_\sigma \sim \mathrm{N}\left(0, \sigma^2\right)$. Hence, the pathloss is normally distributed with a distance dependent expected value, *i.e.*, $PL(d) \sim \mathrm{N}\left(\mu(d), \sigma^2\right)$, where

$$\mu(d) = PL(d_0) + 10n\log_{10}\left(\frac{d}{d_0}\right). \tag{3.3}$$

The reference value $PL(d_0)$ can be estimated based on measurement data, or based on reference measurements at this distance. For LOS scenarios, it is sometimes deterministically calculated based on the free-space pathloss, as

$$PL(d_0) = 20\log_{10}\left(\frac{4\pi d_0}{\lambda}\right). \tag{3.4}$$

Here λ is the wavelength at the given frequency. For NLOS scenarios, the free-space equation does not hold, which means that the reference value in this case must be determined in another fashion. Since it might be difficult to produce reliable measurements of the reference value in NLOS scenarios, it is often estimated based on the measurement data.

Pathloss and Large-scale Fading Estimation

In [29], it was shown that the censoring of data samples below the noise floor can have a significant impact on the estimated pathloss parameters, both for the pathloss exponent, large-scale fading variance and the reference value $PL(d_0)$. Furthermore, as discussed above, note that, in NLOS scenarios, the reference value needs to be estimated, since the theoretical free-space path loss is no longer valid. For these reasons, some of the reported pathloss parameters in the literature, especially for NLOS scenarios, might be inaccurate. In this section, a pathloss estimation technique for censored data is presented.[2]

To completely model the pathloss and large-scale fading for a given data set, we wish to estimate the three parameters of (3.2), i.e., n, $PL(d_0)$ and σ^2. The data under consideration is implicitly assumed to be Gaussian distributed since Ψ_σ is Gaussian in the dB domain. Using (3.2) the data set for L path loss measurements can be modeled as,

$$\mathbf{y} = \mathbf{X}\boldsymbol{\alpha} + \boldsymbol{\epsilon}, \tag{3.5}$$

where

$$\mathbf{y} = \begin{pmatrix} PL(d_1) \\ PL(d_2) \\ \vdots \\ PL(d_L) \end{pmatrix}, \mathbf{X} = \begin{pmatrix} 1 & 10\log_{10}(d_1) \\ 1 & 10\log_{10}d_2) \\ \vdots & \\ 1 & 10\log_{10}(d_L) \end{pmatrix}, \boldsymbol{\epsilon} = \begin{pmatrix} \Psi_{\sigma,1} \\ \Psi_{\sigma,2} \\ \vdots \\ \Psi_{\sigma,L} \end{pmatrix}$$

and

$$\boldsymbol{\alpha} = \begin{pmatrix} PL(d_0) \\ n \end{pmatrix}.$$

By applying ordinary least squares, the parameter $\boldsymbol{\alpha}$ can be estimated as

$$\hat{\boldsymbol{\alpha}} = \left(\mathbf{X}^T\mathbf{X}\right)^{-1}\mathbf{X}^T\mathbf{y}. \tag{3.6}$$

Using the estimates contained in $\hat{\boldsymbol{\alpha}}$, the variance σ^2 can be estimated as

$$\hat{\sigma}^2 = \frac{1}{L-1}(\mathbf{y} - \mathbf{X}\hat{\boldsymbol{\alpha}})^T(\mathbf{y} - \mathbf{X}\hat{\boldsymbol{\alpha}}). \tag{3.7}$$

[2]The estimation method has not been published previously in any journal or paper, and has been derived and implemented by the author of this thesis.

By applying ordinary least squares, the effects of missing or censored samples are not taken into account. It has previously been shown, that the missing samples can have a significant effect on the estimated parameters for both the pathloss exponent, $\hat{n}$ and the large-scale fading variance $\hat{\sigma}^2$. This effect is especially severe for NLOS scenarios, where the received power can be very small.

In order to estimate the pathloss exponent and fading variance of censored data, with a *known* number of missing samples, it is possible to base the estimation on a censored normal distribution. Under this assumption, each data observation follows a normal distribution that is censored from the right. The censoring occurs for data samples where the pathloss is greater than or equal to c. The value $-c$ is a channel gain that corresponds to the noise floor of the channel sounder. In practice, c is chosen with some margin with respect to the noise floor, so that a limited number of samples dominated by noise are included as measurement data.[3] Using the data set in (3.5), the data is assumed to be censored so that observations with values at or above c are set to c_y, i.e.

$$y = \begin{cases} y_i^* & \text{if } y_i^* < c \\ c_y & \text{if } y_i^* \geq c \end{cases} \tag{3.8}$$

where

$$y_i^* \sim N(\mathbf{x}_i\boldsymbol{\alpha}, \sigma^2). \tag{3.9}$$

The probability of observing a censored observation at a distance d is given by

$$P(y \geq c) = 1 - \Phi\left(\frac{c - \mathbf{x_i}\boldsymbol{\alpha}}{\sigma}\right), \tag{3.10}$$

where Φ is the cumulative distribution function (CDF) of the standard normal distribution. Now, by using I as an indicator function that is set to 1 if the observation is uncensored and is set to 0 if the observation is censored, it is possible to write down the likelihood function as

$$l(\sigma, \boldsymbol{\alpha}) = \prod_{i=1}^{L} \left[\frac{1}{\sigma}\phi\left(\frac{y_i - \mathbf{x_i}\boldsymbol{\alpha}}{\sigma}\right)\right]^{I_i} \left[1 - \Phi\left(\frac{c - \mathbf{x_i}\boldsymbol{\alpha}}{\sigma}\right)\right]^{1-I_i}, \tag{3.11}$$

[3]Note that, in practice, the censoring occurs for the power-delay profile (PDP), which means that even if the received power is larger than the noise floor, parts of the PDP are being censored by the noise floor. However, this is assumed to have a small effect on the measured data. Furthermore, assuming that the censoring occurs for the received power makes the estimation procedure much simpler.

where ϕ is the standard normal probability density function (PDF). The log-likelihood $\ln(l)$ can now be written as

$$\sum_{i=1}^{L}\left\{I_i\left[-\ln\sigma+\ln\phi\left(\frac{y_i-\mathbf{x_i}\boldsymbol{\alpha}}{\sigma}\right)\right]+(1-I_i)\ln\left[1-\Phi\left(\frac{c-\mathbf{x_i}\boldsymbol{\alpha}}{\sigma}\right)\right]\right\}. \quad (3.12)$$

Using the log-likelihood $L(\sigma,\boldsymbol{\alpha})=\ln[l(\sigma,\boldsymbol{\alpha})]$, the parameters σ and $\boldsymbol{\alpha}$ are estimated using

$$\arg\min_{\sigma,\boldsymbol{\alpha}}\{-L(\sigma,\boldsymbol{\alpha})\}, \quad (3.13)$$

which is easily solved by numerical optimization of $\boldsymbol{\alpha}$ and σ. Here, it is important to remember that this method is only valid under the assumption that the measured data is appropriately modeled using Eq. (3.2). Therefore, it might be necessary to perform some statistical tests, and to study the residuals, given the estimated parameters. However, the presented method approach can easily be further extended, so that it supports other pathloss models, such as the dual-slope model [29]. As an example, synthetic data at 5.6 GHz was generated according to Eq. (3.2) with known parameters and a synthetic censoring level at c. The parameters were first estimated using ordinary least squares (OLS), *i.e.* Eq (3.6) and (3.7), where the censoring is *not taken into account*. Then, the parameters are estimated using the ML method described above, where the censoring *is taken into account*. The result is shown in Fig. 3.4. The OLS method clearly underestimates both the pathloss exponent, $\hat{n}$, as well as the standard deviation of the large scale fading, $\hat{\sigma}$. The ML method on the other hand, is able to correctly estimate both parameters in this example. This shows the importance of taking the censored data into account, as this can greatly improve the parameter estimates, especially in NLOS or OLOS scenarios, where the received power can be very small, and a large number of measurement points might be censored. Fig. 3.5 shows the same thing as Fig. 3.4, but is for measured data from a vehicle-to-vehicle (V2V) measurement campaign for OLOS scenarios at 5.6 GHz [29].[4] In this case, the parameter estimates for the OLS shows significantly smaller values compared to the parameter estimates for the ML method.

This large discrepancy is due to the large number of censored samples in this data set; about 45 % of the measurement data points are censored. As a result, the OLS, which does not consider the censored samples, greatly underestimates the pathloss exponent and large scale fading.

[4]Note that this frequency is not in the mm-wave frequency band, and is only used as an example. The presented method is expected to be especially useful for outdoor pathloss measurements in the mm-wave band, where the received power can be extremely small.

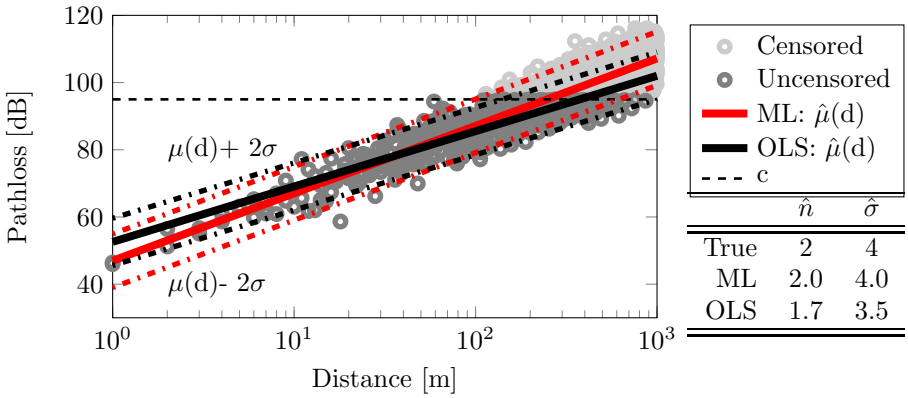

	$\hat{n}$	$\hat{\sigma}$
True	2	4
ML	2.0	4.0
OLS	1.7	3.5

Figure 3.4: Pathloss estimation based on censored synthetic data using the ML estimation method that considers censoring and using OLS without considering censoring. The ML method produces accurate estimates, whereas the OLS method underestimates n and σ.

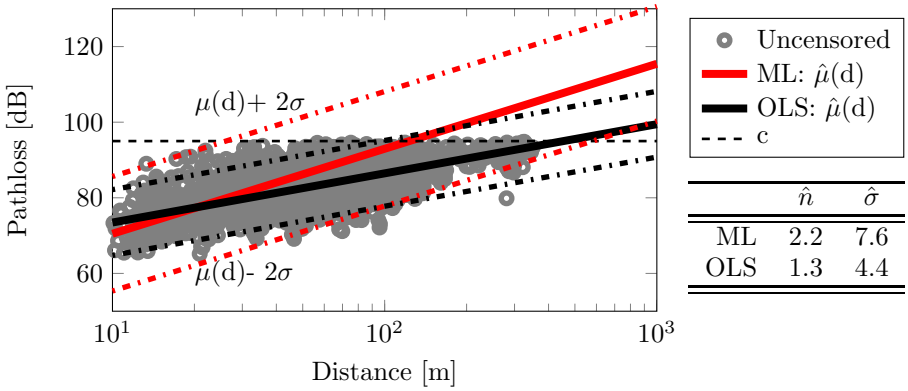

	$\hat{n}$	$\hat{\sigma}$
ML	2.2	7.6
OLS	1.3	4.4

Figure 3.5: Pathloss estimation of censored measurement data, using the ML estimation method that considers censoring and using OLS without considering censoring. Due to the large number of censored data points, there is a large discrepancy between the parameter estimates for the two different methods.

Pathloss models for mm-wave outdoor channels

Outdoor mm-Wave scenarios include backhaul links [6], peer-to-peer ad hoc networks [30] and cellular systems [5]. So far, research on outdoor mm-wave channels have mostly focused on large-scale parameters such as pathloss and shadow fading [31], although some work has been performed regarding the angular properties [32]. Measurement-based parameter estimates for the pathloss and large-scale fading have been reported for various outdoor scenarios at a number of different mm-wave frequencies, e.g.:

- Cellular and peer-to-peer measurements in an urban environment at 38 and 60 GHz [30].
- Urban cellular measurements at 28 GHz [33].
- Campus cellular measurements at 38 GHz [34].
- Campus, urban and in-building cellular measurements at 28 GHz [35].
- Urban cellular at 28 and 73 GHz [32].

References [30,33–35] all use a pathloss reference value for the NLOS scenarios that is based on the free space pathloss value at this distance. This approach will lead to incorrect estimates, as the free space pathloss reference value is not valid for NLOS scenarios, and will cause an overestimation of the pathloss exponent. The overestimation of the pathloss exponent will also cause the large-scale fading variance to be incorrectly estimated. In a subsequent paper [31], the pathloss estimates from [33] and [30], where a fixed free space reference is used, are compared with the estimates obtained when the reference value is being estimated. The results show that when estimating the reference value, both the estimated pathloss exponent and large-scale fading are much smaller compared to when using the free space reference. The paper also investigates the pathloss exponent and large-scale fading for different Tx heights.

It could also be worth mentioning that the results in [30, 31, 33] are all based on highly directional antennas that are rotated, and that the estimates are based on measurements over small angular regions. In [32], the measurements from [33] are used, but the pathloss is estimated based on the power from all directions, and the peak antenna gains are removed from the measurements. The estimated parameters for these omnidirectional measurements, for the NLOS scenarios are shown in Table 3.2. For LOS, the pathloss is modeled according to the free space pathloss with a large-scale fading standard deviation of 8.7 and 8 dB at 28 and 73 GHz, respectively.

It is not straightforward to come up with a general pathloss model that is valid for arbitrary antennas, especially when considering antenna arrays

Table 3.2: Pathloss parameter values for the pathloss exponent n and large-scale fading standard deviation, σ, for outdoor urban cellular environments in NLOS scenarios, as reported in [34].

f [GHz]	n	σ
28	2.92	8.7
73	2.45	8.0

that utilize beamforming. Furthermore, in outdoor scenarios, certain locations might experience significant shadowing due to large obstructing objects such as tall buildings. Further measurements are needed to include additional outdoor environments.

Lastly, for outdoor mm-wave systems, it is sometimes necessary to take the atmospheric absorption and rain attenuation into account. Atmospheric absorption peaks at about 20 dB/km at 60 GHz [36], which means that it is going to be of importance for Tx-Rx separations above 200 m, where the absorption is in excess of 4 dB [37]. The atmospheric attenuation is much less severe at for instance 28, 38 and 73 GHz. The attenuation due to rain is about 10 dB/km for heavy rain at 60 GHz [38], so it is necessary to take both rain and atmospheric attenuation into account for outdoor mm-Wave cellular coverage calculations and for mm-wave point-to-point links over long distances. For indoor communications, it is *not* necessary to take these factors into account.

Pathloss models for 60 GHz indoor channels

There are many papers reporting on pathloss parameters for indoor 60 GHz channels. However, in many of these papers, the influence of the antennas is not de-embedded from the radio channel measurements, which indeed will have an effect on the reported values. Depending on the antenna type and orientation, the environment will be illuminated in different ways. Also, since the antenna arrays are expected to utilize beamforming, and sharp shadow zones can be formed, it is worthwhile to try to find a way of modeling the pathloss that is valid for arbitrary antenna elements and orientations, as well as arbitrary shadowing situations. There is a solution to this problem, but before going into those details, some pathloss parameters presented in the literature will be discussed first, in order to shed some light on why a different approach might be needed.

In [39], Smulders presents an excellent summary and comparison of parameter values reported in the literature, for the pathloss exponents and large-scale

fading variances for different indoor environments in the 60 GHz band. Table 3.3 shows the range of the typical pathloss parameters summarized in [39]. Here, it is evident that the pathloss parameters (pathloss exponent, large-scale fading and reference value) presented in the literature cover a very wide range. Some of these large discrepancies might be attributed to differences in antenna types and orientations. In [39], a generic LOS and NLOS pathloss model is suggested, with $n = 1.7$ and $\sigma = 1.8$ for LOS scenarios and $n = 3.3$ and $\sigma = 4.6$ for NLOS scenarios. However, such a generic model is not always reasonable due to the effects of beamforming and human body shadowing.

Table 3.3: Typical pathloss parameter values for the pathloss exponent n and large-scale fading standard deviation, σ, for various indoor environments at 60 GHz, as reported in [34].

	n	σ	$PL(d_0)$
LOS	0.5-2.5	0.14-5.4	34-84
NLOS	1.64-5.4	1.55-8.6	35-86

In [40], the effects of different antenna patterns on the pathloss estimates were investigated by using different antenna types, antenna orientations and antenna heights. In the paper, omnidirectional, fan-beam and pencil-beam antennas are used. Indoor pathloss parameters for indoor laboratory environments where then estimated for the different antenna types and orientations. Table 3.4 lists parameters for a couple of different antenna combinations. As seen in the table, the parameters cover a very wide range, and some of the parameters are quite extreme. In one case, the pathloss exponent is negative, at $n = -1.5$, which suggests that the power increases with increasing Tx-Rx distances. This is because of the antenna pattern; as the Tx and Rx are moved apart, the direction for the LOS is changed, so that the LOS component is stronger for larger separation distances. Additionally, some of the pathloss reference values are quite extreme, such as $PL(d_0) = 34.8$ dB at 1 m. This can be compared to the free space pathloss at 1 m which is 68 dB at 60 GHz. The presented values are most likely able to emulate value that are similar to ones corresponding to that specific measurement. However, if the pathloss values are extrapolated to regions outside those of the measurements, the values start to become less and less reliable. This is exemplified in Fig. 3.6, where pathloss curves for the presented parameter values are shown. Furthermore, the presented values give no clear indication on what kind of received power one should expect for a certain antenna type and orientation, other than the fact that very large differences in the received power can be expected depending

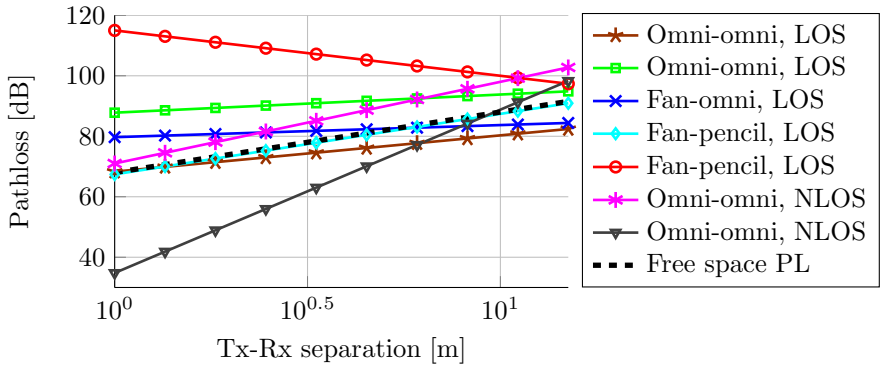

Figure 3.6: Pathloss curves corresponding to the parameters presented in Table 3.4, according to the values in [38].

on the scenario, antenna type and antenna orientation. In order to avoid these issues, a different approach is needed.

Table 3.4: Pathloss parameter values for indoor laboratory environments in the 60 GHz band. The parameters are derived using omni-directional, fan-beam and pencil-beam antennas in different combinations and orientations, from [38].

	Height difference [m]	Tx-Rx antennas	n	σ [dB]	$PL(d_0)$ [dB] ($d_0 = 1$ m)
LOS	0	Omni-omni	1.2	2.7	68.3
	1	Omni-omni	0.6	1.3	87.8
	0	Fan-omni	0.4	1.0	79.7
	0	Fan-pencil	2.0	0.6	67.4
	0	Fan-pencil$_{\pm 35^\circ}$	-1.5	0.8	115
NLOS	0	Omni-omni	5.4	3.9	34.8
	1	Omni-omni	2.7	2.7	71

In [26] (this work), a double-directional indoor propagation channel model was derived, in which the pathloss is not explicitly modeled. Instead, the impulse responses are modeled in an absolute scale with respect to the channel gain. The channel gain for the LOS component (for the propagation channel) was found to be appropriately determined by the free space equation. This way, the pathloss can be implicitly emulated by the channel model, for arbitrary antenna elements and array configurations, by generating power-delay

profiles (PDPs) for a specific scenario. The received power can then be found by integrating the PDP. Alternatively, if one is interested in the received power for a specific frequency, it is possible to look at small-scale averaged frequency transfer functions. This way, the received power as a function of frequency is available, which might be interesting if the antenna pattern in question has a significant frequency dependence. Fig. 3.7, shows the channel gain for LOS and NLOS scenarios at 62 GHz, based on the measurement data and based on the channel model when using isotropic antennas, or, using the measured antenna patterns for the antennas that were used in the measurement. The solid line is the free space pathloss. Also, the figure includes the received power that was measured, and also, for the LOS scenario, data reconstructed for the isotropic case based on the directional estimates for the measurements. Here, we note that the antennas that are used in these measurements are not that directional; the Tx antenna was an omnidirectional biconical antenna with a gain of about 1 dBi and the Rx antenna was an open waveguide with a maximum gain of about 6.5 dBi. However, there is still a clear difference between the received power for the isotropic case and the received power when using the measured antenna patterns. If highly directional antennas were used, pointing in arbitrary directions, the received power would exhibit significantly larger fluctuations. The same is true if more extreme shadowing cases were introduced. It can also be seen that the measured received power agrees quite well with the measurements and the reconstructed data. This method of calculating the received power is of course much more computationally complex compared to using a conventional pathloss model. This drawback is outweighed by the following facts:

1. This method is able to derive pathloss models from the channel model.
2. The received power can be calculated for arbitrary antenna types, antenna orientations and shadowing scenarios. This can be done even if the received power as a function of Tx-Rx separation does not obey the generic pathloss model.
3. As the antenna patterns and the channels are being modeled separately using this method, it is easier to relate to the physical processes that are responsible for the variations in the received power.
4. The pathloss parameters are not needed for the development of the channel model, which is advantageous, since it is difficult to accurately estimate the pathloss parameters in indoor scenarios.

For the isotropic LOS scenario, the pathloss parameters were estimated based on the data generated by the channel model.[5] The results are presented

[5]Ideally, it would be preferable to also estimate this based on measurement data, but

in Table 3.5. For both the omnidirectional case, the pathloss exponent is 2.0, which is the same as for the free space case. This is due to the fact that the LOS component is significantly stronger than the remaining components. On average, the received power for the omnidirectional case is only slightly larger than the received power in free space. For the case with the measured antenna patterns, the estimated pathloss exponent is also 2.0. This is because of the way the data from the channel model was generated in this case; the azimuth direction of arrival and departure for the LOS component was modeled as a uniform random variable over the interval corresponding to the maximum and minimum azimuth angles in the measurement, *i.e.*, $\phi_{\mathrm{LOS}}^{\mathrm{Tx/Rx}} \sim \mathrm{U}\,(\phi_{\mathrm{min}}^{\mathrm{Tx/Rx}}, \phi_{\mathrm{max}}^{\mathrm{Tx/Rx}})$. This was done to facilitate a fair comparison of the channel model data and the measurement data. If the angles were chosen in a different way, for instance based on a specific measurement route, it would be possible to model the received power along this route. Depending on the antenna pattern, it is fully possible for the received power to exhibit a behavior that is *not* appropriately modeled by the generic pathloss model.

For the OLOS scenario, the ratio between the transmitted power , p_{Tx}, and the average received power $\bar{p}_{\mathrm{Rx}}$, emulated by the channel model, is increasing exponentially with the Tx-Rx separation distance, d, as

$$p_{\mathrm{Tx}}/\bar{p}_{\mathrm{Rx}} = p(d_0)\mathrm{e}^{k(d-d_0)},\ d > d_f, \tag{3.14}$$

where d_0 is a reference distance and d_f is the farfield distance. In units of dB, the ratio can be written as

$$\bar{P} = 20\log_{10}(p_{\mathrm{Tx}}/\bar{p}_{\mathrm{Rx}}) = P(d_0) + k_{\mathrm{dB}}(d - d_0). \tag{3.15}$$

When taking the large scale fading into account, the ratio between the received and transmitted power can be described as

$$P = \bar{P} + \Psi_\sigma = P(d_0) + k_{\mathrm{dB}}(d - d_0) + \Psi_\sigma, \tag{3.16}$$

where Ψ_σ is a distribution that describes the large scale fading about the distance-dependent average ratio. This expression can be seen as an alternative description of the pathloss, and is valid for OLOS scenarios. These parameters of Eq. 3.15 were estimated for the emulated NLOS scenario, with measured and isotropic antenna patterns, and are shown in Table 3.5. The fading about the mean power ratio is described by a normal distribution with variance σ^2.

in this case, the number of data points from the measurements are too small, making it impossible to obtain reliable estimates.

Table 3.5: Pathloss parameter estimates based on the channel model in [26].

	Antennas	n	σ	$PL(d_0)$
LOS	Omnidirectional	2.0	0.5	67.8
LOS	Measured	2.0	1.3	65.2
	Antennas	k_{dB}	σ	$P(d_0)$
OLOS	Omnidirectional	1.63	2.6	80
OLOS	Measured	1.69	3.6	79

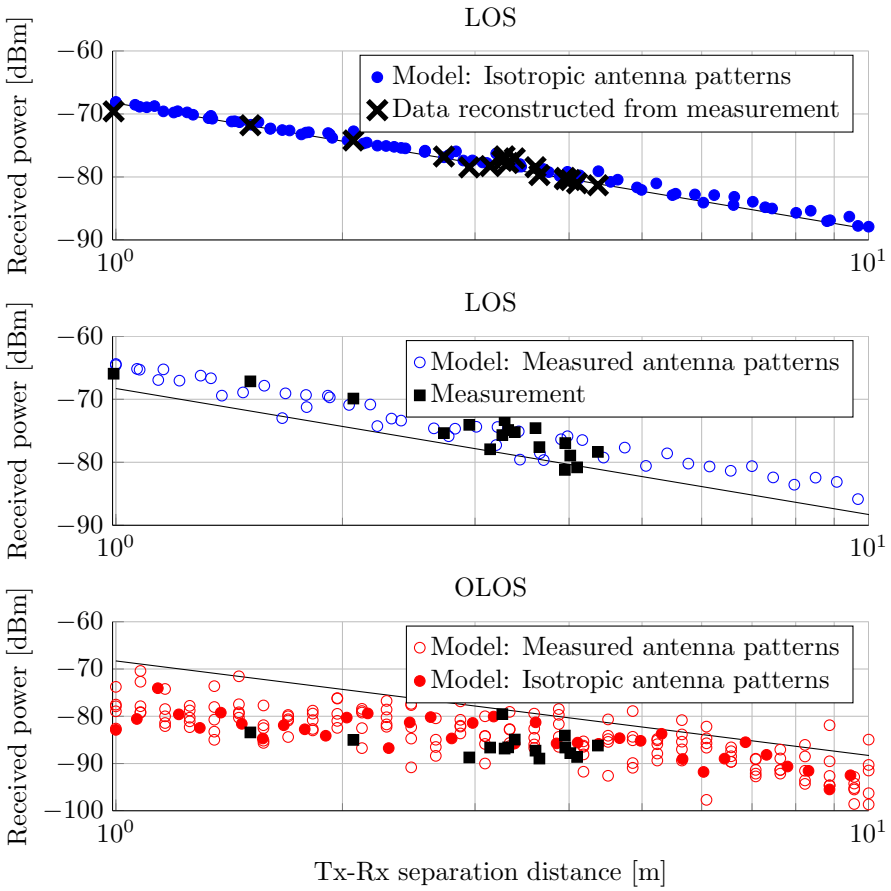

Figure 3.7: Received power for a Tx power of 0 dBm for different Tx-Rx separation distances, based on the channel model and measurements [26].

3.2.2 Power Delay Profile

The power delay profile (PDP) of the radio or propagation channel, sometimes referred to as the power delay spectrum, can be defined as the average channel gain as function of delay. It can be calculated based on measured channel impulse responses (CIRs), $h_{n_r,n_t}(\tau)$. The PDP, $P_h(\tau)$ can then be obtained as

$$P_h(\tau) = \frac{1}{N_t N_r} \sum_{n_t=1}^{N_t} \sum_{n_r=1}^{N_r} |h(\mathbf{s}_{n_r}, \mathbf{s}_{n_t}, \tau)|^2, \tag{3.17}$$

where $\mathbf{s}_{n_t}$ and $\mathbf{s}_{n_r}$ denote the spatial position relative to the array origin for the n_tth Tx and n_rth Rx antenna, respectively.

For indoor LOS scenarios, the PDP contains a LOS component which is significantly stronger (usually around 16-20 dB) than the second strongest component. For delays longer than the one corresponding to the delay for the LOS, the PDP has been observed to have a shape that is exponentially decaying with delay. If the angular domains are considered as well, it can be observed that the majority of the power comes from a number of MPCs that appear in clusters in the angular-delay domain. This will be discussed in detail in section 3.3. For most of the common environment scenarios, such as office, residential, library and conference room environments, the PDP has been observed to exhibit this exponential shape in the delay domain. However, in some more esoteric environments, other PDP shapes have been reported, such as for the ultrasonic inspection room environment in [23], where the PDP is being modeled using a power law model. For the more common types of environments, the exponential part of the PDP is made up of a number of fairly strong specular components, surrounded by weaker specular components and a diffuse part. To the best of the author's knowledge no papers have reported on the diffuse scattering part for mm-wave frequencies.

For the OLOS scenario, the shape of the PDP is very similar to the PDP in a corresponding LOS scenario, except for the LOS component. In Fig. 3.8, a measured PDP for a LOS and a corresponding OLOS scenario is shown, from [41], with estimated cluster decay from [42]. At around 160 ns, there are two outdoor specular reflections coming from a building opposite to the room in question. These reflections are not considered in the analysis for the following reasons: the outdoor reflections are caused by a physical process that is different from the interactions that only occur inside the room, and are thus not contributing to the exponentially decaying shape of the PDP. The exponential decay of the PDP in the delay domain is caused by the fact that the radio waves are likely to undergo an increasing number of interactions with the environment as the delay increases. If the outdoor reflections were to be

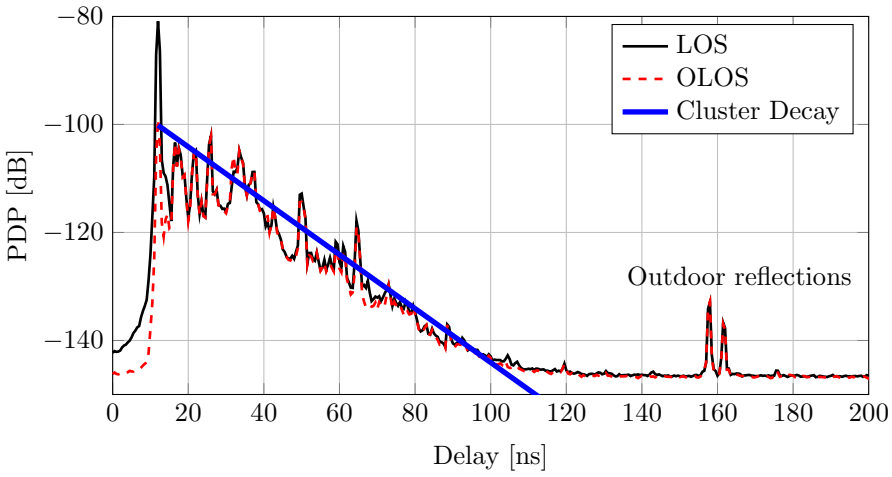

Figure 3.8: Measured indoor PDP for a conference room environment.

included, it would cause the cluster decay to be less steep, and would no longer describe the typical decay for the clusters corresponding to the interactions inside the room. Also, the outdoor reflections are very weak and would rarely be of significance and would furthermore require a large building fairly close, directly opposite to the windows in the room.

For NLOS scenarios, the PDP can take many different shapes depending on the exact shadowing situation, due to the sharp shadow zones that can be formed in the 60 GHz band. Parts of the PDP will have a very small power, corresponding to the directions and delay where the shadowing is present.

RMS Delay Spread

Based on the PDP, a number of important parameters can be derived, such as the mean excess delay and root mean square delay spread (RMS DS). The RMS DS is especially important, as it can give a rough measure of how much inter-symbol-interference (ISI) that is to be expected for a given bit-rate. This is crucial for the design of transceivers, as it sets the complexity for the equalizer in the receiver. The RMS DS, for the time discrete case, can be calculated based on the PDP as

$$S_\tau = \sqrt{\frac{\sum_\tau P_h(\tau)\tau^2}{\sum_\tau P_h(\tau)} - \left(\frac{\sum_\tau P_h(\tau)\tau}{\sum_\tau P_h(\tau)}\right)^2}. \tag{3.18}$$

The RMS DS is a measure of how the multipath power in the channel is spread over the delay. This due to the multipath environment, which causes a number of delayed and scaled copies of the transmitted signal to reach the Rx, which induces time-selective fading. The DS depends on several different factors, such as propagation environment, shadowing situation, antenna types, the choice of polarization for the antennas and any signal processing techniques that are applied to the transmitted signal. If one considers the propagation channel, the DS should ideally only depend on the propagation environment; *i.e.* the exact DS only depends on the room size and structure, the types of objects in the room and their electrical properties (*i.e.*, their complex permittivity), and any shadowing objects that are present.

In the literature, typical values for the mean RMS DS in the 60 GHz band for various typical indoor LOS scenarios range from 4-11 ns [43]. The typical values for the DS in the 60 GHz band are significantly smaller compared to those at lower frequencies. In [44], RMS DS values for outdoor peer-to-peer scenario at 38 and 60 GHz are reported, where the mean was 23.6 and 7.4 ns at 38 and 60 GHz, respectively. Values for the indoor RMS DS at 2.25 and 58 GHz are reported in [45], where it was found that the DS values at 58 GHz are about half of those at 2.25 GHz. The reported mean RMS DS values at 58 GHz are 8.8 and 13.2 ns for LOS and NLOS scenarios, respectively.

It is clear that the DS is in general somewhat smaller for the 60 GHz band compared to lower frequency bands. But, one should keep in mind that the bit rate intended for the 60 GHz band is also much higher, which means that the typical DS the channel exhibits might still be an issue. For this reason, some papers have investigated ways of decreasing the DS in mm-Wave channels. In [46], a number of different beamforming (BF) techniques and their effect on the DS is investigated. Narrowband BF, wideband BF, statistical eigenvector BF and dominant eigenmode transmission techniques are compared, using different array sizes. For all of these beamformers, for 70 % of the occurrences, the RMS DS was reduced to less than 0.5 ns in the LOS scenarios and around 5 ns for the NLOS scenarios. This can be compared to the RMS DS with no BF, where the mean values are around 4 and 9 ns, for LOS and NLOS scenarios, respectively. This shows that any BF technique has the additional benefit of reducing the DS. In [47], the spatio-temporal focusing performance of a time reversal processing technique was evaluated, which showed that this technique also has a great positive impact on the RMS DS. Other papers, such as [48,49], has suggested circular polarization to be used as a way to lower the DS. By using circularly polarized Tx and Rx antennas, the DS can be effectively reduced in LOS scenarios, since odd order specular reflections will have their polarization handedness changed, so that they are greatly suppressed. On the other hand, this solution is not useful for NLOS scenarios, where the trans-

mission typically relies on first order specular reflections. In [50], the DS is not mentioned, but different polarization choices for the Tx and Rx antennas were considered. It was shown that the most robust combination, in terms of polarization mismatch, was to use linear polarization at one end and circular at the other end.

3.2.3 Shadowing

Due to the short wavelength at mm-wave frequencies, the attenuation due to shadowing or obstruction by objects or humans is much more severe compared to at lower frequencies. For this reason, it is necessary to characterize and model the shadowing appropriately. A lot of research has focused on the shadowing due to human bodies in the 60 GHz band. The shadowing has been shown to cause losses of about 5-20 dB for persons walking through the LOS, lasting about 6 s. The shadowing due to a static person blocking the LOS was shown to be about 45-65 dB [51]. The large difference is likely attributed to the exact orientation of the person blocking the LOS; the shadowing region for a person that is crossing the LOS path in a perpendicular fashion is much smaller compared to the region for a static person blocking the LOS while facing one of the antennas. A study of the human body shadowing in an airbus showed fading depths up to 20 dB, lasting up to 8 s [52]. In [53], the shadowing loss due to various human body parts were examined. It was shown that the shadowing loss for the field diffracted around a human leg or a human neck can be in excess of 30 dB. Also, the shadowing loss is highly dependent on the size, shape and location of the shadowing object. Fig. 3.9 shows the theoretical shadowing gain due to perfectly conducting cylinders with various radii equal to 15 and 25 cm, at 2.4 and 60 GHz, as a function of the cylinder position displacement. The shadowing at 60 GHz is significantly larger compared to at 2.4 GHz due to the difference in wavelength.

Human body shadowing models

In [53], it was also shown that the shadowing due to human bodies are similar to that of a metallic cylinder, and that the field diffracted around the cylinder can described by creeping waves. The diffracted field can thus be predicted using the geometrical theory of diffraction (GTD) [53] or uniform theory of diffraction (UTD) [54, 55]. The concept of modeling the human body as a cylinder was examined further in [54], where the shadowing is modeled using circular dielectric cylinders, dielectric elliptic cylinder and multiple-knife edge models. The results show that it is not necessary to consider dielectric properties of skin, since the conductivity is high enough for it to be approximated as a

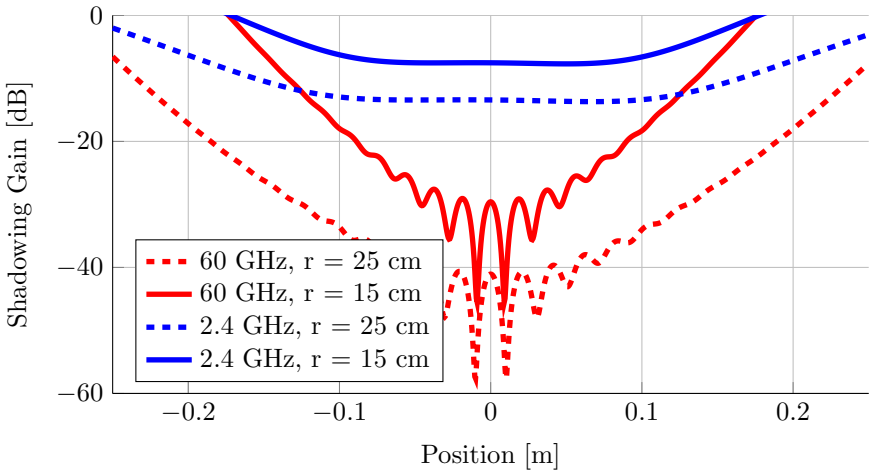

Figure 3.9: Theoretical shadowing gain due to perfectly conducting cylinders at 2.4 and 60 GHz.

perfect electrical conductor, and that there is no significant deviation between circular and elliptic cylinders. The multiple-knife edge serves as a sufficiently good model, which has the benefit of having a low computational complexity.

The IEEE802.11ad model uses this multiple-knife edge model to emulate human body shadowing. The shadowing model combines ray tracing simulations with an electromagnetic knife edge diffraction model and a random walk model for the human movement [56]. This model was subsequently extended and validated in [27] and is originally based on the work in [57].

3.3 mm-Wave MIMO Channel Modeling

This chapter presents double-directional channel models that are typical for indoor 60 GHz systems. The general double directional model is introduced, along with typical inter- and intra-cluster models for rays and clusters. Different modeling approaches for the arrival times, angular distributions and amplitude distributions are also then treated. The inter- and intra-cluster model parameters constitutes the main modeling parameters of typical mm-Wave MIMO channel models.

3.3.1 The Double-directional Channel

The double-directional channel model was proposed in [20] and describes the propagation channel through a number of superimposed plane waves between the Tx and Rx sites. Each plane wave, *i.e.*, MPC, is characterized by a certain complex amplitude, delay and direction of departure and arrival. The generic model for these plane waves can be described as a sum of N plane waves:

$$\begin{aligned} &h_p(\tau, \phi^{\mathrm{Rx}}, \theta^{\mathrm{Rx}}, \phi^{\mathrm{Tx}}, \theta^{\mathrm{Tx}}) = \\ &\sum_{n=1}^{N} \alpha_n \delta\left(\tau - \tau_n\right) \delta\left(\phi^{\mathrm{Rx}} - \phi_n^{\mathrm{Rx}}\right) \delta\left(\theta^{\mathrm{Rx}} - \theta_n^{\mathrm{Rx}}\right) \\ &\qquad \times \delta\left(\phi^{\mathrm{Tx}} - \phi_n^{\mathrm{Tx}}\right) \delta\left(\theta^{\mathrm{Tx}} - \theta_n^{\mathrm{Tx}}\right), \end{aligned} \tag{3.19}$$

where n is the plane wave index, ϕ and θ are the azimuth and elevation angles expressed in local coordinate systems at the Tx and Rx sides, α is the complex amplitude and $\delta(\cdot)$ denotes a Dirac delta function.

Using Eq. (3.19), the wideband MIMO radio channel impulse responses, for arbitrary array configurations and antenna patterns, can then be calculated by considering the complex antenna gains of the Tx and Rx antennas, G_{Tx} and G_{Rx}, respectively, as well as the additional phase shift of each plane wave depending on the exact position of each antenna element at the Tx and Rx sides. The CIR of the radio channel, for a given Tx-Rx antenna combination, with the Tx element at the position $\mathbf{r}_{\mathrm{Tx}} = [x_{\mathrm{Tx}}\ y_{\mathrm{Tx}}\ z_{\mathrm{Tx}}]^{\mathrm{T}}$ and Rx antenna element at $\mathbf{r}_{\mathrm{Rx}} = [x_{\mathrm{Rx}}\ y_{\mathrm{Rx}}\ z_{\mathrm{Rx}}]^{\mathrm{T}}$, can then be calculated as

$$\begin{aligned} h(\tau, \mathbf{r}_{\mathrm{Rx}}, \mathbf{r}_{\mathrm{Tx}}) = &\sum_{n=1}^{N} h_p(\tau_n, \phi_n^{\mathrm{Rx}}, \theta_n^{\mathrm{Rx}}, \phi_n^{\mathrm{Tx}}, \theta_n^{\mathrm{Tx}}) \\ &\times G_{\mathrm{Rx}}(\phi_n^{\mathrm{Rx}}, \theta_n^{\mathrm{Rx}}) G_{\mathrm{Tx}}(\phi_n^{\mathrm{Tx}}, \theta_n^{\mathrm{Tx}}) \mathrm{e}^{\mathrm{j}\mathbf{k}_{\mathrm{Rx}}\mathbf{r}_{\mathrm{Rx}}} \mathrm{e}^{\mathrm{j}\mathbf{k}_{\mathrm{Tx}}\mathbf{r}_{\mathrm{Tx}}}, \end{aligned} \tag{3.20}$$

where the wave vector is described as

$$\mathbf{k} = \frac{2\pi}{\lambda} \left[\cos(\theta)\cos(\phi) \quad \cos(\theta)\sin(\phi) \quad \sin(\theta)\right]. \tag{3.21}$$

Cluster-based Double-directional Models

The double-directional model is often used together with the concept of multi-path clusters. The propagation channel can then be modeled based on stochastic description of the multi-path clusters. Each multi-path cluster contains a fixed number of MPCs, each having similar delays and directions of arrival and departure. The generic double-directional model in Eq. 3.19 is then described

using a different notation, as it now describes a sum all the MPCs in $L+1$ different clusters, where the lth cluster contains K_l+1 number of MPCs:

$$h_p(\tau,\phi^{\mathrm{Rx}},\theta^{\mathrm{Rx}},\phi^{\mathrm{Tx}},\theta^{\mathrm{Tx}}) = \sum_{l=0}^{L}\sum_{k=0}^{K_l}\alpha_{k,l}\delta\left(\tau-T_l-\tau_{k,l}\right)\delta\left(\phi^{\mathrm{Rx}}-\Phi_l^{\mathrm{Rx}}-\phi_{k,l}^{\mathrm{Rx}}\right)\delta\left(\theta^{\mathrm{Rx}}-\Theta_l^{\mathrm{Rx}}-\theta_{k,l}^{\mathrm{Rx}}\right) \times\delta\left(\phi^{\mathrm{Tx}}-\Phi_l^{\mathrm{Tx}}-\phi_{k,l}^{\mathrm{Tx}}\right)\delta\left(\theta^{\mathrm{Tx}}-\Theta_l^{\mathrm{Tx}}-\theta_{k,l}^{\mathrm{Tx}}\right), \quad (3.22)$$

The double-directional channel is now described using inter- and intra-cluster parameters, where the inter-cluster parameters describe the delays and angles of the clusters, whereas the intra-cluster parameters describe the delays and directions for the MPCs in each cluster, with respect to the delays and angles of the cluster centroid.[6] Here, $\alpha_{k,l}$ is the complex amplitude of the kth ray (i.e. MPC) in the lth cluster and T_l, Φ_l^{Tx} and Θ_l^{Tx} are the delay, azimuth direction of departure (DOD) and elevation DOD of the lth cluster, respectively. Similarly, Φ_l^{Rx} and Θ_l^{Rx} describe the azimuth and elevation direction of arrival (DOA), respectively, for the lth cluster. Finally, $\tau_{k,l}$, $\phi_{k,l}^{Tx}$, $\theta_{k,l}^{Tx}$, $\phi_{k,l}^{Rx}$ and $\theta_{k,l}^{Rx}$ are the delay, azimuth DOD, elevation DOD, azimuth DOA and elevation DOA of the kth ray in the lth cluster, respectively. These are the intra-cluster parameters, and are described in delays and angles relative to the delay and angles of the cluster that they belong to.

The parameters for the above inter- and intra-cluster parameters are usually described statistically, but they can also be based on ray tracing or some kind of geometrical model. In the following sections, different modeling approaches for these various parameters, that are typical for 60 GHz indoor scenarios, are described.

3.3.2 Arrival Times

The arrival times for the clusters and the rays within each cluster, are often assumed to follow two different independent Poisson processes, with two different intensities. However, in the wireless channel literature, there are very few papers (if any), that directly estimates the intensities of these two Poisson processes. Instead, a clustering is usually performed so that the delays for the clusters and the delays for the rays in each cluster are known. It is assumed that the clustering is perfect, so that the identified delays are the true ones. Under this assumption, the cluster and ray *inter-arrival times* are correctly

[6] Different definitions of the cluster exists. Sometimes, the cluster centroid refers to the power weighted center of gravity for the cluster, and in other cases, it refers to the strongest component in the cluster or the component that arrives first.

described by two independent exponential probability density functions. The cluster arrival time for each cluster is thus described by an exponentially distributed random variable that is conditioned on the arrival time of the previous cluster, i.e.

$$p(T_l|T_{l-1}) = \Lambda e^{-\Lambda(T_l - T_{l-1})}, l > 0. \tag{3.23}$$

Here, Λ is the cluster arrival rate. Similarly for the ray arrival times, we have

$$p(\tau_{k,l}|\tau_{k-1,l}) = \lambda e^{-\lambda(\tau_{k,l} - \tau_{k-1,l})}, l > 0, \tag{3.24}$$

where λ is the ray arrival rate.

3.3.3 Angular Distributions

The DOD and DOA for the clusters and rays are usually described using different angular distributions. The DOD and DOA for the clusters are highly dependent on the propagation environment and the scattering objects in the environment. The IEEE802.11ad channel model [14] uses ray-tracing and empirical distributions to determine the cluster angles. In the IEEE802.15.3c model [13], only the azimuth cluster DOA is being modeled, and it is modeled as a uniform distribution:

$$\Phi_l^{\mathrm{Rx}} \sim \mathrm{U}\,[0, 2\pi]. \tag{3.25}$$

For the intra-cluster angles, the probability density function for the azimuth and elevation angles are either described using a zero-mean Laplace distribution with standard deviation σ, with probability density function, as

$$p(\phi_{k,l}) = \frac{1}{\sqrt{2}\sigma} e^{-|\sqrt{2}\phi_{k,l}/\sigma|}, \tag{3.26}$$

or, using a zero-mean Normal distribution, as

$$p(\phi_{k,l}) = \frac{1}{\sqrt{2\pi}\sigma} e^{-\phi_{k,l}^2/(2\sigma^2)}. \tag{3.27}$$

The IEEE802.15.3c channel model uses Laplacian distributions, whereas the IEEE802.11ad channel model uses a Normal distribution.

3.3.4 Cluster and Ray Amplitude Distributions

The amplitudes for the clusters and rays have been modeled in various different ways in the literature. In the classical Saleh-Valenzuela (SV) model [18], the mean *power* of the kth ray in the lth cluster is modeled as

$$\bar{\beta}_{k,l}^2 = \bar{\beta}_{0,0}^2 \mathrm{e}^{-T_l/\Gamma} \mathrm{e}^{-\tau_{k,l}/\gamma}, \tag{3.28}$$

where Γ and γ are cluster and ray decay constants, respectively. Also, $\bar{\beta_{0,0}^2}$ is the average power of the first ray in the first cluster. An approach similar to this is being used in the IEEE802.15.3c channel model [13]. Here, the ray and cluster fading was found to be appropriately modeled as being log-normal-distributed.

In the IEEE802.11ad model, a slightly different approach is being used. The gain of the LOS component is determined by the Friis' transmission equation and the gain for the main component of each cluster is modeled as having a mean amplitude given by

$$\bar{\beta}_{0,l} = \frac{g_l \lambda}{4\pi(d + R_l)}, \tag{3.29}$$

where d is the distance between the Tx and Rx, R_l is the is distance the lth cluster has traveled in excess of the Tx-Rx distance, and g_l is a reflection loss coefficient. The reflection loss is being modeled by a truncated log-normal distribution [58]. However, based on the measured data and the estimated truncated log-normal distribution that is presented in [58], it is difficult to tell if this modeling approach is reasonable, and more data is likely needed in order to obtain reliable estimates. For this reason, it is hard to assess the performance of this modeling approach.

The IEEE802.11ad model also uses a slightly different approach for the intra-cluster amplitude distribution. The basic intra-cluster model is shown in Fig. 3.10. The amplitude of the main ray can be determined by Eq. 3.29. The remaining rays in the cluster are described by a number of pre- and post-cursor rays that have an average *amplitude* that decays exponentially on both sides of the main component in the cluster. The rays have uniformly distributed phased and Rayleigh-distributed amplitudes with average amplitudes determined by the pre- and post-cursor average exponential decays and the pre- and post-cursor K-factors.

In [26], the average power of the main component in each cluster is modeled by an exponential cluster decay, whereas the remaining rays in each cluster are modeled using the same basic intra-cluster structure as in Fig. 3.10. However, the fading for both the clusters and rays are modeled by log-normal distributions. Given the large bandwidth of 2 GHz that is being modeled, and the fact that individual rays can be resolved in the directional estimation process, it seems reasonable that the ray and cluster fading are both log-normal. An intuitive explanation for this is that each ray undergoes a number of interactions with the environment, where each interaction cause an interaction loss. If these interaction losses are modeled as independent and identically-distributed normal variables, then the total loss would be log-normal. The Rayleigh distribution on the other hand, typically arise in narrowband cases, where several different plane waves are summed. If the waves can be described as random

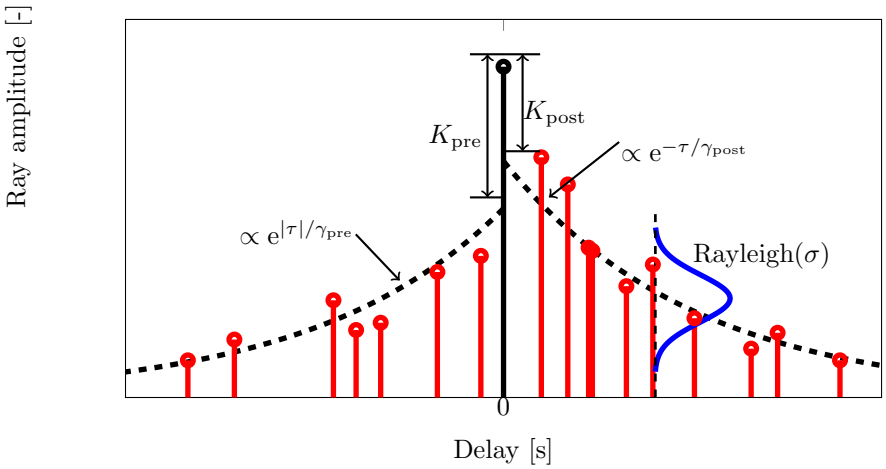

Figure 3.10: Intra-cluster model for the IEEE802.11ad channel model.

complex numbers whose real and imaginary components are i.i.d. Gaussian with equal variance and zero mean, the absolute value of the sum of these plane waves is Rayleigh-distributed.

In [42], it was noted that the cluster decay is a critical parameter for 60 GHz indoor channel models. Due to the fast decay and limited dynamic range in typical 60 GHz channel measurements, it is necessary to consider the truncation of the noise floor in the estimation process. The basic concept for this estimation approach is shown in Fig. 3.11, which shows synthetic data that is truncated by a noise floor. In the log-domain, the exponential decay and log-normal fading can be modeled as a truncated normal distribution with a delay dependent mean, or,

$$\ln(\beta_{0,l}^2) \sim \mathrm{N}\left(\mu(T_l), \sigma^2\right). \tag{3.30}$$

The cluster decay and cluster fading estimates can be greatly improved by this estimation method compared to estimation methods that traditional ordinary least squares methods. The estimated cluster decay for measured data, with and without considering truncation, can be seen in Fig. 3.12. It is evident that the cluster decay is being underestimated when the truncation due to the noise floor is not taken into account.

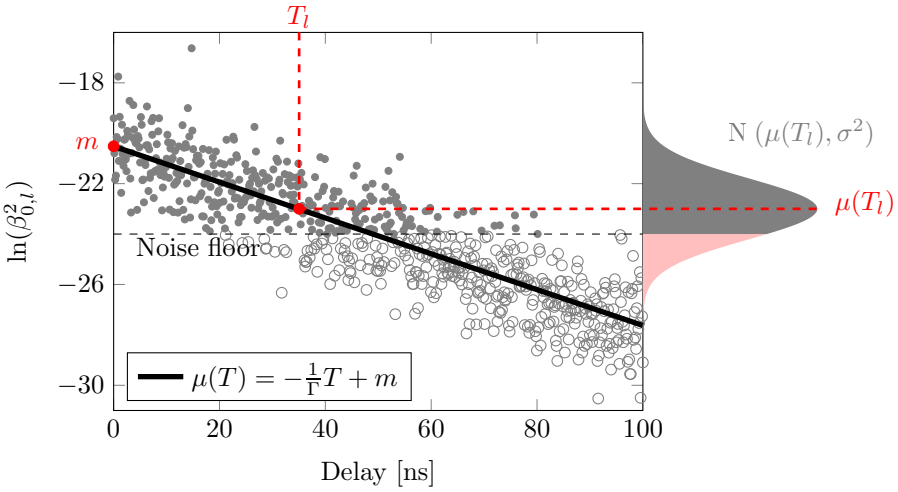

Figure 3.11: The truncation due to the noise floor needs to be taken into account in the cluster decay estimation model.

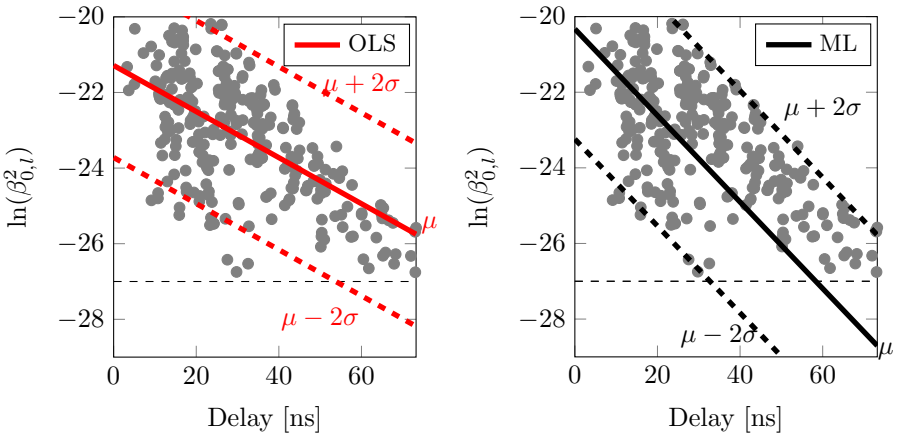

Figure 3.12: Cluster decay and fading estimation, with and without considering truncation.

3.3.5 Polarization

In a multi-path propagation environment, cross-polarized signals are caused by reflection, diffraction and scattering interactions with the environment. Due to the complex interactions with the environment, it is often infeasible to attempt a deterministic approach to determine the depolarization. Instead, the cross-polarization ratios (XPRs) of the propagation paths for different environments are often characterized by typical numerical values, or modeled stochastically. At 60 GHz, XPR values of of 10-20 dB for first and second order reflections have been reported for office environments [59]. In [60], XPR values in the 70 GHz band, in shopping mall, railway and office environments, were observed to be in the range of about 10-30 dB. This indicates that the XPR is larger at these higher frequencies as compared to at lower frequencies. At 5.2 GHz, mean values of the XPR have been reported to be 6.6 and 6.3 dB in office and conference room environments, respectively [61]. In the Winner II channel model [62], the XPR parameter values have mean values of 4-12 dB for 2-6 GHz.

In general, orthogonally polarized elements will exhibit a very low fading correlation. This can be characteristic can be utilized to combat fading through polarization diversity, or to increase the spectral efficiency through spatial multiplexing using multiple-input multiple-output (MIMO) systems with orthogonal antenna elements. The capacity improvement that can be gained using dual-polarized antenna elements and the effectiveness of polarization diversity techniques are highly dependent on the characteristics of the XPRs [61]. As the XPR is greater at mm-wave frequencies compared to lower frequencies, it might be expected that the different polarization techniques might be more efficient at mm-wave frequencies.

Chapter 4

Estimation Methods

4.1 Double-Directional Estimation

As discussed in the previous chapter, the MIMO propagation channel may be modeled using a double-directional channel model for the propagation path parameters. This modeling approach thus requires estimation of the MPC parameters, based on a realistic model. The measured impulse response is usually assumed to consist of specular components, noise and sometimes a diffuse part. A number of different high resolution parameter estimators have been developed for the specific purpose of MPC parameter estimation.

The SAGE algorithm [63,64], is an algorithm that is based on the expectation maximization algorithm, and uses a successive interference cancellation in order to jointly estimate delay, Doppler and azimuth and elevation directions of departures and arrivals. The likelihood function is iteratively evaluated by keeping a subset of the parameters fixed, while maximizing the likelihood function with respect to the remaining subset of the parameters. For the next iteration, these new estimates are then kept fixed to estimate a new subset of the parameters in similar fashion.

RiMAX [65] is another estimation method that aims at improving the parameter estimates by considering a diffuse part in addition to the specular MPCs, so that the diffuse scattering is taken into account in the estimation process. Lastly, in [66], a state based method sequential estimation technique based on extended Kalman filter, is presented. This latter method is especially useful for tracking time-variant channels.

In this thesis, the SAGE algorithm was applied to measured data. In hindsight, it would have been beneficial to use a parameter estimator that also estimates the diffuse part of the impulse response, in order to properly quan-

tify the diffuse part of the impulse response. However, the choice of SAGE as the parameter estimator is motivated by the fact that, for 60 GHz indoor channels, most of the power in the impulse response can be attributed to specular components.

In the SAGE algorithm, it is assumed that the impulse responses consist of a superposition of a finite number of L plane waves, i.e., L number of specular MPCs. These MPCs are each characterized by a complex polarimetric amplitude, $\boldsymbol{\alpha}$, delay, τ and directions of departure, Θ^{Tx}, and arrival, Θ^{Rx}. The transfer function between the mth receive and nth transmit antenna is then assumed to be correctly described by the sum of L different MPCs as

$$H_{m,n}(k, i, \boldsymbol{\alpha}, \tau_l, \Theta^{Rx}, \Theta^{Tx}) = \tag{4.1}$$

$$\sum_{l=1}^{L} \mathbf{G}_{Rx}(m, k, \Theta_l^{Rx})^{\mathrm{T}} \boldsymbol{\alpha}_l \mathbf{G}_{Tx}(n, k, \Theta_l^{Tx}) \mathrm{e}^{-\mathrm{j}2\pi\Delta f \tau_l k} \mathrm{e}^{\mathrm{j}2\pi\Delta t \nu_l i},$$

where $\mathbf{G}_{Tx}$, $\mathbf{G}_{Rx}$ and k is the complex polarimetric antenna patterns of the Tx and Rx, and frequency sub-index, respectively. If the channel is measured in a time-static environment, the Doppler frequency, ν, and the snapshot index, i, can be omitted.

4.2 Clustering Methods

In order to estimate the parameters of a cluster-based channel model, the multi-path component clusters need to be identified somehow. A multi-path cluster is loosely defined as a group of multi-path components that have similar delays and directions of departures and arrivals. Initally, these clusters were identified based on visual inspection [67]. In order to improve the clustering estimates and to allow for automatic detection of clusters, different methods were subsequently introduced. For these automatic clustering methods, a cluster is often defined based on a distance metric or based on a distribution. Typically, a MPC is then usually defined by a vector where the spherical coordinates have been transformed to cartesian coordinates, so that each MPC is described by a vector as

$$\mathbf{Y} = \{\tau_d, x_a, y_a, z_a, x_d, y_d, z_d\},$$

where τ_d is a scaled version of the delay. One of the most popular clustering methods is the so called K-power-means algorithm [68]. It is based on the K-means clustering algorithm, but also includes the path powers in the clustering

procedure. The K-means algorithm is actually a special case of the Gaussian mixture model (GMM) clustering method. In the GMM clustering method, the data is assumed to follow a GMM of the form

$$\mathbf{Y}_i = \sum_{k=1}^{K} w_{ik}\pi(\mathbf{Y}_i|\theta_k). \tag{4.2}$$

Here K is the number of clusters, $w_{ik} = \mathrm{P}(x_i = k)$ are prior probabilities for the multi-path component i belonging to class k, and $\pi(\mathbf{Y}_i|\theta_k)$ denotes a Gaussian density function with parameter mean, μ_k and, covariance matrix, Σ_k (note that $\theta_k = \{\mu_k, \Sigma_k\}$). This model can be estimated using the EM algorithm, where the following steps are iterated until convergence:

- $\forall i \in [1, n]$ and $k \in [1, K]$, set

$$\pi_{ik} = \frac{w_k\pi(\mathbf{Y}_i|\theta_k)}{\sum_{k=1}^{K} w_k\pi(\mathbf{Y}_i|\theta_k)}.$$

- $\forall k \in [1, K]$, let $\pi_k = \sum_{i=1}^{n} \pi_{ik}$ and set $w_k = \pi_k/n$ and

$$\mu_k = \frac{1}{\pi_k}\sum_{i=1}^{n} \mathbf{Y}_i\pi_{ik},$$
$$\Sigma_k = \frac{1}{\pi_k}\sum_{i=1}^{n} \pi_{ik}(\mathbf{Y}_i - \mu_k)(\mathbf{Y}_i - \mu_k)^{\mathrm{T}}.$$

Once convergence is reached, a clustering is obtained by selecting $x_i = \arg\max_k \pi_{ik}$. Note that the K-means clustering is obtained if the covariance matrix is restricted to $\Sigma_k = \sigma^2 I$ and if $\sigma^2 \to 0$. A power weighted version of the GMM has been presented in paper VI of this thesis. There, a clustering method based on a mixture of asymmetric Laplace distributions was presented as well. Other clustering methods, based on for instance hierarchical methods, have also been proposed [69]. In Fig. 4.1, a typical clustering result using the K-power-means algorithm is shown, for an indoor scenario at 62 GHz in a conference room environment [26].

Another problem that needs to be solved when performing mutli-path clustering, is how to determine the number of clusters in a given measurement data set. The standard approach for this is to try to determine the number of cluster based on a clustering index. These indices are normally based on metrics that corresponds to intra-cluster compactness and inter-cluster separation [69].

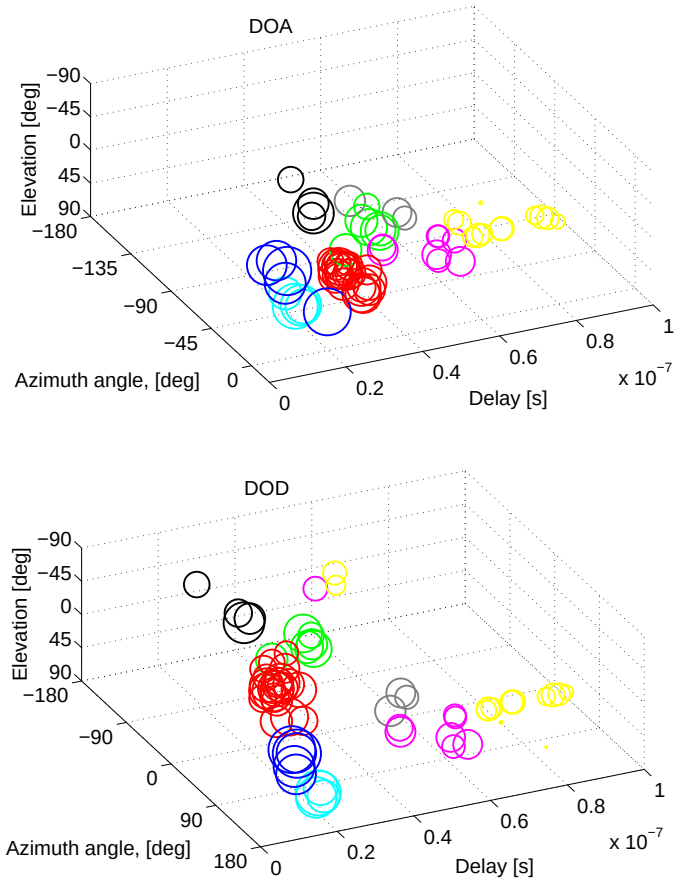

Figure 4.1: Typical clustering result when using the K-power-means algorithm.

Chapter 5

mm-Wave Channel and Antenna Measurements

Due to the technological constraints of the channel sounding devices at mm-wave frequencies, the measurement techniques are somewhat different compared to the state-of-the-art channel sounder techniques that are available for the lower frequency bands. In this chapter, the main channel sounding techniques that are used at mm-wave bands, are briefly presented.

5.1 Rotating Antenna Technique

A technique that has been widely used at 60 GHz and mm-wave frequencies is the rotating antenna technique [70]. This method uses a highly directional antenna that is mechanically rotated in two or three dimensions. Measurements are taken at each angle. This way, the power-angular spectra can be retrieved. The PDP can be obtained by integrating the measurements over the measurement angles. A drawback of this technique is that it requires a large number of measurements in order to cover all directions, which makes it time consuming. For this reason, this method can only be applied to measure channels that are nearly static. In spite of these drawbacks, this method has been found to be very useful. The method can be used with a vector-network analyzer or any other type of channel sounding device, as long as the antenna can be rotated. It is also possible to perform different directional estimation techniques to the measured data.

The accuracy of this method depends on the limitations of the channel sounder as well as the directivity and sidelobes of the antenna pattern for the

antenna that is being rotated. If phase information from the measurement is used, it is also important to consider the influence of possible cables being bent or moved. Furthermore, the phase might be affected by the phase center of the rotating antenna. However, the phase center of the antenna is usually frequency dependent and difficult to estimate.

5.2 Virtual Antenna Array Technique

Another channel sounding technique is based on the virtual antenna array principle. When using this method, a single Tx and a single Rx antenna is typically attached to a mechanical positioning device. The spatial position of the Tx and Rx antenna are then successively changed according to a pre-defined spatial pattern, and measurements are taken at every spatial position. This way, virtual Tx and Rx arrays can be formed, with arbitrary array configurations. The virtual antenna array technique can be used to create measurement data sets suitable for directional estimation. This method has been applied in [26] for indoor measurements in the 60 GHz band. Similar to the rotating antenna technique, the virtual antenna array technique is limited to scenarios that are nearly time-static, and the influence of moving cables or drifts in the measurement instruments have to be considered.

5.3 Real-time Channel Sounders

The main drawbacks of virtual antenna array and rotating antenna array techniques, is that they are limited to time-static scenarios. There are however 60 GHz and mm-wave channel sounders that supports near-real-time measurements. This allows for measuring non-static scenarios, which is necessary to characterize for instance Doppler spreads and dynamic human-body shadowing scenarios. A wideband channel sounder for the 60 GHz band, that supports a bandwidth of 5 GHz, is presented in [21]. In a more recent paper, a dual-polarized ultra-wideband channel sounder with up to 7 GHz instantaneous bandwidth is presented [71]. It has an architecture that allows for easy scalability of the number of receivers, and, depending on the choice of the intermediate frequency, many different bands in the range of 24-66 GHz, with bandwidths of 3.5 or 7 GHz, can be asessed.

Ideally, real-time channel sounding is of course desired. However, the near-real-time channel sounders that have been presented in the literature so far, only include a limited number of Tx and Rx antenna array elements, making it infeasible to perform reliable real-time channel measurements that allow for high resolution directional parameter estimation.

5.4 Antenna Measurements

The antenna patterns of the antennas used in the included papers were measured using a VNA and a positioning system. The co- and cross polarized antenna pattern for a standard V-band open-ended waveguide and a biconical antenna from Flann Microwave (MD249, 50-70GHz) were measured by applying a roll-over-elevation method. The antenna gains were calculated based on the gain-transfer method [72]. The accuracy of the measurements were validated by comparing the measured antenna patterns with the gain specifications from the antenna manufacturer and based on the antenna gain simulated in an electromagnetic full-wave simulator. The measured antenna gains are shown in Fig. 2.3.

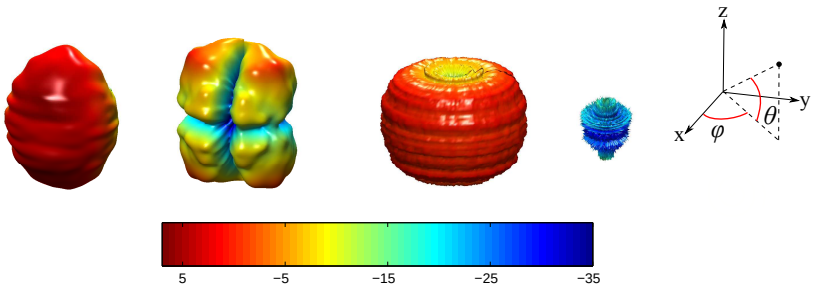

Figure 5.1: Co- and cross-polarized antenna gains at 62 GHz, in units of dBi, for a standard V-band open waveguide and a bi-conical antenna from Flann Microwave. Ordered from left to right, the patterns are for the co-polarized open waveguide, cross-polarized open waveguide, co-polarized biconical and cross-polarized biconical antenna.

Chapter 6

Summary and Contributions

This chapter summarizes the research contributions of the papers included in this thesis and then discusses topics for future work.

6.1 Research contributions

6.1.1 Paper I: Directional Analysis of Measured 60 GHz Indoor Radio Channels using SAGE

This paper puts focus on the double-directional properties of the 60 GHz indoor radio channel.The directional properties of the 60 GHz channel is of significant importance for two main reasons: Firstly, most of the wireless channel models for 60 GHz communications are rooted in the double-directional channel model, where the channel is described in terms of a sum of plane waves. These plane waves are referred to as multi-path components (MPCs). These MPCs needs to be effectively estimated and characterized in order to be able to derive a reliable 60 GHz indoor channel model. Secondly, as 60 GHz indoor channels typically suffer from a much greater signal attenuation compared to the 2 and 5 GHz bands that are commonly used today, 60 GHz communication systems are expected to rely on beamforming to be able to ensure reliable communication. In case of shadowing, for instance by a person blocking the current signal pathway, the signal is re-routed using beamforming to a different direction to make sure that the communication link is still up. For this reason, it is important to characterize the double-directional propagation properties of the MPC param-

eters with respect to power, delay and directions of arrival and departure, so that different beam-forming techniques can be effectively evaluated.

The results in this paper are based on transfer-functions measured from 61 to 65 GHz in a conference room environment, using a vector network analyzer-based system. Electro-mechanical positioners were used to form 7×7 planar virtual arrays at both the Tx-Rx sides. The Rx antenna array was placed at a fixed position close to one of the corners of the room, whereas the Tx antenna array was placed at different positions within the conference room. The measurement campaign includes 17 LOS scenarios as well as 15 NLOS scenarios where the Tx is placed at the same position as in a corresponding LOS scenario, which makes it possible to effectively compare the corresponding LOS and NLOS scenarios. In the NLOS scenario, the Tx is blocked by a computer laptop. The SAGE algorithm is applied to the measurement data in order to obtain maximum-likelihood estimates for the MPC parameters. To the authors best knowledge, this is one of the first papers to present high-resolution MPC parameter estimates for the 60 GHz double-directional channel. Furhtermore, the results include azimuth and elevation parameter estimates for both the direction of arrival and departure, which at the time of publication was not available in the literature.

The results show that the LOS component is quite dominant in the LOS scenario, and is usually about 20 dB stronger than the second strongest component. By comparing the directional properties with the room geometry, the results show that it is possible to correctly identify the signal pathways and to identify the propagation mechanisms involved for the strongest components. This verifies that it is feasible to apply the concept of virtual arrays and high resolution parameter estimators to 60 GHz channel measurement data. First and second order interactions account for the major contribution of the received power. The results also show that finer structures such as ceiling lamps are significant interacting objects, indicating that it is important to include the elevation information and that finer structures should be considered when measuring or modeling typical environments.

By comparing the corresponding LOS and NLOS scenarios, we find that the MPC parameters are *very* similar in the directions that are not covered by the laptop screen. It also shows that diffraction in fact *can* be a significant propagation mechanism in certain cases. Furthermore, the shadowing object does not only affect the LOS component but also any other signal pathways that happen to be shadowed. This shows that it might not be sufficient to just remove the LOS component to emulate a typical NLOS scenario, which is done in the IEEE 802.15.3c channel model.

Lastly, it can be observed that the MPCs appear to be clustered in the angular-delay domain, indicating that the 60 GHz channel could be efficiently

modeled by a cluster-based double directional model.

I am the main contributor of the paper and was responsible for the data analysis and the writing of the paper. Ialso modified a previous version of a SAGE algorithm to also include the frequency dependence of the radio signals. I was involved in all parts of the work, except for the channel measurements, which were performed by co-authors Katsuyuki Haneda and Shurjeel Wyne before I started as a Ph.D. student.

6.1.2 Paper II: On mm-Wave Multi-path Clustering and Channel Modeling

This paper is a presents a double-directional MIMO channel model based on the measurements presented in paper I. For this paper, the parameter estimates from SAGE are improved by estimating a larger number of MPCs and by including the Tx and Rx antenna patterns in the estimation procedure, so that the antenna patterns can be de-embedded. Now, the MPC estimates describe the *propagation channel*, which in contrast to the radio channel is independent of the antenna pattern. This allows us to derive a cluster-based double-directional propagation channel model that is valid for an arbitrary type of antenna element and array geometry.

The MPC parameters are clustered using the well-known K-power-means algorithm and the number of clusters are identified using the Kim-Parks index. Using the results from the clustering algorithm, parameter estimates for a cluster-based double-directional model is presented, evaluated and compared with two 60 GHz industry standard channel models; IEEE 802.15.3c and IEEE802.11ad. It is shown that the spatio-temporal properties of the MPCs are related to the room environment, especially for the elevation angles. For this reason, two different way of modeling the cluster centroids are considered: In the first approach, the cluster centroids are generated deterministically based on a simple ray tracing routine. In the second approach, simple probability distributions are used to randomly generate the cluster centroids. When validating the results for the two methods, it is evident that the stochastic approach shows a better performance when it comes to reproduce the statistical behavior of the channel. The approach based on ray-tracing is lacking in its performance due to an over-simplified description of the environment in the ray-tracing algorithm. The type of description used for the environment in the ray-tracing algorithm is the same as the one used in the IEEE802.11ad model. This shows that if ray-tracing is to be used at 60 GHz, finer structures such as chairs, bookshelves and ceiling lamps need to be included in the model, and that the IEEE802.11ad model might be lacking in its performance.

Lastly, the presented channel model is validated against the measured data

by comparing statistical distributions for the eigenvalues, delay spreads and directional spreads of the channels generated by the model with those from the measurements. The model shows a good statistical agreement with all of these three measures, which shows that the derived model can be used to reproduce the typical statistical behavior of the 60 GHz channel.

I am the main contributor of this paper. I performed the antenna pattern measurements and was responsible for the data analysis and the writing of the paper.

6.1.3 Paper III: Characterization of 60 GHz Shadowing by Human Bodies and Simple Phantoms

For 60 GHz indoor channels, human body shadowing has been shown to have a significant impact on the received power, and beamforming typically needs to be employed to overcome this obstacle. In this paper, we present an experimental, measurement-based characterization of the reflection and shadowing effects in the 60 GHz band caused by human bodies and various phantoms. In the VNA-based measurement setup, highly directional horn antennas are scanned across the object. The measured data is post-processed to remove the influence of cables, amplifiers, antennas and then gated in the delay domain to remove contributions from possible multi-path components that have a delay longer than those of the field diffracted around the shadowing object.

It is shown that the geometrical theory of diffraction can be used to accurately model the diffracted field around simple objects such as a cylinder. The shadowing caused by a metallic cylinder, a water-filled cylinder and a metallic sheet is compared with those of human legs. It is shown that the shadowing is fairly similar for these objects. Finally, the shadowing due to a water-filled human phantom is compared with those of a real person. Results show that the water-filled phantom had shadowing properties similar to those of humans and is thus suitable for use as a human shadowing object in the 60 GHz band.

I am the main contributor of this paper and was involved in all parts of the work. I performed all the measurements myself and was responsible for the data analysis and writing of the paper.

6.1.4 Paper IV: Modeling the Cluster Decay in mm-Wave Channels

During the work with paper II, it was found that the channel model initially overestimated the delay spread. It was found that this overestimation was due to an incorrect estimation of the cluster decay parameter. In this paper, we derive a novel way of estimating the cluster decay and the large scale cluster

fading, wherein the effects of the noise floor are taken into account. In the paper we show that if the effects of the noise floor are *not* taken into account, the cluster decay might be overestimated (corresponding a slower cluster decay) and the cluster fading might be underestimated. The problem is solved by taking possible missing clusters into account through the use of a maximum-likelihood expression based on a truncated normal distribution. It is shown that this method improves the parameter estimates of the cluster decay and fading. When applying these results in the channel model paper, the delay spread is no longer being overestimated. This paper also shows that 60 GHz channel models are sensitive to the cluster decay parameter, which is due to the large cluster K-factor of around 10 dB for the clusters.

I am the main contributor of this paper. I came up with the idea for the paper, was responsible for the data analysis and writing of the paper. David Bolin contributed with ideas for the mathematical formulation of the problem and with implementation aspects of the maximum-likelihood estimator used in the paper.

6.1.5 Paper V: 60 GHz Spatial Radio Transmission: Multiplexing or Beamforming?

In this paper, the capacity improvement capability of spatial multiplexing and beamforming techniques for 60 GHz spatial transmission in an indoor environment is evaluated. In this paper, beamforming refers to the conventional gain focusing by narrow antenna beams in the direction of the strongest propagation path. In the paper, a channel capacity metric that only depends on the richness of multi-path propagation channel and the antenna aperture size, is derived. The paper also derives values for the spatial-degrees-of-freedom (SDoF), which is the maximum number of antenna elements on the aperture that are needed for efficient multiplexing. The results are evaluated based on measured single-polarized 60 GHz radio channels, and shows that the channel offers multiple SDoFs under both LOS and NLOS conditions, given that the receive SNR is sufficiently high. Lastly, the paper compares spatial multiplexing and beamforming techniques in terms of their attainable channel capacity using measured 60 GHz radio channels. This comparison shows that, for a Tx power constraint of -10 dBm, spatial multiplexing is advantageous over beamforming when the antenna aperture size is larger than $1\lambda^2$ and $9\lambda^2$ in LOS and NLOS scenarios, respectively.

Katsuyuki Haneda is the main contributor of the paper. I was responsible for producing the SAGE estimates for the propagation channel, and contributed with ideas, suggestions and by writing parts of the paper.

6.1.6 Paper VI: A Note on Clustering Methods for Wireless Channel Models

This paper deals with different clustering methods for wireless channel models. In the paper, we compare the well-known K-means algorithm with a Gaussian mixture model (GMM) and a novel method based on a mixture of asymmetric Laplace (AL) distributions. Also, a hierarchical clustering method is also presented and it is suggested that this method can be used to get initial cluster estimates for the different clustering methods. In the paper, it is also noted that K-means is a special case of a GMM, and power-weighted versions of all of these clustering methods are also presented. It is shown that the performance of K-means is poor for cases when the cluster shape is uneven, for instance when the cluster spreads are different in the different dimensions. The GMM is able to handle clusters with uneven spread in the different dimensions and is thus superior to K-means. However, if the cluster distribution is not Gaussian, the performance of the GMM might be lacking. For instance, if the cluster shape is AL-distributed, the clustering method based on an AL mixture outperforms the GMM.

I am the main contributor of this paper, and was responsible for writing the paper, the data analysis and the implementation of the hierarchical clustering method. David Bolin contributed with writing of the paper and with the implementation of the GMM. Jonas Wallin contributed with writing of the paper and with the implementation of the AL clustering method.

6.1.7 Paper VII: Polarimetric Channel Measurements at 60 GHz with Realistic Shadowing

Paper VII presents measurement-based results in a small meeting room and a larger conference room. The measurement includes LOS scenarios and NLOS scenarios where the direct path is shadowed by the water-filled phantom that was analyzed in paper III. In these measurements, dual-polarized antenna elements are used at both the Tx and Rx arrays, making it possible to evaluate the influence of polarization orientation on the the system performance. The paper presents experimental values of the cross-polarization ratios (XPRs) of the propagation paths. Furthermore, the eigenvalue spreads of single- and dual-polarized antenna arrays are investigated. Lastly, cluster decay rates for the two different rooms are estimated.

I am the main contributor of this paper, performed the measurements and was responsible for the data analysis and the writing of the paper.

6.2 General Conclusions and Future Work

The wireless channel involves complex processes and has a huge impact on the received signal and the performance of any wireless system. It is therefore necessary to carefully characterize and model the typical behavior of the wireless channel. However, the behavior of the wireless channel can be very different from one frequency band to another and from one scenario to another, making it necessary to characterize channels with respect to the intended frequency and scenario. This thesis has shed some light on the general behavior and characteristics of mm-wave propagation channels, with a special focus on indoor channels in the 60 GHz band. In this section, I would like to share some of my thoughts on some general conclusions about the field and possible areas of future work.

Through my work over the years, I have learned that channel measurements are essential when it comes to channel modeling and channel characterization. The directional analysis in paper I revealed that the indoor 60 GHz channel is dominated by specular reflections, as one might expect. However, it is not easy to predict the signal strength of these specular paths as it depends on the scattering objects present in the environment. At mm-wave frequencies, ray-tracing has proved to be useful at least to some extent. However, as shown in paper II of this thesis, a simple model for the environment, where only the walls, floor, ceiling and a table is taken into account in the ray-tracing routine, is often not enough to accurately predict the behavior of the channel. An interesting topic for future work could be to investigate exactly how detailed the model for the environment geometry and permittivity of the objects need to be, in order for the ray-tracing routine to give accurate-enough results.

For 60 GHz and mm-wave channels, some of the areas that, in my opinion, require urgent attention, are the following:

- Further measurement based characterization and modeling of the polarization properties of mm-wave channels.
- Real-time channel measurements that include a large number of antennas, so that the time-varying directional channel can be investigated.
- Improved modeling of typical cellular mm-wave scenarios, based on real-time channel measurements.
- Currently, many different frequency bands in the range from 15-90 GHz are being researched. Therefore, the current mm-wave modeling and characterization results need to be extended to cover a wider frequency range.

Lastly, another interesting topic for future work, is to look into novel ways of modeling and estimating the wireless channel. Currently, a popular way of modeling the channel has been through the use of double-directional cluster-based channel models. When deriving such channel models, the workflow is typically performed in four different steps, as follows:

1. Perform a measurement campaign in order to gather a large data set.
2. Given a certain signal model for the channel, estimate the components of the channel, using a high-resolution parameter estimator.
3. Cluster the estimated components, using a clustering method.
4. Examine the clustering results in order to propose a suitable channel model, and then estimated the parameters for this model based on the clustering results.

A basic problem with this approach is that steps 2-4 in general are based on different signal models and assumptions, and the parameter results are affected by all of these. In paper VI, a first attempt at trying to combine steps 3-4 was presented. In future work, it would be of interest to try to combine steps 2-4. This could be achieved by having one basic model that includes everything, from the directional signal model, the assumptions regarding clusters and all of the modeling assumptions made in the channel model. So, instead of having three separate models that have little or no connection at all, one single model is used instead. If successful, this approach could potentially improve the performance of the estimated channel model. One should keep in mind, that this approach is quite daunting, since such a model would be very complex and would thus require a lot of work. It is yet unclear if it is possible to accurately estimate the parameters of such a model, as it encompasses so many different aspects.

References

[1] P. Bondyopadhyay, "Sir J.C. Bose diode detector received Marconi's first transatlantic wireless signal of December 1901 (the Italian Navy Coherer Scandal Revisited)," *Proceedings of the IEEE*, vol. 86, no. 1, pp. 259–285, Jan 1998.

[2] Cisco, *Cisco Visual Networking Index: Global Mobile Data Traffic Forecast Update, 20132018.* Cisco, Feb 2014. [Online]. Available: http://www.cisco.com

[3] L. Ohlsson, T. Bryllert, C. Gustafson, D. Sjöberg, M. Egard, M. Ärlelid, and L.-E. Wernersson, "Slot-Coupled Millimeter-Wave Dielectric Resonator Antenna for High-Efficiency Monolithic Integration," *IEEE Transactions on Antenas and Propagation*, vol. 61, no. 4, pp. 1599–1607, 2013. [Online]. Available: http://dx.doi.org/10.1109/TAP.2012.2237005

[4] Y.-P. Zhang, M. Sun, K. Chua, L. Wai, and D. Liu, "Antenna-in-Package Design for Wirebond Interconnection to Highly Integrated 60-GHz Radios," *Antennas and Propagation, IEEE Transactions on*, vol. 57, no. 10, pp. 2842–2852, Oct 2009.

[5] T. Rappaport, S. Sun, R. Mayzus, H. Zhao, Y. Azar, K. Wang, G. Wong, J. Schulz, M. Samimi, and F. Gutierrez, "Millimeter Wave Mobile Communications for 5G Cellular: It Will Work!" *Access, IEEE*, vol. 1, pp. 335–349, 2013.

[6] S. Hur, T. Kim, D. Love, J. Krogmeier, T. Thomas, and A. Ghosh, "Multilevel millimeter wave beamforming for wireless backhaul," in *GLOBECOM Workshops (GC Wkshps), 2011 IEEE*, Dec 2011, pp. 253–257.

[7] M. Beltran, R. Llorente, R. Sambaraju, and J. Marti, "60 GHz UWB-over-fiber system for in-flight communications," in *Microwave Symposium Digest, 2009. MTT '09. IEEE MTT-S International*, June 2009, pp. 5–8.

[8] A. Garcia, W. Kotterman, R. Thoma, U. Trautwein, D. Bruckner, W. Wirnitzer, and J. Kunisch, "60 GHz in-cabin real-time channel sounding," in *Communications and Networking in China, 2009. ChinaCOM 2009. Fourth International Conference on*, Aug 2009.

[9] M. Peter, R. Felbecker, W. Keusgen, and J. Hillebrand, "Measurement-Based Investigation of 60 GHz Broadband Transmission for Wireless In-Car Communication," in *Vehicular Technology Conference Fall (VTC 2009-Fall), 2009 IEEE 70th*, Sept 2009.

[10] W.-H. Chen, S. Joo, S. Sayilir, R. Willmot, T.-Y. Choi, D. Kim, J. Lu, D. Peroulis, and B. Jung, "A 6-Gb/s Wireless Inter-Chip Data Link Using 43-GHz Transceivers and Bond-Wire Antennas," *Solid-State Circuits, IEEE Journal of*, vol. 44, no. 10, pp. 2711–2721, Oct 2009.

[11] G. Zhu, D. Guidotti, F. Lin, Q. Wang, J. Cui, Q. Wang, L. Cao, T. Ye, and L. Wan, "Millimeter wave interchip communication," in *Millimeter Waves (GSMM), 2012 5th Global Symposium on*, May 2012, pp. 471–476.

[12] N. Obeid, M. Heddebaut, F. Boukour, C. Loyez, and N. Rolland, "Millimeter Wave Ultra Wide Band Short Range Radar Localization Accuracy," in *Vehicular Technology Conference, 2009. VTC Spring 2009. IEEE 69th*, April 2009.

[13] IEEE802.15.3c-2009, " Part 15.3: Wireless Medium Access Control (MAC) and Physical Layer (PHY) Specifications for High Rate Wireless Personal Area Networks (WPANs), Amendment 2: Millimeter-wave- based Alternative Physical Layer Extension," *doc.*, Oct. 2009.

[14] I. 802.11-09/0334r8, "Channel Models for 60 GHz WLAN Systems," *IEEE P802.11 Wireless LANs*, May 2010.

[15] J. Kermoal, L. Schumacher, K. Pedersen, P. Mogensen, and F. Frederiksen, "A stochastic MIMO radio channel model with experimental validation," *Selected Areas in Communications, IEEE Journal on*, vol. 20, no. 6, pp. 1211–1226, Aug 2002.

[16] W. Weichselberger, M. Herdin, H. Ozcelik, and E. Bonek, "A stochastic MIMO channel model with joint correlation of both link ends," *Wireless Communications, IEEE Transactions on*, vol. 5, no. 1, pp. 90–100, Jan 2006.

[17] J. Karedal, F. Tufvesson, N. Czink, A. Paier, C. Dumard, T. Zemen, C. Mecklenbrauker, and A. Molisch, "A geometry-based stochastic MIMO

model for vehicle-to-vehicle communications," *Wireless Communications, IEEE Transactions on*, vol. 8, no. 7, pp. 3646–3657, July 2009.

[18] A. Saleh and R. Valenzuela, "A Statistical Model for Indoor Multipath Propagation," *Selected Areas in Communications, IEEE Journal on*, vol. 5, no. 2, pp. 128–137, February 1987.

[19] Q. Spencer, B. Jeffs, M. Jensen, and A. Swindlehurst, "Modeling the statistical time and angle of arrival characteristics of an indoor multipath channel," *Selected Areas in Communications, IEEE Journal on*, vol. 18, no. 3, pp. 347–360, March 2000.

[20] M. Steinbauer, A. Molisch, and E. Bonek, "The double-directional radio channel," *Antennas and Propagation Magazine, IEEE*, vol. 43, no. 4, pp. 51–63, Aug 2001.

[21] T. Zwick, T. Beukema, and H. Nam, "Wideband channel sounder with measurements and model for the 60 GHz indoor radio channel," *Vehicular Technology, IEEE Transactions on*, vol. 54, no. 4, pp. 1266–1277, July 2005.

[22] N. Azzaoui and L. Clavier, "Statistical channel model based on a-stable random processes and application to the 60 GHz ultra wide band channel," *Communications, IEEE Transactions on*, vol. 58, no. 5, pp. 1457–1467, May 2010.

[23] M. Kyro, K. Haneda, J. Simola, K.-i. Takizawa, H. Hagiwara, and P. Vainikainen, "Statistical Channel Models for 60 GHz Radio Propagation in Hospital Environments," *Antennas and Propagation, IEEE Transactions on*, vol. 60, no. 3, pp. 1569–1577, March 2012.

[24] M.-S. Choi, G. Grosskopf, and D. Rohde, "Statistical Characteristics of 60 GHz Wideband Indoor Propagation Channel," in *Personal, Indoor and Mobile Radio Communications, 2005. PIMRC 2005. IEEE 16th International Symposium on*, vol. 1, Sept 2005, pp. 599–603.

[25] S. Geng, J. Kivinen, X. Zhao, and P. Vainikainen, "Millimeter-Wave Propagation Channel Characterization for Short-Range Wireless Communications," *Vehicular Technology, IEEE Transactions on*, vol. 58, no. 1, pp. 3–13, Jan 2009.

[26] C. Gustafson, K. Haneda, S. Wyne, and F. Tufvesson, "On mm-Wave Multipath Clustering and Channel Modeling," *Antennas and Propagation, IEEE Transactions on*, vol. 62, no. 3, pp. 1445–1455, March 2014.

[27] M. Jacob, S. Priebe, T. Kurner, M. Peter, M. Wisotzki, R. Felbecker, and W. Keusgen, "Extension and validation of the IEEE 802.11ad 60 GHz human blockage model," in *Antennas and Propagation (EuCAP), 2013 7th European Conference on*, April 2013, pp. 2806–2810.

[28] A. F. Molisch, *Wireless Communications*. Chicester, U.K: IEEE Press - Wiley, 2011.

[29] T. Abbas, C. Gustafson, and F. Tufvesson, "Pathloss Estimation Techniques for Incomplete Channel Measurement Data," *COST IC1004 10th Management Committee and Scientific Meeting*, May 2014.

[30] T. Rappaport, E. Ben-Dor, J. Murdock, and Y. Qiao, "38 GHz and 60 GHz angle-dependent propagation for cellular amp; peer-to-peer wireless communications," in *Communications (ICC), 2012 IEEE International Conference on*, June 2012, pp. 4568–4573.

[31] G. MacCartney, J. Zhang, S. Nie, and T. Rappaport, "Path loss models for 5G millimeter wave propagation channels in urban microcells," in *Global Communications Conference (GLOBECOM), 2013 IEEE*, Dec 2013, pp. 3948–3953.

[32] M. Akdeniz, Y. Liu, M. Samimi, S. Sun, S. Rangan, T. Rappaport, and E. Erkip, "Millimeter Wave Channel Modeling and Cellular Capacity Evaluation," *Selected Areas in Communications, IEEE Journal on*, vol. 32, no. 6, pp. 1164–1179, June 2014.

[33] Y. Azar, G. Wong, K. Wang, R. Mayzus, J. Schulz, H. Zhao, F. Gutierrez, D. Hwang, and T. Rappaport, "28 GHz propagation measurements for outdoor cellular communications using steerable beam antennas in New York city," in *Communications (ICC), 2013 IEEE International Conference on*, June 2013, pp. 5143–5147.

[34] T. Rappaport, F. Gutierrez, E. Ben-Dor, J. Murdock, Y. Qiao, and J. Tamir, "Broadband Millimeter-Wave Propagation Measurements and Models Using Adaptive-Beam Antennas for Outdoor Urban Cellular Communications," *Antennas and Propagation, IEEE Transactions on*, vol. 61, no. 4, pp. 1850–1859, April 2013.

[35] S. Hur, Y. Cho, T. Kim, and J. Park, "Millimeter-wave Channel Modeling based on Measurements in In-building, Campus and Urban Environments at 28 GHz," in *Euro- COST, IC1004, TD(14)11029*, Sep 2014.

[36] J. Wells, "Faster than fiber: The future of multi-G/s wireless," *Microwave Magazine, IEEE*, vol. 10, no. 3, pp. 104–112, May 2009.

[37] A. F. Molisch and F. Tufvesson, "Propagation Channel Models for Next Generation Wireless Communications Systems," in *Communications, IEICE Tansactions on*, Oct 2014.

[38] Z. Qingling and J. Li, "Rain Attenuation in Millimeter Wave Ranges," in *Antennas, Propagation EM Theory, 2006. ISAPE '06. 7th International Symposium on*, Oct 2006, pp. 1–4.

[39] P. Smulders, "Statistical Characterization of 60-GHz Indoor Radio Channels," *Antennas and Propagation, IEEE Transactions on*, vol. 57, no. 10, pp. 2820–2829, Oct 2009.

[40] H. Yang, P. F. M. Smulders, and M. H. A. J. Herben, "Channel Characteristics and Transmission Performance for Various Channel Configurations at 60 GHz," *Journal on Wireless Communications and Networking, EURASIP*, vol. Article ID 19613, Mar 2007.

[41] C. Gustafson, F. Tufvesson, S. Wyne, K. Haneda, and A. F. Molisch, "Directional analysis of measured 60 GHz indoor radio channels using SAGE," in *2011 IEEE 73rd Vehicular Technology Conference (VTC Spring), 2011-05-15/2011-05-18*. IEEE, May 2011.

[42] C. Gustafson, D. Bolin, and F. Tufvesson, "Modeling the cluster decay in mm-wave channels," in *Antennas and Propagation (EuCAP), 2014 8th European Conference on, 2014-04-06*, Apr 2014.

[43] M. Kyro, K. Haneda, J. Simola, K. Nakai, K.-i. Takizawa, H. Hagiwara, and P. Vainikainen, "Measurement Based Path Loss and Delay Spread Modeling in Hospital Environments at 60 GHz," *Wireless Communications, IEEE Transactions on*, vol. 10, no. 8, pp. 2423–2427, August 2011.

[44] T. Rappaport, E. Ben-Dor, J. Murdock, and Y. Qiao, "38 GHz and 60 GHz angle-dependent propagation for cellular amp; peer-to-peer wireless communications," in *Communications (ICC), 2012 IEEE International Conference on*, June 2012, pp. 4568–4573.

[45] H. Yang, P. Smulders, and M. Herben, "Indoor Channel Measurements and Analysis in the Frequency Bands 2 GHz and 60 GHz," in *Personal, Indoor and Mobile Radio Communications, 2005. PIMRC 2005. IEEE 16th International Symposium on*, vol. 1, Sept 2005, pp. 579–583.

[46] S. Wyne, K. Haneda, S. Ranvier, F. Tufvesson, and A. Molisch, "Beamforming Effects on Measured mm-Wave Channel Characteristics," *Wireless Communications, IEEE Transactions on*, vol. 10, no. 11, pp. 3553–3559, November 2011.

[47] W. Khan, M. Zubair, S. Wyne, F. Tufvesson, and K. Haneda, "Performance Evaluation of Time-Reversal on Measured 60 GHz Wireless Channels," *Wireless Personal Communications*, vol. 71, no. 1, pp. 707–717, 2013. [Online]. Available: http://dx.doi.org/10.1007/s11277-012-0838-5

[48] T. Manabe, Y. Miura, and T. Ihara, "Effects of antenna directivity and polarization on indoor multipath propagation characteristics at 60 GHz," *Selected Areas in Communications, IEEE Journal on*, vol. 14, no. 3, pp. 441–448, Apr 1996.

[49] T. Manabe, K. Sato, H. Masuzawa, K. Taira, T. Ihara, Y. Kasashima, and K. Yamaki, "Polarization dependence of multipath propagation and high-speed transmission characteristics of indoor millimeter-wave channel at 60 GHz," *Vehicular Technology, IEEE Transactions on*, vol. 44, no. 2, pp. 268–274, May 1995.

[50] A. Maltsev, E. Perahia, R. Maslennikov, A. Sevastyanov, A. Lomayev, and A. Khoryaev, "Impact of Polarization Characteristics on 60-GHz Indoor Radio Communication Systems," *Antennas and Wireless Propagation Letters, IEEE*, vol. 9, pp. 413–416, 2010.

[51] P. Karadimas, B. Allen, and P. Smith, "Human Body Shadowing Characterization for 60-GHz Indoor Short-Range Wireless Links," *Antennas and Wireless Propagation Letters, IEEE*, vol. 12, pp. 1650–1653, 2013.

[52] A. Garcia, W. Kotterman, U. Trautwein, D. Brckner, J. Kunisch, and R. Thoma, "60 GHz time-variant shadowing characterization within an Airbus 340," in *Antennas and Propagation (EuCAP), 2010 Proceedings of the Fourth European Conference on*, April 2010.

[53] C. Gustafson and F. Tufvesson, "Characterization of 60 GHz Shadowing by Human Bodies and Simple Phantoms," *Radioengineering*, vol. 21, no. 4, pp. 979–984, 2012.

[54] M. Jacob, S. Priebe, T. Kurner, M. Peter, M. Wisotzki, R. Felbecker, and W. Keusgen, "Fundamental analyses of 60 GHz human blockage," in *Antennas and Propagation (EuCAP), 2013 7th European Conference on*, April 2013, pp. 117–121.

[55] T. Mavridis, L. Petrillo, J. Sarrazin, D. Lautru, A. Benlarbi-Delai, and P. De Doncker, "Theoretical and Experimental Investigation of a 60-GHz Off-Body Propagation Model," *Antennas and Propagation, IEEE Transactions on*, vol. 62, no. 1, pp. 393–402, Jan 2014.

[56] M. Jacob, S. Priebe, A. Maltsev, A. Lomayev, V. Erceg, and T. Kurner, "A ray tracing based stochastic human blockage model for the IEEE 802.11ad 60 GHz channel model," in *Antennas and Propagation (EUCAP), Proceedings of the 5th European Conference on*, April 2011, pp. 3084–3088.

[57] J. Kunisch and J. Pamp, "Ultra-wideband double vertical knife-edge model for obstruction of a ray by a person," in *Ultra-Wideband, 2008. ICUWB 2008. IEEE International Conference on*, vol. 2, Sept 2008, pp. 17–20.

[58] A. Maltsev, R. Maslennikov, A. Lomayev, A. Sevastyanov, and A. Khorayev, "Statistical Channel Model for 60 GHz WLAN Systems in Conference Room Environment," *Radioengineering*, june 2011.

[59] A. Maltsev, R. Maslennikov, A. Sevastyanov, A. Khoryaev, and A. Lomayev, "Experimental investigations of 60 GHz WLAN systems in office environment," *Selected Areas in Communications, IEEE Journal on*, vol. 27, no. 8, pp. 1488–1499, October 2009.

[60] A. Karttunen, K. Haneda, J. Järveläinen, and J. Putkonen, "Polarisation Characteristics of Propagation Paths in Indoor 70 GHz Channels," *COST IC1004, Krakow*, Sep. 2015.

[61] R. I.-R. P.1238-7, "Propagation data and prediction methods for the planning of indoor radio communication systems?and radio local area networks in the frequency range 900 MHz to 100 GHz," *P Series, Radiowave propagation*, Feb. 2012.

[62] P. K. *et. al.*, "WINNER II Channel Models," *D1.1.2 V1.*, Sep. 2007.

[63] J. Fessler and A. Hero, "Space-alternating generalized expectation-maximization algorithm," *Signal Processing, IEEE Transactions on*, vol. 42, no. 10, pp. 2664–2677, Oct 1994.

[64] B. Fleury, M. Tschudin, R. Heddergott, D. Dahlhaus, and K. Ingeman Pedersen, "Channel parameter estimation in mobile radio environments using the SAGE algorithm," *Selected Areas in Communications, IEEE Journal on*, vol. 17, no. 3, pp. 434–450, Mar 1999.

[65] J. Richter, A. Salmi and V. Koivunen, "An algorithm for estimation and tracking of distributed diffuse scattering in mobile radio channels," *Signal Processing Advances in Wireless Communications, IEEE 7th Workshop on*, 2006.

[66] J. Salmi, A. Richter, and V. Koivunen, "Detection and Tracking of MIMO Propagation Path Parameters Using State-Space Approach," *Signal Processing, IEEE Transactions on*, vol. 57, no. 4, pp. 1538–1550, April 2009.

[67] K. Yu, Q. Li, D. Cheung, and C. Prettie, "On the tap and cluster angular spreads of indoor WLAN channels," in *Vehicular Technology Conference, 2004. VTC 2004-Spring. 2004 IEEE 59th*, vol. 1, May 2004, pp. 218–222 Vol.1.

[68] N. Czink, P. Cera, J. Salo, E. Bonek, J.-P. Nuutinen, and J. Ylitalo, "A Framework for Automatic Clustering of Parametric MIMO Channel Data Including Path Powers," *IEEE Vehicular Technology Conference*, sep 2006.

[69] C. Schneider, M. Ibraheam, S. Haefner, and et. al., "On the Reliability of Multipath Cluster Estimation in Realistic Channel Data Sets," *European Conference on Antennas and Propagation, EuCAP*, 2014.

[70] H. Xu, V. Kukshya, and T. Rappaport, "Spatial and temporal characteristics of 60-GHz indoor channels," *Selected Areas in Communications, IEEE Journal on*, vol. 20, no. 3, pp. 620–630, Apr 2002.

[71] R. Muller, D. A. Dupleich, C. Schneider, R. Herrmann, and R. S. Thoma, "Ultrawideband 3D mmWave channel sounding for 5G," in *General Assembly and Scientific Symposium (URSI GASS), 2014 XXXIth URSI*, Aug 2014.

[72] K. Selvan, "A revisit of the reference antenna gain measurement method," in *ElectroMagnetic Interference and Compatibility (INCEMIC), 2006 Proceedings of the 9th International Conference on*, Feb 2006, pp. 467–469.

Part II

Included Papers

Paper I

Directional Analysis of Measured 60 GHz Indoor Radio Channels using SAGE

Directional properties of the radio channel are of high importance for the development of reliable wireless systems operating in the 60 GHz frequency band. Using transfer functions measured from 61 to 65 GHz in a conference room we have extracted estimates of the multi-path component parameters using the SAGE algorithm. In the paper we compare results for line-of-sight (LOS) scenarios and the corresponding non-line-of-sight (NLOS) scenarios and present values of the direction spread at the Tx and the Rx.

©2011 IEEE. Reprinted, with permission, from
C. Gustafson, F. Tufvesson, S. Wyne, K. Haneda and A. F. Molisch
"Directional Analysis of Measured 60 GHz Indoor Radio Channels using SAGE"
in *IEEE 73rd Vehicular Technology Conference* (VTC Spring), Budapest, Hungary, May 2011.

1 Introduction

Significant research activity is currently being undertaken to design next generation high-speed wireless systems operating in the 60 GHz band, in particular for Gbit/s transmission over short distances. Several standards (IEEE 802.15.3c, IEEE 802.11ad) are emerging, and products are available on the market. The 60 GHz band is of interest mainly due to the large bandwidth of at least 5 GHz that is available worldwide. However, the attenuation of radio waves at 60 GHz is very high, for several reasons: (i) the free-space pathloss is proportional to the square of the carrier frequency (assuming constant-gain antennas), and thus much higher than for the 2 and 5 GHz bands commonly used today [1] (ii) the dimensions of physical objects in a room are typically large in relation to the wavelength of 5 mm, resulting in sharp shadow zones and (iii) transmission through obstacles such as walls is low. The challenges related to these propagation characteristics needs to be addressed in order to be able to establish a reliable communication link in the 60 GHz band. One possible solution is to use beamforming where the individual phases of the antenna elements in an array are electronically controlled to achieve a suitable array pattern. Using beam switching [2], beamforming can be designed to direct the beam towards different directions depending on the situation. For instance, if the LOS is blocked, the beam can be steered towards a direction where a strong first order reflection is available.

For the above reasons, the directional properties of the 60 GHz channel is of high importance, as is reflected by the previous work on this topic. In [4], the 60 GHz channel was measured for typical indoor environments using a 1×4 patch array antenna and the SAGE algorithm was used to estimate the direction of arrival (DOA) in azimuth. In [3], highly directional antennas were mechanically steered in order to determine the DOA characteristics for several different environments, including typical building hallways and small to medium sized rooms. The study confirmed that the majority of the components in the LOS scenario could be determined from ray tracing techniques. In this paper, we use the SAGE algorithm and a virtual array setup to analyze the directional properties of measured channels in a conference room. We compare the results for different LOS scenarios with the corresponding NLOS scenarios. The results include estimates of the direction of departure and direction of arrival in both azimuth and elevation, as well as measures of the direction spread.

1.1 The IEEE802.15.3c channel model

A complete channel model for mm-wave systems was developed and standardized by the IEEE802.15.3c working group. It supports several different scenarios, including office, desktop and library scenarios [5]. The angular characteristics of the channel is only considered at the Tx side. A particular simplification is that for desktop, office and library scenarios, the NLOS model is derived from the LOS model by removing the LOS component. In this paper, we investigate by measurement whether such a simplification is a good approximation to reality; i.e., we compare the directional estimates of the LOS scenarios with the corresponding NLOS scenarios where the direct wave is blocked by a computer screen.

2 60 GHz Radio Channel Measurements

The 60 GHz channel was measured in a conference room at Aalto University, Espoo, Finland using a vector network analyzer based system [6]. The measured frequency range was 61-65 GHz, using 2001 frequency points. A 7×7 planar virtual array was used at both the Tx and the Rx side. Using 2-D electromechanical positioners, the Tx and Rx arrays were scanned in the horizontal and vertical planes, respectively. The Tx antenna was a commercial biconical antenna with an omnidirectional pattern in azimuth, while the Rx antenna was an open waveguide. The inter-element spacing was 2 mm in both arrays. The Rx array remained at a fixed location, whereas the Tx array was placed at 17 different positions on top of the tables. A LOS and a NLOS scenario was measured for all positions except for two Tx positions, where only a LOS scenario was measured. The difference between the LOS and NLOS scenarios are made solely by blocking the LOS path with a laptop screen placed 0.42 m away from the Tx. Other objects in the measurement environment and the locations of the arrays were the same for the LOS and NLOS scenarios.

3 Directional analysis

3.1 Signal Model for the Analysis

The measured channel matrix $\mathbf{H}^{\text{meas}}$ is of size 49×49 where each element $h_{m,n}$ contains the channel frequency transfer function between receive and transmit antenna element number m and n, respectively. The transfer function is assumed to be correctly described by the contributions from a finite number of

plane waves as [1]:

$$h_{m,n}\left(k,i,\alpha_l,\tau_l,\Theta_l^{Rx},\Theta_l^{Tx},\nu_l\right) = \tag{1}$$

$$\sum_{l=1}^{L}\alpha_l \mathrm{e}^{-j2\pi\Delta f\tau_l k}G_{Tx}\left(n,k,\Theta_l^{Tx}\right)G_{Rx}(m,k,\Theta_l^{Rx})\,\mathrm{e}^{j2\pi\Delta t\nu_l i},$$

where L is the total number of multipath components (MPCs), α_l, τ_l, Θ_l^{Tx} and Θ_l^{Rx} is the complex amplitude, delay, direction of arrival (DOA) and direction of departure (DOD), respectively. G_{Tx}, G_{Rx} and k is the complex antenna pattern of the Tx and Rx, and frequency sub-index, respectively. Since the channel was measured in a time-static environment with only one snapshot, the Doppler frequency, ν, and the snapshot index, i, can be omitted in (1). In the analysis, an observation bandwidth of 300 MHz around 62 GHz with 26 frequency samples is used.

3.2 The SAGE Algorithm

The SAGE algorithm [7] is an iterative method for obtaining maximum-likelihood estimates of the MPC parameters. In this paper, the SAGE algorithm is used to provide the directional estimates of the channel as well as estimates of the complex amplitudes and the delay. In these evaluations, 50 MPCs are estimated. In our analysis, we have considered synthetic antenna patterns, i.e., each array element is an omni-directional antennna with a phase shift that depends on the direction of the incoming plane wave and the array geometry. The elevation estimates for the DOD of the l:th MPC, θ_l^{Tx}, have ambiguities due to the horizontal array geometry of the Tx array: it cannot be determined whether they arrive from the upper or lower half-space, whereas the measurement arrangement allows such a determination at the Rx. This ambiguity can be resolved by assuming that no double-reflections (via floor and ceiling) occur; in this case MPCs with a DOA in the upper half-sphere have a DOD that also must lie in the upper half-sphere. Measurement results confirm that very few MPCs exhibit the mentioned double-reflections, and furthermore those MPCs have low power.

3.3 Reconstruction Error and Residual Power

The signal model in (1) does not cover spherical waves or diffuse multipath components. As a result, the total power of the extracted MPCs are therefore in general lower than the power of the observed signals at the antenna ports. The

mean square relative reconstruction error ($MSRRE$) and the relative residual signal power, Λ, were calculated using the estimates given by SAGE for $L = 50$ MPCs, as [8]

$$MSRRE = \frac{1}{K}\sum_{k=1}^{K}\left(\frac{||\mathbf{H}_k^{\text{meas}} - \mathbf{H}(L)_k^{\text{re.}}||_F^2 - P_\text{n}}{||\mathbf{H}_k^{\text{meas}}||_F^2 - P_\text{n}}\right) \quad (2)$$

$$\Lambda = 1 - \frac{1}{K}\sum_{k=1}^{K}\left(\frac{||\mathbf{H}(L)_k^{\text{re.}}||_F^2}{||\mathbf{H}_k^{\text{meas}}||_F^2 - P_\text{n}}\right) \quad (3)$$

Here, $\mathbf{H}^{\text{re.}}$ is the matrix reconstructed by the signal model in (1) using L MPC parameters estimated by SAGE. The summation is over the K different frequency sub-indexes and $||\cdot||_F$ denotes the Frobenius norm. In (3), P_n is the estimated noise power from each measurement. The noise power was estimated from a part of the power delay profile where no signals were observed.

The calculated CDFs of the relative residual power and the MSRRE can be seen in figure 1. In the LOS scenario, the residual signal power is less than 7 % for all Tx positions. The residual power in the NLOS scenario is higher, although it is less than 20 % in most cases. The values of the MSRRE are only slightly higher than those of the residual power.

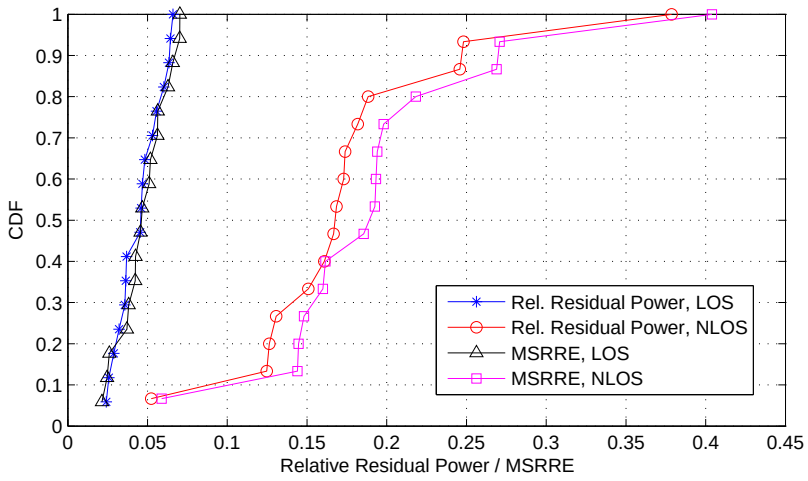

Figure 1: CDFs of the relative residual power and the MSRRE for the different Tx positions in the LOS and NLOS scenarios.

3.4 Direction Spread

The direction spread is calculated as [9]

$$\sigma_\Omega = \sqrt{\sum_{l=1}^{L} |e(\phi_l, \theta_l) - \mu_\Omega|^2 P(\phi_l, \theta_l)}, \tag{4}$$

where μ_Ω and the unit vector for the direction of the l:th component, $e(\phi_l, \theta_l)$, are given by

$$\begin{aligned} \mu_\Omega &= \sum_{l=1}^{L} e(\phi_l, \theta_l) P(\phi_l, \theta_l) \\ e(\phi_l, \theta_l) &= [\cos(\phi_l)\sin(\theta_l),\ \sin(\phi_l)\sin(\theta_l),\ \cos(\theta_l)]^{\mathrm{T}} \end{aligned}$$

Here, P is the normalized power spectrum, while ϕ_l and θ_l is the azimuth and elevation angle of the l:th MPC, respectively.

4 Results

4.1 Directional Estimates

Figure 1 shows the Tx azimuth estimates for all the Tx positions in the LOS and NLOS scenarios. The site map of the conference room where the measurements took place can be seen in figure 3. The length of the lines in figures 1 are proportional to the absolute values of the MPC powers in dB. The power of the direct wave is on the order of 20 dB stronger than the second strongest component for all positions except for positions a4 and a5, where the difference is only 4 dB. When comparing figure 5(a) and 2(b), it becomes evident that the estimates are very similar except in the direction around the direct wave. For all positions in the NLOS scenario, there is a significant component departing in the same azimuth direction as the LOS component in the LOS scenario. When both the elevation and azimuth estimates are taken into account, it is confirmed that these MPCs are diffracted around the top edge of the computer screen. The power of these MPCs is 18-20 dB lower compared to the direct wave in each corresponding LOS scenario. We note that the height difference between the screen and the Tx/Rx is only 7.5 cm.

Figure 3 shows the floorplan with the estimates of the 27 strongest MPCs in the LOS scenario with the Tx in position a3. The black lines are the estimated azimuth DODs and DOAs given by SAGE, while the dashed lines are expected pathways connecting the Tx and the Rx based on geometrical optics. Also shown is the coordinate system that is used as a local coordinate

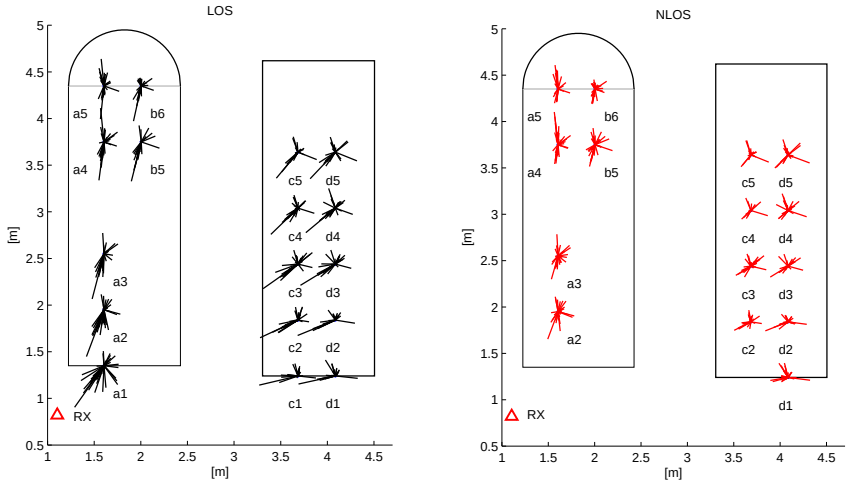

(a) (b)

Figure 2: Tx azimuth estimates for all Tx positions in the LOS and NLOS scenarios. The length of the lines are proportional to the power of each MPC in dB.

system at both the Tx and the Rx. The azimuth angle, ϕ, and the elevation angle, θ, is defined as shown in figure 3. The vertical receive antenna array is oriented such that the antenna boresight is pointing in the direction $(\phi, \theta) = (320°, 0°)$. There is a large number of components centered around the LOS direction. These components could be physically existing MPCs that are created by reflections from the metallic parts of the antenna/waveguide fixtures (even though absorbing materials were placed on the fixtures during the measurements). Some of these components might be artifacts created due to an imperfect subtraction of the LOS component in the successive interference cancellation step in SAGE. This effect could be mitigated by using a complete data model of the antenna patterns.

4.2 Signal Pathways

Table I shows the identified pathways of the components that also are illustrated in Fig. 3. Some of the components appear to be reflected on a window or an object embedded around the window, such as blinds or the frames around the window. One component is reflected on the ceiling and three other components are identified as being reflected on ceiling lamps, which have a metallic cover.

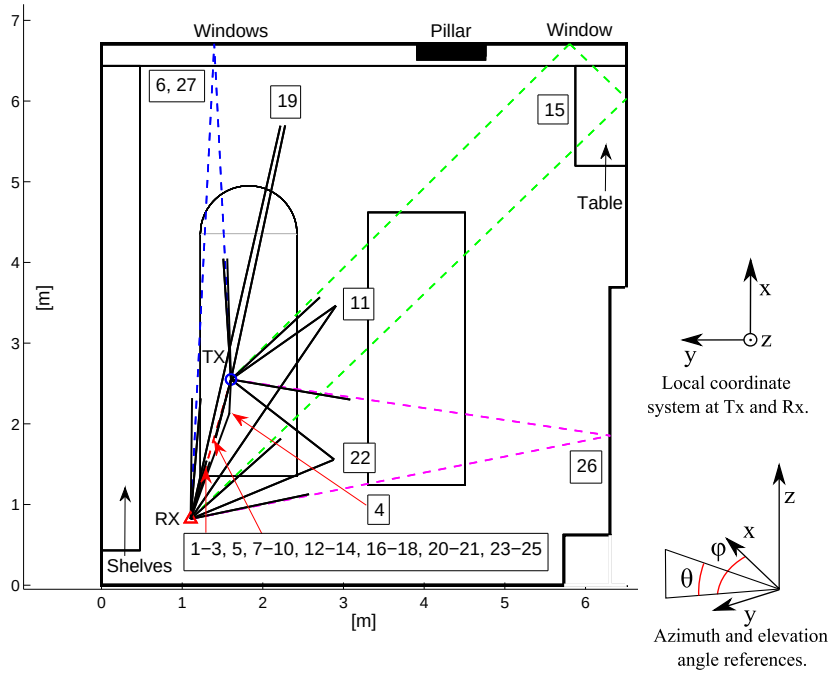

Figure 3: Floorplan of the meeting room where the measurements took place with the Tx in one of 17 positions. The black lines are the azimuth estimates for the 27 strongest components in the LOS scenario.

This suggests that it is important to include the elevation estimates in the description of the directional properties of the channel.

4.3 DOD and DOA estimates

Figure 4 shows the DOD and DOA for the LOS and NLOS scenarios with the Tx in position a3. The diameters of the circles are proportional to the power of each MPC in dB and the color of each circle represents delay in ns. Figure 4(b) contains a larger number of estimates with longer delays compared to figure 4(a). This is due to the fact that - given the fixed total number of estimated MPCs - the LOS scenario (which has many components near the LOS) allows to extract fewer weak, long-delayed components.

For this reason, it is difficult to make a fair comparison between the two figures. However, most of the MPCs in the LOS scenario, beside the one close to the LOS direction, can also be identified in the NLOS scenario. This indicates that MPCs that are not close to the LOS direction have similar directional properties. The strongest MPC in this NLOS scenario is identified as being diffracted on the top of the computer screen. Modeling the NLOS scenario based on the LOS data with the LOS component removed, as done in the 802.15.3c model, would lead to significant errors in this case.

Table 1: Identified signal pathways.

MPC #	Identified signal path	Power [dB]	Delay [ns]
1	Direct wave	-70	7.1
4	Table	-92	7.6
6	Window	-95	28.9
11	Ceiling lamp	-95	22.0
12	Ceiling	-95	13.2
15	Window/wall	-97	45.4
19	Ceiling lamp	-100	30.7
22	Ceiling lamp	-101	18.5
26	Wall	-102	34.0
27	Window	-102	33.0

Figure 5 is the same as figure 4, but with the Tx in position b6 instead. The LOS and NLOS scenarios appear to be more similar in this case. In this NLOS scenario there are some components that are marked "computer", which appear to be reflected on the computer screen and are then reflected on a window. This

is one of few scenarios where there are significant components that are reflected on the screen.

4.4 Direction spread

The calculated CDFs of the direction spread is shown in figure 6. The direction spread at the Rx is lower compared to the Tx, which is due to the fact that the Rx is placed in one of the corners of the conference room. Also, the waveguide antenna elements of the vertical Rx array do not radiate in the backward direction towards this corner. The direction spread of the Tx in the LOS scenario is varying a lot for the different Tx positions. For the two Tx positions a5 and a6, the direction spread is substantially higher than in the remaining positions. In both these positions, there are two strong components (the direct wave and a reflection from a window) that have azimuth estimates that are separated by almost 180 degrees. The components are significantly stronger than the remaining ones and the difference of the estimated power for the two components is about 4 dB. The high direction spread in these two cases is almost entirely attributed to the two strongest components. The implication of this is that the direction spread measure should be viewed together with information about the power distribution of the components. In the NLOS scenario, the direction spread for the Tx is above 0.9 for most positions. However, we note that there are few strong reflections present in the NLOS scenario.

5 Conclusions

The 60 GHz radio channel was measured in a conference room and the SAGE algorithm was applied to the measured data to give estimates of the MPC parameters for LOS and NLOS scenarios. It has been shown that it is possible to identify the signal pathways and corresponding scattering objects for different MPCs of the measured 60 GHz radio channel and that the estimates given by SAGE agree well with the geometry of the measurement site. The study also showed that the directional properties of the channel in the LOS and NLOS scenarios are very similar except around the LOS direction. In the NLOS scenario, diffraction around the objects blocking the LOS was shown to be a significant propagation mechanism, giving rise to an insight into the existing channel models that the NLOS channel cannot be realized just by omitting the LOS component. A comparison of the directional estimates with the geometry of the room suggests that it is important to include the elevation estimates in the description of the directional properties of the channel. Direction spread measures for both the Tx and the Rx were presented for both LOS and NLOS

scenarios.

References

[1] A. F. Molisch, "Wireless Communications", 2nd edition, *Chicester, U.K, IEEE Press - Wiley*, 2011.

[2] X. An, C.-S. Sum, R.V. Prasad, J. Wang, Z. Lan, J. Wang, R. Hekmat, H. Harada, I. Niemegeers, "Beam switching support to resolve link-blockage problem in 60 GHz WPANs," *Proc. of IEEE Int. Symp. on Personal, Indoor and Mobile Radio Communications*, 2009, Tokyo, Japan.

[3] H. Xu, V. Kukshya and T. S. Rappaport, "Spatial and Temporal Characteristics of 60-GHz indoor Channels", *IEEE Journal on Selected Areas in Communications*, Vol. 20, No. 3, April 2002.

[4] M.-S. Choi, G. Grosskopf and D. Rohde, "Statistical Characteristics of 60 GHz Wideband Indoor Propagation Channel", *Proc. 16th Annual IEEE Int. Symposium on Personal, Indoor and Mobile Radio Comm.*, Berlin, Germany, 2005.

[5] S-K. Yong, *et al.*, "TG3c channel modeling sub-commitee final report", *IEEE Techn. Rep.*,15-07-0584-01-003c, Mar. 2007.

[6] S. Ranvier, M. Kyro, K. Haneda, C. Icheln and P. Vainikainen, "VNA-based wideband 60 GHz MIMO channel sounder with 3D arrays", *Proc. Radio Wireless Symp.* 2009, pp. 308-311, San Diego, CA, Jan 2009.

[7] B. H. Fleury, P. Jourdan, and A. Stucki, "High-resolution channel parameter estimation for MIMO applications using the SAGE algorithm", *Proc. 2002 Int. Zurich Seminar on Broadband Communications - Access, Transmission, Networking*, ETH Zurich, Switzerland, Feb. 2002.

[8] S. Wyne. A. F. Molisch, P. Almers, G. Eriksson, J. Karedal, F. Tufvesson, "Outdoor-to-Indoor Office MIMO Measurements and Analysis at 5.2 GHz", *IEEE Trans. on Vehicular Technology*, Vol. 57 , Issue 3, 2008.

[9] B. H. Fleury, First- and second-order characterization of direction dispersion and space selectivity in the radio channel, *IEEE Transactions on Information Theory*, vol. 46, pp. 2027 - 2044, September 2000.

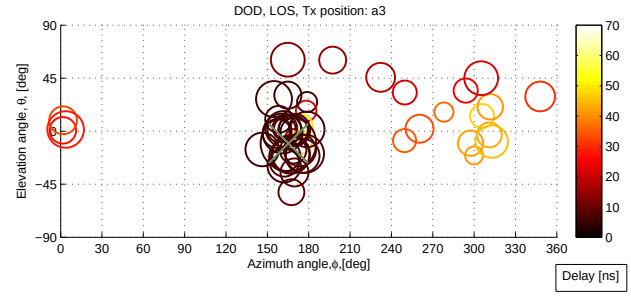

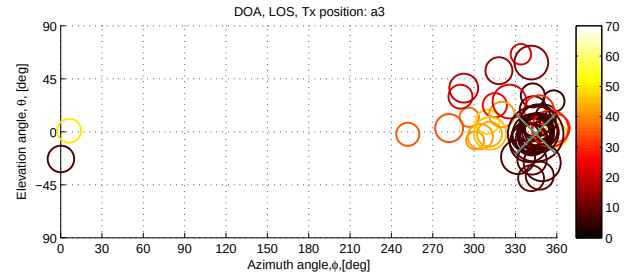

(a)

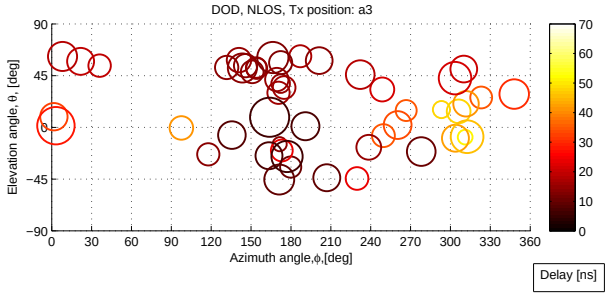

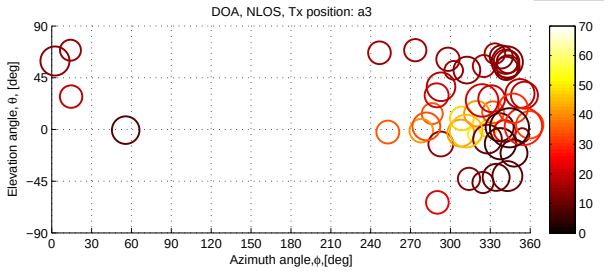

(b)

Figure 4: DOD and DOA for the (a) LOS and, (b) NLOS scenarios with the Tx in position a3.

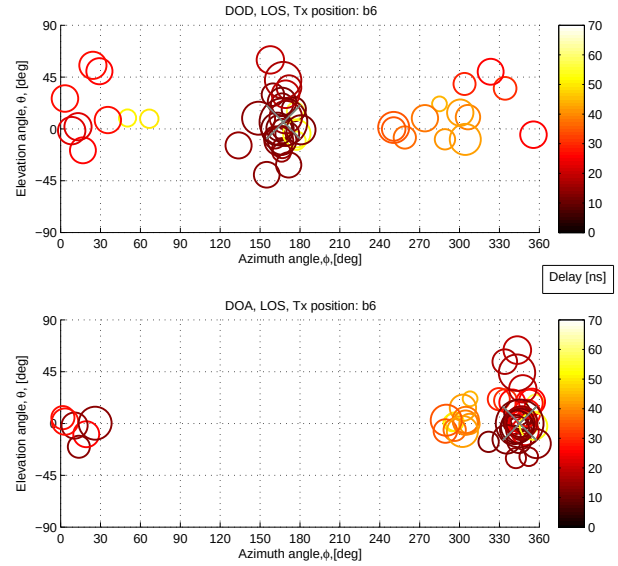

(a)

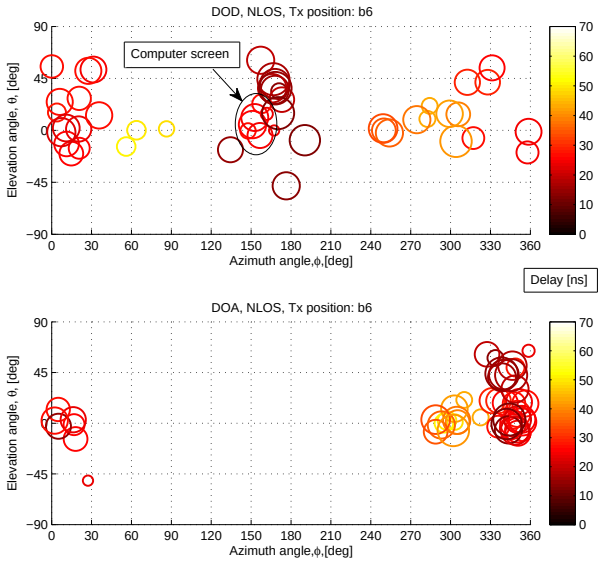

(b)

Figure 5: DOD and DOA for the (a) LOS and, (b) NLOS scenarios with the Tx in position b6.

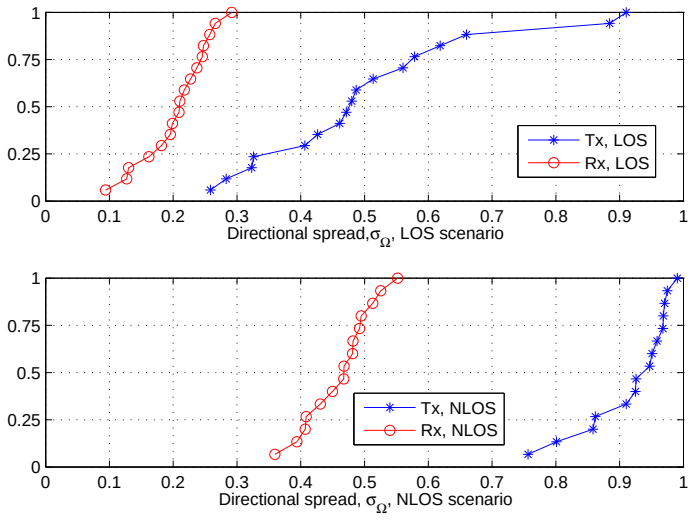

Figure 6: CDFs of the directional spread for the Tx and the Rx in the LOS and NLOS scenarios.

Paper II

On mm-Wave Multi-path Clustering and Channel Modeling

Efficient and realistic mm-wave channel models are of vital importance for the development of novel mm-wave wireless technologies. Though many of the current 60 GHz channel models are based on the useful concept of multi-path clusters, only a limited number of 60 GHz channel measurements have been reported in the literature for this purpose. Therefore, there is still a need for further measurement based analyses of multi-path clustering in the 60 GHz band. This paper presents clustering results for a double-directional 60 GHz MIMO channel model. Based on these results, we derive a model which is validated with measured data. Statistical cluster parameters are evaluated and compared with existing channel models. It is shown that the cluster angular characteristics are closely related to the room geometry and environment, making it infeasible to model the delay and angular domains independently. We also show that when using ray tracing to model the channel, it is insufficient to only consider walls, ceiling, floor and tables; finer structures such as ceiling lamps, chairs and bookshelves need to be taken into account as well.

©2014 IEEE. Reprinted, with permission, from
C. Gustafson, K. Haneda, S. Wyne and F. Tufvesson
"On mm-Wave Multi-path Clustering and Channel Modeling"
in *IEEE Transactions on Antennas and Propagation*, Vol. 62, No. 3, pp. 1445-1455, 2014.

1 Introduction

As the requirements for efficient and reliable wireless communications with high throughput are ever-increasing, novel wireless techniques have to be considered, and the available radio spectrum has to be used efficiently in order to overcome spectrum shortage. Due to the large bandwidth of at least 5 GHz available worldwide [1], the 60 GHz band is a promising candidate for short-range wireless systems that require very high data rates. Efforts have already been made regarding standardization by the IEEE 802.15.3c [2] and IEEE 802.11ad [3] working groups, and some commercial products are already available on the market.

The propagation characteristics in the 60 GHz band are quite different from those in the lower frequency bands commonly used today for cellular communication. Assuming identical transmit powers and antenna gains, the received power at 60 GHz is smaller than that at lower frequencies due to a smaller receive antenna aperture at 60 GHz. Furthermore, since the dimensions of typical shadowing objects are large in relation to the wavelength at 60 GHz, sharp shadow zones are formed, making diffraction an insignificant propagation mechanism [4], Also, due to the high penetration loss of most materials at 60 GHz, multi-path components propagating through walls or other objects typically have low power. Due to these propagation characteristics, highly directional antennas or adaptive beam-forming techniques are required in order to establish a reliable 60 GHz communication link [5].

As the potential benefits of systems operating in the 60 GHz band are directly related to the propagation environment characteristics, realistic and reliable channel models are of vital importance for the design and development of novel 60 GHz technologies. Furthermore, as beam forming techniques are vital for many types of mm-wave communications, the channel should ideally be modeled using a MIMO model that takes the angular characteristics of the channel into account.

The IEEE802.11ad channel model is a MIMO model based on a mixture of ray tracing and measurement-based statistical modeling techniques [6]. It is a cluster-based spatio-temporal channel model that supports several different environments. The measurements for the IEEE802.11ad model were conducted using highly directional antennas that were steered in different directions in order to evaluate and model the cluster parameters of 60 GHz channels.

Several recent studies are directly related to the IEEE802.11ad model and include theoretical investigations regarding capacity [7], spatial diversity techniques [8] and beamforming performance [9], as well as an extended model for human blockage in 60 GHz channels [10].

In this paper, we present measurement-based results for a double-directional

60 GHz MIMO channel model in a conference room environment. Statistical cluster parameters are evaluated and compared with existing 60 GHz channel models. The novel aspect of our proposed channel model is the method by which it models the spatio-temporal properties of the clusters. We provide two different ways of modeling the cluster spatio-temporal properties; one being stochastic and the other a semi-deterministic approach that is based on ray-tracing. Most of the current 60 GHz directional analyses rely on measurements using highly directional antennas that are mechanically steered [11] and sometimes also include ray tracing results [6]. The results in this paper are based on measurements using the virtual antenna array technique. The double-directional estimates for the multi-path components (MPCs) were obtained using the SAGE algorithm. This technique can potentially offer an improved resolution of the MPC parameters compared with techniques based on mechanically steered high-gain antennas [6]. The clustering results were then obtained using an automated clustering algorithm.

2 60 GHz Radio Channel and Antenna Measurements

2.1 Measurement Environment

This work is based on results from a 60 GHz radio channel measurement campaign performed in a conference room with a volume of $6.8 \times 7.0 \times 2.5$ m^3. The IEEE802.11ad working group has performed measurements in smaller conference rooms with volumes of approximately $3 \times 4.5 \times 3$ m^3 [12] and in a slightly larger conference room with a width and length of 6.3 m and 4.3 m [13]. During our measurements, the Rx array was placed at a fixed position in one of the corners of the room whereas the Tx array was placed at one of 17 predefined positions on either of the two tables in the room. As indicated by Fig. 1, 17 different line-of-sight (LOS) measurements were performed at these positions as well as 15 additional obstructed-line-of-sight (OLOS) measurements. In the OLOS scenarios, a laptop computer screen was used to block the direct path between the Tx and the Rx. Further details about the measurements can be found in [14].

2.2 Measurement Equipment and Setup

The 60 GHz radio channel was measured using a vector network analyzer based system [15]. 2-D electromechanical positioners were used to move the Tx and Rx antennas in the horizontal and vertical planes, respectively. A commercial

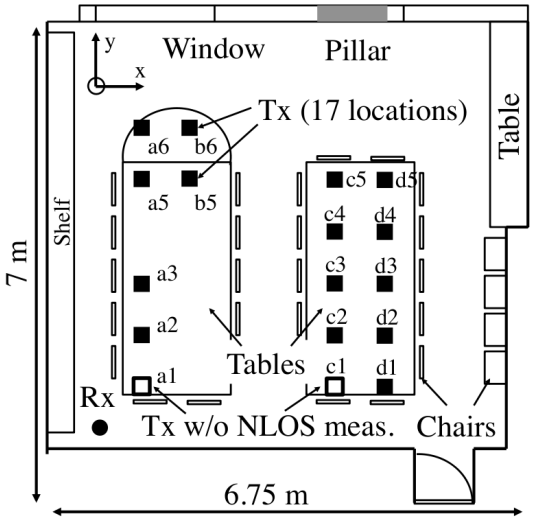

Figure 1: Floorplan of the measured conference room.

biconical antenna, Flann Microwave MD249, with an omnidirectional pattern in azimuth was used at the Tx side, and the Tx virtual array was a horizontal uniform rectangular array with 7×7 elements. The Rx antenna was an open waveguide, vertically polarized and oriented such that the waveguide opening was directed towards the opposite corner of the room compared to where the Rx array was situated. The Rx virtual array was a vertical uniform rectangular array with 7×7 elements. All measurements were performed with the antennas in a vertical-to-vertical (V-V) polarization orientation. The inter-element spacing was 2 mm in both arrays. Back-to-back measurements were performed in order to remove the influence of the coaxial cables, mixers, and feeding waveguides.

2.3 Antenna measurements

The co- and cross-polarized antenna gains of the Tx- and Rx antenna were first measured using a setup based on a vector network analyzer (VNA) and electromechanical positioners. A standard gain horn antenna with known gain and high cross-polarization discrimination ratio was used as the reference antenna. Electromagnetic absorbers were used to cover equipment in the close vicinity of the antenna, such as the VNA, positioners and tables. Also, since the measurements were performed in a large open area in a room, the data will

also include effects due to possible multi-path propagation within the room. A simple time-domain gating technique was employed to filter the measured data and remove parts of the impulse response with longer delays. The frequency range in the measurement was 60-64 GHz, yielding a time resolution of 0.25 ns. The gain transfer method [16] was then employed to calculate the antenna gain. Due to the small wavelength and considering the alignment accuracy of the measurement setup, it was not possible to extract the phase responses of the antennas precisely. Fig. 2 shows the co- and cross-polarized antenna gains of the Rx antenna at 62 GHz. The cross-polarized antenna gain of the biconical Tx antenna (not shown) is low in all directions, whereas the cross-polarized antenna gain of the open waveguide is fairly high in certain directions.

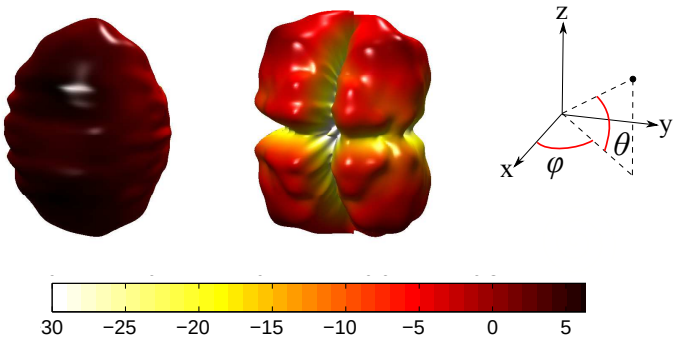

Figure 2: Co-polarized (left) and cross-polarized (right) Rx antenna gain in dBi of the open waveguide at 62 GHz.

Using the measured co- and cross-polarized data, it was possible to estimate the cross-polarization discrimination ratio (XPD) of the antennas as

$$\mathrm{XPD}(\phi,\theta)|_{\mathrm{dB}} = G_{co}(\phi,\theta)|_{\mathrm{dB}} - G_{cross}(\phi,\theta)|_{\mathrm{dB}}. \quad (1)$$

In other words, we define the antenna XPD to be the difference between the co-polarized and cross-polarized antenna gain in a certain angular direction. This is of importance since the measurements were performed only with V-V polarization, which means that it is not possible to employ a full polarimetric estimation of the complex amplitudes in SAGE. Instead, only the complex gain of the V-V component is estimated. This means that the SAGE algorithm only produces accurate results for MPCs in directions where the XPDs of the Tx and Rx antennas are large [17]. In total, less than 5% of the total number of

MPCs in all scenarios were located in directions were the XPD was lower than 20 dB.

3 Multi-path Estimation and Clustering

3.1 The SAGE algorithm

The measured transfer functions are assumed to be correctly described by a finite number of plane waves, i.e. multi-path components (MPCs). Each MPC is described by its complex amplitude, delay, direction of departure (DOD) and direction of arrival (DOA). In order to estimate these MPC parameters, the SAGE algorithm is used. A double-directional analysis using SAGE based on the same measurements was previously presented in [18], and the reader is referred to that paper for details regarding the signal model for the analysis. This work improves the SAGE estimates of [18] by employing a more detailed model for the gain patterns of the antennas used in the measurements. By taking the gain of the antennas into account, the estimated results describe the propagation channel.

The SAGE analysis was performed over an observation bandwidth of 200 MHz centered at 62 GHz with 26 equi-spaced frequency samples. The estimated MPCs can be used to model the 2 GHz band from 61–63 GHz because the multi-path parameters do not change drastically over this frequency band. This assertion is justified by the fact that neither the power angular profiles [19], nor the SAGE estimates change drastically when evaluated at center frequencies of 61, 62 and 63 GHz.

3.2 Clustering Method

In this paper, a cluster is defined as a group of multi-path components having similar delays and directions of departure and arrival. The estimated MPCs are grouped into clusters using the K-power-means algorithm wherein the multi-path component distance is used as a distance metric in parameter space [20]. For the validation of the number of clusters, the Kim-Parks index [21] was utilized. The Kim-Parks index, KP, can be considered as a normalized version of the Davies-Bouldin index. It is calculated using an over- and under-partition measure function, v_o and v_u, that are normalized with respect to the minimum and maximum number of clusters, C_{min} and C_{max},

$$KP(C) = v_o(C) + v_u(C). \tag{2}$$

The optimal number of clusters, C_{opt}, for a certain scenario is then given by

$$C_{opt} = \underset{C}{\operatorname{argmin}} \left\{ KP(C) \right\}, C_{min} \leq C \leq C_{max}. \tag{3}$$

In practice, the largest number of clusters is set to be a number that is large enough to make sure that the correct number of clusters is identified. For a more detailed description of the Kim-Parks index, the reader is referred to [21]. The Kim-Parks index was chosen over the combined validation scheme as it produced consistent results that agreed better with the number of cluster identified based on a visual inspection. When using the Kim-Parks index, the number of identified clusters ranged from 6 to 12 in the LOS scenario and 8 to 12 in the OLOS scenario. Fig. 3 show typical clustering results for the direction of departure. Similar results were obtained for the direction of arrival. Each circle represents an MPC and the colors indicate identified clusters and the radius of each circle is proportional to the power of each MPC. In order to get more consistent results in the LOS and OLOS scenarios, the clustering in the LOS scenarios are performed without including the LOS component. That way, the power levels are similar in both scenarios. It is possible to exclude the LOS component from the clustering since this component can be treated deterministically. The clustering results for the LOS and OLOS scenarios are very similar. The main differences between the LOS and OLOS scenarios are

1. A strong LOS component present in the LOS scenario.
2. A number of components are present in the OLOS scenario that are diffracted around the computer screen.

4 Survey of 60 GHz Channel Models

4.1 The Extended Saleh-Valenzuela Model

Based on the clustering results, a number of statistical 60 GHz channel model parameters can be derived. One of the most widely used channel models based on clusters is the extended Saleh-Valenzuela model, where the impulse response, h, is given by Eq. (4).

$$\begin{aligned} &h(t, \Theta_{\mathrm{rx}}, \Theta_{\mathrm{tx}}) = \\ &\sum_{l=0}^{L} \sum_{k=0}^{K_l} \beta_{k,l} \mathrm{e}^{j\chi_{kl}} \delta\left(t - T_l - \tau_{k,l}\right) \delta\left(\Theta_{\mathrm{rx}} - \Omega_l - \omega_{k,l}\right) \delta\left(\Theta_{\mathrm{tx}} - \Psi_l - \psi_{k,l}\right) \end{aligned} \tag{4}$$

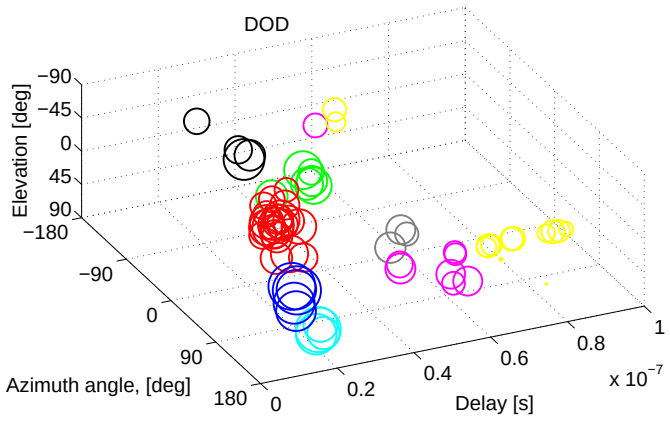

Figure 3: Typical clustering result for the direction of departure.

Here, $\beta_{k,l}$ is the complex amplitude of the kth ray (i.e. MPC) in the lth cluster and T_l, Ω_l and Ψ_l are the delay, DOA and DOD of the lth cluster, respectively. Similarly $\tau_{k,l}$, $\omega_{k,l}$ and $\psi_{k,l}$ are the delay, DOA and DOD of the kth ray in the lth cluster, respectively. Finally, $\delta(\cdot)$ is the Dirac delta function and the phase of each ray, $\chi_{k,l}$, is assumed to be described by statistically independent random variables uniformly distributed over $[0, 2\pi)$. The mean power of the kth ray in the lth cluster is given by

$$\overline{\beta_{k,l}^2} = \overline{\beta(0,0)^2} e^{-T_l/\Gamma} e^{-\tau_{kl}/\gamma}, \tag{5}$$

where Γ and γ are the cluster and ray decay constants, respectively, and $\overline{\beta(0,0)^2}$ is the average power of the first ray in the first cluster [22].

If the delay and angular domains can be modeled independently, the cluster and ray arrival time distributions may be described by two Poisson processes. Under this assumption, the cluster and ray inter-arrival times are typically described by two independent exponential probability density functions. The cluster arrival time for each cluster is thus described by an exponentially distributed random variable that is conditioned on the arrival time of the previous cluster, i.e.

$$p(T_l|T_{l-1}) = \Lambda e^{-\Lambda(T_l - T_{l-1})}, l > 0. \tag{6}$$

Here, Λ is the cluster arrival rate. Similarly for the ray arrival times, we have

$$p(\tau_{k,l}|\tau_{k-1,l}) = \lambda e^{-\lambda(\tau_{k,l} - \tau_{k-1,l})}, l > 0, \tag{7}$$

where λ is the ray arrival rate.

The extended S-V model relies on the assumption that the delay and angular domains can be modeled independently. As will be shown later, this assumption might not be valid for 60 GHz channels. Instead, it is necessary to either jointly model the angular and delay domains using a joint angular-delay distribution [23], or to use a deterministic approach based on ray tracing, which is done in the IEEE 802.11ad channel model [6]. This will be discussed further in section VI.

4.2 The IEEE 802.15.3c Channel Model

In the IEEE802.15.3c channel model, the extended S-V model of eq. (4) is used with the addition of a LOS component that is derived deterministically. It is a SIMO model that only models the DOA. The cluster DOA is modeled using a uniform distribution in the range $[0, 2\pi)$. Cluster arrival times are modeled using a certain cluster arrival rate as in eq. 6 [24].

4.3 The IEEE 802.11ad Channel Model

The IEEE802.11ad channel model is similar to that of the extended S-V model. However, in contrast to the 802.15.3c model, the delay, DOD and DOA for clusters are derived from empirical distributions for different types of first and second order clusters stemming from, e.g., ceiling and wall-ceiling interactions. The gain of the clusters are determined based on propagation and reflection losses, where the reflection losses are modeled using truncated log-normal distributions. The rays within each cluster are modeled using a central ray and a number of pre- and post-cursor rays. The pre- and post-cursor rays are modeled using different arrival times, λ_{pre} and λ_{post}, decay rates, γ_{pre} and γ_{post}, and average ray amplitudes. The pre- and post-cursor rays also have K-factors, K_{pre} and K_{post}, related to the amplitude of the main ray [6].

5 Clustering Results

Cluster-based channel models rely on two sets of parameters, namely inter- and intra-cluster parameters, describing the clusters and the rays in each cluster, respectively. In this section, results regarding the estimated inter- and intra-cluster parameters are presented and related to the channel models discussed above.

5.1 LOS component

In our model, the Tx-Rx distance is assumed to be known and is used as an input to the model. For the LOS scenarios, the power of the direct wave (the LOS component) is modeled deterministically based on the free space path loss. The delay of the LOS component is determined by the Tx-Rx separation. Furthermore, the location of the Tx and Rx arrays are assumed to be known, so that the DOD and DOA of the LOS component can be determined.

5.2 Inter-cluster Parameters

The cluster peak power is taken as the strongest MPC in each cluster. In this paper, we estimate the cluster decay using the cluster power and delay in absolute units, making it possible to estimate the cluster decay without normalizing the clusters with respect to delay and power of the first cluster. This also allows the noise floor to be kept at a constant level for all the different measurements. This way, the effect of clusters that might be located below the noise floor, and might thus have been missed, can be taken into account by modeling the clusters using a truncated normal distribution. Then, the cluster decay constant Γ was estimated based on a likelihood expression for this truncated model [25]. The cluster peak power and the result of the truncated regression is shown in Fig. 4.

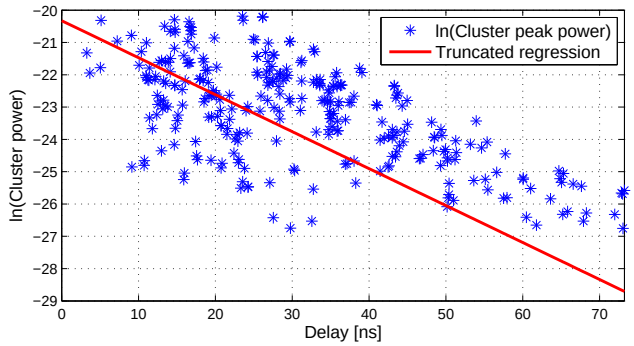

Figure 4: Cluster peak power as a function of absolute delay and the estimated cluster decay based on a truncated model for the clusters.

As the LOS component already is being modeled deterministically, it was omitted when estimating the cluster decay for the LOS scenario. When estimating the decay constants for the LOS and OLOS scenarios separately, they were both estimated to be $\Gamma = 8.7$ ns. Hence, the cluster decay can be modeled

using the same value for both the LOS and OLOS scenarios. Fig. 4 shows the cluster peak power for the LOS and OLOS scenarios combined. The estimated data for the combined data also yielded a value of $\Gamma = 8.7$ ns.

It was found that the cluster peak power variation around the mean could be appropriately modeled using a log-normal distribution, which corresponds to a normal distribution in the dB-domain. The estimated value for the standard deviation of this normal distribution was found to be the 6.4 dB in both the LOS and OLOS scenarios.

The cluster inter-arrival times can be described by an exponential distribution. Fig. 5 shows a CDF of the cluster inter-arrival times and an exponential distribution with an MLE of the parameter Λ. For both the LOS and OLOS scenarios, the estimated cluster arrival rate is $1/\Lambda = 5$ ns.

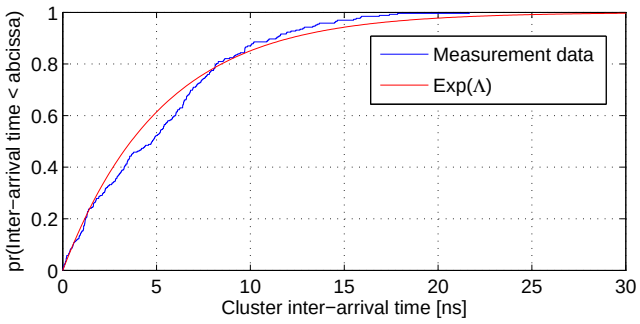

Figure 5: CDF of the cluster inter-arrival times and an exponential distribution with a MLE of the parameter Λ.

5.3 Modeling Cluster Angles and Delays

As shown in Fig. 6 and 7 below, it is not feasible to assume independence between the delay and angular properties of clusters. In the IEEE802.11ad model, this dependence is taken into account by modeling the cluster delays and angles deterministically, based on ray tracing results. In this paper, we consider two different ways of modeling the spatio-temporal properties of clusters; one being stochastic and one being deterministic (i.e. based on ray tracing). These two approaches both have their own strengths and weaknesses, depending on the intended use:

- Ray tracing is site-specific, which could be an advantage when assessing the performance at a specific site. However, when it comes to assessing

the overall statistics of 60 GHz MIMO channels, it requires accurate ray tracing results for many different Tx- and Rx-positions, making it ineffective.

- Conversely, a stochastic model can not provide information about a specific room or site, but can effectively reproduce the stochastic properties of 60 GHz channels in a given type of environment.

From now on, these two models are referred to as the ray tracing model and the stochastic model and they are presented in detail below.

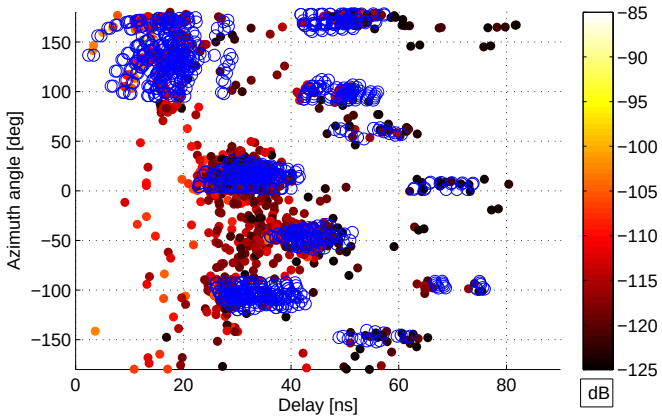

Figure 6: Delay and azimuth angles of estimated multi-path components (dots) and ray-tracing results for first, second and third order reflections (circles).

Ray tracing model

In the deterministic model, a ray tracing algorithm is used to determine the first and second order reflections, and the corresponding azimuth and elevation angles, as well as delays. In this paper, a simple three-dimensional image-based ray tracing algorithm is used, where the conference room is modeled as a parallelepiped with the same overall dimensions as the conference room and with tables as the only objects in the room. The conference room geometry is modeled in the same way in the IEEE802.11ad model [6] and has the advantage of being simple to use for modeling purposes. Fig. 6 compares the delay and azimuth angles of the estimated multi-path components with those of a ray-tracing simulations for all LOS scenarios. The elevation angles are not shown

here for improved clarity. There is an overall agreement between the ray-tracing and measurement results, but at the same time, a large number of significant MPCs that have been estimated are *not* accurately captured by the ray tracing algorithm. The high resolution estimates of MPC delays and angles were matched with the furniture placement in the room such that it was confirmed that most of these MPCs were interacting with objects such as ceiling lamps, chairs and bookshelves, i.e. objects that are not included in the ray tracing model.

The results from the ray tracing algorithm can not be used directly with the parameters derived for the intra-cluster parameters, since the ray-tracing results are inconsistent with the cluster definition used in the clustering algorithm. When employing ray tracing, a number of possible reflections are identified, and all of these could be modeled as clusters. However, the intra-cluster parameters are all based on the results found using the clustering algorithm. In this algorithm, a cluster is defined as a group of MPCs that are close to each other in the spatio-temporal domain, whereas the clusters found using ray tracing are based on the physical interaction with the environment. As a result, the number of clusters found using ray tracing is significantly larger than those based on the clustering algorithm. Therefore, the multi-path component distance (MCD) metric [26] is used to group rays that are close to each other in the spatio-temporal domain. The MCD is calculated for a combination of two different reflections, i and j, as

$$\mathrm{MCD}_{ij} = \sqrt{||\mathrm{MCD}_{\mathrm{DOD},ij}||^2 + ||\mathrm{MCD}_{\mathrm{DOA},ij}||^2 + \mathrm{MCD}_{\tau,ij}^2}$$

where the delay distance is given by

$$\mathrm{MCD}_{\tau,ij} = \xi \frac{|\tau_i - \tau_j|}{\Delta\tau_{max}} \frac{\tau_{std}}{\Delta\tau_{max}}. \tag{8}$$

Here, $\Delta\tau_{max} = \max_{ij}\{|\tau_i - \tau_j|\}$, and τ_{std} is the standard devation of the delays. For our purposes, $\xi = 3$ was found to be a suitable delay scaling factor. The MCD for angular data is given by $\mathrm{MCD}_{\mathrm{DOD/DOA},ij} = \frac{1}{2}|\mathbf{a}_i - \mathbf{a}_j|$, where

$$\mathbf{a}_i = [\sin(\theta_i)\cos(\phi_i), \sin(\theta_i)\sin(\phi_i), \cos(\theta_i)]^{\mathrm{T}}$$

Before calculating the MCD, all rays are sorted with respect to their delays. Then, the MCD between the ray with the shortest delay and all other rays are calculated, and all rays with a MCD < 0.25 are grouped together with the ray with the shortest delay. Then, the same thing is done again for the remaining

rays, until all rays have been assigned to a group. The cluster delays and angles are then determined as the delay and angles of the rays with the shortest delays in each group.

Stochastic model

In the stochastic model, the cluster angles are modeled using conditional probabilities. The cluster delays, T_k, are are modeled based on exponentially distributed cluster inter-arrival times. Then, the cluster elevation angles, Θ_k are determined using a joint pdf for the elevation angles conditioned on the cluster delay, i.e.,

$$f(T_k, \Theta_k) = f(\Theta_k|T_k)f(T_k), \tag{9}$$

where $f(\Theta_k|T_k)$ is the conditional cluster elevation pdf and $f(T_k)$ is the marginal pdf for the cluster delay. This conditional pdf is determined empirically by considering the possible elevation angles for first and second order reflections in a room with certain dimensions. The idea is that this conditional pdf should reflect upon the possible elevation angles for several different scenarios, with the Tx and Rx placed at different height. Here, we note that this paper only includes measured results for a single height of the Tx and Rx arrays. However, for the conditional pdf, we consider hypothetical scenarios where the Tx is located at a table at different heights, h_1, varying from 5-40 cm above the table, emulating a laptop or a similar device. The Rx is located at heights, h_2, varying from 5 cm above the table height up to 5 cm from the ceiling, thereby emulating a device such as a DVD-player, projector or internet access point.

Then, three different curves are used to put bounds on the possible elevation angles for the clusters. The first two curves, the upper and lower bounds, are determined by the maximum and minimum elevation angles for the second order reflections as a function of delay. The third bound, the shortest delay bound, is given by the curve for the shortest possible delay at a given elevation angle for a specific Tx-Rx separation, and is thus different for different scenarios. These three curves are shown in Fig. 7, together with the estimated Tx elevation angles of the MPCs as a function of delay.

Based on the measured data and ray tracing simulations, approximately 40% of the clusters are located within +/-5° of the horizontal plane. Therefore, we assign a 40% probability for the clusters to be located in the horizontal plane and a 60% probability of being located within the area bounded by the dashed curves in fig. 7. The clusters that are not assigned to the horizontal plane are randomly placed at a certain elevation angle using a uniform distribution over

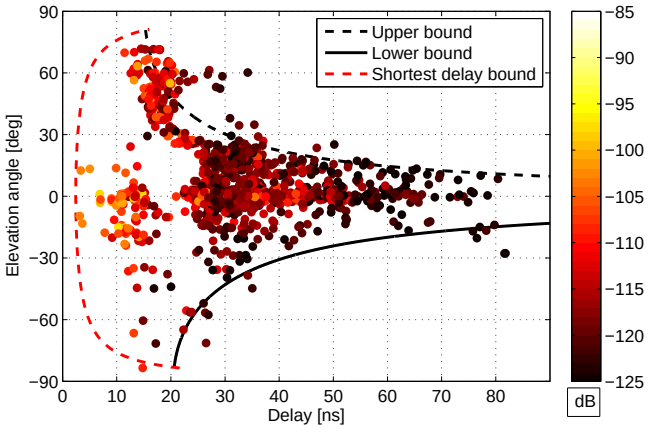

Figure 7: Elevation-delay dependence model for the stochastic channel model.

the supported elevation angles for the given delay, i.e.,

$$f(\Theta_l|T_l) = \frac{1}{\Theta_{\max}(T_l) - \Theta_{\min}(T_l)}. \tag{10}$$

The values $\Theta_{\min}(T_l)$ and $\Theta_{\max}(T_l)$ are the smallest and largest possible elevation angles at a given delay, respectively. The azimuth cluster angles are, for simplicity, modeled using a uniform distribution over the interval $[0, 2\pi)$.

5.4 Intra-cluster Parameters

Our clustering results confirm that the clusters generally consist of a main peak surrounded by weaker components with longer *and* shorter delays. Hence, we adopt the same basic intra-cluster delay model as in [6], where each cluster consist of a number of pre- and post-cursor rays. The ray inter-arrival times were calculated by taking the delay of each pre- and post-cursor ray and subtracting it with the previous one, thereby creating a set of conditional arrival times.

Fig. 8 shows CDFs for the ray inter-arrival times for the pre- and post-cursor rays in the LOS scenario and CDFs for exponential distributions with MLEs of the rate parameters λ_{pre} and λ_{post}.

Next, the mean ray decay rates and K-factors for the pre- and post-cursor rays, γ_{pre}, γ_{post}, K_{pre} and K_{post}, were calculated by normalizing each ray

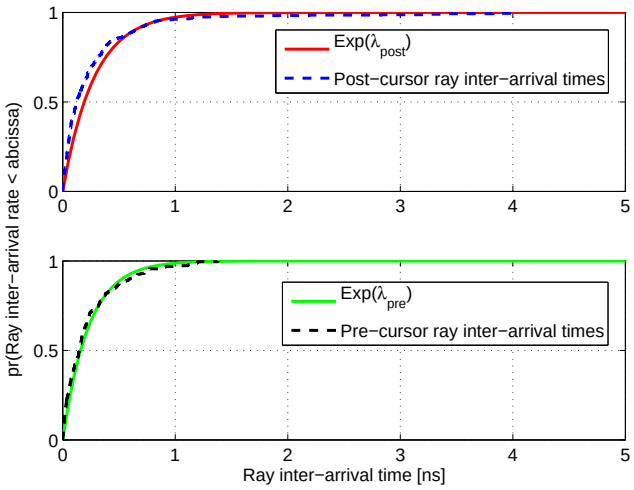

Figure 8: CDF of the ray inter-arrival times for the pre- and post-cursor rays in the LOS scenario, and exponential distributions with MLEs of the parameters λ_{pre} and λ_{post}.

with respect to the delay and mean amplitude of each associated cluster and performing a linear regression.

Then, the normalized path amplitude gain distribution of the pre- and post-cursor rays could be calculated by normalizing each ray with respect to the mean ray amplitudes at a certain delay. The power of the pre- and post-cursor rays are appropriately modeled using a log-normal distribution, or a normal distribution in the dB-domain. In Fig. 9, CDFs of the post-cursor ray power distributions for the LOS and OLOS scenarios are shown. The standard deviation of the normal distributions are very similar for both the pre- and post-cursor rays as well as for the LOS and OLOS scenarios, with values in the range of 5.6 to 7.1 dB. These values are similar to the standard deviation for the cluster peak power (i.e. the power of the main ray in each cluster), where the standard deviation is 6.4 dB.

The intra-cluster angles were calculated by taking the difference of the ray angles and the associated cluster centroid angles. Our results show that a good fit to the measured inter-cluster angles, $\omega_{k,l}$, is achieved by a zero-mean Laplace distribution with standard deviation σ, with probability density function

$$p(\omega_{k,l}) = \frac{1}{\sqrt{2}\sigma} e^{-|\sqrt{2}\omega_{k,l}/\sigma|}. \tag{11}$$

Fig. 10 shows the CDF of the intra-cluster azimuth angles of arrival in the LOS scenario, and a Laplacian distribution. Similar curves were obtained for both the LOS and OLOS scenarios in both the azimuth and elevation domains. We also note that the intra-cluster angles for the azimuth and elevation domains showed very small correlation coefficients, indicating that they can be modeled independently. The estimated values of the variance σ for the azimuth intra-

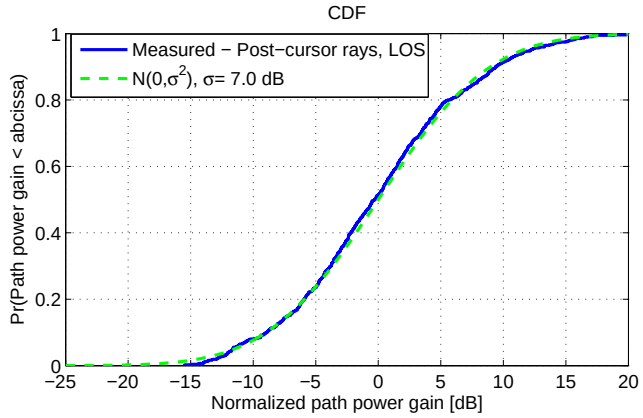

(a)

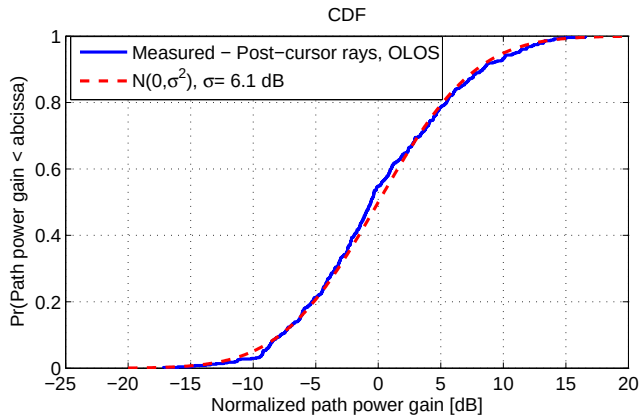

(b)

Figure 9: CDFs of the normalized path power gains of the post-cursor rays and a normal distribution with a MLE of the variance σ^2, for the (a) LOS and (b) OLOS scenarios.

cluster angles for the DOD and DOA were 0.7 and 0.3 radians, respectively. This difference is most likely attributed to the difference in placement of the Tx and Rx arrays. The Rx array is located close to one of the corners of the room. For the elevation intra-cluster angles, the values of σ for DOD and DOA were estimated to be 0.2 and 0.3 radians, respectively.

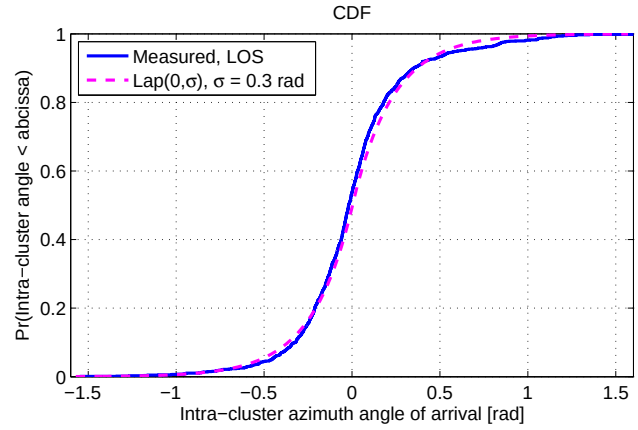

(a)

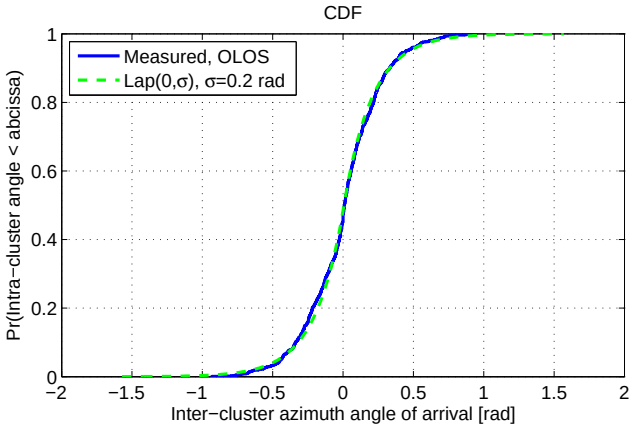

(b)

Figure 10: CDFs of the intra-cluster azimuth angles of arrival and normal and Laplace distributions with MLEs for the standard deviation σ, for the (a) LOS and (b) OLOS scenarios.

6 Channel Model Comparison

In this section, the extracted channel model parameters are compared with those of the IEEE802.11ad and IEEE802.15.3c channel models. Also, the number of clusters and number of rays inside each cluster is also discussed.

6.1 The IEEE 802.11ad Channel Model

In the IEEE802.11ad conference room channel model, the inter-cluster parameters are largely based on ray tracing results and empirical distributions [6]. For instance, the time and angle of arrival for clusters, as well as attenuation due to reflections, are all modeled using empirical distributions. Hence, it is not possible to compare the inter-cluster parameters of our proposed model with the IEEE802.11ad model.

However, our proposed model adopts the same basic intra-cluster model used in [6], making it possible to compare the two models. In Table I, the estimated intra-cluster time-domain parameters for the LOS and OLOS scenarios are presented and compared with the values from the IEEE802.11ad channel model for the conference room environment.

Table 1: Intra-cluster time-domain parameters; Comparison with the IEEE802.11ad Conference Room Model

Parameter	Notation	LOS	OLOS	802.11ad
Ray decay time	γ_{pre} [ns]	4.6	4.8	3.7
	γ_{post} [ns]	4.7	4.5	4.5
Ray K-factor	K_{pre} [dB]	8.6	10.3	10
	K_{post} [dB]	9.0	11.0	14.2
Ray arrival rate	λ_{pre} [1/ns]	0.90	1.1	0.37
	λ_{post} [1/ns]	0.90	1.0	0.31

Our results show larger values for the ray arrival rates and somewhat larger ray decay times. These differences might be explained in part by differences in the measurement environment but also due to differences in how the data analysis is performed. Since the rays in our analysis are estimated using a high-resolution algorithm in a real furnished environment, a larger number of rays might be detected, resulting in a different ray arrival rate. The ray K-factors are however similar.

6.2 The IEEE802.15.3c Channel Model

The 802.15.3c channel model uses a Laplacian or Gaussian distribution, with standard deviation σ_ϕ, to model the intra-cluster azimuth angular distribution of the rays inside each cluster. The cluster and ray powers are modeled using lognormal distributions with standard deviations σ_c and σ_r, respectively. This is in agreement with the findings in this paper, and our proposed model also employs a Laplacian distribution for the intra-cluster angular distribution and log-normal distributions for the cluster and ray powers.

The IEEE802.15.3c channel model supports several different scenarios and channel model parameters have been presented for desktop, office, residential, kiosk and library scenarios [24]. Among these, the library scenario is most similar to the conference room scenario considered in this paper. In Table II, channel model parameters (both inter- and intra-cluster parameters) for the IEEE802.15.3c library LOS scenario are compared with the parameters of our model.

Table 2: Inter- and Intra-cluster time-domain parameters; Comparison with the IEEE802.15.3c Library Model

Parameter	Notation	LOS	OLOS	802.15.3c
Cluster arrival rate	Λ [1/ns]	0.2	0.2	0.25
Ray arrival rate	λ [1/ns]	0.9	1.0-1.1	4.0
Cluster decay rate	Γ [ns]	8.7	8.7	12
Ray decay rate	γ [ns]	4.6-4.7	4.5-4.8	7.0
Cluster log-normal st. d.	σ_c [dB]	6.4	6.4	5.0
Ray log-normal st. d.	σ_r [dB]	7.0-7.1	5.6-6.1	6.0
Ray DOD azimuth st. d.	σ_ϕ [deg]	40	23	10
Ray DOA azimuth st. d.	σ_ϕ [deg]	17.2	17.3	N/A
Ray DOD elevation st. d.	σ_θ [deg]	11.4	12.1	N/A
Ray DOA elevation st. d.	σ_θ [deg]	17.2	17.5	N/A

It can be observed that our results show smaller values for the ray arrival rate compared to the 15.3c model. On the other hand, our results for the ray arrival rate is also larger compared to that of the IEEE802.11ad model. Furthermore, our results show larger values for the standard deviations of the intra-cluster angular Laplacian distribution, especially for the DOD in the LOS scenario. The reason for this could be related to differences in how the rays

and clusters are identified.

6.3 Number of clusters and rays

In our results, we observed 6-12 and 8-12 clusters in the LOS and OLOS scenarios, respectively, with an average of 10 clusters for both scenarios. The average number of clusters in the 15.3c model is 9, whereas the IEEE802.11ad model has a fixed value of 18 clusters. This difference is due to the fact that the clusters in the IEEE802.11ad model are identified using ray tracing, and several of those clusters would be grouped into one cluster when using a clustering algorithm.

The observed number of rays inside each cluster ranged from 1 up to 38 in one extreme case. The mean observed number of rays in each cluster was 7 for LOS and 9 for OLOS. It was found that the number of rays in each cluster could be modeled using an exponential distribution. However, we have found that due to the ray decay and the large K-factor for the rays, only the first 2-10 rays make a significant contribution to the overall statistics of the simulated channel. Hence, the number of rays in each cluster is set to a fixed number in our model; 6 pre-cursors and 8 post cursor rays for each cluster. The same values are used in the IEEE802.11ad model.

7 Channel Model Validation

In order to assess the performance of the developed channel model, it needs to be validated. In this section, in order to verify the performance of the model, the following metrics are used to compare the outputs from the channel models with the results from the measurements: the relative eigenvalues of the MIMO channel matrices, the RMS delay spread and the direction spread. A large number of MIMO channel matrices were generated using the ray tracing and stochastic models, using the same array geometry, antenna patterns and array positions as in the measurements. For each array position, frequency transfer functions, $\mathbf{H}(f) \in \mathbb{C}^{N_t \times N_r}$, were generated for the same 49×49 MIMO configuration as in the measurement, using a bandwidth of 2 GHz in the frequency range of 61-63 GHz, with 1001 frequency points. This frequency range was chosen since 60 GHz wireless systems typically use bandwidths as large as 2 GHz [2], [3]. Based on these results, we compare the statistical results from the model with the measurements for the three chosen metrics.

Eigenvalues

The relative eigenvalues were calculated for a large number of 9×9 MIMO channel matrices. These 9×9 channel matrices are formed using rectangular subarrays based on the larger 49×49 channel matrices at each Tx/Rx array position. We define the nth relative eigenvalue to be

$$\lambda_{n,rel.} = \frac{\lambda_n}{\sum_{i=1}^{I} \lambda_i}. \tag{12}$$

The relative eigenvalues are normalized with respect to the sum of all eigenvalues, which means each relative eigenvalue can be interpreted as a fraction of the total instantaneous channel power. Fig. 11 shows CDFs of the four strongest eigenvalues for the stochastic and ray tracing models as well as the measurements, for both the LOS and OLOS scenarios, using all Tx array positions. Both the stochastic and ray tracing models agree well with the measurement data, with a slightly better agreement for the stochastic model.

RMS Delay Spread

The RMS delay spread (RMS DS) was calculated based on the power-delay profiles (PDPs) from the measurements and for the realized PDPs generated by the two models. The PDPs are calculated based on the channel impulse responses (CIRs). Each CIR, $h(\tau)$, is derived by applying a Hann window to $\mathbf{H}(f)$ in order to suppress side lobes, and then taking the inverse Fourier transform. The PDP, $P_h(\tau)$ is then obtained as

$$P_h(\tau) = \frac{1}{N_t N_r} \sum_{n_t=1}^{N_t} \sum_{n_r=1}^{N_r} |h(\mathbf{s}_{n_r}, \mathbf{s}_{n_t}, \tau)|^2, \tag{13}$$

where $\mathbf{s}_{n_t}$ and $\mathbf{s}_{n_r}$ denote the spatial position relative to the array origin for the n_tth Tx and n_rth Rx antenna, respectively.

The RMS DS is often calculated by only including values in the PDP that are within a certain range from the peak value. In this paper, we apply a 30 dB dynamic range when calculating the RMS DS. The RMS DS is then calculated as

$$S_\tau = \sqrt{\frac{\sum_\tau P_h(\tau)\tau^2}{\sum_\tau P_h(\tau)} - \left(\frac{\sum_\tau P_h(\tau)\tau}{\sum_\tau P_h(\tau)}\right)^2}. \tag{14}$$

Fig. 12 shows CDFs of the calculated RMS DS for the LOS and OLOS scenarios. It can be noted that both models agree well with the measured RMS DS for the LOS scenario, as seen in Fig. 12 (a). For the RMS DS in the OLOS scenarios seen in Fig. 12 (b), the ray tracing model seems to underestimate the RMS DS. The reason for this is not known, but might be related to the fact the ray tracing model does not model all the details present in the room and also always places clusters at the same delays and angles for a given Tx-Rx setup.

The stochastic model on the other hand, has a median value that agrees well with the measured values in the OLOS scenario, but exhibits a much larger variation compared to the measured results. Given that only 15 measured values of the RMS DS is available for this comparison, it is difficult to tell whether this variation is reasonable or not. Based on reported values of the RMS DS in the literature for similar scenarios [27], we argue that the values of the RMS DS modeled by the stochastic modeled is reasonable.

Direction Spread

Lastly, the direction spread was chosen as a metric to evaluate and compare the statistical angular properties of the models and the measurements. For this comparison, the MPC estimates from SAGE for the measurements are used in the evaluation. The direction spread, σ_Ω, is calculated for each scenario, using L MPCs, as [28]

$$\sigma_\Omega = \sqrt{\sum_{l=1}^{L} |\boldsymbol{e}(\phi_l, \theta_l) - \boldsymbol{\mu}_\Omega|^2 P(\phi_l, \theta_l)}, \tag{15}$$

where $P(\phi_l, \theta_l)$ is the normalized power spectrum, whereas ϕ_l and θ_l denote the azimuth and polar angles of the lth MPC, respectively. The mean direction, $\boldsymbol{\mu}_\Omega$, and the unit vector for the direction of the lth MPC, $\boldsymbol{e}(\phi_l, \theta_l)$, are each given by

$$\boldsymbol{\mu}_\Omega = \sum_{l=1}^{L} \boldsymbol{e}(\phi_l, \theta_l) P(\phi_l, \theta_l), \tag{16}$$

$$\boldsymbol{e}(\phi_l, \theta_l) = [\cos(\phi_l)\sin(\theta_l), \sin(\phi_l)\sin(\theta_l), \cos(\theta_l)]^T.$$

Fig. 13 shows CDFs of the direction spread at the Tx side for the models and measurements. The stochastic model tends to agree quite well with the

measurement results, whereas the ray tracing model tend to underestimate the direction spread, especially for LOS scenarios. This is likely explained by the fact that an oversimplified geometry was used in the ray tracing model. In the measurements, there are several strong reflections from objects in the environment such as ceiling lamps and bookshelves [18], and these effects are not taken into account if the room is modeled as rectangular box with tables as the only objects in the ray tracing routine. This shows that it is of importance to include finer details in the environment when using a ray tracing-based approach. As a result, this makes it even more challenging to develop a simple ray tracing-based model that effectively models the statistical behavior of 60 GHz radio channels.

8 Conclusions

In this paper, we have presented measurement-based results for a 60 GHz double-directional MIMO channel model. The measurements were performed in a conference room using a VNA-based measurement system with 7×7 planar virtual arrays at both the Tx and Rx sides. The measurements included results from 17 LOS and 15 OLOS scenarios. A large number of MPCs were estimated using the SAGE algorithm and then clustered using the K-power-means algorithm. As the antenna patterns were de-embedded in the SAGE algorithm, the proposed channel model supports different antenna types and array geometries.

The intra-cluster properties describing the rays in each cluster are modeled stochastically. Estimated parameters for the ray decay time, K-factor and arrival rate have been presented. It has also been shown that the intra-cluster angles are appropriately modeled using a zero-mean Laplacian distribution and that the ray power distribution around the mean can be modeled using a log-normal distribution. Furthermore, we have shown that the angular characteristics of the MPCs and clusters exhibit a clear delay dependence related to overall geometry of the room as well as the objects in the room. Our proposed channel model includes two novel methods of modeling the cluster angular and delay properties; one semi-deterministic model using ray tracing and one stochastic model using joint angular-delay pdfs. Both of these models have been validated against the measurement data using three different metrics; the relative eigenvalues, the RMS delay spread and the direction spread. Both models agree reasonably well with the measured data. We have also provided a detailed comparison of the channel model parameters with those of the IEEE802.11ad and 802.15.3c channel models.

References

[1] R. C. Daniels, R. W. Heath, "60 GHz Wireless Communications: Emerging Requirements and Design Recommendations", *IEEE Veh. Tech. Mag.*, vol. 2, no. 3, pp. 4150, Sep. 2007.

[2] IEEE802.15.3c-2009, Part 15.3: Wireless Medium Access Control (MAC) and Physical Layer (PHY) Specifications for High Rate Wireless Personal Area Networks (WPANs), Amendment 2: Millimeter-wave- based Alternative Physical Layer Extension, Oct. 2009.

[3] IEEE802.11ad draft, Part 11: Wireless LAN Medium Access Control (MAC) and Physical Layer (PHY) Specifications Amendment 3: Enhancements for Very High Throughput in the 60 GHz Band, Dec. 2011.

[4] C. Gustafson, F. Tufvesson, "Characterization of 60 GHz Shadowing by Human Bodies and Simple Phantoms", *Radioengineering*, vol. 21, no. 4, December 2012.

[5] X. An, C. Sum, R. V. Prasad, J. Wang, Z. Lan, J. Wang, R. Hekmat, H. Harada, and I. Niemegeers, Beam switching support to resolve link-blockage problem in 60 GHz WPANs, *Proc. IEEE Int. Symp. on Personal Indoor and Mobile Radio Comm.*, pp. 390-394, Sep. 2009.

[6] A. Maltsev, R. Maslennikov, A. Lomayev, A. Sevastyanov, A. Khorayev, "Statistical Channel Model for 60 GHz WLAN Systems in Conference Room Environment", *Radioengineering*, vol. 20, no. 2, June 2011.

[7] S. J. Lee, W. Y. Lee, "Capacity of millimetre-wave multiple-input multiple-output channels in a conference room," *IET Communications*, vol.6, no.17, pp. 2879-2885, November 27 2012.

[8] M. Park; H. K. Pan, "A Spatial Diversity Technique for IEEE 802.11ad WLAN in 60 GHz Band," *IEEE Communications Letters*, vol.16, no.8, pp. 1260-1262, August 2012.

[9] X. Zhu, A. Doufexi, T. Kocak, "Beamforming performance analysis for OFDM based IEEE 802.11ad millimeter-wave WPANs," *8th International Workshop on Multi-Carrier Systems and Solutions* (MC-SS), 2011, pp. 1,5, 3-4 May 2011.

[10] M. Jacob, S. Priebe, T. Kurner, M. Peter, M. Wisotzki, R. Felbecker, W. Keusgen, "Extension and validation of the IEEE 802.11ad 60 GHz human blockage model," *7th European Conference on Antennas and Propagation* (EuCAP), pp. 2806-2810, 8-12 April 2013.

[11] H. Xu, V. Kukshya and T. S. Rappaport, Spatial and Temporal Characteristics of 60-GHz indoor Channels, *IEEE Journal on Selected Areas in Communications*, Vol. 20, No. 3, April 2002.

[12] A. Maltsev, et. al., "Channel Models for 60 GHz WLAN Systems" *IEEE 802.11-09/0334r8*, May 2010.

[13] H. Sawada, S. Kato, K. Sato, H. Harada, et. al., "Intra-cluster response model and parameter for channel modeling at 60GHz (Part 3)" *IEEE 802.11-10/0112r1*, Jan 2010.

[14] S. Wyne, K. Haneda, S. Ranvier, F. Tufvesson, and A. F. Molisch "Beamforming Effects on Measured mm-Wave Channel Characteristics" *IEEE Transactions on Wireless Communications* Vol:10, No. 11, 2011.

[15] S. Ranvier, M. Kyro, K. Haneda, C. Icheln and P. Vainikainen, VNA-based wideband 60 GHz MIMO channel sounder with 3D arrays, *Proc. Radio Wireless Symp.*, pp. 308-311, San Diego, CA, Jan 2009.

[16] K.T. Selvan, "A revisit of the reference antenna gain measurement method," *Proceedings of the 9th International Conference on Electromagnetic Interference and Compatibility*, (INCEMIC), pp.467-469, 23-24 Feb. 2006

[17] M. Landmann, M. Kaske, R.S. Thoma, "Impact of Incomplete and Inaccurate Data Models on High Resolution Parameter Estimation in Multidimensional Channel Sounding," *IEEE Transactions on Antennas and Propagation* , vol.60, no.2, pp.557-573, Feb. 2012

[18] C. Gustafson, F. Tufvesson, S. Wyne, K. Haneda, A. F. Molisch, "Directional analysis of measured 60 GHz indoor radio channels using SAGE" *IEEE 73rd Vehicular Technology Conference* (VTC Spring), Budapest, Hungary, May 2011.

[19] K. Haneda, C. Gustafson, S. Wyne, "60 GHz Spatial Radio Transmission: Multiplexing or Beamforming?" *IEEE Trans. on Antennas and Propagation*, vol.PP, no.99, 2013.

[20] N. Czink, P. Cera, J. Salo, E. Bonek, J.-P. Nuutinen, J. Ylitalo, "A framework for automatic clustering of parametric MIMO channel data including path powers", *IEEE 64th Vehicular Technology Conference*, pp.1-5, 25-28 Sept. 2006

[21] D.-J. Kim, Y.-W. Park, and D.-C. D.-J. Park, A Novel Validity Index for Determination of the Optimal Number of Clusters, *IEICE Trans. Inf. & Syst.*, vol. E84-D, No. 2, pp. 281-285, 2001.

[22] Q. H. Spencer, B.D. Jeffs, M. A. Jensen, A. L. Swindlehurst, "Modeling the statistical time and angle of arrival characteristics of an indoor multipath channel," *IEEE Journal on Selected Areas in Communications*, vol.18, no.3, pp.347-360, March 2000.

[23] C.-C. Chong, C.-M. Tan, D. I. Laurenson, S. McLaughlin, M. A. Beach, A. R. Nix, "A New Statistical Wideband Spatio-Temporal Model for 5 GHz Band WLAN Systems", *IEEE Journal on Selected Areas in Communications*, Vol. 21, No. 2, Feb. 2003.

[24] S-K. Yong, et al., TG3c channel modeling sub-commitee final report, *IEEE Techn. Rep.*,15-07-0584-01-003c, Mar. 2007.

[25] C. Gustafson, D. Bolin, F. Tufvesson, "Modeling the cluster decay in mm-Wave channels", *8th European Conference on Antennas and Propagation (EuCAP)*, Hague, 6-11 April, 2014.

[26] N. Czink, P. Cera, J. Salo, E. Bonek, J.-P. Nuutinen and J. Ylitalo, "Improving clustering performance using multipath component distance", *Electronics Letters*, 5th Jan. 2006 Vol. 42 No. 1.

[27] S.-K. Yong, P. Xia, A. Valdes-Garcia, "60 GHz Technology for Gbps WLAN and WPAN: From Theory to Practice", *Wiley*, 2011.

[28] B. H. Fleury, "First- and second-order characterization of direction dispersion and space selectivity in the radio channel", *IEEE Transactions on Information Theory*, vol. 46, pp. 2027 - 2044, September 2000.

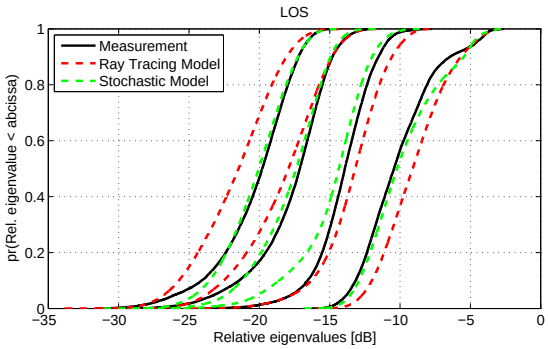

(a)

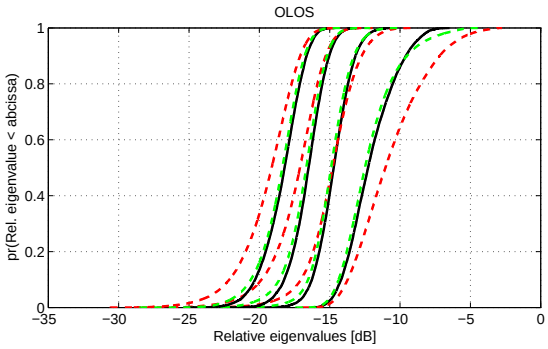

(b)

Figure 11: CDFs of the four strongest relative eigenvalues for the measurement data and for a large number of realizations using the ray tracing and stochastic models in the LOS (a) and OLOS (b) scenarios.

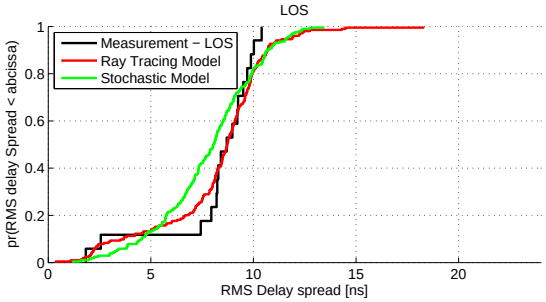

(a)

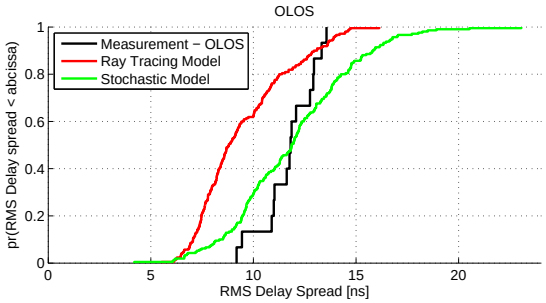

(b)

Figure 12: CDFs of the RMS delay spreads for the measurement data and for a number of realizations using the ray tracing and stochastic models, for the LOS (a) and OLOS (b) scenarios.

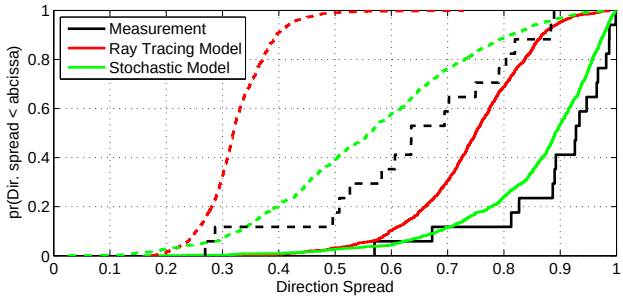

Figure 13: CDFs of the Tx direction spread in the LOS (dashed curves) and OLOS scenarios (solid curves).

Paper III

Characterization of 60 GHz Shadowing by Human Bodies and Simple Phantoms

The 60 GHz band is very promising for high data rate (>1 Gb/s) wireless systems operating at short ranges. However, due to the short wavelengths in this frequency band, the shadowing effects cuased by human bodies and furniture are severe and needs to be modeled properly. In this paper, we present an experimental, measurement-based characterization of the reflection and shadowing effects in the 60 GHz band caused by human bodies and various phantoms, in order to find simple phantoms suitable for use in human shadowing measurements. It is shown that a water-filled human phantom serves as a good choice for this purpose.

©2012 IEEE. Reprinted, with permission, from
C. Gustafson and F. Tufvesson
"Characterization of 60 GHz Shadowing by Human Bodies and Simple Phantoms",
in *Radioengineering*, Vol. 21, No. 4, pp. 979-984, 2012.

1 Introduction

Next generation wireless systems operating in the 60 GHz band are currently being designed to provide very high data rates (> 1 Gb/s) for short range communications. Products are already on the market and several standards, such as the *IEEE* standards *802.11ad* [1] and *802.15.3c* [2], are available or under development. Propagation in the 60 GHz band is characterized by a large free-space path loss, low transmission through obstacles and also suffer from sharp shadow zones that can be caused by e.g. furniture or humans. Measurement results have shown that shadowing due to moving human bodies have a significant impact on the propagation of millimeter waves and fading depths of around -20 dB [3] or in the range of -18 to -36 dB [4] have been reported. For propagation and performance analyses, it is therefore of vital importance to have a good model for human interaction such as shadowing and reflection.

Measurements of moving people require real-time systems, which at 60 GHz usually limits the number of Tx and Rx antennas that can be used. Real-time multi-antenna channel sounders at 60 GHz are rare but do exist. Such a channel sounder was presented in [5] and has since been used to characterize the shadowing events due to human bodies using two access points and one Tx [3]. Some measurements do require a larger number of antennas, which can exclude the possibility of using real-time measurements. So far, this has usually been the case when studying the directional properties of the 60 GHz band. Such measurements are typically performed using virtual arrays [6] or highly directional antennas that are mechanically steered [7] and requires that the channel is nearly static. Measurement-based results of the directional properties that also includes the effects of human shadowing are however scarce.

In the literature, ray tracing is often used to simulate the effects of human interaction and the human body is modeled in several different ways. In [8], the authors present a 60 GHz human blockage model developed within the framework of the *IEEE 802.11 Task Group ad*. The model is based on ray tracing and includes a knife edge diffraction model which is an extension of the work in [9]. In [8], the human blockage is modeled using two double knife edges for the body and two single knife edges for diffraction over a human head. In [10], a diffraction based model is used to study network link connectivity, where the human body is approximated by a perfectly conducting cylinder. The authors in [11] employ a ray tracing technique to study human body shadowing at 60 GHz, where the human body is modeled by a cylinder with a partition of salt water that is circumscribed by a parallelepiped. The models used in [8], [10] and [11] are efficient ways to simulate the shadowing effects in the 60 GHz band. However, these effects still needs to be further characterized using measurement

based results, and the human body models used in the above studies might not be appropriate for use in measurements. In more recent studies, 60 GHz human phantoms with appropriate dielectric properties, suitable for use in on-body antenna measurements, are being developed [12], [13]. The aim of this paper is to find a more simple human phantom suitable for use in 60 GHz human shadowing measurements. In such measurements, the Tx and Rx antennas are typically placed at a far-field distance from the shadowing object, and it is only required that the phantom have the appropriate shadowing and reflection properties. For this reason, we present a measurement-based characterization of the shadowing and reflection properties of human bodies and various human phantoms.

2 Measurement Setup and Methods

2.1 Measurement Equipment

In our measurements, transfer functions were measured using an Agilent E8361A vector network analyzer (VNA). The measured frequency range was 58-62 GHz, using 1601 points, a stepped sweep and an IF-bandwidth of 1 kHz. Fig. 1 shows the basic measurement setup. A V-band horn antenna with a gain of 20 dB was used at both the Tx and Rx. The setup also utilizes a power amplifier (PA) with a gain of 20 dB and a low-noise amplifier (LNA) with a gain of 30 dB, both of which are connected to a high frequency coaxial cable using a coaxial to waveguide transition. High accuracy electromechanical positioners are used to scan the antennas linearly in a cross section plane of the shadowing object.

Since the measurements are performed using a VNA and antenna positioners, it is important that the shadowing object remains still during the entire measurement. Due to the short wavelength of about 5 mm, it is difficult to measure the human blockage since even breathing may cause a person to move too much. For this reason, we initially consider the shadowing due to human legs for the investigation. This makes it easier to make reproducible measurements and to compare the results with simple theoretical models. Four different types of shadowing objects are considered initially: human leg, a plastic cylinder filled with water or wrapped with aluminum foil, and a thin metallic sheet. The cylinder has a diameter of 11 cm and the PVC plastic is about 3 mm thick. The metallic sheet is 11 cm wide and has a thickness of 1 mm. In the measurement of the human legs, the main beam of the antennas were directed at

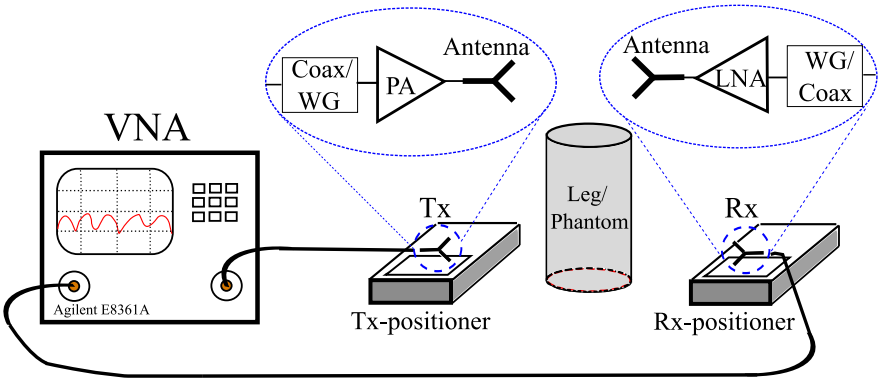

Figure 1: Measurement setup.

the lower part of one thigh. At this part of the leg, the four different measured legs had approximate diameters in the range of 11-12.7 cm. As a final step, the shadowing of a more realistic human phantom is compared with those of human bodies.

2.2 Measurement procedure

Two different types of measurements were performed to characterize the shadowing. In the first, one antenna is placed at a fixed and centered position behind the shadowing object. The other antenna is then moved linearly across the width of the object. In the second measurement, both antennas are scanned across the width of the object simultaneously. The distance from each antenna to the object is set to 70 cm, and the polarization is vertical to vertical unless otherwise specified. In each measurement, a line-of-sight (LOS) measurement was performed as a reference, where the shadowing object was removed. The VNA was calibrated and a back-to-back measurement was performed to remove the influence of the coaxial to waveguide transition. The measured data is then post processed to remove the influence of the PA and LNA and then gated in the delay domain to remove contributions from possible multi-path components with delays that are longer than those of the diffracted field. We then define the shadowing gain as

$$g_{\mathrm{S}}(f, \mathbf{r}_{\mathrm{Tx,Rx}}) = H_{\mathrm{Shadow}}(f, \mathbf{r}_{\mathrm{Tx,Rx}}) / H_{\mathrm{LOS}}(f, \mathbf{r}_{\mathrm{Tx,Rx}}), \tag{1}$$

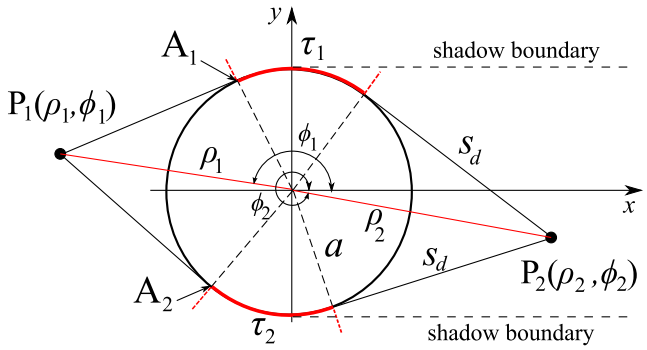

Figure 2: Diffraction around a perfectly conducting cylinder.

where H_{Shadow} and H_{LOS} are the post processed frequency transfer functions of the shadowing and LOS measurements, respectively, and $\mathbf{r}_{\text{Tx,Rx}}$ denotes the position of the Tx/Rx.

2.3 Diffraction by a Cylinder

The diffraction around a perfectly conducting cylinder, as shown in Fig. 2, can be analytically calculated using a model based on the geometrical theory of diffraction (GTD) [14]. A normally incident wave with a linearly polarized E-field in the z-direction is assumed.

The amplitude of the incident E-field reaching the glancing points A_1 and A_2 is denoted E_i. The diffracted E-field at the position P_2, E_z, can then be written as

$$E_z = \sum_{n=1}^{N} D_n^e E_i \frac{\exp(-jks_d)}{\sqrt{8jks_d}} \Big[\exp\{-(jk+\Omega_n^e)\tau_1\} + \exp\{-(jk+\Omega_n^e)\tau_2\}\Big] \quad (2)$$

The incident rays each travel a distance along the cylinder (τ_1 and τ_2) and are attenuated according to the attenuation constant Ω_n. For the E-field, this constant is given by

$$\Omega_n^e = \frac{\alpha_n}{a} M \mathrm{e}^{j\pi/6}. \quad (3)$$

Table 1: Complex permittivity at 60 GHz

	ϵ_c	Ref.
Skin	$7.98 - j10.91$	[15]
Fat	$2.51 - j0.84$	[15]
Infiltrated Fat	$4.40 - j3.13$	[15]
Muscle	$12.85 - j15.74$	[15]
Water (20° C)	$11.9 - j19.5$	[12]

Finally, D_n and M are each given by

$$D_n = 2M\{\mathrm{Ai}'(-\alpha_n)\}^{-2}\mathrm{e}^{j\pi/6}, \quad M = \left(\frac{ka}{2}\right)^{1/3} \tag{4}$$

Here, $-\alpha_n$ denotes the zeros of the Airy function $\mathrm{Ai}(\cdot)$, k is the wavenumber and a is the radius of the cylinder.

2.4 Dielectric Properties

The dielectric proerties of human tissue is of importance when developing human phantoms. At 60 GHz, the penetration depths in tissues are typically small, which could indicate that it is important that the outer layer of the phantom has dielectric properties similar to those of human skin. Table 1 lists some typical values of the complex permittivity, $\epsilon_c = \epsilon' - j\epsilon''$, at 60 GHz, for human skin, fat, muscle and of pure water at 20° C. We note that the dielectric properties of pure water at 20° C are more or less similar to those of muscles. For a more detailed discussion about the dielectric properties at 60 GHz, the reader is referred to [12] and the references therein.

The dielectric properties of PVC plastics at 70 GHz and above have been reported to have typical values around $\epsilon_{c,\mathrm{PVC}} = 2.9 - j0.03$ [16], which indicates that the dielectric loss in PVC at 60 GHz is low compared to skin. However, this also indicates that the real part of the permittivity of PVC at 60 GHz could be similar to that of uninfiltrated fat. A PVC phantom could be covered with an appropriate layer with dielectric properties similar to those of skin to create a layered model of the human skin/fat layers. This is however outside the scope of this paper.

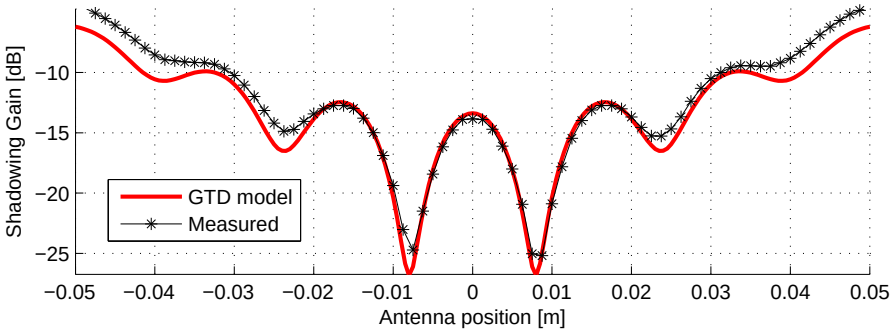

Figure 3: Shadowing gain for the metallic cylinder and for the GTD model. The Tx and Rx are moved simultaneously across the width of the cylinder.

3 Results

3.1 Theoretical vs. Measured Shadowing Gain

Fig. 3 shows the measured and theoretical shadowing gain for the metallic cylinder when the Tx and Rx are moved simultaneously across the width of the cylinder. The theoretical curve was calculated using the GTD model described above. The curves show a good overall agreement with a slightly worse agreement close to the edge of the shadowing boundary. This can be attributed to the fact that the theoretical GTD model used is no longer valid close to the transition region about the shadow boundary. However, in the deep shadow region, the GTD model can predict the shadowing gain accurately and shows that the diffracted field can be described by so called *creeping waves* along the surface of the cylinder.

Using the GTD model, the shadowing gain was calculated for different metallic cylinders with radii ranging from 5-25 cm. The result is shown in Fig. 4. As a reference, the radius of the cylinder used to model the human body in [11] is 15 cm.

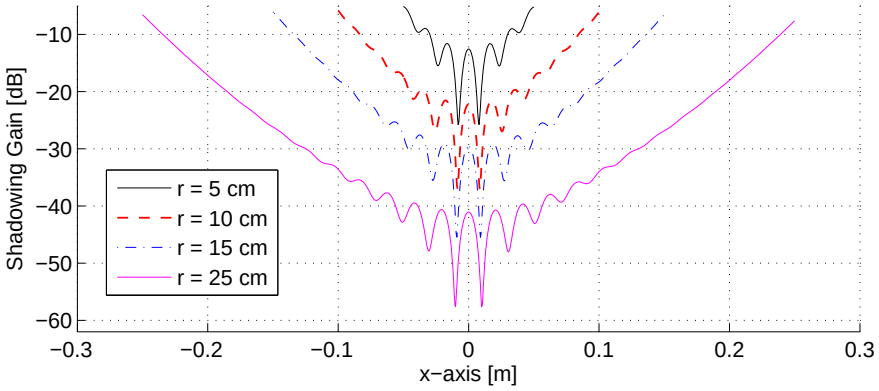

Figure 4: Calculated shadowing gain for metallic cylinders with different radii, using the GTD model.

3.2 Shadowing Gain for various Objects

Fig. 5(a) shows the measured shadowing gain for different shadowing objects as a function of Tx position with the Rx at a fixed position. All objects show similar diffraction patterns with slightly different shapes. The diffraction patterns for the legs display assymmetry, which could be explained by the fact that the legs are not perfectly cylindrical. The metallic and water filled cylinder show a better agreement to the shadowing gain of the legs as compared to the metallic sheet.

In Fig. 5(b), both the Tx and the Rx are moved simultaneously, which makes the diffraction dips occur more frequently over distance. The metallic cylinder shows a good agreement with the shadowing gain of the legs, especially for person A. The leg of this person had a diameter of approximately 11.3 cm, which is close to that of the cylinder.

3.3 Polarization

So far, only vertical-to-vertical polarization has been considered. For this reason, the shadowing gain of a persons leg was measured using both vertical-to-vertical (V-V) and horizontal-to-horizontal (H-H) polarization. The result is seen in Fig. 2, which shows that the shadowing loss is greater for V-V

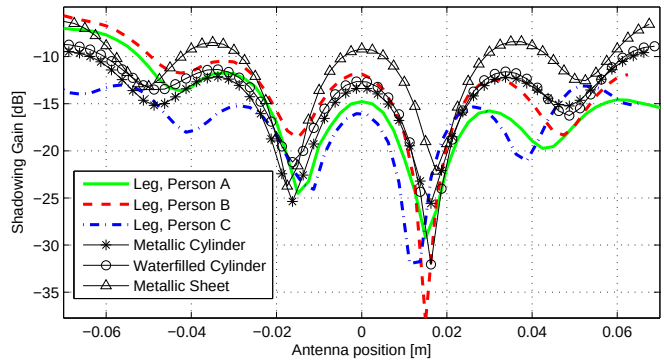

(a)

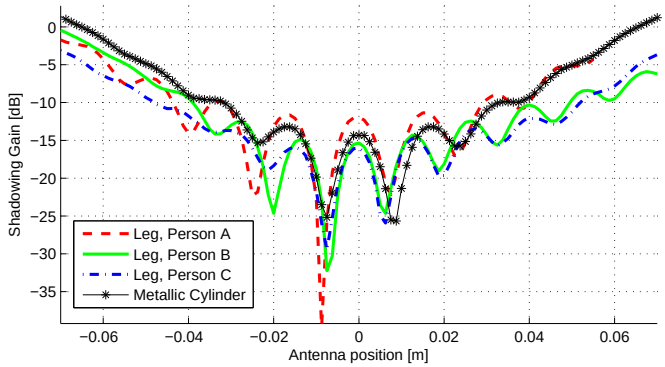

(b)

Figure 5: Shadowing gain for different shadowing objects with (a) a fixed Rx and (b) with the Tx and Rx moved simultaneously.

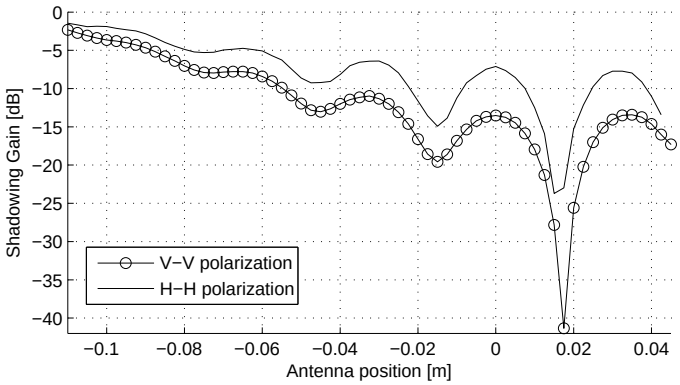

Figure 6: Shadowing Gain for a leg, with vertical-to-vertical and horizontal-to-horizontal polarization.

polarization.

This is due to a higher diffraction loss for fields that are parallel to the surface of the shadowing object. For this particular measurement, the difference between V-V and H-H polarization is about 5-6 dB in the deep shadow region. However, this difference could be even greater for other shadowing objects where the waves traverse a longer distance along the surface of the shadowing object. When considering a more general shadowing scenario, it is difficult to say if V-V or H-H polarization is to be preferred, since diffraction may occur around the shoulder, head or the sides of a person.

3.4 Reflection

The diffraction patterns of the metallic and water filled cylinder turned out to be quite similar. However, in order to find an appropriate phantom suitable for use in measurements, the reflection needs to be considered as well. Fig. 7 shows the measured reflection for the metallic cylinder, the waterfilled cylinder and a human leg. The reflection from the metallic cylinder is more than 4 dB higher than for the waterfilled cylinder, while the reflection from the leg is fairly similar to that of the waterfilled cylinder.

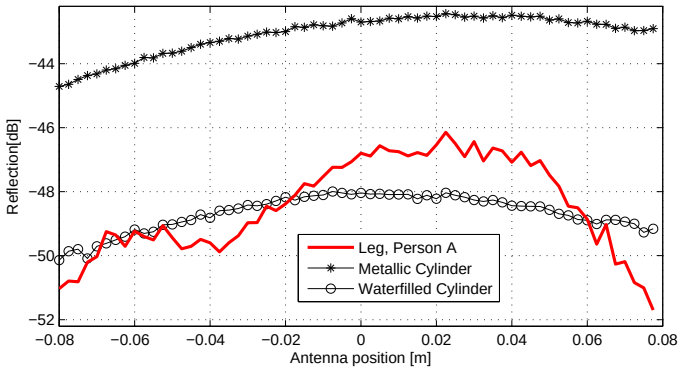

Figure 7: Measured reflection from a human leg and the metallic and waterfilled cylinders.

3.5 A Realistic Human Phantom

For reasons explained above, only simple phantoms have been considered so far. The next step is to try to find a human phantom with a more realistic shape, that also is suitable for use in measurements. Since the water-filled PVC cylinder had reflection and shadowing properties similar to those of a human leg, it could be reasonable that a water-filled human phantom would be a good candidate for 60 GHz shadowing measurements. In order to verify if this is the case, a series of measurements were performed, comparing the shadowing gain of the water-filled human phantom shown in Fig. 8 with those of humans. The shell of this phantom is made of a type of fiberglass and has a thickness of about 3 mm, which is the same as for the PVC cylinder. The dielectric properties of this shell at 60 GHz is however unknown, which is an issue.

Two different types of measurements were performed in order to compare the shadowing caused by the human phantom with that of humans. The dashed lines in Fig. 8 indicate the distances over which the antennas were scanned, for the two different scenarios. In the first scenario, both antennas are placed at a distance of 70 cm from the phantom and are moved in a cross-section plane along one of the shoulders. This resembles a scenario where a person stands up and blocks the line-of-sight between the Tx and Rx.

In the second scenario, the antennas are instead moved across the neck of the phantom. Again, both antennas were moved simultaneously over this distance

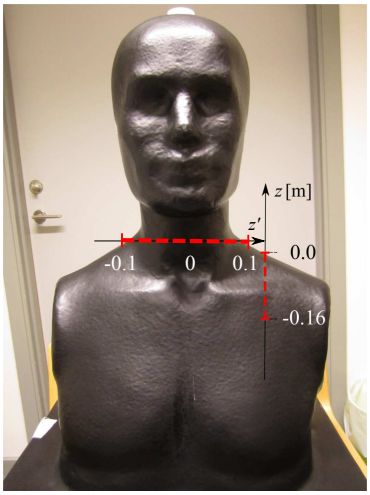

Figure 8: A human phantom. The dashed line indicates the distance over which the antennas are scanned. Corresponding measurements using humans were also performed.

and the polarization is V-V. For both scenarios, the phantom was replaced with humans and great care was taken to ensure that the persons were sitting as close as possible to the original position of the phantom. Each person tried to remain as still as possible during the duration of the entire measurement. The measured shadowing gain for the shoulder scenario is shown in Fig. 9 for three different persons and the human phantom. The shadowing gain of all three persons show higher values in the deeper shadow region when compared to the human phantom. The curve for person A shows a trend similar to the human phantom. The measurement for person B also shows a good agreement for certain parts of the curve. The poor agreement for curve C could be caused by movement of the person during the measurement. Furthermore, this particular phantom does not have any arms, which could influence the results, making it difficult to properly evaluate the results.

For this reason, an improved measurement setup was used for the neck scenario, where the person was monitored using a video recording to ensure that no movement took place. Also, a person with a neck size similar to that of

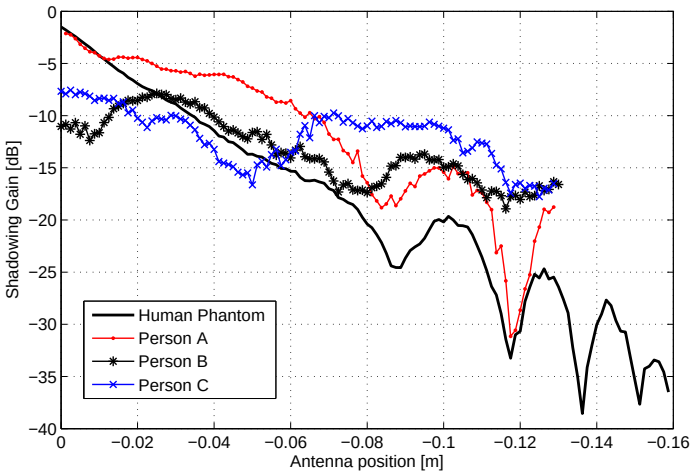

Figure 9: Shadowing gain for the shoulder cross-section.

the human phantom was chosen for the measurement. The shadowing gain was measured across the neck in order to minimize the influence from the arms of the person. Furthermore, this scenario resembles the shadowing due to a human leg, making it easier to verify that the measurement results are reasonable. The shadowing gain for this scenario is shown in Fig. 10 for the person and the human phantom. The two curves show a good agreement, both in the deep shadowing region and close to the lit region. This indicates that the water filled human phantom is suitable for use in 60 GHz shadowing measurements.

3.6 Future Work

Our results show that the physical dimensions of the shadowing objects have a large impact on the shadowing at 60 GHz. In future work, a larger set of measurements are needed to assess the influence of varying body sizes as well as to characterize the typical shadowing features of an average person. The influence of clothing might need to be investigated as well, since only few examples of this exist at 60 GHz [17].

Figure 10: Shadowing gain for the neck cross-section.

4 Conclusions

We have performed a measurement based investigation of the 60 GHz shadowing gain of human bodies and various phantoms in order to find a phantom suitable for use in measurements. It has been concluded that the measured shadowing gain of human legs are similar to those of the phantoms that were studied. The best agreement was found for the metallic and water-filled cylinder. The metallic sheet also showed a similar pattern with a slighlty higher gain. However, from a measurement point of view, any knife edge type of phantom, such as the metallic sheet, has the drawback of being sensitive to the exact orientation of the phantom. Furthermore, the reflection properties of such a phantom would be an issue. Comparing the reflection properties of a human leg with those of the metallic cylinder, it was found that the reflection from the metallic cylinder was higher than for the leg by around 4 dB. The water-filled cylinder on the other hand, showed a fairly good agreement with the reflection from the human leg. Based on these results, a water-filled human phantom with a more realistic shape was then considered. This phantom was found to have shadowing properties similar to those of humans. This indicates that the water filled human phantom is appropriate for use in human shadowing measurements at 60 GHz.

References

[1] Status of Project IEEE 802.11ad - Very High Throughput in 60 GHz, Available at: http://www.ieee802.org/11/Reports/tgad_update.htm

[2] Yong, S-K., et al.,"TG3c channel modeling sub-commitee final report", *IEEE Techn. Rep.*,15-07-0584-01-003c, 2007.

[3] A.P. Garcia, W. Kotterman, R.S. Thoma, U. Trautwein, D. Bruckner, J. Kunisch, "60 GHz Time-Variant Shadowing Characterization within an Airbus 340". COST2100, Wien, Austria, Sep. 2009.

[4] S. Collogne, G. Zaharia, G.E. Zein, "Influence of the Human Activity on Wideband Characteristics of the 60 GHz Indoor Radio Channel". *IEEE Transactions on Wireless Communications* 3(6), 2389-2406.

[5] A.P. Garcia, W. Kotterman, R.S. Thoma, U. Trautwein, D. Bruckner, J. Kunisch, "60 GHz in-Cabin Real-Time Channel Sounding", 3rd Int. Workshop on Broadband MIMO Channel Measurement and Modeling. IWonCMM, Xi'an, China, August 25, 2009.

[6] C. Gustafson, F. Tufvesson, S. Wyne, K. Haneda, A.F. Molisch, "Directional Analysis of Measured 60 GHz Indoor Radio Channels using SAGE", *IEEE 73rd Vehicular Technology Conference* (VTC Spring), 2011.

[7] H. Xu, V. Kukshya, T.S. Rappaport, "Spatial and Temporal Characteristics of 60-GHz indoor Channels". *IEEE Journal on Selected Areas in Communications*, Vol. 20, No. 3, April 2002.

[8] M. Jacob, S. Priebe, A. Maltsev, et al., "A ray tracing based stochastic human blockage model for the IEEE 802.11ad 60 GHz channel model", *Antennas and Propagation (EUCAP)*, 11-15 April 2011.

[9] J. Kunisch, J. Pamp, "Ultra-wideband double vertical knife-edge model for obstruction of a ray by a person". *IEEE ICUWB*, 2008.

[10] S. Singh, et al., "Blockage and Directivity in 60 GHz Wireless Personal Area Networks: From Cross-Layer Model to Multihop MAC Design". *IEEE Journal on Selected Areas In Communications*, 2009.

[11] A. Khafaji, R. Saadane, J.E. Addabi, M. Belkasmi, "Ray Tracing Technique based 60 GHz Band Propagation Modelling and Influence of People Shadowing". *World Academy of Science, Engineering and Technology*, 2008.

[12] N. Chahat, M. Zhadobov, R. Sauleau, S.I. Alekseev, "New Method for Determining Dielectric Properties of Skin and Phantoms at Millimeter Waves Based on Heating Kinetics". *IEEE Tans. on Microwave Theory and techniques*, January 2012.

[13] N. Chahat, M. Zhadobov, S.I. Alekseev, R. Sauleau, "Human skin-equivalent phantom for on-body antenna measurements in the 60 GHz band", *Electron. Lett.*, to appear.

[14] G.L. James, "Geometrical Theory of Diffraction for Electromagnetic Diffraction", 3rd ed., *IEEE Electromagnetic Wave Series*.

[15] S. Garbiel, R. W. Lau, C. Gabriel, The dielectric properties of biological tissues: III. Parametric models for the dielectric spectrum of tissues, *Phys. Med. Biol.* 41 (1996) 22712293.

[16] A. Elhawil, L. Zhang, J. Stiens, C. Tandt, N.A. Gotzen, G. V. Assche, R. Vouncx, "A Quasi-Optical Free-Space Method for Dielectric Constant Characterization of Polymer Materials in mm-wave Band", *Proceedings Symposium IEEE/LEOS Benelux Chapter*, 2007, Brussels.

[17] M. Zhadobov, N. Chahat, R. Sauleau, C. L. Quement, Y.L. Drean, "Millimeter-wave interactions with the human body: state of knowledge and recent advances". *International Journal of Microwave and Wireless Technologies*, 2011, 3(2), 237-247.

Paper IV

Modeling the Cluster Decay in mm-Wave Channels

The cluster power is an important parameter for cluster-based wireless channel models. This paper addresses modeling and estimation of the cluster power for wireless channels. A novel way of estimating the cluster decay and cluster fading, where the effects of the noise floor is taken into account, is presented. Due to the noise floor present in the measurement, only a limited number of clusters are available when estimating the cluster decay. It is shown that the estimated cluster decay and cluster fading can be improved if the effects of the noise floor and cluster fading are modeled and taken into account in the estimation step. If the noise floor is not taken into account in the estimation of the cluster decay, the resulting model can overestimate the RMS delay spread. Further, the paper includes estimates of the cluster decay and fading based on measured clusters for an indoor wireless mm-Wave channel in a conference room environment.

©2014 IEEE. Reprinted, with permission, from
C. Gustafson, D. Bolin and F. Tufvesson
"Modeling the Cluster Decay in mm-Wave Channels",
in *8th European Conference on Antennas and Propagation* (EuCAP), The Hague, Netherlands, pp. 804-808, 2014-04-06.

1 Introduction

Realistic wireless channel models are essential for the development of wireless systems and techniques. Wireless systems operating in the millimeter wave frequency range has gained a lot of interest over the recent years and the 60 GHz band has received special attention due to the large bandwidth that is available worldwide [1]. Efforts have already been made regarding standardization by the IEEE 802.15.3c [2] and IEEE 802.11ad [3] working groups, and some commercial products are already available on the market.

The propagation characteristics in the 60 GHz band are inherently different from those in the lower frequency bands. Furthermore, the 60 GHz band has not been researched to the same extent as lower frequency bands, which makes it essential to properly characterize all aspects of the various propagation characteristics. Wireless channel models typically rely on a set of model parameters. An important part of these parameters are the ones that describe the characteristics of the cluster power. The cluster power has been modeled in various different ways for the 60 GHz band. In this paper, we are mainly focusing on a framework that is based on the Saleh-Valenzuela model [4]. A version of the Saleh-Valenzuela model is used in the IEEE802.15.3c channel model [2]. There, the cluster power is mainly characterized by the cluster decay rate and the cluster fading. Usually, the average cluster power is assumed to be exponentially decaying with delay, but some modified versions have also been proposed. For instance in [5], a flat-to-exponential breakpoint model was suggested for the cluster decay.

In this paper, we present a novel method, where the cluster decay and cluster fading is estimated by taking the effects of assumed missing clusters, located below the noise floor, into account. We provide some numerical examples as well as results based on measured data for a wireless mm-Wave channel in a conference room environment [6]. Using a simple numerical example, with known parameters, we show that if the noise floor is not taken into account, the estimated cluster decay and cluster fading can deviate significantly from the true value in certain cases. We also use the channel model presented in [6] to show how the modeled RMS-delay spread can be affected if the missing clusters are not taken into account in the estimation.

The estimation method presented in this paper is also applicable to other frequency bands and to many other estimation problems. Due to the fact that wireless channel measurements always are limited by noise and that fading can cause the signal to vary significantly, the method could be useful in many other wireless estimation problems. For example, it could be applied when estimating the path loss exponent and the variance of the shadow fading. In general, the method is especially useful for data with missing samples due to noise and with

a variance that is fairly large in relation to the dynamic range of the observed samples.

2 Cluster Decay Model

The cluster decay model considered in this paper is based on an extended Saleh-Valenzuela model [4], [7]. In such models, the cluster power and the cluster delay is often expressed relative to the average power of the first cluster and relative to the delay of the first cluster, respectively. For modeling purposes, we shall depart from this convention and instead express the cluster power and cluster delay using the same units as in the measurement. In this paper, $\beta_{0,l}^2$ denotes the cluster power of the lth cluster, with its power expressed as the received power relative to the transmit power. Similarly, T_l, denotes the propagation delay of the lth cluster, with delay expressed in seconds. The reason for using these units, is that it makes it possible to estimate the channel model parameters for the cluster power without having to normalize each data set with respect to the delay and power of the first cluster. This way, the noise floor from each measurement is kept at a constant level and is the same for all data sets, and can easily be taken into account in the estimation. In addition, the variance of the large scale fading process of the clusters is decreased as absolute values are used instead of relative values for the estimates.

2.1 Probability distribution for the Cluster Power

The cluster power $\beta_{0,l}^2$ is modeled using the expression

$$\ln(\beta_{0,l}^2) = -\frac{1}{\Gamma}T_l + m + \epsilon_l, \tag{1}$$

where T_l is the propagation delay of the lth cluster, Γ is the cluster decay time constant, m is a reference level and where $\epsilon_l \sim \mathrm{N}\,(0, \sigma^2)$ is the cluster fading. Hence, $\ln(\beta_{0,l}) \sim \mathrm{N}\,(\mu, \sigma^2)$, with expected value

$$\mu = \mathrm{E}\{\ln(\beta_{0,l}^2)\} = -\frac{1}{\Gamma}T_l + m. \tag{2}$$

Here we note that, although m can be interpreted as the expected value of $\ln(\beta_{0,l}^2)$ at a propagation delay of 0 seconds, it should *not* be interpreted in a physical sense, since the model under consideration is only valid when the Tx and Rx are placed at a far-field distance from each other. However, given m and Γ, it is possible to calculate a useful measure, such as the expected value of the received cluster power at a distance of 1 m.

As $\ln(\beta_{0,l}^2)$ is Gaussian, the distribution for the cluster power $\beta_{0,l}^2$ is log-normal with probability density function

$$p(\beta_{0,l}^2) = \frac{1}{\sqrt{2\pi}\sigma\beta_{0,l}^2}\exp\left(-\frac{(\ln(\beta_{0,l}^2)-\mu)^2}{2\sigma^2}\right). \tag{3}$$

Furthermore, taking the expected value of the cluster power yields

$$\mathrm{E}\{\beta_{0,l}^2\} = \exp\left(m+\frac{\sigma^2}{2}\right)\exp\left(\frac{-T_l}{\Gamma}\right), \tag{4}$$

i.e., the expected value of the cluster power is exponentially decaying with delay. This is essentially the same way of modeling the cluster decay as done in the well-known Saleh-Valenzuela model [4].

3 Estimation

Given a set of measured data, we wish to estimate the parameters of Eq. (1), i.e. the constants m and Γ, as well as the variance σ^2. Here, we make the assumption that these parameters do not change for different locations within the room. Under this assumption, it is possible to combine the different measured data sets into one large data set that can be used for the estimation. Using Eq. (1), with $\boldsymbol{\alpha} = (m \quad -1/\Gamma)^T$, the data set can be modeled as

$$\mathbf{y} = \mathbf{X}\boldsymbol{\alpha} + \boldsymbol{\epsilon}, \tag{5}$$

where

$$\mathbf{y} = \begin{pmatrix} \ln(\beta_{0,1}) \\ \ln(\beta_{0,2}) \\ \vdots \\ \ln(\beta_{0,L}) \end{pmatrix}, \quad \mathbf{X} = \begin{pmatrix} 1 & T_1 \\ 1 & T_2 \\ \vdots & \vdots \\ 1 & T_L \end{pmatrix}, \quad \boldsymbol{\epsilon} = \begin{pmatrix} \epsilon_1 \\ \epsilon_2 \\ \vdots \\ \epsilon_L \end{pmatrix}.$$

Using ordinary least squares, the parameter $\boldsymbol{\alpha}$ can be estimated as

$$\hat{\boldsymbol{\alpha}} = \left(\mathbf{X}^T\mathbf{X}\right)^{-1}\mathbf{X}^T\mathbf{y}. \tag{6}$$

Given $\hat{\boldsymbol{\alpha}}$, the variance σ^2 can be estimated as

$$\hat{\sigma}^2 = \frac{1}{L-1}(\mathbf{y}-\mathbf{X}\hat{\boldsymbol{\alpha}})^T(\mathbf{y}-\mathbf{X}\hat{\boldsymbol{\alpha}}). \tag{7}$$

However, when estimating the parameters this way, the effects of the noise floor are not taken into account, and are thus only applicable for cases when the effects of the noise floor are insignificant. In practice, there is a noise floor present in the measurement, and $\mathbf{y}$ is only observed if $\mathbf{y} > c = \ln(P_{noise})$, where P_{noise} is the relative power of the noise floor present in the measurement. The value of P_{noise} is assumed to be known and constant over different measurement sets. In practice, this value is estimated based on measurement data. Due to the noise floor, each observation follows a truncated normal distribution,

$$y_i \sim N_c(\mathbf{x}_i\boldsymbol{\alpha}, \sigma^2). \tag{8}$$

The likelihood expression for this distribution is given by

$$l(\sigma, \boldsymbol{\alpha}) = \prod_{i=1}^{n} \frac{\frac{1}{\sigma}\phi(\frac{y_i - \mathbf{x}_i\boldsymbol{\alpha}}{\sigma})}{1 - \Phi(\frac{c - \mathbf{x}_i\boldsymbol{\alpha}}{\sigma})}, \tag{9}$$

where $\phi(\cdot)$ is the probability density function for the standard normal distribution and $\Phi(\cdot)$ is its cumulative distribution function, and hence Eq. (9) can be written as

$$l(\sigma, \boldsymbol{\alpha}) = \prod_{i=1}^{n} \frac{\frac{1}{\sqrt{2\pi}\sigma}\exp(-\frac{1}{2\sigma^2}(y_i - \mathbf{x}_i\boldsymbol{\alpha})^2)}{\frac{1}{2}(1 - \operatorname{erf}(\frac{c - \mathbf{x}_i\boldsymbol{\alpha}}{\sqrt{2}\sigma}))}, \tag{10}$$

where $\operatorname{erf}(\cdot)$ is the error function. Using the log-likelihood $L(\sigma, \boldsymbol{\alpha}) = \ln[l(\sigma, \boldsymbol{\alpha})]$, the parameters σ and $\boldsymbol{\alpha}$ are estimated using

$$\arg\min_{\sigma, \boldsymbol{\alpha}} \{-L(\sigma, \boldsymbol{\alpha})\}. \tag{11}$$

which is easily solved by numerical optimization of $\boldsymbol{\alpha}$ and σ.

4 Results

4.1 Estimation using Synthetic Data

Before proceeding to measured data, we first consider an example using synthetic data generated according to the model in Eq. (1), with known values for Γ, m and σ. The data was generated using 700 samples. A synthetic noise level was introduced at $\ln(P_{noise}) = -24$, separating the observable samples from the unobservable ones, yielding approximately 350 observable samples for the estimation, which is only slightly more than the number of samples available

for the measured data. Then, the model parameters for the synthetic data were estimated in two ways. For the first set of parameters, ordinary least squares are employed without considering the effects of the noise floor, i.e. Eq. (6) and (7) are used based on the observable samples. For the second set of parameters, Eq. (11) is used, which takes the effects of the noise floor into account.

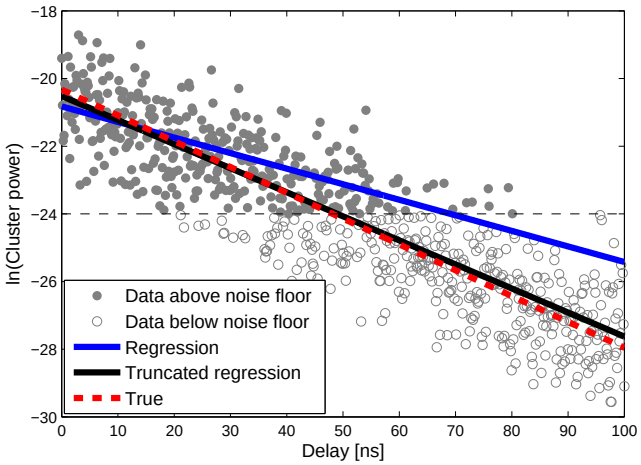

Figure 1: Estimation based on synthetic data with a noise floor located at $\ln(P_{noise}) = -24$.

Fig. 1 shows the synthetic data and the estimated cluster decay using these two methods, as well as the true cluster decay. It can be observed that when using a truncated regression, the estimates for the cluster decay agrees quite well with the true cluster decay. However, when performing a regression without considering any truncation, the cluster decay estimates are less accurate, especially for the cluster decay. This means that the expected value of the cluster power will deviate from the true value with increasing delay. As a result, clusters with long delays generated based on these estimates will have a power that often is larger than the values typically observed in the measurement. In Section 4.3, we will show, using measured data, that this can have a severe effect on the modeled RMS-delay spread.

Table 1 shows the true and estimated values of the parameters for the synthetic data used in Fig. 1. It shows that, for this specific example, when performing a regression without considering truncation, Γ is overestimated and the standard deviation σ is underestimated. In general, the estimation error when neglecting the truncation can be more or less severe depending on the

Table 1: Estimated parameters for synthetic data.

	m	Γ [ns]	σ
Regression w/o truncation	-20.6	13.2	0.99
Regression with truncation	-20.3	9.0	1.15
True values	-20.3	8.7	1.21

exact signal-to-noise ratio (SNR), slope and variance in each specific case. However, for cases with a limited SNR and a variance that is large in relation to the dynamic range of the samples, the type of behavior illustrated in the above example can be expected.

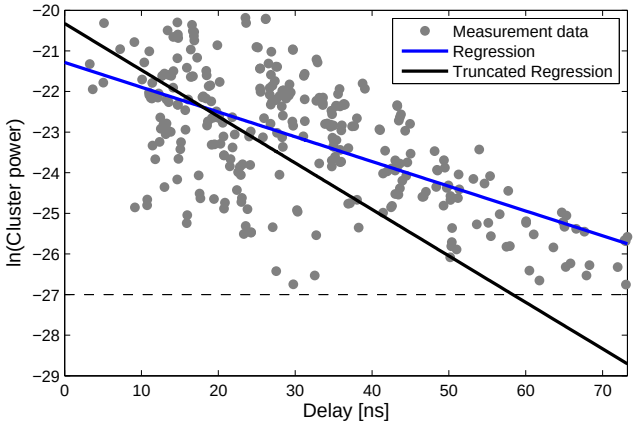

Figure 2: Estimation based on measured data at 62 GHz in a conference room environment with an estimated noise floor at $\ln(P_{noise}) = -27.1$.

4.2 Estimation using Measured Data

Using measured data for the cluster power in a conference room environment at 62 GHz [6], we estimate the model parameters of Eq. (1) in the same way as before. The measurement data consists of 17 different line-of-sight (LOS) and 15 obstructed line-of-sight (OLOS) scenarios. The data for the cluster power in the LOS scenario does not include the LOS component, since this component is being modeled deterministically. Here, we assume that the cluster decay

and cluster fading parameters are the same in the LOS and OLOS scenarios. This assumption was justified by estimating these parameters for the LOS and OLOS scenarios separately, which only revealed minor differences between the different estimates.

Fig. 2 shows the straight lines for the estimated cluster decay for the two different estimation techniques and Table 2 shows the values of the estimated parameters. When the truncation is not considered, the estimated cluster decay time constant is $\hat{\Gamma} = 16.4$ ns, which is nearly twice as large as the estimated value found using the truncated regression, namely $\hat{\Gamma} = 8.7$ ns. Also, similar to what was found in the previous example, the estimates $\hat{m}$ and $\hat{\sigma}$ are slightly larger for the truncated regression compared to that of the regression without considering truncation.

Table 2: Estimated parameters for measured data.

	m	Γ [ns]	σ
Regression w/o truncation	-21.3	16.4	1.21
Regression with truncation	-20.3	8.7	1.47

Clearly, these two different approaches yield quite different results. In order to give an illustrative example of the typical differences one might encounter for these two approaches, two different power-delay profiles (PDPs) are generated using the stochastic channel model presented in [6]. In the example, the two different PDPs are generated using the cluster decay parameters estimated with and without truncation, respectively.

These two PDPs are shown in Fig. 3, along with the measured PDP for this specific Tx-Rx separation (the Tx-Rx separation is assumed to be known in the channel model). The generated PDPs are reasonably similar to the measured PDP for delays up to 55 ns in this specific example. For delays larger than this, it can be observed that the PDP based on estimates without truncation is significantly stronger compared to the measured PDP. This kind of effect can cause the RMS-delay spread (RMS-DS) to be overestimated.

For an additional comparison, the average PDP (APDP) is caluclated based on the PDPs that were measured and based on the PDPs generated using the channel model. The APDP is calculated using N different PDPs, as

$$\text{APDP} = \frac{1}{N}\sum_{n=1}^{N} P_{h,n}(\tau), \tag{12}$$

where $P_{h,n}(\tau)$ is the nth PDP. The APDP for the measurements and the models

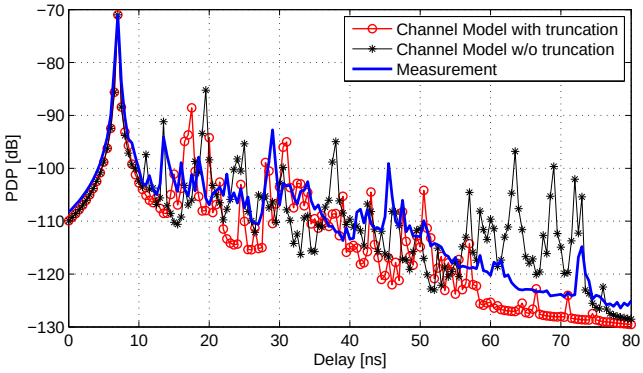

Figure 3: A measured PDP and single realizations based on the stochastic channel model in [6] with and without truncation.

with and without truncation, as well as the corresponding residuals, are shown in Fig. 4(a) for the LOS scenario and in Fig. 4(b) for the OLOS scenario.

First, we note that the Tx-Rx separations for the measured and modeled PDPs corresponds to delays of about 3 to 15 ns, and only 15 and 17 PDPs are available when calculating the APDP for the LOS and OLOS scenarios, respectively. As a result, this causes the uneven shape that is observed in the APDP for delays in the range from 0-15 ns.

In the LOS scenario, both models agree fairly well with the measured APDP. However, the model without truncation overestimates the APDP for longer delays, whereas the model with truncation seems to underestimate the APDP slightly for longer delays. For delays in the range of 0-15 ns, both models agree well with the measurement. This is explained by the fact that the LOS component is being modeled deterministically.

For the OLOS scenario, it can be noted that for delays smaller than 15 ns, the measured APDP is significantly smaller compared to the modeled APDP. This difference could be caused by the fact that only 15 PDPs are used to calculate the APDP for the OLOS measurement. The model with truncation agree quite well with the measurement for delays longer than 15 ns, whereas the model without truncation consistently overestimates the APDP for delays longer than 45 ns.

4.3 RMS Delay Spread

The above examples illustrated effects which suggests that the RMS-DS could be overestimated. In order to verify if this is the case, a large number of PDPs were generated in the same way as before, for several different Tx-Rx separations. Then, the RMS-DS was calculated based on each of these PDPs, $P_h(\tau)$ as

$$S_\tau = \sqrt{\frac{\sum_\tau P_h(\tau)\tau^2}{\sum_\tau P_h(\tau)} - \left(\frac{\sum_\tau P_h(\tau)\tau}{\sum_\tau P_h(\tau)}\right)^2}, \tag{13}$$

with τ being the delay. This was done for both the line-of-sight (LOS) and obstructed line-of-sight (OLOS) scenarios. The result is plotted as a CDFs of the RMS-DS for the channel model using estimates with and without truncation and also includes the measured RMS-DS.

The result is shown in Fig. 5(a) for the LOS scenario and in Fig. 5(b) for the OLOS scenario.

In the LOS scenario, the RMS-DS for the truncated regression model seems to agree quite well with the measured values, whereas the model without truncation seems to overestimate the RMS-DS. For the OLOS scenario, both models have much larger tails as compared to the CDF of the measured RMS-DS. However, given that only 15 samples are available for the measured RMS-DS in this case, it is difficult to tell whether the heavy tails are appropriate or not. Based on reported values of the RMS-DS for 60 GHz indoor channels in the literature [8], we argue that these tails for the CDFs are reasonable.

5 Conclusions

In this paper, we present a novel way of estimating the cluster decay and cluster fading, wherein the effects of the noise floor is taken into account. It has been shown that in cases where the SNR is limited and the variance of the cluster power is large in relation to the dynamic range of the samples, the effect of the noise floor can have a significant impact on the estimated cluster decay parameters, due to missing samples. This problem is solved by taking the missing information into account in the model through the use of a truncated normal distribution and by estimating the parameters based on a likelihood expression for this distribution. Numerical examples have been presented, including measurement based results for clusters in a wireless mm-Wave channel in a conference room environment. The results show that if

the noise floor is not taken into account, the RMS delay spread might be overestimated.

References

[1] R. C. Daniels, R. W. Heath, "60 GHz Wireless Communications: Emerging Requirements and Design Recommendations", *IEEE Veh. Tech. Mag.*, vol. 2, no. 3, pp. 41-50, Sep. 2007.

[2] IEEE802.15.3c-2009, Part 15.3: Wireless Medium Access Control (MAC) and Physical Layer (PHY) Specifications for High Rate Wireless Personal Area Networks (WPANs), Amendment 2: Millimeter-wave- based Alternative Physical Layer Extension, Oct. 2009.

[3] IEEE802.11ad draft, Part 11: Wireless LAN Medium Access Control (MAC) and Physical Layer (PHY) Specifications Amendment 3: Enhancements for Very High Throughput in the 60 GHz Band, Dec. 2011.

[4] A. A. M. Saleh, R. A. Valenzuela, "A statistical model for indoor multipath propagation", *IEEE Journal on Selected Areas of Communications*, SAC-5:128-13, Feb. 1987.

[5] A. Davydov, A. Maltsev, A. Sadri, "Saleh-Valenzuela Channel Model Parameters for Library Environment", doc.: IEEE 802.15-06-0302-02-003c, July 2006.

[6] C. Gustafson, K. Haneda, S. Wyne, F. Tufvesson, "On mm-Wave Multipath Clustering and Channel Modeling", *IEEE Transactions on Antennas and Propagation*, Submitted.

[7] Q. H. Spencer, B.D. Jeffs, M. A. Jensen, A. L. Swindlehurst, "Modeling the statistical time and angle of arrival characteristics of an indoor multipath channel," *IEEE Journal on Selected Areas in Communications*, vol.18, no.3, pp. 347-360, March 2000.

[8] S.-K. Yong, P. Xia, A. Valdes-Garcia, "60 GHz Technology for Gbps WLAN and WPAN: From Theory to Practice", *Wiley*, 2011.

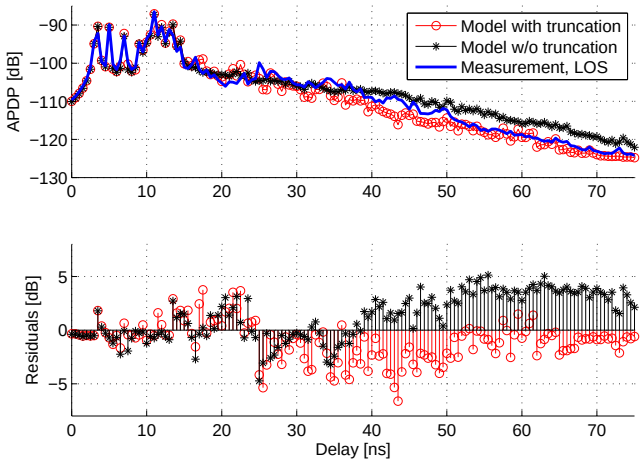

(a)

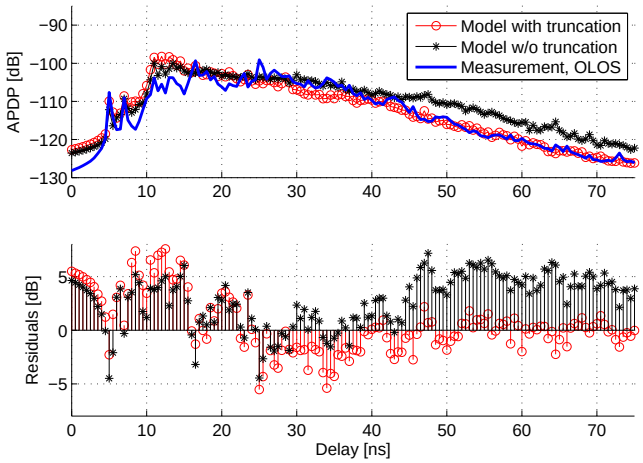

(b)

Figure 4: Average power delay profiles for the LOS (a) and OLOS (b) scenarios for the measurements and using the model with and without truncation. The residuals between the measurements and models are also shown, indicating that the model without truncation overestimates the APDP for longer delays.

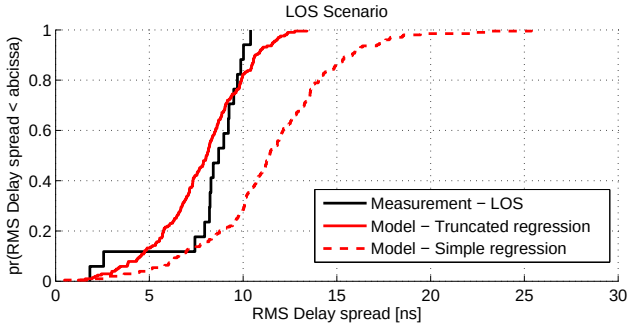

(a)

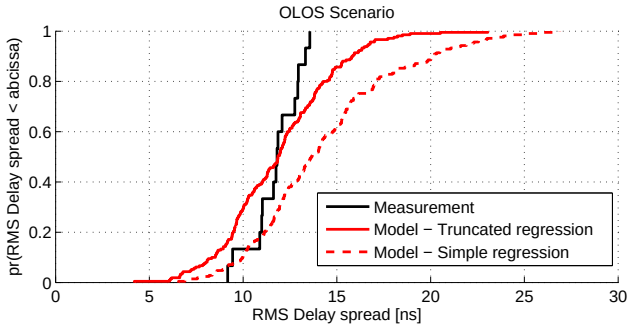

(b)

Figure 5: CDFs of the RMS delay spreads for measured data and using the channel model with cluster power parameters estimates based on the considered estimation techniques for the LOS (a) and OLOS (b) scenarios.

Paper V

60 GHz Spatial Radio Transmission: Multiplexing or Beamforming?

This paper compares the capacity improvement capability of spatial multiplexing and beamforming techniques for 60 GHz spatial transmissions in a multi-carrier radio system such as orthogonal frequency division multiplexing. The term beamforming in this paper refers to the conventional gain focusing, for the strongest propagation path, by narrow antenna beams. Our channel capacity metric depends only on the multipath richness of the propagation channel and the antenna aperture size, but is otherwise independent of the realization of antenna elements on the aperture. Our analysis also reveals the spatial degrees-of-freedom (SDoF) of the radio channel, which is the maximum number of antenna elements on the aperture for efficient spatial multiplexing. We evaluate the capacity and SDoF of single-polarized 60 GHz radio channels measured in a conference room environment. Our results show that the radio channel offers multiple SDoFs both in line-of-sight (LOS) and non-LOS (NLOS) scenarios such that spatial multiplexing can improve the channel capacity, provided that the receive signal-to-noise ratio (SNR) is sufficiently high to utilize them. Under -10 dBm of the transmit power, the high receive SNR is guaranteed when the antenna aperture size is larger than $1\lambda^2$ in LOS and $9\lambda^2$ in NLOS scenarios, respectively.

©2013 IEEE. Reprinted, with permission, from
K. Haneda, C. Gustafson and S. Wyne
"60 GHz Spatial Radio Transmission: Multiplexing or Beamforming?",
in *IEEE Transactions on Antennas and Propagation*, Vol. 61, No. 11, pp. 5735-5743, 2013.

1 Introduction

The millimeter-wave 60 GHz radio frequency band is considered to be one of the most promising candidates for short-range high-data-rate communications due to a wide bandwidth of several GHz available worldwide [1]. Recent standardization activities for 60 GHz radio technologies in wireless personal and local area networks have brought the technology into the practical domain [2, 3]. Another distinguished feature of 60 GHz radio systems, when compared with conventional short-range wireless systems operating at 2 and 5 GHz, is the capability of dense spatial communications because of the short wavelength of 5 mm. A physically small antenna aperture can be electrically large and hence is capable of steering high-gain narrow beams towards the strongest propagation path [4–6]. Since the propagation attenuation is fairly high in the 60 GHz band, enhancement of a signal-to-noise ratio (SNR) at the receive (Rx) side through beamforming is an important feature in the link design. Furthermore, because many antenna elements can be implemented on the small aperture, it is possible to increase the channel capacity significantly by spatial multiplexing if the Rx SNR is sufficiently high [7, 8]. In both spatial multiplexing and beamforming, interaction between the antennas and the propagation conditions determines the attainable performance of a radio link such as channel capacity. This paper provides insights on the attainable performance of such spatial transmission schemes by:

- Deriving the spatial degrees-of-freedom (SDoF) of 60 GHz radio channels, which are defined by the antenna aperture size and the propagation condition. The SDoF is the maximum number of antenna elements on the aperture for efficient spatial multiplexing [9];
- Evaluating channel capacity in the 60 GHz band for a multi-carrier radio system such as orthogonal frequency division multiplexing (OFDM), in such a way that the capacity depends only on the propagation condition and antenna aperture size but otherwise is independent of the realization of antenna elements on the aperture; and finally,
- Comparing spatial multiplexing and beamforming techniques in terms of their attainable channel capacity using measured 60 GHz radio channels.

The capacity gains that can be leveraged from spatial radio transmission depend on both the propagation conditions and the antenna configuration. In the literature several metrics such as the channel capacity, the number of dominant eigenchannels, and the eigenvalue dispersion have been used to gauge the capacity enhancement potential of multiple-input multiple-output (MIMO) antenna systems. However, when these metrics are evaluated with a specific

configuration of antenna arrays, applicability of the results is limited to the evaluated antenna configurations only. To obtain more generic estimates of capacity improvement that are applicable to various antenna geometries, we evaluate a channel capacity that depends on the propagation conditions and the antenna aperture size only, but is otherwise independent of the antenna geometry. The capacity evaluated in this manner is called the intrinsic channel capacity [10], which has been investigated in literature [11–15]. In the course of evaluating the channel capacity, we also discuss the maximum number of dominant eigenchannels for a given propagation condition and the transmit (Tx) and Rx antenna aperture size – termed the SDoF of the radio channel – that closely relates with the intrinsic capacity. The SDoF is a measure of the number of antenna elements on the aperture that can efficiently contribute to increasing the channel capacity via spatial multiplexing. The SDoF is also the spatial multiplexing gain in the high SNR regime [11]. The SDoF for multiple antenna channels has been studied for canonical channels [8, 13, 14, 16] and for measured radio channels [9, 17, 18]. The studies of the SDoF and the capacity for 60 GHz channels still require efforts based on measurements since the corresponding results at the lower frequency bands may not be applicable necessarily. For example, investigations of measured 60 GHz radio channels have shown much weaker diffraction effects than the lower frequency channels [19], which can influence the channel capacity and the SDoF. Therefore we address a difference of the SDoF estimates at 60 and 5 GHz. Throughout the paper, we assume an OFDM-type multi-carrier system as a framework for the capacity and SDoF evaluation, making it possible to analyze the channels and systems based on narrowband assumption and hence keeping the analysis simplified yet realistic. The analysis furthermore is under an assumption that we are free from transceiver imperfections such as limited dynamic range, non-linearity, noise figure, and implementation losses. Finally, we rule out antenna superdirectivity [8, 12] because it is an extremely narrowband characteristic and needs an extra analytical framework for proper evaluation even under the usual narrowband assumption of the channels and systems.

In the remainder of the paper, we first discuss about separation of radio and propagation channels in Section II. The discussion forms bases for the intrinsic channel capacity and the SDoF derived in Section III. Our 60 GHz radio channel measurements in an office room are introduced in Section IV. Finally, the SDoF estimates and the capacity are reported in Section V for various antenna aperture sizes, for different Tx-Rx distances, and for line-of-sight (LOS) and non-LOS (NLOS) scenarios. The results reveal that spatial multiplexing does work at 60 GHz both in LOS and NLOS scenarios because of the availability of multiple SDoFs, provided that the Rx SNR is sufficiently high to utilize them. Under -10 dBm of the Tx power, the high Rx SNR is

guaranteed when the antenna aperture size is larger than $1\lambda^2$ in LOS and $9\lambda^2$ in NLOS scenarios, respectively. Conclusions are given in Section VI.

2 The Radio Channel and Propagation Channel

For the purpose of deriving the intrinsic capacity and the SDoF, we first make a distinction between the radio channel and the propagation channel. The radio channel includes all effects of the antenna element and propagation channel, while the propagation channel itself is only influenced by the antenna aperture size but is otherwise independent of the antenna element on the aperture.

2.1 Overview

A narrowband MIMO radio system is expressed in an equivalent baseband form as

$$\boldsymbol{y} = \boldsymbol{H}\boldsymbol{x} + \boldsymbol{\xi}_{\mathrm{n}} \tag{1}$$

where $\boldsymbol{x}$ is an input signal vector to the Tx antenna ports, $\boldsymbol{H}$ is a transfer function matrix of a MIMO radio channel, $\boldsymbol{y}$ and $\boldsymbol{\xi}_{\mathrm{n}}$ are the output signal and the complex white Gaussian noise vectors at the Rx antenna ports, respectively. We assume that the antenna arrays can be enclosed by a minimum sphere with a radius r_0 on each side of the Tx and Rx. The radio channel includes the Tx and Rx antenna arrays as well as the propagation medium in-between, while the term propagation channel refers to a response of an electromagnetic field *after* being radiated from the Tx antenna and *until* captured by the Rx antenna. Therefore, the propagation channel response is determined solely by the boundary conditions of the radio propagation environment and material properties, *e.g.*, complex permittivity and conductivity, and not by the way the antenna radiates and receives the electromagnetic field. Analogous to the matrix representation of the MIMO radio channel $\boldsymbol{H}$, we will describe a matrix representation of the MIMO *propagation* channel using coupling coefficients of electromagnetic propagation modes between the Tx and Rx antenna apertures.

The separation of the radio and propagation channels is discussed in [20] using the so-called double-directional analysis of radio channels. Estimating directions of departure and arrival of plane waves at the Tx and Rx ends with known antenna radiation patterns allows de-embedding of the antenna properties and estimation of the propagation channel. The relationship between the radio and propagation channels is depicted in Fig. 1. An implicit assumption of the propagation channel estimates, which is derived from the double-directional analysis, is that they depend only on the size of the Tx and Rx antenna aperture sizes and that the characteristics of the individual antenna element are

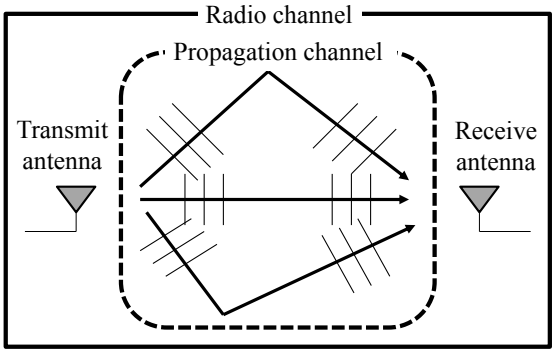

Figure 1: The propagation channel can be extracted from radio channel measurements using a double-directional analysis, subject to provision of appropriate models for radiation patterns of the Tx and Rx antennas.

de-embedded. This is because the antenna aperture size determines the angular resolution of the antenna beams and therefore sets the granularity of the propagation channel description.

2.2 Propagation Channel

The propagation channel can be expressed in different formats. We first discuss a plane wave expression of the channel as a reference, as they are widely used in popular multiple-antenna channel models such as the WINNER [21] and COST models [22]. We then describe a spherical wave expression of the channel which brings several advantages in analyzing the SDoF and the intrinsic channel capacity over the plane wave expression. We show that the plane and spherical wave expressions of the propagation channel are uniquely inter-related to each other.

The narrowband propagation channel is usually described by a set of plane waves as [20]

$$\mathrm{P_p} = \{\boldsymbol{\alpha}_l, \boldsymbol{\Gamma}_l, \boldsymbol{\Gamma}'_l\}_{l=1}^{L}\,, \tag{2}$$

where $\boldsymbol{\alpha} \in \mathbb{C}^{2\times 2}$ is a polarimetric complex amplitude, $\boldsymbol{\Gamma} = [\phi\ \theta]$ and $\boldsymbol{\Gamma}' = [\phi'\ \theta']$ are vectors composed of azimuth and polar angles of the radiation and reception on the Tx and Rx sides, respectively. The notation a_l means that a parameter value a for the l-th plane wave.

The plane wave expression of the propagation channel corresponds to the

one in the spherical wave domain as [23]

$$\mathrm{P_s} = \{R_{j'j}\}_{j=1,j'=1}^{\infty}, \tag{3}$$

where

$$R_{j'j} = \sum_{l=1}^{L} \boldsymbol{f}_{j'}^{H}(\boldsymbol{\Gamma}_l')\boldsymbol{\alpha}_l \boldsymbol{f}_j(\boldsymbol{\Gamma}_l), \tag{4}$$

$\boldsymbol{f}_j(\boldsymbol{\Gamma}) = [f_{\mathrm{V},smn}(\boldsymbol{\Gamma})\ f_{\mathrm{H},smn}(\boldsymbol{\Gamma})]^T$ denotes a far-field electric field intensity of the j-th spherical wavemode at the Tx, the subscripts V, H denote vertical and horizontal polarization respectively, and $\cdot^T$ denotes a transpose operation. The index j is related to the s, m, and n-th spherical wavesmodes as $j = 2\{n(n+1)+m-1\}+s$ [24], finally $(\cdot)^H$ denotes the Hermitian transpose. We stress that $\boldsymbol{f}$ is *not* an antenna radiation pattern, but are operators of the spherical Fourier transform to convert from the plane to the spherical wave domains. In this work the far-field is expressed in terms of the vertical and horizontal polarizations as,

$$f_{\mathrm{V},1mn}(\boldsymbol{\Gamma}) = k_{mn}(-\mathrm{j})^{n+1}\left(\frac{\mathrm{j}m\bar{P}_n^{|m|}(\cos\theta)}{\sin\theta}\right), \tag{5}$$

$$f_{\mathrm{H},1mn}(\boldsymbol{\Gamma}) = k_{mn}(-\mathrm{j})^{n+1}\left(-\frac{\mathrm{d}}{\mathrm{d}\theta}\bar{P}_n^{|m|}(\cos\theta)\right), \tag{6}$$

$$f_{\mathrm{V},2mn}(\boldsymbol{\Gamma}) = k_{mn}(-\mathrm{j})^{n}\left(\frac{\mathrm{d}}{\mathrm{d}\theta}\bar{P}_n^{|m|}(\cos\theta)\right), \tag{7}$$

$$f_{\mathrm{H},2mn}(\boldsymbol{\Gamma}) = k_{mn}(-\mathrm{j})^{n}\left(\frac{\mathrm{j}m\bar{P}_n^{|m|}(\cos\theta)}{\sin\theta}\right), \tag{8}$$

$$k_{mn} = \frac{2}{\sqrt{2n(n+1)}}\left(-\frac{m}{|m|}\right)^m e^{\mathrm{j}m\phi}, \tag{9}$$

where $\bar{P}_n^{|m|}(\cdot)$ is the normalized associated Legendre function with the order of m.

According to (3) and (4), the propagation channel is expressed by an infinite number of spherical waves, similar to the corresponding plane wave expression which requires a huge number of plane waves, *i.e.*, a very large L to model diffuse propagation phenomena [25]. It is noteworthy that the spherical waves can express the propagation channel by a matrix $\boldsymbol{R}$ having the coefficients $R_{j'j}$, while the plane wave expression needs to have both the angles and the complex amplitude of the multipath components to describe the propagation channel.

2.3 Radio Channel

An entry of the narrowband MIMO radio channel matrix $\boldsymbol{H}$ in (1), h, is expressed by the sum of L plane waves weighted by the Tx and Rx antenna patterns as

$$h = \sum_{l=1}^{L} \boldsymbol{a}'^{H}(\boldsymbol{\Gamma}_l')\boldsymbol{\alpha}_l \boldsymbol{a}(\boldsymbol{\Gamma}_l) \tag{10}$$

where $\boldsymbol{a}(\boldsymbol{\Gamma}) = \boldsymbol{g}(\boldsymbol{\Gamma}) \exp\{\mathrm{j}k_0\langle \boldsymbol{u}, \boldsymbol{d}\rangle\}$, the operation $\langle \boldsymbol{a}, \boldsymbol{b}\rangle$ denotes an inner product of vectors $\boldsymbol{a}$ and $\boldsymbol{b}$, $\boldsymbol{g}(\boldsymbol{\Gamma}) = [g_{\mathrm{V}}(\boldsymbol{\Gamma})\ g_{\mathrm{H}}(\boldsymbol{\Gamma})]^T$ is the far-field radiation pattern of the antenna element in the direction $\boldsymbol{\Gamma}$, $\boldsymbol{d}$ is the position vector of the antenna element, and finally,

$$\boldsymbol{u} = [\sin\theta\cos\phi \quad \sin\theta\sin\phi \quad \cos\theta]^T. \tag{11}$$

The same entry of the narrowband MIMO radio channel can also be expressed by $\boldsymbol{R}$ as [26]

$$h = \boldsymbol{q}'^{H}\boldsymbol{R}\boldsymbol{q} \tag{12}$$

where $\boldsymbol{q}$ and $\boldsymbol{q}'$ are spherical wave coefficients of the Tx and Rx antenna elements. They are related to the far-field antenna radiation pattern as

$$\boldsymbol{a}(\boldsymbol{\Gamma}) = \sum_{j=1}^{\infty} \boldsymbol{f}_j(\boldsymbol{\Gamma}) q_j \tag{13}$$

for all the possible directions $\boldsymbol{\Gamma}$.

3 Metrics for the Evaluation of Spatial Radio Transmission Performance

This section defines the SDoF and intrinsic channel capacity based on the propagation channel described in Section II. The SDoF and capacity of spatial multiplexing is derived from the propagation channel expressed in the spherical wave domain (3). In contrast, the capacity of beamforming is derived using the plane wave expression of the propagation channel (2). In both cases, we assume a multi-carrier radio system such as OFDM with each subcarrier showing flat fading characteristics.

3.1 The Spatial Degrees-of-Freedom

Given an antenna aperture size at the Tx and Rx and a propagation condition, the SDoF is the maximum number of eigenchannels for any radio channels

realized by antenna elements on the apertures under the propagation condition. The SDoF is determined by inherent multipath richness of the propagation channel and the antenna aperture size [13]. For a given multipath richness, larger SDoF can be observed using larger antennas on the Tx *and* Rx sides. Elaborating based on the plane wave expression of the radio channel (10), larger antennas can produce narrower beams in the angular domain and allow more non-overlapping pathways to illuminate the multipath propagation channel. An illustration in Fig. 2 helps understand the SDoF. The figure shows a multipath cluster distribution over an azimuth-polar angle plane. As the antenna aperture is larger, it is possible to create more orthogonal beams simultaneously within the multipath cluster distribution, namely, to increase the SDoF of the radio channel. The SDoF can also be explained by the spherical wave expressions in (12). The number of dominant spherical wavemodes is determined by the antenna aperture sizes at the Tx and Rx because of their mode truncation property [24]. A rule of thumb of the truncation is characterized in terms of the n-modes representing the polar angle characteristics as

$$N = \lfloor k_0 r_0 \rfloor + \epsilon, \tag{14}$$

where k_0 is a wavenumber in the free space, r_0 is a minimum radius enclosing the whole volume of the antenna, $\lfloor \cdot \rfloor$ is the floor function, and ϵ is an uncertainty factor taking values between 0 and 10 for practical antennas [24]. The underlying physics behind the truncation is that an electromagnetic field described by a mode higher than the order N attenuates rapidly as it radiates from an antenna and does not propagate over space. Only modes with smaller orders than N can propagate as a far-field over space and reach the Rx antenna. The attenuation of each mode is expressed by the spherical Hankel function of the first kind, which is illustrated in Fig. 2.4 of [24]. The truncation n-mode, *i.e.*, N in (14), is related to the total number of effective spherical waves as $J = 2N(N+2)$. Therefore, the dimension of propagation channel matrix, $\boldsymbol{R}$, is determined as $J' \times J$. This means the use of a larger antenna aperture leads to a larger dimension of $\boldsymbol{R}$. The SDoF of the radio channel is given by the rank of $\boldsymbol{R}$, and is an upper bound of the number of eigenchannels of any radio channels realized by antenna elements on the aperture [17], *i.e.*,

$$\mathrm{rank}(\boldsymbol{H}) \leq \mathrm{rank}(\boldsymbol{R}), \tag{15}$$

where the equality holds only if the antenna elements exploit the available multipaths in the propagation environment properly. Larger antenna apertures give more SDoF if propagation channel conditions are favorable.

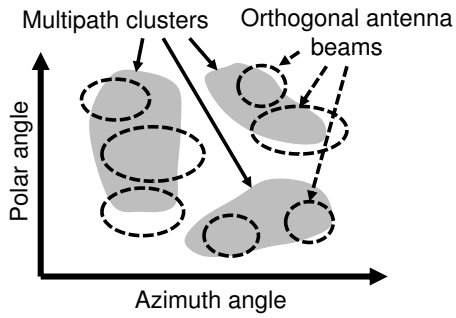

Figure 2: An illustration of the SDoF in a multipath propagation channel: the SDoF is the maximum number of orthogonal beams that an antenna array can create simultaneously within a multipath cluster distribution.

3.2 Channel Capacity

Spatial Multiplexing

We use the intrinsic channel capacity as a metric to discuss the implication of the SDoF for spatial multiplexing. The intrinsic channel capacity was proposed by Wallace and Jensen to define the channel capacity that can be realized by antenna apertures exploited in multipath propagation environments [10]. Similarly to the SDoF, the intrinsic channel capacity does not depend on the particular realization of antenna elements on the aperture, and can be derived by performing the waterfilling power allocation to the eigenchannels of the propagation channel matrix expressed in the spherical wave domain, $\boldsymbol{R}$. The dimension of $\boldsymbol{R}$ is determined by antenna aperture size at the Tx and Rx according to the mode truncation (14). Denoting the singular value decomposition (SVD) of the propagation channel matrix as $\boldsymbol{R} = \boldsymbol{U}\boldsymbol{\Sigma}\boldsymbol{V}^H$, the intrinsic channel capacity is given by

$$C_{\text{mux}} = B \log_2 \det \left(\boldsymbol{I}_D + \frac{\boldsymbol{\Sigma}\boldsymbol{S}\boldsymbol{\Sigma}}{\sigma^2} \right) \tag{16}$$

where B is the system bandwidth, σ^2 is noise variance at the Rx, $\boldsymbol{I}_D$ is a square identity matrix of dimension $D \leq \min(J', J)$, $\boldsymbol{S} = \text{diag}\,[s_1, \cdots, s_D]$ is a diagonal power allocation matrix at the Tx with entries of

$$s_i = \max \left(\mu - \frac{\sigma^2}{|\lambda_i|^2}, 0 \right), \tag{17}$$

where $|\lambda_i|$ is the i-th strongest singular value composing the diagonal matrix $\mathbf{\Sigma}$, and μ is determined such that $\sum_{i=1}^{D} s_i = P_\mathrm{t}$ is fulfilled, P_t is the total power input to the Tx antenna aperture. In the high SNR regime, the SDoF serves as the upper bound of the spatial multiplexing gain of any antenna systems implemented on the aperture. Similarly to the SDoF, improvement in capacity by spatial multiplexing becomes more prominent as a larger antenna aperture is installed at the Tx and Rx.

Beamforming

The capacity of conventional beamforming is compared with that of spatial multiplexing. The conventional beamforming in this paper refers to the use of the antenna beam directing the maximum gain to the strongest propagation path. Therefore we use the plane wave expression of the propagation channel (2). Since a spherical antenna volume is considered, its cross section forms a circular antenna aperture for any direction of the propagation path. The directivity of the circular antenna aperture on the x-y plane is given in the complex amplitude domain as [27]

$$g_\mathrm{d}(u_x, u_y) = \frac{2\pi r_0}{\lambda} \frac{J_1(2\pi u)}{\pi u}, \tag{18}$$

where $J_1(\cdot)$ is the Bessel function of the first kind, λ is wavelength in vacuum, and

$$u_x = \frac{r_0}{\lambda} \sin\theta \cos\phi, \quad u_y = \frac{r_0}{\lambda} \sin\theta \sin\phi, \tag{19}$$

and therefore

$$u = \sqrt{u_x^2 + u_y^2} = \frac{r_0}{\lambda} \sin\theta. \tag{20}$$

The directivity takes the maximum at $\theta = 0$ and does not depend on ϕ because the antenna aperture is symmetric with respect to the z-axis. When the strongest propagation path comes from a direction $\mathbf{\Gamma}_0 = [\theta_0, \phi_0]$, the directivity (18) is rotated so that the effective circular aperture size is the largest for the path. The directivity after rotation to the direction $\mathbf{\Gamma}_0$ is given by $g_\mathrm{d}(u_x - u_{x0}, u_y - u_{y0})$, where

$$u_{x0} = \frac{r_0}{\lambda} \sin\theta_0 \cos\phi_0, \quad u_{y0} = \frac{r_0}{\lambda} \sin\theta_0 \sin\phi_0. \tag{21}$$

The radio channel response after the beamforming is

$$h_\mathrm{bf} = \sum_{l=1}^{L} g'_\mathrm{d}(u'_{xl} - u'_{x0}, u'_{yl} - u'_{y0}) \alpha_l g_\mathrm{d}(u_{xl} - u_{x0}, u_{yl} - u_{y0}), \tag{22}$$

where α_l is a summation of complex amplitude entries in $\boldsymbol{\alpha}_l$. The channel capacity after beamforming therefore yields

$$C_{\mathrm{bf}} = B \log_2 \left(1 + \frac{P_{\mathrm{t}}}{\sigma^2} |h_{\mathrm{bf}}|^2 \right). \tag{23}$$

The capacity formula of beamforming (23) is different from that of spatial multiplexing (16). The difference comes from the ways the antenna aperture is excited. Beamforming maximizes the antenna gain for a single propagation path at the expense of no parallel transmission, while spatial multiplexing based on the SVD weight forms the maximum number of orthogonal modes for parallel transmission at the expense of reduced directional gain. When there is only a LOS and no multipath in the channel visible over the Rx noise level, the excited pattern of beamforming is equivalent to that of spatial multiplexing if a single-polarized transmission is considered. When other multipaths are visible over the noise or when multi-polarization transmission is taken into account, the excited pattern of beamforming is different from the ones of spatial multiplexing because of the difference in maximization strategy. This leads to the differences of attained channel capacity as detailed in Section V-B.

4 60 GHz MIMO Radio Channel Measurement and Modeling

4.1 Measurement Environments

MIMO radio channel measurements at 60 GHz band were performed in a meeting room of a modern office building. The room has dimensions of $6.8 \times 7.0 \times 2.5$ m^3. During the measurements the Rx array remained fixed at one location of the room, while a channel measurement was performed by placing the Tx array at one of 17 predefined positions located on table tops as shown in Fig. 3. There was a LOS between the Tx and Rx. In addition, NLOS scenarios were also measured except at two positions shown in Fig. 3. The measured NLOS scenarios were created by blocking the first Fresnel-zone of the LOS connection with a laptop screen. Most of the measurements were performed during nighttime when there were no other people in the building, and when measuring during the day the movement of people was prevented in the vicinity of the measurement area to maintain a time-static measurement environment.

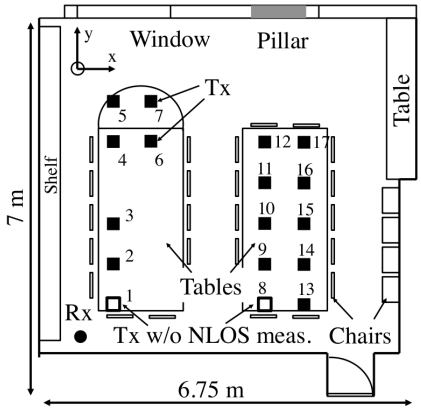

Figure 3: Floor plan of the 60 GHz MIMO radio channel measurements.

4.2 Measurement Equipment

Channel measurement equipment consists mainly of a vector network analyzer (VNA), frequency up/down converters, two electromechanical scanners installed on the Tx and Rx sides, and a control computer [28]. The channel transfer functions were measured by the VNA with a Tx power +7 dBm in a continuous wave mode and with a frequency range from 61 to 65 GHz. A virtual planar array was formed at the Tx on the horizontal plane using one of the 2-D electromechanical scanners. The Tx antenna element was a vertically polarized commercial biconical antenna with an omnidirectional pattern in azimuth. The virtual planar antenna array was also formed on the Rx side on the vertical plane using another 2-D scanner. A vertically polarized open waveguide having a unidirectional radiation pattern was used as the Rx antenna element. Heights of the Tx antenna and the center element of the Rx antenna array were both 1.1 m above the floor. With these Tx and Rx array settings, we model a practical case of data transmission from a DVD player or similar device, placed on the table, to a high-definition display device placed at the corner of the room. The aperture sizes of the 2-D virtual antenna arrays at the Tx and Rx are 12×12 mm^2, which can be enclosed by a sphere with a cross section of $9\lambda^2$ at 60 GHz. The measurement SNR was more than 40 dB for all the Tx-Rx combinations. Prior to measurements the equipment was back-to-back calibrated; the response of the VNA, frequency-converters, RF cables, connectors, and waveguides were then removed from the measured frequency responses in a post-processing step, before the analysis.

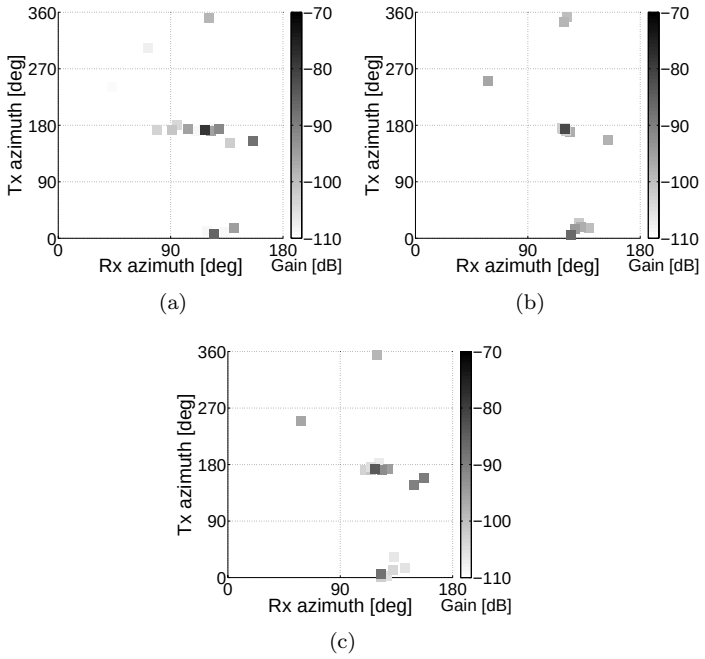

Figure 4: Power angular profile of estimated multipaths at Tx location 9 in a LOS condition with varying center frequencies: (a) 61, (b) 62, and (c) 63 GHz.

4.3 Plane Wave Estimation

Parameters of the multipath plane waves are estimated from the back-to-back calibrated channel transfer functions of the measurements using the SAGE algorithm [29]. The estimated parameters include the ones in (2), namely the azimuth and polar angles at the Tx and Rx and complex amplitude of each multipath. Propagation delays were also estimated, but we did not use them since the SDoF and the capacity in Section III was derived for a narrowband channel. The assumption is justifiable since we consider a multi-carrier radio system with subcarriers showing flat fading characteristics. We also assume that the multipath parameters do not change drastically over the measured frequency band from 61 to 65 GHz, because the relative bandwidth is at most 5 %. The assumption is reasonable according to Fig. 4 that exemplifies the similarity of power angular profiles of estimated multipaths in a LOS condition

for three radio frequencies centered at 61, 62, and 63 GHz with 300 MHz bandwidth. Plane wave parameters estimated at 62 GHz center frequency were used in the following SDoF and capacity evaluation. The amplitude estimates in (2) contain only single non-zero entry corresponding to the vertically transmitted and received component because the antennas used in the measurements were vertically polarized. Measured cross-polarization discrimination ratio (XPD) of the antennas revealed that only a small fraction of the estimated multipath components were located in directions where the antennas exhibit a low XPD. The parameter estimation involves radiation patterns of the Tx and Rx antennas to calibrate their effects on the estimated parameters. Therefore the parameters represent characteristics of the propagation channel seen from the Tx and Rx antenna aperture. The number of estimated multipaths was less than 50, and the multipaths were attributed to the LOS, specular reflections from a table, window frame and blind, wall, and scattering from ceiling lamps. Though the horizontal virtual antenna array at the Tx suffers from elevation ambiguity, it is possible to identify the multipaths from the ceiling and table uniquely at the Rx using the vertical virtual antenna array. Furthermore, delay estimates of each propagation path enables us to identify scatterers better in combination with angular estimates. The estimated propagation paths constituted more than 90 % of the total received power of the measurements. The remainder of the power can be attributed to radio propagation phenomena that did not fit the plane wave model and to noise. The magnitude of the LOS was 4 to 18 dB larger than that of other multipaths depending on the Tx-Rx distance. The longer distance tends to show less difference of the magnitude between the LOS and multipaths.

5 Results and Discussions

5.1 SDoF Estimates

The plane wave parameter estimates are converted to the spherical wave expression using (4), and then the rank of the propagation channel matrix $\boldsymbol{R}$ was derived. The dimension of $\boldsymbol{R}$ was determined by the antenna aperture size in (14) with $\epsilon = 0$. The Tx and Rx antenna aperture size is considered identical in this analysis, hence $\boldsymbol{R}$ is always a square matrix. Figure 5(a) shows eigenvalue distributions of the propagation channel $\boldsymbol{R}$ at Tx antenna location 4 for various antenna aperture size. Larger antenna aperture leads to more eigenvalues visible in the figure because of the increased capability of the antenna aperture to resolve multipaths in the angular domain. We define the rank estimates to be the number of eigenvalues exceeding $-t$ dB in magnitude

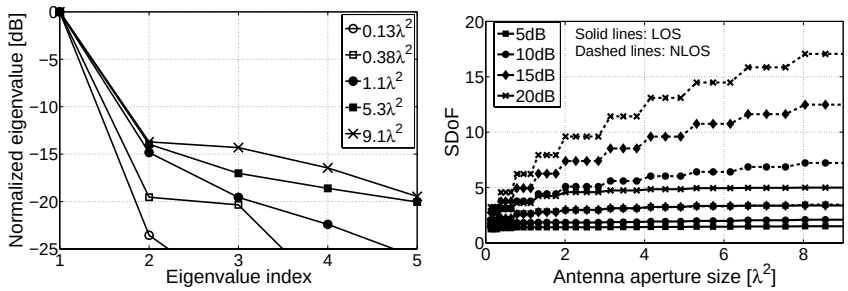

(a) (b)

Figure 5: (a) Normalized eigenvalue distribution of the propagation channel $\boldsymbol{R}$ at Tx location 4 for various antenna aperture sizes, (b) Relationship between the SDoF and the antenna aperture size at Tx location 4. The SDoF is plotted for different threshold levels, *i.e.*, $t = 5, 10, 15,$ and 20 dB. In (b), results from LOS and NLOS are overlaid.

relative to the strongest one, where $t = 5, 10, 15,$ and 20 are tested in the following analysis. The effect of small-scale fading is averaged out by taking the mean over the rank estimates from 100 small-scale realizations of $\boldsymbol{R}$. Different realizations of $\boldsymbol{R}$ were obtained by adding a random phase to the complex amplitude of the propagation paths $\boldsymbol{\alpha}$ [30].

Figure 5(b) shows the estimated DoF for increasing antenna aperture size at Tx location 4. For the LOS case, the SDoF saturates around the antenna aperture size of $2\lambda^2$, while the SDoF of the NLOS case does not show the saturation until the antenna aperture size of $9\lambda^2$ because of the presence of more multipaths. The step increase of the curves is attributed to the floor function of the spherical wavemode truncation due to antennas in (14).

Figure 6 illustrates the SDoF variation over Tx-Rx distances in LOS and NLOS scenarios. The Tx and Rx antenna aperture size was fixed at $9\lambda^2$. In the LOS scenario, the SDoF stays less than 2 in any Tx-Rx distance if the threshold level is 5 and 10 dB according to Fig. 6(a). The SDoF for 15 and 20 dB threshold indicate an increasing trend as the Tx-Rx distance is longer. The noticeable increase was observed for Tx-Rx distances beyond 2.5 m and the largest SDoF was 4.2 and 8.8 for 15 and 20 dB threshold levels, respectively. The SDoF in the NLOS scenario shows significantly different trend compared to the LOS scenario as shown in Figure 6(b). The SDoF is almost the same for any Tx-Rx distance. The SDoF with $t = 5$ shows similar level as in LOS scenarios, while the SDoF with other t indicated twice or three times larger

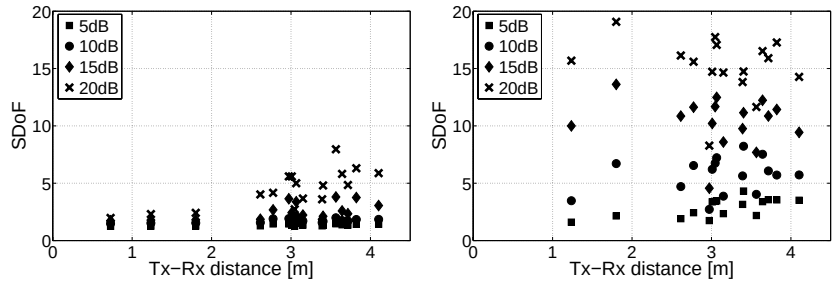

Figure 6: Distance dependence of the SDoF at the antenna aperture size of $9\lambda^2$. The SDoF is plotted for different threshold levels, *i.e.*, $t = 5, 10, 15$, and 20 dB. (a) LOS and (b) NLOS scenarios.

SDoF compared to the LOS scenarios.

The results reveal a possibility to obtain the spatial multiplexing gain using the eigenchannels. In the LOS scenario, since the second strongest eigenchannel is at least 10 dB weaker than the first according to Fig. 5(a), the Rx SNR needs to be more than 10 dB for effective spatial multiplexing. In the NLOS scenario, the second eigenchannel is at least 3 dB weaker than the first, so a larger spatial multiplexing gain is expected than in the LOS scenarios, provided that the Rx SNR high enough to utilize the eigenchannels corresponding to the second strongest eigenvalue and even weaker ones. When the SNR is high enough, at most 8 and 20 antennas are sufficient to perform effective spatial multiplexing in the considered LOS and NLOS scenarios, respectively. Even 5 and 13 antennas can work efficiently to capture eigenchannels down to -15 dB relative magnitude in the LOS and NLOS scenarios. It is worth recalling here that the radio channel measurement and modeling in this paper deals with only a single polarization. Exploiting multiple polarizations on the Tx and Rx sides will naturally lead to larger SDoF than the present analysis [31].

Finally, we provide some insights into the SDoF dependence on operating radio frequencies by referring to [18] which reports the SDoF of indoor *dual-polarized* multi-antenna radio channels at 5.3 GHz radio frequency. Since our measurements concern single-polarized channels, it is roughly possible to compare the SDoFs in [18] with those of the present paper by doubling them. In LOS scenarios, the SDoF at 60 GHz is less than half of that at 5 GHz for the same electrical antenna aperture size when a distance between the Tx and Rx is less than 2 m. This can be explained by the dominance of the LOS power

relative to other multipath components at 60 GHz. As the distance is longer, there is no clear difference of the SDoF between 5 and 60 GHz because they vary significantly depending on local scattering environments. Furthermore, the SDoF of NLOS channels at 60 GHz shows a comparable or even larger value than a multipath-rich LOS channel at 5 GHz for the same electrical antenna aperture size. These observations imply clear differences of multipath richness in 5 and 60 GHz channels, which in particular are the dominance of the LOS power and an angular distribution of multipaths. We must emphasize, however, that these insights are fairly general, and therefore, additional measurements and in-depth propagation analyses are essential to obtain more concrete insights.

5.2 Channel Capacity

Finally, the ergodic channel capacity is derived for spatial multiplexing and beamforming. Instantaneous capacity is defined in (16) for spatial multiplexing and (23) for beamforming. Taking the mean of the instantaneous capacity over various small-scale fading realizations of the channel gives the ergodic channel capacity. As in the derivation of the SDoF, adding the random phase to the complex amplitude of the propagation paths generated the small-scale realizations of the channel. The noise variance at the Rx is derived by $\sigma^2 = kTB \cdot 10^{\frac{NF}{10}}$ where k is the Boltzmann constant, T is the absolute temperature of the environment and NF is the noise figure of the Rx. Parameter values for the capacity calculation is summarized in Table 1. We show the intrinsic capacity for channels with different antenna aperture size at the Tx and Rx, and with different distances between the Tx and Rx. We assume that the Tx and Rx antenna aperture size is identical for the sake of simplicity of the analysis.

Table 1: Parameters for the channel capacity evaluation.

Parameter	Symbol	Value
System bandwidth	B	2 GHz
Tx power	P_{t}	-10 dBm
Temperature	T	293 K
Rx noise figure	NF	10 dB

Figure 7 shows the variation of the capacity over different antenna aperture size. The figures collect results from all the Tx-Rx combinations, and hence, contain multiple curves. Figure 7(a) illustrates the capacity of spatial multiplexing that increases as the aperture size is larger, as in the case of the SDoF.

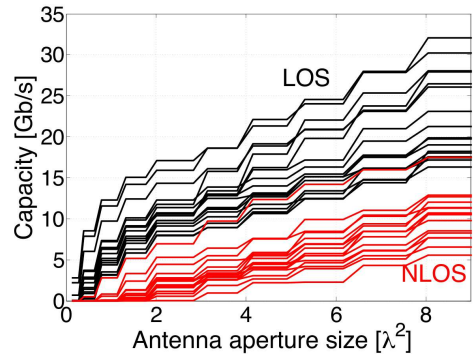

(a)

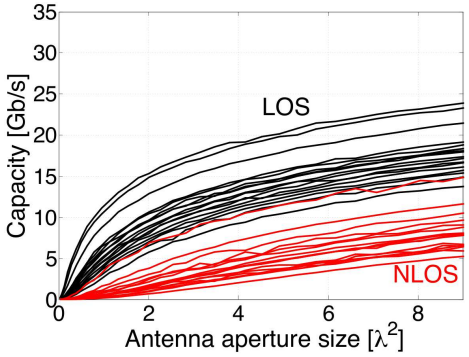

(b)

Figure 7: Ergodic channel capacity as a function of the antenna aperture size with (a) spatial multiplexing and (b) beamforming.

The slope of the capacity increase is 1.4 to 2.5 Gbps/λ^2 in LOS and 0.9 to 1.8 Gbps/λ^2 in NLOS scenarios, respectively. The slower increase in NLOS scenarios stems from the lower Rx SNR. Increasing the antenna aperture size also leads to higher capacity in the beamforming as shown in Fig. 7(b) because of the enhanced gain for the strongest propagation path. When antenna is larger than $2\lambda^2$, the capacity increases with 1.3 Gbps/λ^2 in LOS and 0.7 to 1.3 Gbps/λ^2 in NLOS scenarios, respectively, though the rate of capacity increase is not linear with respect to the antenna aperture size but is actually logarithmic.

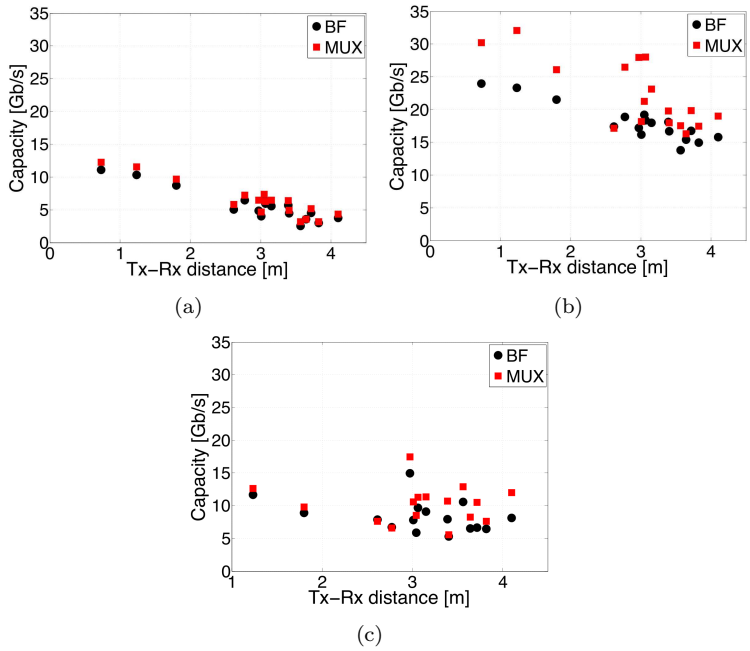

Figure 8: Comparison of the ergodic channel capacity for beamforming and spatial multiplexing. (a) LOS scenario with $1\lambda^2$ and (b) $9\lambda^2$ antenna aperture size and (c) NLOS scenario with antenna aperture size of $9\lambda^2$.

Figures 8(a) and 8(b) show the capacity for channels with different Tx-Rx distances in the LOS scenarios. Antenna aperture size of the Tx and Rx is $1\lambda^2$ for Fig. 8(a) and $9\lambda^2$ for 8(b). When the antenna aperture size is $1\lambda^2$, beamforming performs as robust as spatial multiplexing. As the antenna size becomes $9\lambda^2$, the capacity of spatial multiplexing is mostly higher than that of beamforming. The degree of capacity improvement by spatial multiplexing is more apparent when the Tx-Rx distance is shorter than 3 m because the Rx SNR is high enough to take advantage of the multiple SDoFs available above the noise level. Figure 8(c) illustrates the capacity for the NLOS scenarios with $9\lambda^2$ antenna aperture size. The capacity gain is found only when the Tx-Rx distance is longer than 3 m, implying lack of SDoF when the distance is shorter than 3 m. As a result, beamforming performs as good as spatial multiplexing until 3 m distance. It was also found that the capacity gain due to spatial multiplexing is remarkable only when the antenna aperture size becomes as large as $9\lambda^2$ to guarantee sufficiently high Rx SNR.

6 Conclusions

This paper used the SDoF and the intrinsic channel capacity as metrics to study the effectiveness of spatial multiplexing in 60 GHz radio systems based on the OFDM-type multi-carrier transmission. The results revealed that spatial multiplexing can work at 60 GHz even in the LOS scenarios. This is because of multiple SDoFs available in the radio channels, typically up to 5 and 13 in the LOS and NLOS scenarios, respectively, for the -15 dB threshold level relative to the strongest eigenchannel. Under the Tx power constraint of -10 dBm, spatial multiplexing is advantageous over beamforming when the antenna aperture size is larger than $1\lambda^2$ and $9\lambda^2$ in LOS and NLOS scenarios, respectively. When the link budget is limited due to electrically small antennas and long Tx-Rx distances, beamforming approximates the capacity of spatial multiplexing. Spatial multiplexing is a worthwhile option when the Rx SNR is favorable and a higher peak data rate is required.

A hybrid approach of beamforming and spatial multiplexing can be a sound compromise to take advantage of both techniques [8]. The present analysis considers only vertically polarized Tx and Rx antennas. As it is reported in various studies, the use of multiple polarizations improves the channel capacity significantly with spatial multiplexing, *e.g.*, [31]. Therefore, there is larger potential in spatial multiplexing to outperform beamforming when using antenna systems supporting multiple polarizations. However, we leave it as a subject of future investigations.

Acknowledgement

The authors would like to thank three anonymous reviewers for their valuable comments to improve the manuscript.

References

[1] R. C. Daniels and R. W. Heath, "60 GHz wireless communications: emerging requirements and design recommendations," *IEEE Veh. Tech. Mag.*, vol. 2, no. 3, pp. 41–50, Sep. 2007.

[2] IEEE802.15.3c-2009, Part 15.3: Wireless Medium Access Control (MAC) and Physical Layer (PHY) Specifications for High Rate Wireless Personal Area Networks (WPANs), Amendment 2: Millimeter-wave-based Alternative Physical Layer Extension, Oct. 2009.

[3] IEEE802.11ad draft, Part 11: Wireless LAN Medium Access Control (MAC) and Physical Layer (PHY) Specifications – Amendment 3: Enhancements for Very High Throughput in the 60 GHz Band, Dec. 2011.

[4] W. F. Moulder, W. Khalil, and J. L. Volakis, "60-GHz two-dimensionally scanning array employing wideband planar switched beam network," *IEEE Ant. Wireless Prop. Lett.*, vol. 9, pp. 818–821, 2010.

[5] X. An, C.-S. Sum, R. Prasad, J. Wang, Z. Lan, J. Wang, R. Hekmat, H. Harada, and I. Niemegeers, "Beam switching support to resolve link-blockage problem in 60 GHz WPANs," in *Proc. IEEE Int. Symp. Personal, Indoor Mobile Radio Commun. (PIMRC 2009)*, pp. 390–394, Tokyo, Japan, Sep. 2009.

[6] S. Wyne, K. Haneda, S. Ranvier, F. Tufvesson, and A.F. Molisch, "Beamforming effects on measured mm-wave channel characteristics," *IEEE Trans. Wireless Commun.*, vol. 10, no. 11, pp. 3553–3559, Nov. 2011.

[7] S. Ranvier, S. Geng, and P. Vainikainen, "Mm-wave MIMO systems for high data-rate mobile communications," in *Proc. Int. Conf. Wireless Commun., Veh. Tech., Inf. Theory, and Aerospace & Electronic Sys. Tech. (Wireless VITAE 2009)*, pp. 142–146, Helsinki, Finland, May 2009.

[8] E. Torkildson, U. Madhow, and M. Rodwell, "Indoor millimeter wave MIMO: Feasibility and performance," *IEEE Trans. Wireless Commun.*, vol. 10, no. 12, pp. 4150–4160, Dec. 2011.

[9] K. Haneda, A. Khatun, C. Gustafson, and S. Wyne, "Spatial degrees-of-freedom of 60 GHz multiple-antenna channels," in *Proc. 77th IEEE Veh. Tech. Conf. (VTC2013-Spring)*, Dresden, Germany, June 2013.

[10] J. W. Wallace and M. A. Jensen, "Intrinsic capacity of the MIMO wireless channel," in *Proc. Veh. Tech. Conf.*, vol., 2, pp. 701–705, Vancouver, BC, Canaday, Sep. 2002.

[11] A. Burr, "Capacity bounds and estimates for the finite scatterers MIMO wireless channel," *IEEE J. Sel. Areas Commun.*, vol. 21, no. 5, pp. 812–818, May 2003.

[12] M. L. Morris, M. A. Jensen, and J. W. Wallace, "Superdirectivity in MIMO systems," *IEEE Trans. Ant. Prop.*, vol. 53, no. 9, pp. 2850–2857, Sep. 2005.

[13] A. S. Y. Poon, D. N. C. Tse, and R. W. Broadersen, "Impact of scattering on the capacity, diversity, and propagation range of multiple-antenna channels," *IEEE Trans. Inf. Theory*, vol. 52, no. 3, pp. 1087–1100, Mar. 2006.

[14] M. D. Migliore, "On the role of the number of degrees of freedom of the field in MIMO channels," *IEEE Trans. Ant. Prop.*, vol. 54, no. 2, pp. 620–628, Feb. 2006.

[15] M. A. Jensen and J. W. Wallace, "Capacity of the continuous-space electromagnetic channel," *IEEE Trans. Ant. Prop.*, vol. 56, no. 2, pp. 524–531, Feb. 2008.

[16] A. S. Y. Poon, R. W. Brodersen, and D. N. C. Tse, "Degrees of freedom in multiple-antenna channels: a signal space approach," *IEEE Trans. Inf. Theory,* vol. 51, no. 2, pp. 523–536, Feb. 2005.

[17] K. Haneda, A. Khatun, M. Dashti, T. Laitinen, V.-M. Kolmonen, J. Takada, and P. Vainikainen, "Measurement-based evaluation of the spatial degrees-of-freedom in multipath propagation channels," *IEEE Trans. Ant. Propag.*, vol. 61, no. 2, pp. 890–900, Feb. 2013.

[18] K. Haneda, A. Khatun, V.-M. Kolmonen, and J. Salmi, "Dynamics of spatial degrees-of-freedom in MIMO mobile channels," *7th European Conf. Ant. Prop. (EuCAP 2013)*, Gothenburg, Sweden, pp. 2716–2720, Apr. 2013.

[19] M. Jacob, S. Priebe, R. Dickhoff, T. Kleine-Ostmann, T. Schrader, and T. Kurner, "Diffraction in mm and sub-mm wave indoor propagation channels," *IEEE Trans. Micro. Theory. Tech.*, vol. 60, no. 3, pt. 2, pp. 833–844, Mar. 2012.

[20] M. Steinbauer, A. F. Molisch, and E. Bonek, "The double-directional radio channel," *IEEE Ant. Prop. Mag.*, vol. 43, no. 4, pp. 51–63, Aug. 2001.

[21] P. Kyösti *et al.*, IST-WINNER D1.1.2 WINNER II channel models, https://www.ist-winner.org/WINNER2-Deliverables/D1.1.2v1.1.pdf.

[22] L. Liu, J. Poutanen, F. Quitin, K. Haneda, F. Tufvesson, P. D. Doncker, P. Vainikainen, and C. Oestges, "The COST2100 MIMO channel model," *IEEE Wireless Communications*, vol. 19, no. 6, pp. 92–99, Dec. 2012.

[23] A. A. Glazunov, M. Gustafsson, A. F. Molisch, F. Tufvesson, and G. Kristensson, "Spherical vector wave expansion of Gaussian electromagnetic

fields for antenna-channel interaction analysis," *IEEE Trans. Ant. Prop.*, vol. 57, no. 7, pp. 2055–2067, July 2009.

[24] J. E. Hansen, *Spherical near-field antenna measurement,* IEE Electromagnetic waves series 26, Peter Peregrinus, London, UK, 1998.

[25] N. Czink, F. Kaltenberger, Y. Zhou, L. Bernado, T. Zemen, and X. Yin, "Low-complexity geometry-based modeling of diffuse scattering," in *Proc. 4th European Conf. Ant. Prop.*, pp. 1–4, Barcelona, Spain, Apr. 2010.

[26] A. A. Glazunov, M. Gustafsson, A. F. Molisch, and F. Tufvesson, "Physical modeling of MIMO antennas and channel by means of the spherical vector wave expansion," *IET Microwaves, Antennas and Propagation*, vol. 3, no. 2, pp. 214–227, Mar. 2009.

[27] S. J. Orfanidis, Electromagnetic Waves & Antennas, Ch. 17, Radiation from Apertures. [Online] http://www.ece.rutgers.edu/ orfanidi/ewa/.

[28] S. Ranvier, M. Kyrö, K. Haneda, C. Icheln and P. Vainikainen, "VNA-based wideband 60 GHz MIMO channel sounder with 3D arrays," in *Proc. Radio Wireless Symp. 2009*, pp. 308-311, San Diego, CA, Jan. 2009.

[29] C. Gustafson, F. Tufvesson, S. Wyne, K. Haneda, and A. F. Molisch, "Directional analysis of measured 60 GHz indoor radio channels using SAGE," in *Proc. 73rd Veh. Tech. Conf. (VTC2011-Spring)*, Budapest, Hungary, May 2011.

[30] S. Takahashi and Y. Yamada, "Propagation-loss prediction using ray tracing with a random-phase technique, *IEICE Trans. Fundamentals*, vol. E81-A, no. 7, pp. 1445–1451, July 1998.

[31] P. Kyritsi, D. C. Cox, R. A. Valenzuela, and P. W. Wolniansky, "Effect of antenna polarization on he capacity of a multiple element system in an indoor environment," *IEEE J. Sel. Areas. Commun.*, vol. 20, no. 6, pp. 1227–1239, Aug. 2002.

Paper VI

A Note on Clustering Methods for Wireless Channel Models

A fundamental part of the estimation procedure for cluster-based wireless channel models is the clustering of data. The goal is usually to identify the number of clusters and their properties and then to use this information to model the channel. Often, some simple clustering method, such as the K-means algorithm, is used for this purpose. However, the clustering method uses certain assumptions about the data, which typically are different from the channel model assumptions, and is thus leading to a mismatch between the clustering model being used and the channel parameters being estimated. A more reasonable method is therefore to use the distributional assumptions of the channel model while clustering the data and estimating the parameters. In the paper, we present a clustering method based on asymmetric Laplace mixtures and compare this to clustering using the K-means algorithm and Gaussian mixtures. Power weighted versions of these methods are also derived and compared. The different methods are compared using directional data from 60 GHz indoor measurements in a conference room environment.

submitted to *IEEE Transactions on Wireless Communications*, Nov. 2014, as
C. Gustafson, D. Bolin, J. Wallin and F. Tufvesson,
"A Note on Clustering Methods for Wireless Channel Models",

1 Introduction

As the wireless propagation channel plays a fundamental role in the overall characteristics of any wireless communication system, it is necessary to have reliable channel models to support and enable the development of new wireless systems. Over the last decade, a popular approach has been to use double-directional [1], cluster-based channel models, such as geometry based stochastic channel models (GSCMs). In these models, the propagation channel is described in terms of the complex amplitudes, delays as well as departure and arrival angles of a number of clustered multi-path components (MPCs). The fact that the MPCs appear in clusters is quite significant, as this implies that cluster-based models can take the spatial and temporal correlation of the MPCs into account. It has been shown that statistical channel models that do not take the clustering into account tend to overestimate the channel capacity [2]. Furthermore, when using a double-directional channel model, the antenna patterns can be de-embedded from the measurement data, making it possible to develop a MIMO channel model that supports arbitrary antennas and array geometries. A couple of standardized wireless channel models that utilize the concept of clusters include the WINNER channel model [3], the COST 2100 model [4] and the 60 GHz channel models IEEE802.15.3c [5] and 802.11ad [6].

A fundamental part of the estimation procedure for cluster-based channel models is the clustering of data. The goal in the clustering process is to identify the number of clusters and their properties and then to use this information to model the channel. A multi-path cluster can loosely be defined as a group of MPCs having similar delays and angles of departure and arrival. However, there is no universally agreed-upon definition of a multi-path cluster, which means that the clustering results largely depend on how the clusters are identified or estimated. Initial work used visual inspection to identify clusters [7]. This approach has largely been abandoned in favor of automatic clustering algorithms such as K-means (or a power-weighted version of K-means), Fuzzy-c-means or hierarchial clustering [8].

Even though these methods typically are used only as algorithms for clustering the data, the methods make implicit assumptions regarding the distribution of the data. A well-known fact about the K-means algorithm is that it is equivalent to a clustering method based on a Gaussian mixture model (GMM) with restrictions on the covariance matrices for the Gaussian components. We will clarify the modeling assumptions that are made if the K-power-means algorithm is used by presenting a power-weighted GMM clustering method which has the K-power-means algorithm as a special case.

For both the GMM and the K-means clustering methods, one makes Gaussianity assumptions regarding the data, which might not be appropriate for

clustering of multi-path components. In fact, the clustering of the data is typically only used as a fist step in a larger model framework. For example, the K-means algorithm may be used to cluster the data, and given the clustered measurements, statistical models are estimated for the clusters. A popular channel modeling approach is to assume Laplace distributions for the intra-cluster-variations. From a statistical point of view, it would be more appropriate to use the correct intra-cluster models when clustering the data. Because of this, we present a Laplace-mixture model and a power-weighted version, which can be used for simultaneous clustering and estimation of the intra-cluster distributions.

The structure of the paper is as follows. Section 2 gives an introduction to the K-means algorithm, Hierarchical clustering methods and the GMM clustering method. This section also introduces power-weighted versions as well as the Laplace-based clustering method. Some issues and aspects of the different clustering methods are highlighted in Section 4. The different methods are compared using measured data in Section 6, and Section 7 finally contains a discussion of the results and suggestions for further topics of research.

2 Clustering algorithms

A cluster is typically defined as a group of multi-path components having similar delays and directions of departure and arrival.

The vector $\{\tau, \theta_d, \varphi_d, \theta_a, \varphi_a\}$ consisting of the delay, departure angles, and arrival angles for a multi-path component is in the space $\mathbb{R} \times \mathbb{S} \times \mathbb{S}$, which is somewhat difficult to work with due to the spherical topology. Therefore, it is common to make a change of variables from spherical coordinates to cartesian coordinates for the angles, i.e.,

$$\{x_\star, y_\star, z_\star\} = \{\sin(\theta_\star)\cos(\varphi_\star), \sin(\theta_\star)\sin(\varphi_\star), \cos(\theta_\star)\}$$

where now $\{x_a, y_a, z_a\} \in \mathbb{R}^3$ and $\{x_d, y_d, z_d\} \in \mathbb{R}^3$. Let

$$\mathbf{Y} = \{\tau_d, x_a, y_a, z_a, x_d, y_d, z_d\}$$

be the vector of the multi-path components in $\mathbb{R}^+ \times \mathbb{R}^3 \times \mathbb{R}^3$ and note that measuring distances in this space corresponds to the Multi-path component distance proposed by [9]. Here, τ_d is a scaled version of the delay.

2.1 Hierarchical Clustering

Several different hierarchical clustering algorithms exist in the literature. In this paper we consider a hierarchical clustering algorithm based on the bottom-up approach that clusters n multi-path components (MPCs), $\mathbf{Y}_1, \ldots, \mathbf{Y}_n$. In

this algorithm, the pairwise distances between each MPC pairs are first calculated using the euclidean distance metric, i.e.,

- $\forall i, j \in [1, n]$, $i \neq j$, let $d_{i,j} = \|\mathbf{Y}_i - \mathbf{Y}_j\|$.

In this paper, the euclidean distance is used as a distance metric, but it is also possible to use other metrics. Starting with n single MPC clusters, $n-1$ new clusters are formed by grouping MPCs together based on the shortest centroid distance. This procedure is then repeated for a decreasing number of clusters until all MPCs form one single cluster. This way, clustering results for $K = 1, 2, 3, \ldots, n$ number of clusters are being calculated using this method. In this work, the hierarchical clustering method is used to calculate initial clustering estimates for the other clustering methods presented here. This way, the same initialization is used for the different methods.

2.2 K-means Clustering

The most popular method for clustering multi-path components is the K-means algorithm. Assuming that we have n components $\mathbf{Y}_1, \ldots, \mathbf{Y}_n$ that should be clustered and by letting x_i denote the class belonging of the ith component, the K-means algorithm clusters the data by first assigning a mean μ_k to each class and then iterating the following two steps until convergence:

- $\forall i \in [1, n]$, let $x_i = \arg\min_k \|\mathbf{Y}_i - \mu_k\|$.
- $\forall k \in [1, K]$, let $\mu_k = \frac{1}{\sum_{i=1}^{n} \mathbb{I}(x_i = k)} \sum_{i=1}^{n} \mathbb{I}(x_i = k)\mathbf{Y}_i$,

where $\mathbb{I}(x_i = k) = 1$ if $x_i = k$ and 0 otherwise.

2.3 Gaussian Mixture-Model Clustering

It is well-known that the method above is a special case of the Gaussian mixture model (GMM) clustering method. In the GMM clustering method, the data is assumed to follow a GMM of the form

$$\mathbf{Y}_i = \sum_{k=1}^{K} w_{ik}\pi(\mathbf{Y}_i|\theta_k). \tag{1}$$

Here K is the number of clusters, $w_{ik} = \mathrm{P}(x_i = k)$ are prior probabilities for the multi-path component i belonging to class k, and $\pi(\mathbf{Y}_i|\theta_k)$ denotes a Gaussian density function with parameter mean, μ_k and, covariance matrix, Σ_k (note that $\theta_k = \{\mu_k, \Sigma_k\}$). This model can be estimated using the EM algorithm [10], where the following steps are iterated until convergence:

- $\forall i \in [1, n]$ and $k \in [1, K]$, set

$$\pi_{ik} = \frac{w_k \pi(\mathbf{Y}_i|\theta_k)}{\sum_{k=1}^{K} w_k \pi(\mathbf{Y}_i|\theta_k)}.$$

- $\forall k \in [1, K]$, let $\pi_k = \sum_{i=1}^{n} \pi_{ik}$ and set $w_k = \pi_k/n$ and

$$\mu_k = \frac{1}{\pi_k} \sum_{i=1}^{n} \mathbf{Y}_i \pi_{ik},$$
$$\Sigma_k = \frac{1}{\pi_k} \sum_{i=1}^{n} \pi_{ik} (\mathbf{Y}_i - \mu_k)(\mathbf{Y}_i - \mu_k)^{\mathrm{T}}.$$

Once convergence is reached, a clustering is obtained by selecting $x_i = \arg\max_k \pi_{ik}$. Note that the K-means clustering is obtained if we restrict $\Sigma_k = \sigma^2 I$ and let $\sigma^2 \to 0$.

2.4 Power-weighted clustering

A popular modification to the K-means method for clustering of multi-path components is the K-power-means method [11]. The idea behind the method is that observations with small power should affect the clustering less than observations with large power. Because of this, the K-power-means method replaces the updating step of the cluster centers with the power-weighted version

$$\mu_k^{(j+1)} = \frac{\sum_{i=1}^{N} p_i \mathbb{I}(x_i = k) \mathbf{Y}_i}{\sum_{i=1}^{N} p_i \mathbb{I}(x_i = k)}, \tag{2}$$

where p_i is the observed power of observation i.

Since the K-means and GMM clustering methods assume Gaussian mixture models for the data, it is of interest to find what model is assumed if the power-weighted version is used. The natural power-weighted extension of the GMM clustering method is to consider a model

$$\pi(\mathbf{Y}_i; \theta) = \sum_{k=1}^{K} w_{ik} \pi(\mathbf{Y}_i|\theta_k)^{p_i}, \tag{3}$$

where p_i is the measured power of the observation $\mathbf{Y}_i$ and $\pi(\mathbf{Y}_i|\theta_k)^{p_i}$ is renormalized so that it is a density.

Writing down the augmented likelihood and performing the usual steps of the EM algorithm, the EM estimator of the parameters is obtained by iterating the following steps until convergence:

- $\forall i \in [1, n]$ and $k \in [1, K]$, set

$$\pi_{ik} = \frac{w_k \pi(\mathbf{Y}_i|\theta_k)^{p_i}}{\sum_{k=1}^{K} w_k \pi(\mathbf{Y}_i|\theta_k)^{p_i}}. \tag{4}$$

- $\forall k \in [1, K]$, let $\pi_k = \sum_{i=1}^{n} p_i \pi_{ik}$, set $w_k = \sum_{i=1}^{n} \pi_{ik}/n$ and

$$\begin{aligned} \mu_k^{(j+1)} &= \frac{1}{\pi_k} \sum_{i=1}^{N} p_i \pi_{ik} \mathbf{Y}_i, \\ \mathbf{\Sigma}_k^{(j+1)} &= \frac{1}{\pi_k} \sum_{i=1}^{N} p_i \pi_{ik} (\mathbf{Y}_i - \mu_k^{(j+1)})(\mathbf{Y}_i - \mu_k^{(j+1)})^{\mathrm{T}}. \end{aligned} \tag{5}$$

An equivalent formulation of the model (3) when the mixture distributions are Gaussian is to use the model

$$\mathbf{Y}_i = \sum_{k=1}^{K} w_{ik} \mathrm{N}\,(\mathbf{Y}_i; \mu_k, p_i^{-1} \Sigma_k). \tag{6}$$

That is, we scale the covariance matrix for observation i by the power p_i. The K-power-means algorithm is a special case of this method if we restrict $\Sigma_k = \sigma^2 I$ and let $\sigma^2 \to 0$. We can also imagine restricting Σ_k to be diagonal, which may be reasonable for channel models since it allows us to capture different variances of the different multi-path components while keeping the number of parameters at a manageable level. We will compare these different models in Section 6.

The formulation (6) gives us some insights into what modeling assumptions that are made if the K-power-means or the power weighted GMM clustering method is used. In essence, we allow for greater variability of observations with low power. Allowing the observations with greater power to influence the parameter estimates more than those with low power may be a good idea, but from a physical point of view it may be difficult to motivate this modeling assumption.

Another point that should be made is that there does not seem to be any physical motivation behind why the K-power-mean algorithm should scale the measurements by the power in linear scale. One could imagine scaling the covariance matrix by any function of the power, $f(p_i)$, such as the logarithm. An interesting question is if we from data can estimate the function f and thereby determine the optimal choice of the power scaling, or if the function f should, somehow, be decided a priori based on physical principles. This is however outside the scope of this work.

3 Laplace-based Clustering

In practice, clustered multi-path components are often observed to be non-Gaussian with asymmetric and heavy-tailed distributions. In the case when an observation in a cluster is assumed to be a vector of independent random variables (corresponds in the Gaussian case to assume Σ to be diagonal) a natural alternative to the Gaussian distribution is the Asymmetric Laplace (AL) distribution. Previously, symmetric Laplace distributions were used for some channel model parameters [12].

The density for AL is given by (see [13])

$$f(x;\mu,\delta,\sigma) = \frac{1}{\sqrt{2\sigma^2+\mu^2}} e^{-\sqrt{\frac{2}{\sigma^2}+\frac{\mu^2}{\sigma^4}}|x-\delta|+\frac{\mu}{\sigma^2}(x-\delta)},$$

where μ defines the asymmetry, δ the mode and σ^2 the scale of the distribution. An important property of the Laplace distribution, that is used in the EM-algorithm below, is that it is a normal mean-variance mixture. That is, if Y is an AL random variable then

$$Y = \delta + \mu V + \sigma\sqrt{V}Z, \tag{7}$$

where equality is in distribution, V is standard exponential random variable and $Z \sim N(0,1)$.

By the independence assumption, equation (3) can be written as

$$\pi(\mathbf{Y}_i|\theta_k) = \prod_{j=1}^{m} f(Y_{i,j};\mu_{j,k},\delta_{j,k},\sigma_{j,k})^{p_i}, \tag{8}$$

or equivalently

$$\pi(\mathbf{Y}_i|\theta_k) = \prod_{j=1}^{m} f(Y_{i,j};p_i^{-1}\mu_{j,k},\delta_{j,k},\sigma_{j,k}p_i^{-1}), \tag{9}$$

where m is the number of dimensions.

We will now present the power-weighted Laplace clustering method. It should be noted that the ordinary (non-power-weighted) Laplace clustering method is obtained as the special case when assuming $p_i \equiv 1$. The method is, as in the Gaussian case, based on the EM-algorithm, and is derived in the appendix.

The EM estimator of the AL parameters is obtained by iterating the following steps until convergence:

- $\forall i \in [1,n]$ and $k \in [1,K]$, set

$$\pi_{ik} = \frac{w_k \pi(\mathbf{Y}_i|\theta_k)^{p_i}}{\sum_{k=1}^{K} w_k \pi(\mathbf{Y}_i|\theta_k)^{p_i}},$$

- $\forall k \in [1,K]$ and $\forall j \in [1,m]$ compute $H_{k,j} = \sum_{i=1}^{n} p_i^2 e_{i,1} \pi_{i,k} y_{i,j}^2$ and

$$\begin{aligned} \mathbf{Q}_{k,j} &= \begin{Bmatrix} \sum_{i=1}^{n} p_i^2 e_{i,k,1} \pi_{i,k} & \sum_{i=1}^{n} p_i \pi_{i,k} \\ \sum_{i=1}^{n} p_i \pi_{i,k} & \sum_{i=1}^{n} e_{i,k,2} \pi_{i,k} \end{Bmatrix}, \\ \mathbf{b}_{k,j} &= \begin{Bmatrix} \sum_{i=1}^{n} p_i^2 e_{i,k,1} \pi_{i,k} y_{i,j} \\ \sum_{i=1}^{n} p_i \pi_{i,k} y_{i,j} \end{Bmatrix}, \end{aligned}$$

  where

$$e_{i,k,1} = \frac{p_i |y_i - \delta_k|}{\sqrt{\frac{\mu_k^2}{\sigma_k^2} + 2\sigma_k^2}},$$

$$e_{i,k,2} = \frac{|y_i - \delta_k| \sqrt{\frac{\mu_k^2}{\sigma_k^2} + 2\sigma_k^2} + \frac{\sigma_k^2}{p_i}}{p_i (y_i - \delta_k)^2}.$$

- $\forall k \in [1,K]$ set $w_k = \frac{1}{n} \sum_{i=1}^{n} \pi_{ik}$. Furthermore $\forall j \in [1,m]$, set

$$\begin{Bmatrix} \delta_{j,k} \\ \mu_{j,k} \end{Bmatrix} = \mathbf{Q}_{k,j}^{-1} \mathbf{b}_{k,j},$$

$$\sigma_{k,j} = \frac{1}{\sum_{i=1}^{n} \pi_{i,k}} \left(H_{k,j} - \mathbf{b}_{k,j}^{\mathrm{T}} \begin{Bmatrix} \delta_{j,k} \\ \mu_{j,k} \end{Bmatrix} \right).$$

4 Benefits of using mixture models

There are several notable differences between the K-means algorithm, the hierarchical methods, and the model-based methods, some of which we highlight in this section.

Overlapping clusters and uncertain components: Both K-means and hierarchical clustering methods assigns hard decisions to the multi-path components, meaning that each component is assigned to a certain cluster with a probability of 1. Furthermore, these methods have no built in way of dealing with clusters that are partly overlapping. As a result, these methods are more likely to be affected by outliers and are expected to perform poorly in cases with overlapping clusters. To overcome these problems, ad hoc methods of removing outliers, such as the cluster pruning in [11], are sometimes applied in an effort to reduce the number of possible outliers and to try to achieve a clustering with well separated clusters. However, the cluster pruning affects the result of the estimated parameters and furthermore lowers the number of samples available for the estimation of the remaining channel model parameters. In contrast to this, clustering methods based upon mixture models have an inherent way of dealing with overlapping clusters by estimating the *mixture* of clusters. Furthermore, the components are weighted according to their probability of belonging to a certain cluster, which makes these methods less sensitive to uncertain components or outliers.

Uneven cluster shapes: The K-means algorithm treats each data dimension equally and it is implicitly assumed that the cluster spreads in the different dimensions are the same (or at least similar), which means that the K-means algorithm tries to achieve a clustering with hyper-spherical clusters. Due to this, K-means is expected to perform poorly for clusters with an uneven shape, *e.g.* when the cluster spreads in the different dimensions are dissimilar. Clustering methods based on mixtures do not suffer from these issues, since the variances for the different dimensions are estimated in the clustering procedure. For the GMM, an unconstrained covariance matrix would in principle allow for arbitrary cluster shapes. However, from a practical point of view, it seems reasonable to restrict the covariance matrix Σ to be diagonal. This simplifies the channel modeling and more importantly, keeps the number of parameters to be estimated at a reasonable level while still maintaining the ability to capture clusters with different spreads (*i.e.* variances) in the different dimensions.

Scaling of the delay dimension: Since K-means treats each data dimension equally, the data for the delay domain, with units typically in ns, needs to be appropriately scaled. In [11], a scaling of the delay is introduced, which also includes an ad hoc factor, ξ, which can be adjusted to give the delay domain more or less significance. The value of ξ is arbitrary, but is usually somewhere

between 1 and 25. Different values of ξ will yield distinctly different clustering results and no physical motivation seems to exist for the exact value of ξ. This problem is also present in hierarchical clustering algorithms, since the clustering of the data is based solely on a distance measure. For mixture models, this problem is not an issue, since the variances of the different dimensions are allowed to be different. We note that it is still advisable to scale the data for the delay domain by an appropriate factor in order to avoid numerical problems. As long as numerical problems are avoided, the clustering results will be similar even if different scaling factors are used.

Different assumptions in the clustering and channel modeling: Finally, the different assumptions made by *any* type of clustering algorithm will influence the result. Usually, these assumptions are quite different from the ones made in the channel modeling. When using a mixture model, it is possible to jointly cluster MPCs *and* estimate some of the MPC parameters. When using K-means, all MPC parameters must be estimated in a subsequent step after the clustering has been achieved.

Issues associated with power-weighted clustering: The concept of power weighted clustering suffers from a few isuess. As mentioned previously, there seems to be no physical motivation behind the exact function that scales the data with respect to power and different scaling functions will yield different results. This is due to the fact that the power weighting allows observations with greater power to influence the parameter estimates more than those with lower power. However, in previous work where the K-power-means algorithm is used, the power weighting is *not* taken into account when estimating the parameters based on the residuals from the K-power-means algorithm. This is not ideal from a modeling point of view, since the estimated parameters could be considered to depend on the power when this kind of power weighting is used. This issue is further complicated by the fact that there exists a physical dependence of the power and delay, which makes it difficult to take the power-dependence due to the power weighting of the estimated cluster parameters into account. Lastly, when applying power-weights, the effective sample size is reduced, which might be a problem when the data is based on a limited number of measurement scenarios.

5 Clustering using synthetic data

In this section, we compare the different presented clustering methods by using synthetic data with Gaussian and Asymmetric Laplace-distributed clusters, with known parameters for the distributions, in an effort to demonstrate the benefits of using clustering methods based on mixtures.

5.1 Gaussian-distributed clusters

We first consider 10 different scenarios with 6 clusters each, with random cluster centroids. Each clusters consists of 20 components that are normally distributed in five different dimensions, with a mean equal to the associated cluster centroid. In Table 1, the estimated standard deviations for the data based on the mixture estimated by the GMM, as well as based on a ML-estimate for the residuals from the GMM and the K-means algorithm. This shows that the parameters estimated based on the mixture are close to the true values. The parameters based on the ML-estimate for the residual from the GMM are slightly worse compared to the parameters estimated in the mixture. This illustrates one of the benefits of using mixture-based clustering methods, as the parameters of the mixture are jointly clustered and estimated. On the other hand, the K-means algorithm tends to overestimate the standard deviations, which is due to the issues discussed above.

Table 1: Estimated parameters of the standard deviation, σ, for the Gaussian distribution, for synthetic data in five dimensions.

	True	GMM mixture	GMM residual	K-means residual
	σ	$\hat{\sigma}$	$\hat{\sigma}$	$\hat{\sigma}$
d_1	0.20	0.22	0.24	0.26
d_2	0.50	0.50	0.52	0.56
d_3	0.20	0.20	0.21	0.24
d_4	0.50	0.50	0.53	0.51
d_5	0.20	0.21	0.23	0.36

5.2 AL-distributed clusters

Now, we we consider the same number of scenarios, clusters and components, but generate synthetic clusters that are AL-distributed. The data has different known parameters for the asymmetry, μ, and the standard deviation σ. This data is clustered based on the AL mixture, the GMM and the K-means algorithm. When basing the results upon the residuals, a maximum-likelihood estimator based on the AL probability density function is used to estimate the parameters. Table 2 shows the estimated standard deviation $\hat{\sigma}$, based on these different methods.

The estimates for the standard deviation based directly on the estimated AL mixture and based on the AL residuals are quite close to the true values. However, the parameters are being overestimated when basing the results on

Table 2: Estimated parameters of the standard deviation, σ, for the AL-distribution, for synthetic data in five dimensions.

	True	AL mixture	AL residual	GMM residual	K-means residual
	σ	$\hat{\sigma}$	$\hat{\sigma}$	$\hat{\sigma}$	$\hat{\sigma}$
d_1	0.40	0.40	0.41	0.45	0.45
d_2	0.30	0.33	0.34	0.36	0.40
d_3	0.25	0.24	0.25	0.31	0.40
d_4	0.20	0.23	0.23	0.27	0.32
d_5	0.20	0.19	0.20	0.28	0.30

Table 3: Estimated parameters of the asymmetry, μ, for the AL distribution, for synthetic data in five dimensions.

	True	AL mixture	AL residual	GMM residual	K-means residual
	μ	$\hat{\mu}$	$\hat{\mu}$	$\hat{\mu}$	$\hat{\mu}$
d_1	0.3	0.30	0.30	0.22	0.22
d_2	0	0.02	0.02	0.02	0.00
d_3	0.2	0.22	0.22	0.17	0.15
d_4	0	0.06	0.06	0.00	0.00
d_5	0.1	0.18	0.19	0.07	0.07

the residuals from the GMM or K-means algorithm. As expected, the K-means algorithm has the poorest performance of the different methods. Table 3 shows the asymmetry parameter estimates, $\hat{\mu}$. The results based on the AL mixture and AL residuals are quite close to the true values, except for dimension d_5, where the asymmetry is being overestimated. For the results based on the GMM and the K-means algorithm, the asymmetry is being underestimated, which is due to the inherent assumptions made in these methods.

6 Clustering using measured data

The clustering methods discussed in this paper have been applied to measured data at 62 GHz in a conference room environment. The angular-delay properties of the data, as well as the power, were previously estimated using the SAGE algorithm [12]. For the mixture models, we assume that an observation of a cluster forms a vector of independent random variables. In the Gaussian case, this corresponds to assume that the covariance matrix Σ is diagonal. This

assumption is necessary to keep the number of parameters to be estimated at a manageable level. Furthermore, in this paper, it is assumed that, except for the mean of the GMM, $\boldsymbol{\mu}_k$, and the mode, δ, for the AL distribution, the cluster parameters are the same for each cluster. Lastly, for all of these clustering algorithms, the number of clusters is not identified automatically. In previous work, the number of clusters was typically identified using some sort of cluster validation index. For this work, we assume that the number of clusters is known for each scenario. The number of clusters are based on the previous results in [12], where the clustering was performed using K-means and the number clusters was identified using the Kim-Parks index. The number of clusters ranged from 6 to 12.

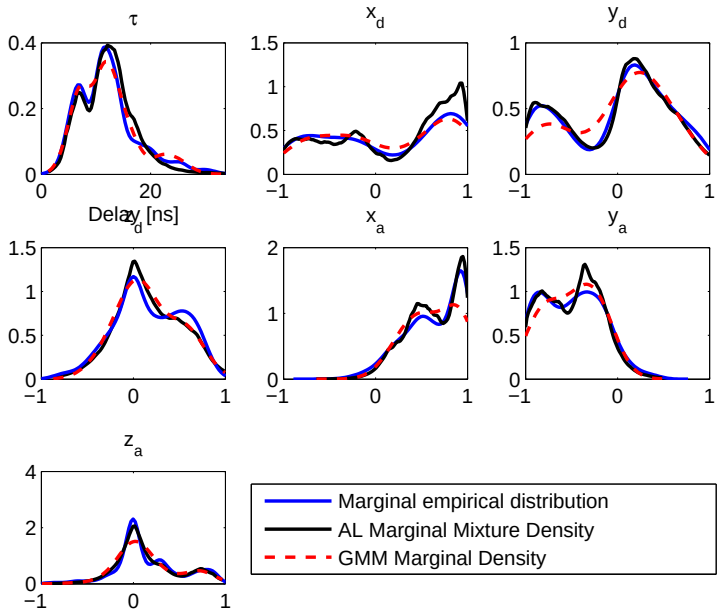

Figure 1: Marginal empirical distributions for all the measurements, the AL mixture model and the Gaussian mixture model.

Figure 1 shows the marginal empirical distributions of all the measurements as well as for the marginal distributions estimated by the AL and GMM clustering algorithms. The GMM seems to have a poor fit for some cases where there is a sharp variation in the marginal distribution. However, the AL mix-

ture also deviates from the measured marginal empirical distribution in some cases.

It is important to note that, as the data is clustered based on the delays and the cartesian coordinates, the different clustering algorithms have inherent modeling assumptions about the delays and the cartesian coordinates. The GMM (and the K-means algorithm) assumes that the observations for the cartesian coordinates and delays are normally distributed, whereas the AL mixture model assumes asymmetric Laplace-distributed observations. These assumptions will have an impact on the clustering results. In previous work, channel model parameters have often been derived directly from the clustering data, by performing a maximum-likelihood estimation of the parameters based on the residuals from the clustering algorithm.

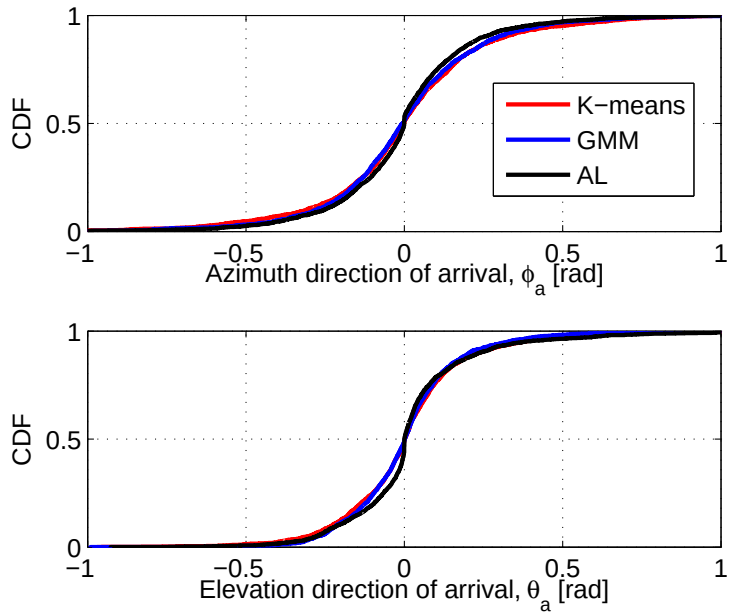

Figure 2: CDFs of the residuals for the angles ϕ_a and θ_a based on the K-means algorithm, the Gaussian mixture model (GMM) and the asymmetric Laplace (AL) mixture model.

Figure 2 shows the CDFs of the residuals for the azimuth and elevation directions of arrival, based on the K-means algorithm, the Gaussian mixture

model (GMM) and the asymmetric Laplace (AL) mixture model, without using any power-weighting. As seen here, the CDFs are quite similar for the K-means algorithm and the GMM. The residuals for the angles of departure and arrival were calculated by transforming back from the cartesian coordinates. The CDFs of the angles are fairly similar, except that the residuals for the AL clustering algorithm have heavier tails and more values close to the cluster center, corresponding to a more spiky shape of the probability density function.

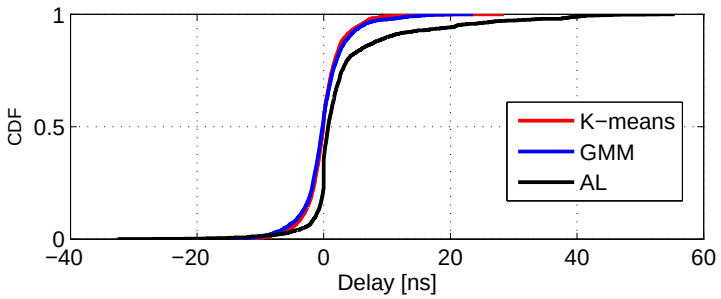

Figure 3: CDFs of the residuals for the delays, based on the K-means algorithm, the Gaussian mixture model (GMM) and the asymmetric Laplace (AL) mixture model.

CDFs of the residuals for the delays are shown in Figure 3. For the GMM and the K-means algorithm, the delays are symmetric around zero, which is a direct effect of the modeling assumptions in the clustering algorithms. The CDF for the AL mixture is asymmetric with much heavier tails. Furthermore, the probability of having components arriving earlier than the cluster center is much smaller for the AL clustering results. This shows that the clustering method can have a significant impact on the estimated cluster parameters. The K-means and GMM tend to find clusters with components that are evenly distributed around the cluster centroid due to the Gaussian assumption. For example, in the power weighted case, these algorithms will tend to assign multi-path components arriving before a strong multi-path to the same cluster.

6.1 Parameter estimates based on different clustering methods

In this section, we compare the residuals for the three different clustering methods. Then, we also estimate parameters for the asymmetry, μ, and mode, δ, for the different dimensions based on the residuals for the different clustering algorithms, using a maximum likelihood method for the AL distribution. These

results are also compared with the parameter estimates of μ and δ from the AL clustering algorithm. Here, we also note, that when clustering using for instance the GMM, it would make more sense to calculate the estimates for the Gaussian distribution, since this clustering method assumes Gaussian-distributed data. However, if the data is assumed to follow an asymmetric Laplace distribution, then, the AL mixture model should provide better results.

Table 4 shows the estimated parameters of μ and δ with no power weighting. First, we note that results for K-means and GMM are quite similar. They both show small values for the asymmetry, which is likely due to the Gaussian assumption. The estimates for the AL are quite different from the results for the K-means algorithm and GMM, which implies that the choice of clustering algorithm will have a big impact on the clustering results. Furthermore, we note that the AL clustering results exhibits quite small values for the asymmetry with respect to the angles, but a larger asymmetry for the delay, which will have a significant effect on the channel model parameters.

Table 4: Estimated parameters of the asymmetry, μ, and the standard deviation, σ, of the AL distribution for arrival angles, departure angles and delay, for K-means, GMM and AL-clustering.

	K-means	GMM	AL	K-means	GMM	AL
	μ	μ	μ	σ	σ	σ
τ	0.01	0.04	0.31	0.31	0.36	0.46
ϕ_a	0.00	0.00	-0.02	0.34	0.32	0.31
θ_a	0.01	0.00	0.04	0.25	0.25	0.25
ϕ_d	0.00	0.02	-0.00	0.28	0.26	0.23
θ_d	0.01	0.01	0.02	0.21	0.18	0.19

7 Discussion and Conclusion

It has been pointed out that all clustering algorithms make assumptions regarding the data. For instance, when the K-means algorithm or a GMM is used for clustering, it is implicitly assumed that the data is Gaussian. These clustering methods might still be very useful for clustering data that is indeed *not* Gaussian. However, these assumptions will still influence the estimated parameters and the clustering results, and a better clustering could perhaps be achieved using a different clustering algorithm. In this paper, we have presented a clustering algorithm based on an asymmetric Laplace mixture model. This model is more complex compared to the K-means and the GMM, but has the advantage of being based on modeling assumptions that are closer to

the assumptions made in many cluster based channel models. In this paper, we have presented results using the GMM and the AL clustering methods. It should be noted that the clustering algorithms also will influence the channel model parameters that are not included in these clustering methods, such as cluster and ray decays, arrival rates and fading distributions. The impact these clustering algorithms have on these channel model parameters will be investigated in future work.

Power weighted versions for the K-means, GMM and the AL mixture model have also been provided. Power-weighting allows for greater variability of observations with low power. However, the power-weighting does not take the fact that the mean multi-path component power depends on the delay into account. This means that clusters with large delays will in general have a greater variance. This might be a good idea, but it has also been pointed out that there seems to be no apparent physical motivation on how to scale the covariance matrix as a function of the power. Furthermore, when applying power-weights, the effective sample size is reduced, which might be a problem when the data is based on a limited number of measurement scenarios.

Lastly, the change of variables from spherical to cartesian coordinates is standard practise and makes the modelling easier; however, a better choice would be to define the model directly on the space $\mathbb{R}^+ \times \mathbb{S} \times \mathbb{S}$ of delay and angles. One way of doing this is to replace parts of the Gaussian mixture with a mixture of Kent distributions.

8 Appendix

In this section we derive the laplace-based clustering method presented in Section 3. The method is based on the EM-algorithm, which we assume is known to the reader, see for instance [10] for an introduction.

The parameter that are to be estimated are the cluster parameters $\theta_k = \{\delta_k, \mu_k, \sigma_k\}$ for $k = 1, \ldots, K$. To derive the formulas in the method, we note that an AL random variable can be represented as normal mean-variance mixture with mixture variable v_i. We will also use the standard formulation of mixture models using indicator variables by $z_{ik} = \mathbb{I}(x_i = k)$ for the class belongings. To simplify the presentation, we only derive the formulation in the one dimensional case; however, the multidimensional results follow almost immediately since the dimensions are assumed to be independent.

The expectation used in the E-step at iteration s of the EM algorithm is

$$\begin{aligned}\mathrm{Q}\left(\theta,\theta^{(s-1)}\right) &= \sum_{i=1}^{n}\mathbb{E}[\log\pi(y_i,\mathbf{z}_i,v_i|\boldsymbol{\Theta})|\star] \\ &= \sum_{i=1}^{n}\mathbb{E}\left(\mathbb{E}\left[\log\pi(y_i,\mathbf{z}_i,v_i|\theta)|\,\mathbf{z}_i,\star\right]|\,\star\right) \\ &= \sum_{i=1}^{n}\mathbb{E}\left(\sum_{k=1}^{K}z_{ik}\mathbb{E}\left[*\right]|\,\star\right),\end{aligned}$$

where $\mathbb{E}\left[*\right]=\mathbb{E}\left[\log\pi(y_i,v_{i,k}|\theta,z_{i,k}=1)|\,z_{i,k}=1,\star\right]$, and $\star$ denotes $\{p_i,y_i,\theta^{(s-1)}\}$. The second equality is due to the tower property of the expected value and third comes from the mixture formulation using the indicator variables $z_{i,k}$.

From formulation (7) one can deduce that $\pi(y_i,v_{i,k}|\theta)$ is proportional (with respect to θ) to $\pi(y_i|v_{i,k},\theta,z_{i,k}=1)$. With $D_{ik}=y_i-\delta_k-p_i^{-1}v_{ik}\mu_k$ we thus have

$$\begin{aligned}&\mathbb{E}\left[\log\pi(y_i,v_{i,k}|\theta,z_{i,k}=1)|\,z_{i,k}=1,\star\right] \\ &\quad=-\log(\sigma_k)-\mathbb{E}\left[D_{ik}^{\mathrm{T}}\frac{p_i^2v_{i,k}^{-1}}{2\sigma_k^2}D_{ik}|z_{i,k}=1,\star\right]+C \\ &\quad=-\log(\sigma_k)-\frac{p_i^2\mathbb{E}[v_{i,k}^{-1}|z_{i,k}=1,\star](y_i-\delta)^2}{2\sigma_k^2} \\ &\qquad-\frac{\mathbb{E}[v_{i,k}|z_{i,k}=1,\star]\mu_k^2}{2\sigma_k^2}+\frac{p_i(y_i-\delta_k)\mu_k}{\sigma_k^2}+C,\end{aligned}$$

where C is a constant independent of θ. The expectations in the expression above have closed form expressions presented below in Section 8.1. Nothing in the equation above depends on $\mathbf{z}$, and we therefore have

$$\begin{aligned}&\sum_{i=1}^{n}\sum_{k=1}^{K}\mathbb{E}\left(z_{ik}\mathbb{E}\left[\log\pi(y_i,v_{i,k}|\theta,z_{i,k}=1)|\,z_{i,k}=1,\star\right]|\,\star\right) \\ &\quad=\sum_{i=1}^{n}\sum_{k=1}^{K}\mathbb{E}\left(z_{ik}|\star\right)\left(-\log(\sigma_k)-\frac{p_i^2\mathbb{E}[v_{i,k}^{-1}|\star](y_i-\delta)^2}{2\sigma_k^2}\right. \\ &\qquad\left.-\frac{\mathbb{E}[v_{i,k}|\star]\mu_k^2}{2\sigma_k^2}+\frac{p_i(y_i-\delta_k)\mu_k}{\sigma_k^2}\right)+C.\end{aligned}$$

Interchanging the sums and using that

$$\mathbb{E}\left(z_{ik}|p_i,y_i,\theta^{(s-1)}\right)=\mathbb{E}\left(\mathbb{I}(x_i=k)|p_i,y_i,\theta^{(s-1)}\right)=\pi_{ik}$$

simplifies the equation above to

$$\sum_{k=1}^{K}\left(-\frac{1}{\sigma^2}\begin{Bmatrix}\delta_k\\ \mu_k\end{Bmatrix}^{\mathrm{T}}\mathbf{Q}_k\begin{Bmatrix}\delta_k\\ \mu_k\end{Bmatrix}+\frac{2}{\sigma^2}\mathbf{b}_k^{\mathrm{T}}\begin{Bmatrix}\delta_k\\ \mu_k\end{Bmatrix}\right.$$
$$\left.-\frac{1}{\sigma^2}\mathbf{H}_k-\log(\sigma_k)\sum_{i=1}^{n}\pi_{i,k}\right)+C,$$

where $\mathbf{Q}_k$, $\mathbf{b}_k$ and $\mathbf{H}_k$ are the one-dimensional versions of $\mathbf{Q}_{k,j}, \mathbf{b}_{k,j}$ and $\mathbf{H}_{k,j}$ in the method in Section 3. Differentiating the expression with respect to the parameters and setting the equations to zero, yields the desired updating expressions for the parameters presented in Section 3.

8.1 Expectations

To make the formulas more compact, set

$$a=\frac{\mu_k^2}{\sigma_k^2}+2,$$
$$b=p_i^2\frac{(y_i-\delta_k)^2}{\sigma_k^2}.$$

Using the expressions for expectations GIG random variables (See e.g. [14]) and using recurrence relations for the Bessel functions (see [15]) gives the following formulas for the desired expectations

$$\mathbb{E}[V_{i,k}|\star]=\sqrt{\frac{a}{b}}\frac{K_{3/2}(\sqrt{ab})}{K_{1/2}(\sqrt{ab})}=\frac{\sqrt{ab}+1}{b},$$
$$\mathbb{E}[V_{i,k}^{-1}|\star]=\sqrt{\frac{b}{a}}\frac{K_{-1/2}(\sqrt{ab})}{K_{1/2}(\sqrt{ab})}=\sqrt{\frac{b}{a}},$$

where $K_\lambda(\cdot)$ is the modified Bessel function of the second kind.

References

[1] M. Steinbauer, A. Molisch, and E. Bonek, "The double-directional radio channel," *Antennas and Propagation Magazine, IEEE*, vol. 43, no. 4, pp. 51–63, Aug 2001.

[2] K.-H. Li, M.-A. Ingram, and A. Van Nguyen, "Impact of clustering in statistical indoor propagation models on link capacity," *Communications, IEEE Transactions on*, vol. 50, no. 4, pp. 521–523, April 2002.

[3] P. Kyösti *et. al.*, "WINNER II Channel Models," *D1.1.2 V1.*, Sep. 2007.

[4] L. Liu, C. Oestges, J. Poutanen, K. Haneda, P. Vainikainen, F. Quitin, F. Tufvesson, and P. Doncker, "The Cost 2100 MIMO Channel Model," *Wireless Communications, IEEE*, vol. 19, no. 6, pp. 92–99, December 2012.

[5] IEEE802.15.3c-2009, " Part 15.3: Wireless Medium Access Control (MAC) and Physical Layer (PHY) Specifications for High Rate Wireless Personal Area Networks (WPANs), Amendment 2: Millimeter-wave- based Alternative Physical Layer Extension," Oct. 2009.

[6] A. Maltsev, R. Maslennikov, A. Lomayev, A. Sevastyanov, and A. Khorayev, "Statistical Channel Model for 60 GHz WLAN Systems in Conference Room Environment," *Radioengineering*, june 2011.

[7] K. Yu, Q. Li, D. Cheung, and C. Prettie, "On the tap and cluster angular spreads of indoor WLAN channels," in *Vehicular Technology Conference, 2004. VTC 2004-Spring. 2004 IEEE 59th*, vol. 1, May 2004, pp. 218–222 Vol.1.

[8] C. Schneider, M. Ibraheam, S. Hafner, M. Kaske, M. Hein, and R. Thoma, "On the reliability of multipath cluster estimation in realistic channel data sets," in *Antennas and Propagation (EuCAP), 2014 8th European Conference on*, April 2014, pp. 449–453.

[9] N. Czink, P. Cera, J. Salo, E. Bonek, J.-P. Nuutinen, and J. Ylitalo, "Improving clustering performance using multipath component distance," *Electronics Letters*, vol. 42, p. 33, 2006.

[10] A. P. Dempster, N. M. Laird, and D. B. Rubin, "Maximum likelihood from incomplete data via the EM algorithm," *Journal of the Royal Statistical Society. Series B (Methodological)*, vol. 39, no. 1, pp. 1–38, 1977.

[11] N. Czink, P. Cera, J. Salo, E. Bonek, J.-P. Nuutinen, and J. Ylitalo, "A Framework for Automatic Clustering of Parametric MIMO Channel Data Including Path Powers," *IEEE Vehicular Technology Conference*, sep 2006.

[12] C. Gustafson, K. Haneda, S. Wyne, and F. Tufvesson, "On mm-Wave Multi-path Clustering and Channel Modeling," *IEEE Transactions on Antennas and Propagation*, p. 14451455, Mar 2014.

[13] S. Kotz, T. Kozubowski, and K. Podgorski, *The Laplace Distribution and Generalizations: A Revisit With Applications to Communications, Exonomics, Engineering, and Finance*, ser. Progress in Mathematics Series. Birkhäuser Boston, 2001.

[14] B. Jørgensen, *Statistical properties of the generalized inverse Gaussian distribution*, ser. Lecture notes in statistics. Springer, 1982, vol. 9.

[15] "Nist digital library of mathematical functions," online companion to [16]. [Online]. Available: http://dlmf.nist.gov/

[16] F. W. J. Olver, D. W. Lozier, R. F. Boisvert, and C. W. Clark, Eds., *NIST Handbook of Mathematical Functions*. New York, NY: Cambridge University Press, 2010, print companion to [15].

Paper VII

Polarimetric Propagation Channel Characterization at 60 GHz with Realistic Shadowing

This paper presents results based on polarimetric radio channel measurements at 60 GHz in a small meeting room room and in an empty, unfurnished conference room. The measurements in the small meeting room were performed using dual-polarized virtual antenna array elements at both the Tx and Rx sides and includes LOS and NLOS scenarios. In the unfurnished conference room, a directional horn antenna was scanned in the azimuth plane and the Rx antenna was an omnidirectional antenna. Based on these measurements, the paper presents experimental values for the cross-polarization ratios (XPRs) of the propagation paths as well as cluster decay parameter estimates for the two different rooms. Lastly, the eigenvalue spreads of dual and single-polarized antenna arrays are investigated.

To be submitted to *IEEE Wireless Propagation Letters*, as,
C. Gustafson and F. Tufvesson
"Polarimetric Propagation Channel Characterization at 60 GHz with Realistic Shadowing"

1 Introduction

Frequency bands in the millimeter-wave range, i.e., bands in the frequency range of $\sim 30 - 300$ GHz, are promising candidates for short-range high data-rate wireless radio systems. However, accurate characterization and modeling of the propagation channel is required in order to be able to efficiently make use of the available bandwidth in the mm-wave range. To the authors' best knowledge, only a few papers deal with the polarization characteristics of mm-wave propagation channels, and there is a lack of knowledge on how to properly model those. In general, orthogonally polarized elements will exhibit a very low correlation. This characteristic can be utilized to combat fading through polarization diversity, or to increase the spectral efficiency through spatial multiplexing using multiple-input multiple-output (MIMO) systems with orthogonal antenna elements. The effectiveness of these polarization techniques are highly dependent on the characteristics of the XPRs [1]. At 60 GHz, XPR values of of 10-20 dB for first and second order reflections have been reported for office environments [2]. In [3], XPR values in the 70 GHz band, in shopping mall, railway and office environments, were observed to be in the range of about 10-30 dB. This indicates that the XPR is larger at these higher frequencies as compared to at lower frequencies. At 5.2 GHz, mean values of the XPR have been reported to be 6.6 and 6.3 dB in office and conference room environments, respectively [1]. In the Winner II channel model [4], the XPR parameter values have mean values of 4-12 dB for 2-6 GHz. In this paper, we present experimental values of the XPRs of the propagation paths at 60 GHz, based on indoor measurements in a small meeting room and an empty, unfurnished conference room. Furthermore, cluster decay rates are estimated and eigenvalue spreads are investigated.

2 Channel Measurements

2.1 Small meeting room

The small meeting room has a floor size that is 3 m×4 m . The meeting room contains a table, bookshelves, a whiteboard and has a window at the wall. The Rx is placed in one of the corners of the room, emulating a device such as a TV-screen. The Tx is placed in different locations at the table. For the NLOS scenarios, a water-filled human phantom is placed in a chair, blocking the direct path between the Tx and Rx. Such a phantom has previously shown realistic shadowing behavior at mm-wave frequencies [5]. The Rx used in the measurement was an open waveguide and the Tx was a biconical antenna.

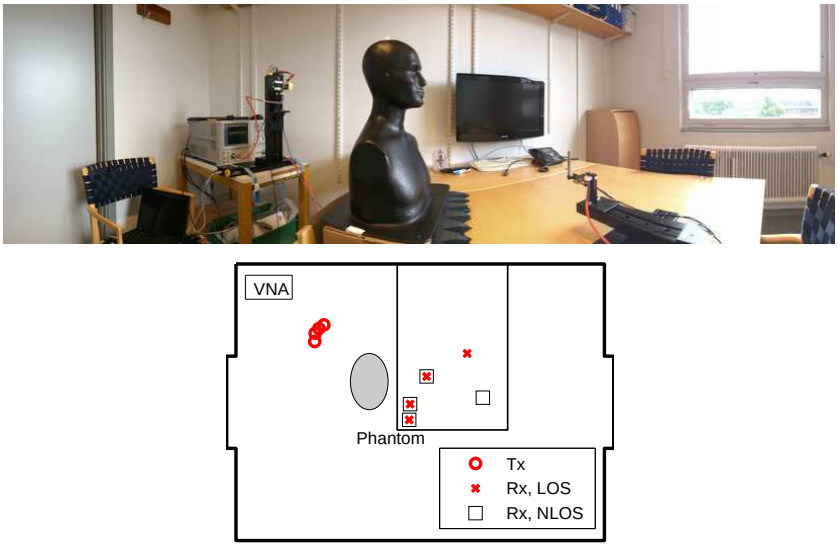

Figure 1: Measurement setup in the small meeting room (left) and floor plan of the LOS and NLOS measurements (right).

The measurements in the small meeting room is based on the virtual antenna array technique. Electromechanical positioners are used to move the antennas, forming a virtual array. The orientation of the antennas were changed so that the E-field was vertically and horizontally polarized, on both sides. At the Tx, the virtual array formed a 5×5 dual polarized rectangular array in the horizontal plane. Similarly, at the Rx side, the virtual array formed a 5×5 dual polarized rectangular array in the vertical plane. Together, the virtual arrays emulates a 25×25 dual-polarized MIMO system with 50×50 virtual antenna ports. In total, 4 LOS and 4 NLOS measurements were performed in the small meeting room, resulting in a measurement set of $20,000$ impulse responses. The measurements were performed with a vector network analyzer (VNA), measuring frequency transfer functions from 58-62 GHz, using 801 equally spaced frequency points with a transmit power of - 7 dBm for each virtual Tx antenna port. Additionally, a power amplifier (PA) and a low-noise amplifier (LNA) were connected directly to the Tx and Rx antenna, respectively. The influence of the coaxial cables, PA, LNA and coaxial-to-waveguide transitions was removed from the measured data in a post-processing step, using back-to-back measurements.

2.2 Unfurnished Conference Room

The conference room is unfurnished, with one door on one side of the room and with two windows on the other side of the room. The walls are made of brick covered in plaster and the floor is carpeted. In this room, the rotating antenna technique was employed. A directional horn antenna with a gain of about 20 dBi and half power beam-width of 18° was used as a Rx antenna. The Rx was placed in the center of the room, mounted to a rotation stage. The Tx was an omnidirectional biconical antenna with a gain of approximately 1 dBi, and was placed at a distance of 1.3 m from the Rx antenna. A PA and an LNA was used at the Tx and Rx, respectively. The Rx was rotated and transfer functions were measured every 1° using a VNA, with the same settings as in the small meeting room. The measured data was calibrated using a back-to-back measurement, and the peak antenna gains were removed from the measurement data.

3 Results

For the small meeting room, the SAGE algorithm was applied on the measured data in order to produce double-directional estimates of the multi-path components. Measured data for the co- and cross-polarized antenna patterns were included in the SAGE algorithm, so that the antenna gains were de-embedded from the data. For the conference room measurements, the impulse responses for each measurement angle was plotted on top of the basic floor plan, with the delay scaled with the speed of light, so that it corresponds to a path distance. This is shown in Fig. 2, for V-V and H-V polarization combinations. The figure also includes mirrored images of the Tx, based on the locations of the walls in the room. The peaks in the impulse responses for V-V and H-V polarization were then identified based on a local peak search around the mirror images. A peak is considered to be observed if its power is more than 3 dB above the noise floor of the impulse resonse, and, that the peak is at least 6 dB stronger than the smallest value in that local area. An ad hoc search area of $\pm 5°$ and ± 0.75 ns around the mirror image was found the be appropriate.

3.1 Cross-polarization ratios

The cross-polarization ratio for the propagation paths is defined here as the ratio between the power of the co-polarized component of a multi-path component (MPC) to its corresponding cross-polarized component. Each MPC is

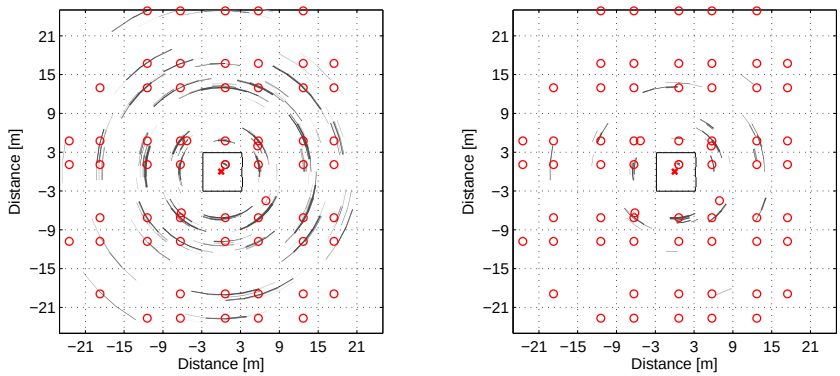

Figure 2: Measured impulse responses in the conference room for co-polar (top) and cross-polar (bottom) configurations of the Rx antenna. The mirror images for the Tx location are also shown as circles.

assumed to have a complex amplitude defined as

$$\boldsymbol{\alpha} = \begin{pmatrix} \alpha_{VV} & \alpha_{VH} \\ \alpha_{HV} & \alpha_{HH} \end{pmatrix}. \tag{1}$$

The cross-polar propagation path ratios are then defined as

$$XPR_V = \frac{|\alpha_{VV}|^2}{|\alpha_{HV}|^2}, \quad XPR_H = \frac{|\alpha_{HH}|^2}{|\alpha_{VH}|^2}. \tag{2}$$

The XPR values found based on the results from SAGE algorithm for the meeting room, and based on the peak detection method described above can be seen in Fig. 3. No significant difference was found for the line-of sight (LOS) and non-line-of-sight (NLOS) scenarios, so the data set for LOS and NLOS were combined. The values are in the range of 10-30 dB, which is in agreement with the values reported in [3]. Since the values for the different environments and polarizations are quite similar, the data for all XPRs were combined into one data set. The mean and variance of a normal distribution was estimated using maximum-likelihood based on the combined data set. The combined data set and the estimated normal distribution is shown in Fig. 4. The estimated mean and standard deviation of the normal distribution was $\mu = 17.1$ dB and $\sigma = 5.2$ dB, respectively. The measurement data for the conference room was also used to calculate the XPR values for all delays and measurement angles. Only values where the measured impulse response sample

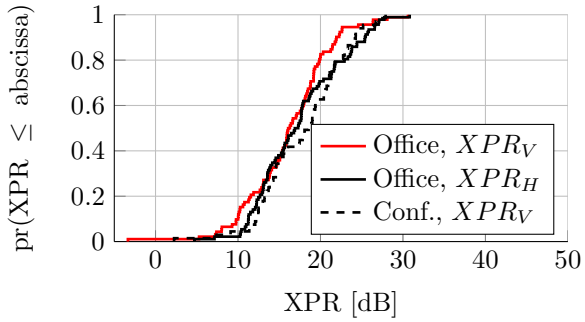

Figure 3: Cumulative distribution function for the propagation path XPRs in meeting room and conference room environments.

was above the noise floor, for both the co- and cross-polarized, were included when doing this. The XPR values now cover a wider range compared to the specular XPRs, as it now also includes diffuse scattering. The ML-estimates for a normal distribution gave the parameter values $\mu = 8.3$ dB and $\sigma = 6.5$ dB.

3.2 Eigenvalues

Eigenvalue distributions were investigated based on the measurements in the small meeting room. Smaller sub-arrays were created based on the larger virtual arrays used in the measurement. A large number of rectangular 2×2 sub-arrays, at both the Tx and Rx sides, with inter-antenna element distance of 2 mm were created. These sub-arrays were created with three different antenna orientations: V-V, V-H and a combination with 2 vertical and 2 horizontal antenna elements at each side. This way, the sub-arrays for each polarization combination have the same number of antenna elements, and were used to measure in the same spatial position.

The eigenvalues for all of these 4×4 MIMO channel matrices corresponding to these subarrays were calculated for each polarization combination, using all the measured frequency points and all of the measured LOS and NLOS scenarios. The eigenvalues were normalized with respect to the median value of the strongest eigenvalue for each polarization combination, in order to facilitate a comparison of the eigenvalue spreads. As seen in Fig. 5, the eigenvalue spread for the 4×4 MIMO channels in LOS scenarios are significantly smaller compared to the spreads for arrays with H-H and V-V polarization orientation of the antennas. For the NLOS scenarios, the eigenvalue spreads are not that

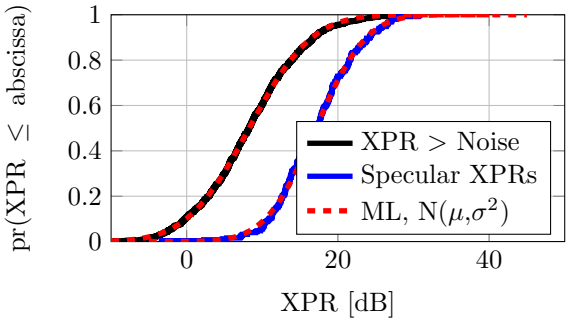

Figure 4: Cumulative distribution functions of the XPRs for all specular paths, and for the all the XPRs in the conference room based on impulse response sample above the noise floor and Gaussian distributions based on ML-estimates for the data.

different for the different polarization combinations.

3.3 Cluster decay

The cluster decay was estimated based on both the SAGE results for the small meeting room and based on the measurements in the unfurnished conference room. For the modeling of the cluster decay and cluster fading, the reader is referred to [6]. We note that the cluster decay estimation assumes that the measurement data is describing the peak power of the cluster, i.e., the main multi-path component of a cluster. For the conference room measurement, this assumption is justified since the measurement data only includes specular reflections that are observed in an unfurnished room. As previously observed in [7], the main component in each cluster is usually attributed to specular reflections. For the SAGE results in the meeting room environment, the assumption is justified by the fact that the results from the SAGE algorithm was set to only estimate 30 MPCs in each scenario. Upon examining the results, very few components were attributed to non-specular interactions.

Fig. 6 shows the estimated cluster decay based on the conference room measurements, for V-V and H-V polarization combinations. In this case, the estimates are based on ordinary least squares (OLS) and a maximum likelihood (ML) expression for censored data. The censored data is assumed to be located at delays corresponding to the calculated path distances for the mirror images of the Tx antenna, where the received power is below the noise floor. The ML method is likely to produce more accurate results, but is however not

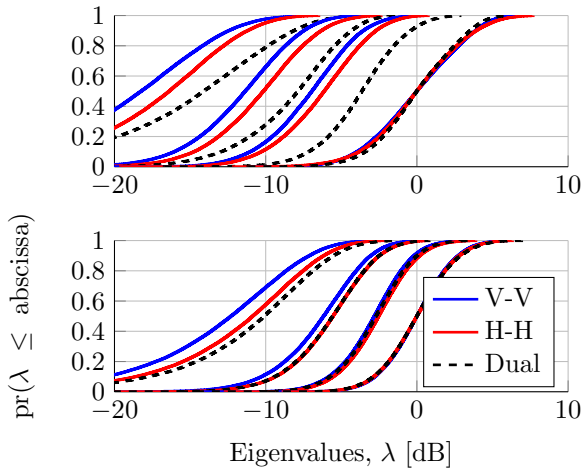

Figure 5: Cumulative distribution function of the four eigenvalues of 4×4 MIMO channel matrices, based on all measurements in the meeting room environment, for LOS and NLOS scenarios and different polarization orientations of the Tx and Rx array antennas.

that different from the results for the OLS. The estimated parameters based on ML for the cluster decay and fading are shown in Table I. The values for the cluster decay constants for V-V and H-V are quite similar, which indicates that it might reasonable to model the cluster decay using a single cluster decay parameter. Furthermore, the estimated parameters for the V-V polarization are very similar to the estimates for a conference room presented earlier in [6]. In that case, the conference room was slightly larger, and the estimated parameters were based on MPC estimates that were clustered using an automatic clustering algorithm. This indicates that it could be feasible to accurately estimate the cluster decay using the rotating antenna technique in an unfurnished room.

For the meeting room scenarios, the cluster decay was estimated based on an ML estimator for a truncated normal distribution [6]. The estimated cluster decay is shown in Fig. 7, for all four polarization combinations. The estimated parameters are shown in Table I. The cluster decay constant for the meeting room is smaller than for the conference room, corresponding to a steeper cluster decay in the meeting room environment. A smaller room size is likely to give rise to a steeper cluster decay, since the MPCs are likely to experience a larger number of interactions as a function of delay in a smaller environment.

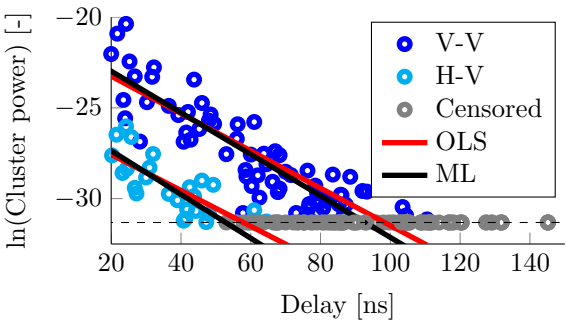

Figure 6: Cluster decay estimation based on the conference room measurement data, using ordinary least squares (OLS) and a maximum likelihood (ML) expression for censored data, for V-V (top) and H-V (bottom) polarization orientations.

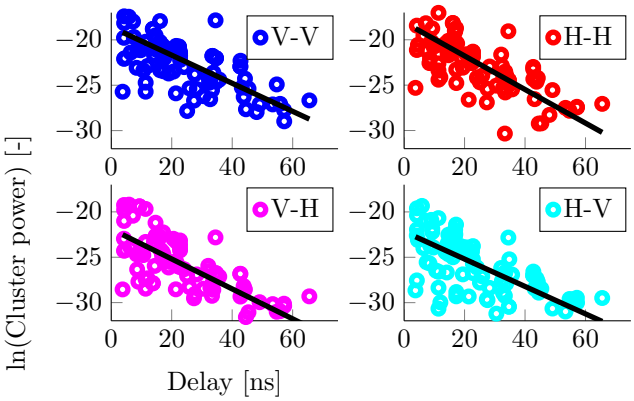

Figure 7: Cluster decay estimation based on the meeting room measurement data, using a ML expression for truncated data, for the different polarizations.

Table 1: Estimated cluster decay for the meeting and conference room.

Enivronment	Pol.	m	Γ [ns]	σ [dB]
Conference room	VV	-20.7	8.7	1.41
Conference room	HV	-25.0	8.3	0.97
Meeting room	VV	-18.6	6.5	2.5
Meeting room	HH	-18.1	6.1	2.5
Meeting room	VH	-21.9	6.1	2.6
Meeting room	HV	-22.1	6.6	2.6

4 Conclusions

This paper presents experimental values for the specular propagation path XPRs, based on measurements in a small meeting room and in an empty, unfurnished conference room. The results show that the specular XPRs are in the range of 5-30 dB, that can be modeled as normally distributed random variables with a mean and standard deviation of 17.1 dB and 5.2 dB, respectively. The eigenvalue spreads for 4×4 MIMO channels with different polarization combinations of the Tx and Rx antenna elements have been investigated. It was shown that the eigenvalue spreads are significantly smaller for dual polarized antenna arrays compared to co-polarized arrays in the LOS scenario. This means that polarization, as expected, provides an efficient way to nearly double the spectral efficiency for LOS mm-wave communication. In the NLOS scenario, no significant difference of the spreads were observed. Furthermore, the paper presents values for the cluster decay rates for the meeting room and conference room environments. The cluster decay rate for the co- and cross-polarized components were found to be very similar, indicating that it might be possible to model the cluster decay using a single cluster decay constant. The cluster decay constants for the different polarizations were estimated to be in the range of 8.3-8.7 ns for the conference room and 6.1- 6.6 ns for the small meeting room. The cluster decay rate is highly dependent on the room size, with a smaller cluster decay constants for smaller rooms, corresponding to a steeper decay.

References

[1] ITU-R, "Propagation data and prediction methods for the planning of indoor radio communication systems and radio local area networks in the frequency range 900 MHz to 100 GHz," *Radiowave propagation*, Feb. 2012.

[2] A. Maltsev, R. Maslennikov, A. Sevastyanov, A. Khoryaev, and A. Lomayev, "Experimental investigations of 60 GHz WLAN systems in office environment," *Sel. Ar. in Comm., IEEE Journal on*, vol. 27, no. 8, pp. 1488–1499, October 2009.

[3] A. Karttunen, K. Haneda, J. Järveläinen, and J. Putkonen, "Polarisation Characteristics of Propagation Paths in Indoor 70 GHz Channels," *COST IC1004, Krakow, Poland*, Sep. 2014.

[4] P. Kyösti and *et. al.*, "WINNER II Channel Models," *D1.1.2 V1.*, Sep. 2007.

[5] C. Gustafson and F. Tufvesson, "Characterization of 60 GHz Shadowing by Human Bodies and Simple Phantoms," *Radioengineering*, vol. 21, no. 4, pp. 979–984, 2012.

[6] C. Gustafson, D. Bolin, and F. Tufvesson, "Modeling the cluster decay in mm-wave channels," in *Antennas and Propagation (EuCAP)*, April 2014.

[7] C. Gustafson, K. Haneda, S. Wyne, and F. Tufvesson, "On mm-Wave Multipath Clustering and Channel Modeling," *Antennas and Propagation, IEEE Transactions on*, vol. 62, no. 3, pp. 1445–1455, March 2014.